Medical Image Analysis for the Detection, Extraction and Modelling of Vascular Structures

By

Iván Macía Oliver

Dissertation presented to the Department of Computer Science and Artificial Intelligence in partial fulfillment of the requirements for the degree of

Doctor of Philosophy

PhD Advisor:

Prof. Manuel Graña Romay

At

The University of the Basque Country
Donostia - San Sebastián
2012

Contents

List of Figures

List of Tables

List of Algorithms

Chapter 1

Introduction

This chapter provides the general introduction to the Thesis intended to allow a quick appraisal of its contents, contributions, supporting publications and structure.

Section 1.1 provides the motivation behind this line of research. Section 1.2 enumerates the objetives set for the Thesis. Section 1.3 enumerates the contributions of this Thesis. Section 1.4 enumerates the publications obtained while working in this Thesis. Section 1.6 details the structure of the Thesis.

1.1 Motivation

Vascular-related diseases are among the most important public health problems nowadays. Heart and cerebrovascular diseases are respectively the first and third cause of death in 2006 in the U.S.A [55]. Malignant tumors are the second cause of death, and their growth is directly associated with vessel recruitment and angiogenesis [57]. Besides, vascular diseases are one of the principal causes of death and disability in people with diabetes [31]. These facts are enough justification for the research efforts providing a better understanding of the structure of the vascular system and related processes and diseases, and leading to any improvement of diagnostic and intervention procedures.

The vessel structure of the blood circulatory system is one of the most complex structures of the body. Blood vessel anatomy has been studied from castings and in-vivo examinations in order to build models that provide valuable insight into the normal and variant circulatory anatomy and that helps to understand the causes, evolution and outcome of several vascular-related diseases. However, many answers to simple questions about vascular morphology and angiogenesis remain open[139].

Recent advances on medical imaging provide high resolution 3D images of the vessel structures, so that the generation of accurate patient-specific geometric *in-vivo* vessel models [8] and related quantitative measurements has become feasible. This has resulted in a wide range of new applications for computer-assisted diagnostic, intervention and follow-up of vascular-related diseases. Image-based vessel analysis provides valuable information for planning and navigation during interventional procedures, both to avoid damaging vital structures and to use vessels as anatomical landmarks for orientation and localization of structures of interest. Moreover, comprehensive image-based vascular analysis has opened new horizons in the discovery and understanding of the vascular structure and underlying processes, such as angiogenesis and blood circulation, that may help to understand the evolution of diseases in which vascular structures play an important role [15] [142].

In the recent years, a vast variety of methods and approaches has emerged dealing with vascular extraction, analysis and modelling with increasing complexity [87]. In order to accelerate the research in the area it is necessary to identify the constituing components or building blocks of the different methods, their individual influence, their relationship, and the influence and sensitivity of their parameters, so as to build robust and efficient methods that can be used in a clinical setup. Moreover, it is necessary to provide the scientific community with verified and well designed tools that allow to compare results obtained from different methods, replace some individual components and reproduce the experiments without extra effort on implementation.

From the modelling point of view, we have detected the lack of a widely accepted knowledge representation model for vascular networks that is able to store in a structured manner the information obtained from the extraction algorithms in such a way that can readily be used in the clinical applications. Such a model is needed for the future development of the field and for our own applications.

This thesis pretends to be a little contribution in the aforementioned directions.

1.2 Objectives

1.2.1 General Objectives

- Develop a generic and verstatile information model for storing and accessing information describing vascular structures.

- Develop a set of methods for robust automated detection, extraction, quantification and analysis of vessels depicted in volumetric angiographic modalities, such as Computerized Tomography Angiography (CTA) or Magnetic Resonance Angiography (MRA).

- Perform a clinical validation of the developed methods, to ensure that can be used in clinical practice due to their accuracy, robustness and speed.

- Develop specific methods for the automated analysis and follow-up of Abdominal Aortic Aneurysms (AAA) after Endovascular Repair (EVAR) as depicted in CTA images.

- Contribute to the field of vascular image analysis by providing some insight into existing methods, developing new modelling and analysis paradigms and providing tools to reproduce the experiments and compare different approaches.

1.2.2 Operational Objectives

- Develop an information model for vascular structures. The model should accommodate easily the information obtained from the vascular structures by the extraction algorithms that take a vascular (angiographic) image as source. The model should also provide a versatile, intuitive and adequate structure for the development and practice of clinical applications of vascular image analysis.

- Study the underlying components and parameter setup of the most successful vascular detection algorithms. The focus here is on a subset of medialness functions, that provide measures of the likelihood of an image point to be on the centerline. We explore both differential and integral approaches.

- Propose a generic framework for vascular tracking algorithms, which is a subset of vascular extraction algorithms that deal with direct centerline extraction. Study how this framework accommodates existing approaches and may allow to generate complex schemes and study the influence of components working individually or as a group, such as the choice of section estimation algorithm or vesselness function.

- Develop a novel method for the segmentation of AAAs after EVAR, with special focus on the thrombus segmentation, as it is the most challenging structure. The method should be suitable for clinical routine, which implies that is fast, robust, has a small set of parameters easy to setup and with little sensitivity and allows for easy correction of the results.

- Provide the scientific community with a software toolkit for vascular image analysis, that implements many popular approaches to vascular detection and extraction in a seamless framework, that allows comparing different approaches in a simple way for scientific discovery and rapid prototyping of vascular applications.

1.3 Contributions of the Thesis

1.3.1 Scientific Contributions

- Chapter 2 provides an extensive review on studies on vascular morphology, vascular-related diseases, vascular imaging (aka angiographic) modalities, techniques for vascular extraction and analysis from these images and practical applications of vessel analysis. It also provides a novel taxonomy of vessel attributes to be incorporated into a Vessel Knowledge Representation model for vessels.

- Chapter 3 postulates a *Vessel Knowledge Representation* (VKR) model that is suitable for representing, in a compact and structured, manner the geometrical, topological and contextual information obtained from the vascular analysis, in such a manner that can be used in practical clinical applications.

- Chapter 4 provides more insight into existing ideal cylinder shape models for vascular anaylisis, basically the cylinder and toroid models, by providing alternative reference frames and studying the behaviour of the principal image curvatures both theoretically and experimentally. It also proposes a new Helix model in order to study the influence of both, the geometric shape curvature and torsion, in the image curvatures. Finally it studies different section profiles for these models, in order to infer some conclusions about the scales to be used in the image analysis of real tubular shapes.

- Chapter 5 consists of a review of edge and ridge detection techniques in images and their relationship with the detection of curvilinear structures.

- Chapter 6 provides a detailed analysis of the scales to be used when applying some relevant vascular detection functions (aka *vesselness* functions). It identifies different types of scaling parameters in these detectors, and tests their individual influence and their relationship against synthetic datasets with different noise levels, in order to establish some scale selection criteria for these detectors in real datasets.

- Chapter 7 proposes an architecture for modelling vascular tracking processes, which is a subset of vessel extraction methods, called *Generalized Vascular Tracking (GVT) Framework*. We demonstrate how the different components and stages of the GVT process model provides a systematic approach to vascular tracking that incorporates different components into the system with increasing complexity.

- Chapter 7 also proposes, in the context of the GVT Framework, a novel method for vascular section estimation during tracking procedures. It incorporates an optimization stage that uses specific modified vascular detectors as cost functions, in order to obtain accurate vascular sections when the direct detection approach fails. We demonstrate the validity of this new approach with experiments using real datasets.

- Chapter 8 provides a novel segmentation method for both the lumen and thrombus of AAAs after EVAR as they are depicted in Computed Tomography Angiography (CTA) images.

- Chapter 8 also proposes a method for the automatic detection and quantification of endoleaks present in AAA thrombus as depicted in CTA images. To the best of our knowledge, there were no previous works in the literature dealing with this specific task.

1.3.2 Technological Contributions

The main technological contributions of this thesis are implemented in the Image-based Vascular Analysis (IVAN) Toolkit, which is a set of C++ software libraries for vascular detection, analysis and modelling in medical imaging developed using concepts of generic programming. Due to its design, this toolkit may provide the scientific community with an important tool to accelerate discovery and encourage reproducible in the field of vascular image analysis. The IVAN toolkit provides the following specific technological contributions:

- An implementation of the VKR model whose design allows for extension and inclusion of new concepts.
- A repository of *vesselness* detectors which includes several popular approaches in the literature, designed to be easily extended by incorporation of new methods or modification of existing ones.
- An implementation of the GVT Framework whose design allows for the interchange of components or the addition of different stages so as to provide flexibility in the design of complex vascular tracking methods. This provides a means to test the influence of the different components both individually and in conjunction.
- A means of generating synthetic models of ideal shapes as volumetric images, such as the cylinder, toroid or helix models of Chapter 4, with different cross-sections, shape and image parameters and noise levels.
- A means of reproducing the experiments developed in this thesis.

Many of these functionalities have been used in the experiments developed in this thesis.

1.4 Publications

- Ivan Macia, Manuel Graña, Celine Paloc. Knowledge Management in Image-based Analysis of Blood Vessel Structures. *Knowledge and Information Systems* 30(2):457-491, 2012.
- Iván Macía, Manuel Graña. Vascular Section Estimation in Medical Images Using Combined Feature Detection and Evolutionary Optimization. In Proc. Hybrid Artificial Intelligent Systems (HAIS), 503-513, 2012.
- Ivan Macia, Manuel Graña, Josu Maiora, Celine Paloc, Mariano de Blas. Detection of Type II Endoleaks in Abdominal Aortic Aneurysms After Endovascular Repair. *Computers in Biology and Medicine* 41(10): 871-880, 2011.
- I. Macia, M. Graña, and C. Paloc. Towards a Proposal for a Vessel Knowledge Representation Model. R. Setchi et al. (Eds.): Knowledge Based and Intelligent Information and Engineering Systems KES 2010, Part IV, LNAI 6279, 80-87. Springer Heidelberg, 2010.
- Legarreta, J., Boto, F., Macía, I., Maiora, J., García, G., Paloc, C., Graña, M., de Blas, M. Hybrid Decision Support System for Endovascular Aortic Aneurysm Repair Follow-up. In Proc. Hybrid Artificial Intelligence Systems, 500-507, 2010.

- Maiora, J., García, G., Macía, I., Legarreta, J., Boto, F., Paloc, C., Graña, M., Abuín, J. Thrombus Volume Change Visualization after Endovascular Abdominal Aortic Aneurysm Repair. In Proc. Hybrid Artificial Intelligence Systems, 524-531, 2010.
- Maiora, J., Garcia, G., Tapia, A., Macia, I., Legarreta, J.H., Paloc, C., De Blas, M. & Grana, M. Thrombus Change Detection After Endovascular Abdominal Aortic Aneurysm Repair. International Journal of Computer Assisted Radiology and Surgery. Springer-Verlag, Vol. 5 (Suppl 1), pp. S15, 2010.
- Iván Macia Oliver, Jon Haitz Legarreta, Céline Paloc, Manuel Graña, Josu Maiora, Guillermo García. Segmentation of Abdominal Aortic Aneurysms in CT Images using a Radial Model Approach. Intelligent Data Engineering and Automated Learning - IDEAL, Emilio Corchado, Hujun Yin (eds) LNCS 5788, Springer Verlag, 2009.
- I. Macía, J.H. Legarreta, F.Boto, C.Paloc, M. Graña, G. García, J. Maiora, M. de Blas. Segmentación de Aneurisma Abdominal de Aorta en Imágenes CT Mediante un Modelo Radial: Estudio Preliminar. XXVIII Congreso Anual de la Sociedad Española de Ingeniería Biomédica, CASEIB 2009.
- Josu Maiora, Guillermo García, Arantxa Tapia, Ivan Macía, Jon Haitz Legarreta, Manuel Graña. Stent Graft Change Detection after Endovascular Abdominal Aortic Aneurysm Repair. Intelligent Data Engineering and Automated Learning - IDEAL, Emilio Corchado, Hujun Yin (eds) LNCS 5788, Springer Verlag, 2009.

1.5 Vascular Image Analysis Pipeline

The *Vascular Image Analysis Pipeline*, depicted in Figure 1.1, represents, in a very compact manner, the different sources of information (in orange) and processes (in blue) involved in the development of a clinical application of vascular image analysis.

From the source angiographic images a first stage of detection or enhancement of vascular structures is performed. This is usually followed by an extraction stage which isolates the vascular structures obtaining additional geometric, topological or clinical information about the vascular structures. Depending on the approach, the detection and extraction stage may be considered as a single operation. The information resulting from the extraction process is stored in an information model of vascular structures so it can be used efficiently by the clinical applications. The quantification stage involves obtaining quantitative or qualitative information on the vascular structures and, depending on the operation performed, can follow the detection or extraction stages or may only need the information stored in the model. In any case, the information obtained in this stage is also stored in the model.

Despite the direction of the processing pipeline is from left to right, the requirements are usually built the other way. The clinical application determines which information is needed and in turn determines the image study to be performed on the patient. This in turn determines the most suited detection and extraction methods methods used to obtain the necessary information for the clinical applications.

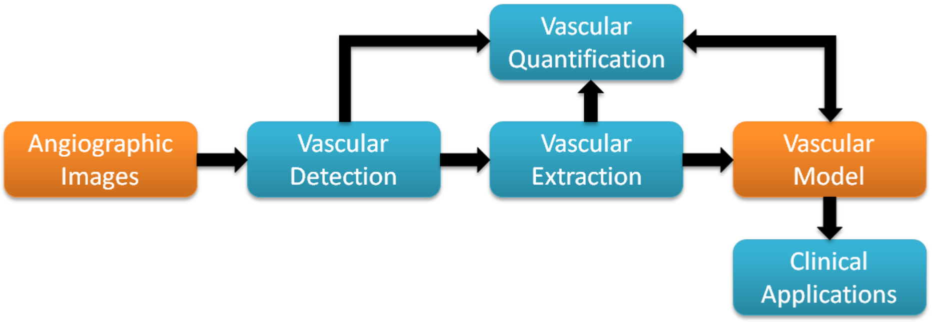

Figure 1.1: Vascular Analysis Pipeline

1.6 Structure of the Thesis

The structure of this thesis follows the vascular image analysis pipeline depicted in Figure 1.1. Following this scheme, *Chapter 2* introduces the general problem of vascular image analysis, describing the clinical applications and the anatomical and algorithmic information that is used to build the vascular information model that is postulated in *Chapter 3*. *Chapter 4* describes and analyzes some ideal shape models of vascular structures that will be used in the detection and extraction stages. *Chapter 5* introduces some concepts of image analysis of edge, ridge and curvilinear structures. *Chapter 6* focuses on the detection of vascular structures, with special emphasis on the parameter and scale selection of some popular vesselness functions. *Chapter 7* postulates a framework for vascular tracking for direct vascular centerline extraction whose utility is tested experimentally in synthetic and real datasets. *Chapter 8* deals with the specific clinical application of analysis of AAA after EVAR. Due to the size of the vascular structures involved (the aorta), the shape of the abdominal aneurysm (which is a blob-like structure) and the endoleaks (which can be regarded as amorphous), this problem is treated separatedly since it requires specific methods of analysis that are not described in the previous chapters.

Chapter 2

Overall review

In this chapter we review some background ideas of the ensuing chapters of the Thesis. To set the stage we review Vascular Morphology and some facts of vascular related diseases serve as an introduction for the main applications in the field of modelling and visualization of vessel structures. Next, we provide an overview of the angiographic modalities for image-based diagnostic of vascular-related diseases, as well as the applications and vessel information which is considered relevant for diagnosis in the clinical practice. We will comment on the current computational techniques for vessel information extraction from the angiographic images. Finally we discuss the need for a Knowledge Representation Model in this area of medical image processing.

The structure of the chapter is as follows: Section 2.1 introduces some biological ideas about vascular morphology. Section 2.2 gives a short review of vascular diseases. Section 2.3 is referred to image based diagnosis information and tools. Section 2.4 introduces the algorithms for vessel extraction from angiographic images. Section 2.5 introduces the Knowledge Representation Model (KRM).

2.1 Vascular Morphology

The efficient distribution and collection of nutrients requires a blood vessel branching tree structure, except at the level of the capillaries. Vascular networks are asymmetric tree structures, in which each parent branch, with diameter D_1, is bifurcated (except in very rare cases) into two branches with smaller diameters (D_2 and D_3). The tree may be also locally unbalanced regarding the diameters of child branches ($D_2 \neq D_3$) and the number of bifurcations along each path from the root to the leaves of the each subtree [68]. Geometric models for the description of vessel bifurcations were first proposed by Murray [116, 150] and later by Oka and Nakai [121] specifying relationships between vessel widths and angles based on physiological observations.

Recent studies [69, 190] have discovered that the construction of the vascular trees obeys a set of scaling laws which minimize both, the energy cost of fluid transportation, which decreases as the diameters increase, and the energy cost of construction and maintenance of the vessel structure, which increases with larger diameters. These scaling laws are morphometric relationships between the arterial volume, cumulative length, and diameter of a branch and its distal subtree. In particular, it can be seen that, in order to minimize the power needed to maintain the blood circulation operation over the network, the diameter relationship between a parent branch and its two child branches is:

$$D_1^k = D_2^k + D_3^k, \tag{2.1}$$

with average values of k typically between 2 and 3.

With respect to the vessel sections, in a simplistic approach the vessel sections can be assumed to be circular but, in fact, most of the times it has some smooth irregular round shape. The thickness of the vessel wall is non-negligible, but most imaging modalities only depict the vessel *lumen*, which is the space where the blood flows. Few imaging modalities, such as Intravascular Ultrasound (IVUS), can image the vessel wall.

In order to estimate the complexity and branching frequency of the human vascular trees [32, 154, 59, 61, 60, 62], several studies used and adapted the *Strahler order* of branching complexity [157], defined originally for hidrology studies but applicable to all branching, tree-like structures. The original Strahler ordering system assigns the order 1 for the smallest branches. When two vessels join into a confluent vessel, the order of the confluent vessel is increased by 1 if the two child vessels have the same order; otherwise the parent assumes the order of the highest order child. However, the use of the original order as defined by Strahler encountered the problem of diameter overlapping among vessels of consecutive orders in morphometry analysis of very large trees. In order to take into account the vessel radius, the *Diameter-defined Strahler Ordering System* [70] incorporated a new rule stating that: “When a vessel of order n meets another vessel of order $\leq n$, the confluent vessel is assigned order $n+1$ only if its diameter exceeds that of the lower order vessel by a certain amount, which is determined by the statistical distribution of the diameters of each order”. In practice, threshold computation must be iterative, since the diameter distribution has to be recalculated when the order is assigned. Applied to haemodynamic studies, this enhanced ordering system provides a reasonable and systematic way to handle main arteries that vary considerably in diameter along their length, such as the main pulmonary artery. In a morphometric study of the human lung vasculature casts [62] it was found that, in pulmonary arterial and venous trees, the relationship between the order of a branch [70] and its diameter follows closely a logarithmic scale. They found a maximal order of 15 for both arterial and venous trees of the human lung.

In order to represent the connectivity of asymmetric branches and to distinguish serial and parallel branches of the same order, three new concepts were introduced in [70]: *Vessel Segment*, *Vessel Element* and *Connectivity Matrix*. A *Vessel Segment*, corresponding to a branch, is the portion of vessel between two bifurcations. A *Vessel Element* is defined as a set of serially connected segments of same order. Statistical data of diameters and lengths are obtained for segments and elements. Haemodynamic flow circuits are composed of vessel elements. Ratios of segment/element can also be calculated for each order. The *Connectivity Matrix* is an upper triangular matrix, in which each element $C(m,n)$ is the ratio of the total number of elements of order m

whose parents are elements of order *n* divided by the total number of elements of order *n*.

The advent of new ismaging techniques such as Microcomputed Tomography and advanced algorithms for vascular segmentation, quantification and analysis, has recently improved the possibility of performing detailed studies of vascular morphology, i.e. in the coronary [177], renal[119] and pulmonary trees [137], and the ability to perform comparisons in populations [185], enhancing the understanding the structure, and physiology and patology of the corresponding organs.

2.2 Vascular-related Diseases

There are two main types of vascular accidents which occur with death consequences in about 5% of the population over 65 years-old: haemorrages and embolysms. Haemorrages can be produced by vessel ruptures due to aneurysms. An *aneurysm* is a local growth of the vessel diameter due to weakening of the vessel wall that suffers increased local elasticity. Aneurysms occur most commonly in arteries at the base of the brain (circle of Willis) and in the thoracic and abdominal aorta. Embolysms and thrombosis are obturations of the vessels as a consequence of a progressive abnormal local reduction or the vessel diameter or *stenosis* (pl. stenoses). There are several causes or conditions that lead to stenosis such as atherosclerosis, birth defects, diabetes, infection, inflammation or ischemia among others. Atherosclerosis is a condition in which the arterial wall thickens, due to the accumulation of a mixture of substances such as calcium, cholesterol fibrin and macrophage blood cells, which causes stenosis or occlusion of the vessel or aneurysms due to excessive compensation by enlargement of the vessel. The possibility of performing early diagnoses of aneurysms, stenoses or other vascular accidents may avoid further complications and thus, will decrease the morbidity and mortality associated to vascular-related diseases. There exists evidence [9] that regions of the vessel wall exposed to disturbed flow, such as at bifurcations and regions of high curvature, are prone to the initiation and development of atherosclerosis. Identification of such regions by geometrical analysis may provide further insight into the development of this disease.

There are some pathological conditions for which blood vessels play an important role in their evolution. The most important case is the vascularization of malignant tumors. In order for the cancer cells to obtain appropriate nutrients to grow and to get rid of waste material, tumors need to be vascularized. Tumors achieve this by several methods such as cooption (use of pre-existing vessels) and angiogenesis [57]. Furthermore, most of the conditions induce changes in vessels at different levels. Cancer induces the development of abnormal, tortuous vessels [44], that can be reverted by successful treatment [66]. Images of the retina may provide information on pathological changes caused by local ocular diseases and early signs of certain systemic diseases [6, 189, 27, 179]. Other examples may be hypertension and diabetes, which induce the narrowing of the arteries. For example, a recent study has shown that retinal vessel microvascular structure is associated to risk of mortality from ischemic heart disease and stroke [179].

2.3 Image-based Diagnosis

An introductory overview of medical imaging modalities is needed to understand their ability to produce images of the blood vessels, their possible application as tools in clinical and research studies, and the requirements that the image processing and knowledge representation techniques need to take into account. The diagnostic support provided by the vessel structure images is further made concrete by the specification of precise attribute measurements.

2.3.1 Angiographic Modalities

Nowadays, there are many medical imaging modalities and protocols devised specifically for the visualization of vessels, that are generally denoted with the term *angiography*. Some of them include the injection of a modality-specific contrast agent that enhances the visualization of blood vessels[1].

- *Digital Substraction Angiography* (DSA) is an evolution of the original *X-ray Angiography* (XA) technique, that digitally subtracts a pre-contrast image from a contrasted images obtained after injection of a contrast agent. Until recently, DSA has been considered the standard vessel imaging technique in many diagnostic and interventional procedures, such as assessment of renal and carotid artery stenosis, cerebral aneurysms, acute limb ischemia or arterio-venous malformations (AVMs) among others. The main advantage of DSA imaging is that it allows real-time, live visualization of very thin vessel structures, and thus can be used during interventional procedures. However, DSA involves radiation exposure, is a 2D modality and, more importantly, is an invasive procedure and thus, it has an associated risk of small complications. DSA is gradually being replaced by some non-invasive 3D imaging techniques, such as *Computerized Tomography Angiography* (CTA) and *Magnetic Resonance Angiography* (MRA).

- CTA images are standard Computerized Tomography (CT) images generated by contrast injection simultaneously with the image acquisition. Depending on the synchronization of the image acquisition with the flood flow, different contrasts may be obtained, such as those corresponding to the arterial phase, venous phase, post-constrast phase, etc., that depict several stages of the contrast inflow into the vessels. Some of the applications of CTA imaging are analysis of stenosis in renal arteries, aortic aneurysms, brain aneurysms or AVMs, atherosclerosis assessment and detection of vein clots in legs. The main drawback of the technique is the radiation dose that the patient receives during the scanning procedure. With the advent of multidetector technology and improved computational image reconstruction schemes, acquisition haves increasing spatial resolution obtained in faster times with less radiation dose.

---

[1] The first coronary *X-ray angiography* (XA) was performed accidentally by Sones and Shirey in 1958 [155]. While injecting contrast material in the right ventricle, the catheter slipped into the right coronary artery and for the first time discovered the advantages of imaging the vessels.

Figure 2.1: Examples of Angiographic Modalities. From left to right XA of the coronaries, DSA of the brain vessels, MRA in venous phase and CTA showing stent after endovascular aortic aneurysm repair.

- MRA comprises several techniques based on Magnetic Resonance Imaging (MRI). The techniques are based either on imaging flow effects or on using contrast agents, like in *Constrast-enhanced MRA* (CE-MRA). Vessel images can also be obtained by adequate pulse sequences without contrast. *Time-of-flight MRA* (ToF-MRA) uses a short echo time and flow compensation to enhance contrast of blood vessels. It is commonly used in the head and neck, where it gives very high resolution image, but has problems in areas of slow blood flow such as aneurysms. *Phase-contrast MRA* (PC-MRA) manipulates the phase of the MR signal providing both, the vessel image and the corresponding flow speed. PC-MRA has larger acquisition times, since the techniquerequires acquisitions in the three basic orientations (axial, sagittal and coronal). Recent MRI techniques include *Fresh Blood Imaging* (FBI) [115] and *Susceptibility Weighted Imaging* (SWI), also called *BOLD Venography* [136, 186]. The main advantage of MRA compared to CTA is the absence of radiation exposure while maintaining very high image quality, though spatial resolution is lower in MRA than in CTA. However, as acquisition times are larger, motion artifacts are more likely to appear.

- *Vessel Ultrasound* imaging is a non-invasive procedure that allows live blood vessel visualization. Combined with the technique of Doppler ultrasound, it also gives measures of blood flow. It can help the physician to visualize and assess, stenoses, aneurysms, varicose veins and many other vessel accidents. The main problem is its low signal-to-noise ratio which gives poor image quality.

- *Optical* imaging can also be used to image vessels, as in *Retinal Fundu*s images, where vessel analysis is used in the assessment of retinopathy and as an early sign of systemic diseases [6]. Other recent techniques, such such as non-invasive *Near-infrared* (NIR) imaging can be used for visualizing vessels through the skin [49].

- *Intravascular Ultrasound* (IVUS) provides a means of imaging the vessel wall by using a catheter equipped an ultrasound transducer.

- A recent development is the study of the mechanic properties of vessel wall by *Magnetic Resonance Elastography* [181].

2.3.2 Applications of Vessel Analysis

As the technology of vessel imaging evolves, improving the quality and quantity of information about vessel structure that can be obtained, the applications have also flourished. Here we enumerate some of the current ones, that will motivate the knowledge representation and manipulation tools to be discussed below.

- Surgery:
  - Surgery planning: allows the surgeon to evaluate the alternative actions and prepare for the intervention [148].
  - Planning and navigation [166] during interventional therapy and biopsy : here vessel structures are critical by themselves, but also serve as spatial reference or anatomical landmarks for planning and navigation. It has strong real-time requirements, because the vessel structure may be changing during the intervention. Sometimes it requires fusion of diverse imaging modalities to improve the interaction.
  - Training of surgeons and interventional radiologists using annotated virtual reality systems [165], virtual atlases, etc.
- Cancer studies:
  - Non-invasive estimation of tumor malignancy and growth by vessel quantification and localization of abnormal vessel clusters [24, 25].
  - Simulation and study of vessel angiogenesis, which is an important factor in malignant tumor growth [44].
- Diagnosis of vessel-related diseases:
  - Characterization of retinal-related diseases such as diabetic retinopathy or retinopathy of prematurity by induced changes in vessel attributes such as diameter and tortuosity [27].
  - Quantification of stenosis and aneurysms [67].
  - Decission support systems [97] for vessel-related disease [85].
- Image registration using vessel as landmarks [112]. This is typically used in non-rigid registration [81].
- Studies of vessel morphometry [62] and haemodynamics [162]:
  - Construction of geometric models of vessel trees [68] which allow direct visual diagnosis and fast and interactive visualization and exploration, and provide by themselves a good understanding of the (patient-specific) vessel network structure and morphology.
  - Discovering of statistical properties of attributes of vessels in healthy and diseased populations [26].

  - Performing comparative studies, possibly with the help of anatomical atlases, for assessment of vascular diseases, malformations and abnormalities.
  - Simulation of arterial flow and pressure in organs that cannot be accessed by direct measurement [146], in aneurysms [168] or for detecting regions of turbulent flow prone to atherosclerosis, such as bifurcations and high-curvature regions [9].

2.3.3 Vessel Attributes

The main concern in this section is about measurements that can be somehow obtained from the images and used as a basis for diagnosis or any of the applications enumerated above. These measurements are the relevant attributes of the KRM proposed below for the feasible applications, therefore their identification from the literature survey is an important step in the KRM definition. We must also take into account the possility that the user may specify some qualitative attributes, which are not the result of any quantitative model, though the user may base its observation on results from computational image processing. They are used by the clinician to perform diagnoses or intervention decision upon their direct inspection. Structural attributes refer to the morphological and structural description of the vessel network. They are mostly used for intervention planning and some diagnoses based on structural morphology and complexity, like angiogenesis. The quantitative description of each vessel branch and bifurcation are the bricks of the decision support and model building processes.

Qualitative Vessel Attributes

- *Vessel Shape*: provided by direct visualization of volumes containing (contrasted) vessels, or surface reconstructions of the vessel walls.

- *Vessel Section Shape*: needs some processing and abstraction from the image in order to obtain an adequate representation. It may include the vessel wall or not, depending on the imaging modality.

- *Anatomical Location*:more important than the absolute anatomical position of the vessels is the relative position of the vessels with respect to adjacent organs or structures of interest, specially pathological structures. It may require some image registration techniques to obtain the corrected relative location.

Structural Vessel Attributes

- *Vessel Network Topology*: the topological structure and interconnections of the vascular network.

- *Total Number of Branches*: when restricted to a space, it is a measure of vessel density.

- *Depth Level*: this is the level of a branch with respect to the root branch of the vessel network, that is, the minimum number of bifurcations that separate the current branch from the root branch.
- *Strahler Number*: a numerical measure of branching complexity [157, 70].
- *Branching Frequency*: the number of bifurcations and distance between them.
- *Ratios of Branch Radii*: several measures can be obtained as ratios of branch radii in a bifurcation. The *branching ratio* and the *area expansion ratio* are related to the portion of flux going into each branch in a bifurcation [5].

Quantitative Vessel Attributes

- *Diameter*: is an immediate indicative of an aneurysm or stenosis.
- *Length*: though the absolute length of a branch may not be significative by itself, and its significance is relative, it can be used to calculate other important properties such as tortuosity.
- *Size/Volume*: volume and size of the vessels in a region of interest provides quantitative measurements of vessel growth.
- *Tortuosity*: is a property of a curve being twisted, having many turns. There have been several attempts to quantify this property [175]. Tortuosity is a sign of vessel abnormality usually associated to disease. Bullitt *et al.* [26] distinguish three types of blood vessels tortuosity:
  - *Type 1*: where vessels elongate and become tortuous. This may occur in conditions such as retinopathy, prematurity, hypertension and aging.
  - *Type 2*: vessels that make frequent changes of direction and may appear as a “bag of worms”, as occurs in arteriovenous malformations and within hypervascular tumors.
  - *Type 3*: high-frequency low-amplitude oscillations or ’wiggles’, associated to the neovascularity of malignant tumors.
- *Surface Area*: as arteries bifurcate and convert into arterioles and capillaries, the total surface area for the same blood supply increases.
- *Section Area*: this is the area of the vessel cross-sections, which lie in the normal plane to the medial line or centerline.
- *Blood Velocity*: differences in blood velocity can be measured or simulated in order to find stagnancy regions or abnormal circulation patterns.
- *Elasticity*: of the vascular walls that may change due to plaque accumulation or the presence of aneurysms.

2.4 Vessel Extraction and Analysis in Angiographic Images

The literature on algorithms for vessel detection and extraction from angiographic images is huge [87, 124, 71, 16, 42]. The approaches differ in the assumptions made about the shape and structure of the physical vessels, the medical imaging modalities, the mathematical models describing the vessels, the image features used to detect them, and the algorithmic schemes to extract them. In a recent outstanding review [87], vessel lumen segmentation techniques are categorized according to the underlying models (assumptions on appearance and geometry of the real vessels as shown in the images) image features (quantitative image metrics used to detect the vessels), and extraction schemes, (the algorithm used to extract the vessels, according to the assumed models and defined image features), sometimes with the help of data mining algorithms [184]. We proceed to describe the most important angiographic image-based vessel modelling and extraction (segmentation) techniques, emphasizing the most salient elements that are are explicitly modelled in our knowledge representation framework.

2.4.1 Vessel Models in Image-based Analysis

In image-based analysis of vascular networks, there are two main types of assumptions and models used for vessels: *photometric* models and *geometric* models. *Photometric* models deal with the generation of vessel images in the corresponding angiographic modalities. They are modality dependent, used for image processing, and outside the scope of this paper. On the other hand, *geometric* vessel models describe elements such as branches, corresponding cross-sections, bifurcations and relationships in the vessel tree. They are relevant to the definition of our knowledge-based model which is more influenced by geometrical considerations.

Surface-only models of vessels, defined by polygonal meshes, which may be obtained directly from vessel segmentations by polygonal reconstruction [45], are not relevant to our endeavour because they are rather difficult to manipulate and useless as the basis for structural analysis and representation.

Vessels are elongated structures, except in some very specific (pathological) cases. For this reason, one of the most common approaches is to use the centerline as the main shape descriptor. The centerline corresponds to the medial loci of the vessel [17], centered inside the lumen, and constituting the centroid of successive cross-sections. The centerline allows to describe objects in terms of a tree of “elemental figures” [132]. However, it is very sensitive to vessel boundary details, so there has been an extensive research in algorithms that obtain smoother centerlines, such as Voronoi skeletons [117], shock loci of reaction-diffusion equations [152], “cores” (height ridges of medialness functions) [131] and distance transforms [20].

From the vessel’s centerline, the external contour can be modelled as a generalized cylinder [4], that is, a tubular shape with a curvilinear axis (the centerline) and varying width along its length, which is usually defined by the cross-sections along the centerline. Different shape descriptors can be used to define these cross-sections (see figure 3.4). Constraints can be imposed on the successive sections in order to maintain spatial coherence when producing 3D models of vessels [120]. Sometimes the external surface of the vessel can be modelled explicitly [45] or implicitly [164] [9] from the vessel centerline. A mesh surface model of the vessel wall can also be obtained by sweeping the cross-sectional contours [73, 118].

The tree structure of vessel networks is naturally described in the form of a graph, more specifically as trees (directed acyclic graphs) [52, 23, 148, 3, 128, 113]. A vessel graph is obtained from the segmentation by skeletonization (see 2.4.2) and analysis of line structures. The graph description is useful for operations such as pruning, trimming, correcting and reconnecting of vessel branches via graph-based techniques after initial extraction. Graph-based representations can be mapped back into visual representations providing a better insight into the vascular structure by means of symbolic renderings [52] or surface reconstructions from centerline and section data [42].

2.4.2 Extraction Schemes

Because of its central importance, we dwell on the methods for centerline extraction found in the literature. Note that initial vessel volume segmentation can be obtained by techniques such as simple thresholding, region-growing [19], wave tracking [135] or vessel-adapted level-sets methods [99] among others.

Centerline Extraction by Skeletonization: Centerlines can be extracted by 3D skeletonization of an initial volume vessel segmentation. Thinning algorithms [127] are based on iteratively removing points on the border of the object that do not modify its topology (simple points). The remaining set of points is the topological skeleton. The problem is that they usually provide a centerline at a pixel/voxel level. Subvoxel accuracy may be obtained by other methods, such as flux of gradient vectors of distance functions [20].

Direct Centerline Extraction: In some cases, a rough estimation of each slice's centerline point is enough to provide an approximate segmentation of the vessel tree, that may be useful for a more refined segmentation. This can be done by obtaining complete surfaces from the centerline, or on a section-by-section basis, by fitting models of sections or by extracting the section image planes and obtaining the boundaries by segmentation as in [83] (Figure 3.4).

The first approach to centerline extraction is interactive manual selection of centerline points and interpolation with or without an underlying mathematical curve model, such as a B-spline. However, this method is not very precise, and automatic algorithms are desiderable.

Direct centerline tracking algorithms start from a initial point or set of points, selected manually or automatically in the centerline or its vicinity, and try to iteratively extract consecutive vessel centerline points, usually by estimating vessel direction, until the end of the branch or tree is reached. Most of these methods also estimate the local vessel normal (section plane) and scale (approximate diameter) and differ mainly in the image features used for centerline tracking, in their ability to handle bifurcations and in their robustness to noise. We have found in the literature methods based on tracking multi-scale *medialness*[2] features [10], analysis of connected components of spheres [29], Kalman filtering [182], moments of inertia [54] and Bayesian tracking [86] among others.

Centerlines can also be obtained as *minimum cost paths* (geodesic paths) between start and end points detected on a branch or on the whole vessel tree. The inverse of the features or metrics used to estimate *medialness* measures can be used in this case as cost functions [176], minimized by optimization algorithms such as Dijkstra's shortest paths [38], graph-based schemes [122, 176], or the Fast Marching algorithm [2] used in [37].

Global Centerline Detection: Centerlines can also be obtained by calculating vesselness or medialness features in the whole region of interest and by obtaining patches of centerlines by connected local maxima (ridges) of these features [133]. These patches are usually too wide and usually need to be skeletonized in order to obtain the medial representation that corresponds to the centerline. Other operations involve pruning, for removal of noisy branches, and reconnection of broken branches, as vessel features sometimes yield low values at bifurcations. For the reconnection, local strategies of the aforementioned minimum cost paths approaches can be used between candidate reconnection points.

2.4.3 Vascular Feature Models

Several vessel (disease-related) features can also be modelled. *Stenosis* are usually modelled as local diameter reductions [46, 89]. *Aneurysms* are more difficult to model and quantify due to their shape variability. Specific models have been proposed for cerebral [114] and aortic [105, 101] aneurysms. *Calcifications and stents* often appear as hyperintense structures. Recently, methods have been proposed that combine appearance and geometric models for the segmentation of these structures from CTA images [72, 167]. Recently, we proposed an automatic method for the detection of *endoleaks* after endovascular repair of aortic aneurysms [104].

2.5 Knowledge Representation Model

There are some examples of specialized vessel representation systems in the literature. The *Vascular Modelling Toolkit* [130] focuses on the geometric modelling of vascular structures in order to generate surface and mesh models suitable for structural and haemodynamic studies. Gerig *et al.* [52] proposed a symbolic model that encodes shape features and structure relationships of vessels obtained from segmentations of angiographic images, and applied it to the analysis of cerebral vasculature in MRA images. The hybrid model proposed by Puig *et al.* [134] provides information of the topological relationships of the vessels and incorporates vascular accidents such as aneurysms and stenoses as special vessel segments. It is organized in three

---

[2] A medialness function quantifies to which degree a point is part of the centerline

layers: global structure, which is a graph-based structure, vascular surface and volume model. The model is constructed from segmented MRA images with application in a computer-assisted neurovascular system. The model proposed here tries to overcome some limitations of these early models, through a general yet flexible knowledge representation of vascular systems.

Common elements, components and stages found in our experience and literature review.

- In most of the cases, it is valid the assumption that the vessels are elongated, tube-like objects, whose length is much larger than the diameter.
- Vessels appear as hyperintense[3] structures (sometimes hypo) in the vascular imaging modalities, brighter that their neighboring tissues, though sometimes we can find contrast agent inhomogeneity or imaging artifacts.
- Homogeneity in vessel size and photometric intensity is desiderable, but usually it is necessary to deal with varying vessel widths and intensity inhomogeneities.
- The use of a vessel centerline, as a descriptor of the shape of the vessel and extraction and modelling of sections, is also a common element.
- Some schemes reuse well-known features, such as *medialness* functions. or intermediate representations, such as medial-based representations or skeletons.
- Some common processing stages can be identified in families of algorithms, for example, in vessel tracking procedures.

In fact, as emphasized in [87] many vessel algorithms rely on increasingly complex combinations of existing techniques, sometimes operating at different levels of abstraction. The identification of the building blocks that constitute the extraction schemes and the explicitation of some hidden assumptions and abstractions used in their conception is a crucial step for a better understanding of the underlying concepts for the improvement existing methods. This explicitation can be performed through the development of unified frameworks, which implement the most commonly used models, features and algorithms and identifying their appropriate settings.

In ensuing chapters of this Thesis, we propose a unified framework focused on the modelling of vascular vessel networks and related qualitative and quantitative information. The framework models the vessel network in such a way that is easy to be handled by extracting schemes based on image analysis, but also to be converted into other representations suitable in several applications (see Figure 3.1). Such a framework will allow:

- an increased automation of the processes, which, in turn, increases the reproducibility of the experiments and allows to perform large quantitative studies which would be impossible to tackle otherwise.

---

[3] Hypointense vessel can be converted to hyperintense just by inverting the image intensities.

- a quantitative comparison of the performance of different techniques under the same conditions and with known implementations, that may provide better insight into their behavior and that may lead to their optimization.
- an efficient reusability of components that will allow faster prototyping and more reproducibility in research studies.

Chapter 3

Vessel Knowledge Representation

We have detected the lack of a widely accepted knowledge representation model in the area of Blood Vessel analysis. We find that such a tool is needed for the future development of the field and our own research efforts. It will allow easy reuse of software pieces through appropriate abstractions, facilitating the development of innovative methods, procedures and applications. After the identification of the key representation elements and operations, we propose a Vessel Knowledge Representation (VKR) model that would fill this gap. We give insights on its implementation based on standard Object Oriented Programming (OOP) tools and paradigms. The VKR would easily integrate with existing medical imaging and visualization software platforms, such as the Insight ToolKit (ITK) and Visualization Toolkit (VTK).

The structure of the chapter is as follows: Section 3.2 describes the requirements for a Vessel Knowledge Representation (VKR) model. Section 3.3 gives details of the VKR. Section 3.4 provides some implementation details. Section 3.5 gives some final conclusions of this chapter.

3.1 Introduction

The diversity of medical and biological applications and the availability of huge amounts of high-quality information for vessel analysis has raised the problem of vascular knowledge representation in its full multi-faceted complexity . The purpose of this paper is to discuss appropriate knowledge representation and manipulation tools for vessel structures which could serve as a common ground for the development of compatible and reusable systems. We frame this study in the diversity of applications found in the literature, and in our actual research experience [104, 85, 108, 107, 105, 109, 106]. We contribute a *Vessel Knowledge Representation* (VKR) model that, due to its efficiency and versatility, may be used for a wide variety of image-based vessel extraction schemes and vessel analysis applications. This model aims to fill an information management gap that we have detected in the literature dealing with vessel structures computerized extraction and analysis of vascular structures.

We have in mind two objectives when proposing the *Vessel Knowledge Representation* (VKR) *Model*:

1. to ease the definition of new algorithms, providing a kind of road map of tools and applications.
2. to allow the easy reuse of previously generated pieces of software. The visualization of image processing as a kind of pipeline, allows the visualization of software reutilization as building blocks in this pipeline. This approach is common to some other medical imaging processes, like brain mapping.

3.2 Requirements of the Vessel Knowledge Representation (VKR) Model

The VKR model is being defined through a process of identification and abstraction of structural, geometrical and morphological properties of vessels in the literature and in our own research experience. This leads to the identification of data structures, operations and components used in the most common models and schemes for vessel extraction. This model can then be converted into an appropriate data representation, such as a mesh surface model, a refined segmentation or a symbolic visual representation. When rendered, these representations can be used for localization and for interactive exploration of the VKR model and underlying properties in some of the applications described above. Alternatively, these derived data representations can also be used, for example, for numerical studies, such as simulations of haemodynamics, structural analysis or other medical and research applications out of the scope of this paper. The VKR model must include the geometry and topology of vessel trees with constituting branches, bifurcations and sections, as well as vascular accidents such as stenoses, aneurysms and abnormal regions, such as those feeding neighboring tumors. Models of these physical entities and related concepts used in vessel analysis applications must be devised and structured by using object-oriented design techniques.

We can make more precise some desired properties of our VKR model design:

- *Versatility*:
  - Modelling of low level entities, such as vessel centerlines or sections, without compromising higher level elements, such as the global graph-based model of the vessel tree and its traversal mechanisms.
  - Allowing several coexisting representations of the same vascular system, providing easy transformation among representations. This idea is illustrated in Figure 3.2 where different graph-based representation of the same vascular tree are shown.
  - Decoupling algorithms from underlying data structures. Abstract mechanisms must be provided for accessing, traversing and manipulating the data.

- *Efficiency*: as data amounts are huge in this kind of applications, and time requirements are increasingly tight, efficiency in terms of computational time and use of resources is highly desired.

- *Utility*: to be useful the VKR must take into account actual design practices and constraints from:

  - The actual state of the art vessel extraction algorithms (see section 2.4.2) that may have been used for generating the vessel data structure from the angiographic image data.
  - A broad range of clinical and research applications that will be increasing in complexity and response time requirements.

- *Complexity Hierarchy*: the framework should be able to provide different levels of complexity and abstraction in order to represent the vessel structures at different levels. The structures need to be represented at least at the tree, branch and section level and at each level geometric, topological and semantic information layers need to be managed.

- *Integration* : we require that the knowledge representation framework can be easily integrated with pre-existing frameworks which deal with certain specific models, processes and data structures efficiently, such as the *Insight Toolkit (ITK)* [187], for medical image segmentation, registration and analysis and the *Visualization Toolkit (VTK)* [144], for visualization of resulting vascular structures together with image data.

3.3 Model Description

3.3.1 The VKR Model in Context

The VKR model is the core of the diverse operations and functions related with vessel analysis techniques, as shown in the workflow diagram depicted in Figure 3.1. The boxes in this diagram correspond to data types of some kind, while the labeled arrows correspond to transformations or manipulations of the data. We have omitted the closed operations, such as branch pruning or image filtering. The VKR vessel representation can be obtained directly (see 2.4.2) from the angiographic image or volume or indirectly from the results of an intermediate image segmentation process. In the latter case, the segmentation detects the image/volume regions corresponding to the vessels, from which the vessel representation can be obtained by skeletonization (see 2.4.2), to obtain the centerlines, followed by section or boundary estimation. Alternatively, a set of disconnected volume vessel regions can be obtained by a global detection process of vessel features, followed by pruning and/or reconnection of centerline patches (see 2.4.2). We include in the diagram obvious storage and retrieval operation of the VKR to/from a file or database. The VKR model is the natural domain to perform measurements which can be added to it as an enrichment.

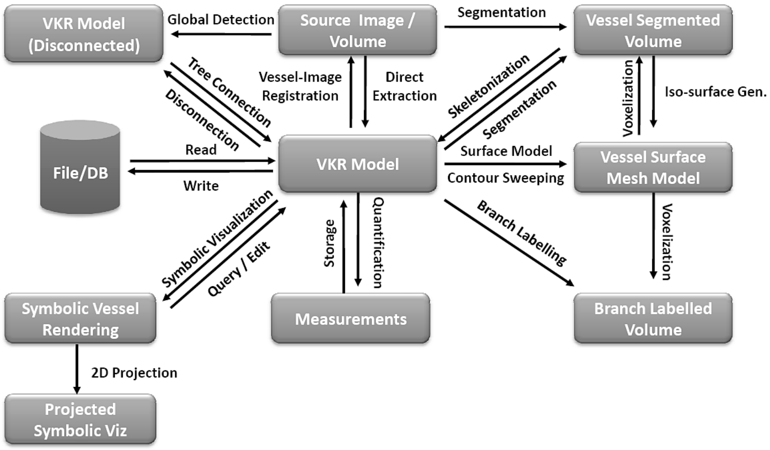

Figure 3.1: VKR Workflow Diagram

By assigning symbolic graphical representations or *glyphs* (such as lines, spheres, cones or more complicated shapes...) to the underlying components of the VKR model, a symbolic visual representation of the vessel tree can be obtained. This may be used as a roadmap, for agile exploration and interaction, or may be directly overlaid or projected onto the angiographic images, slices, or volumes in order to provide visual cues.

The VKR model can be the basis to build up a surface mesh of the vessel boundaries[1] by several techniques such as contour sweeping of the cross-sections or by an explicit or implicit surface model as explained in 2.4.1. The VKR model can also be used to generate a mask or Region of Interest (ROI) on the CTA/MRA volume for further processes. The VKR data can be then converted into a mesh surface by iso-surface reconstruction [98]. Generated surface meshes can then be used for direct visualization and navigation, possibly mixed with other symbolic, surface, volume or slice renderings, in a kind of Augmented Reality computational environment. In the same spirit, the identified and labeled branches can be mapped into the CTA/MRA volume or mesh surface, allowing increased interaction via direct structure picking. The mapping can go both ways, allowing the access to the VKR model from the visualization of the CTA/MRA volume, and visualization of CTA/MRA data corresponding to VKR selections.

3.3.2 Data Structures

The data structures of the model are designed in order to describe qualitative (i.e. section shape, anatomical location, diagnostic annotations) and quantitative (section area,

---

[1] This is only feasible with volumetric angiographies, but the model is able to handle 2D representations too

curvature) information (Figure 3.5) in such a way that can be handled efficiently both by the extraction schemes and by the final applications while keeping a high degree of versatility. The data structures represent vessel information at different levels ranging from a complete vascular network to a vessel center or boundary point.

3.3.2.1 Vessel Graph

In general, we can consider the vessel network as a binary tree structure since in most cases bifurcations split a branch into two [62], with some exceptions like the Circle of Willis in the brain [146]. Therefore, a graph representation is the natural choice for the structural representation in the VKR.

A graph typically consists of nodes, representing the modelled concepts, and edges, that connect the nodes and represent their relationships, which is in terms of parent/child for tree structured graphs. In our case, a *VesselNode* represents an abstraction of an element used for vessel representation and analysis at graph level. Such an element may be a vessel branch, bifurcation or vessel accident, among others. Anatomical vessel branches are modelled as nodes[2] (*BranchNode*) and if we need to assign properties to the bifurcations, we can also explicitly model them (*BifurcationNode*). In order to provide more modelling flexibility, we define also *Composite* nodes, which make use of the *Composite Pattern* [51] in order to group nodes. This way the group of nodes acts as a single entity, hiding their internal relationships and offering the possibility of building a hierarchy of several levels of abstraction complexity in the graph.

By inheritance of node objects we are also able to model conditions that occur in the branches themselves or in the surroundings (*FeatureNode*). We allow also nodes to model some abstract concepts, such as annotations that may be of interest in diagnostic applications. The properties of each node type are defined by specific attributes and operations and the use of OOP techniques such as polymorphism.

Our graph-based model, however, is not restricted to a tree structure, to provide the flexibility in its definition, that is necessary in some applications. For example, the number of parents of a node is not limited to one, although anatomical branches in general have a single parent. This flexibility allows for several types of representation of the same vessel network. The structure of these representations is open, since nodes can be, in principle, arranged in any desired manner. However, our model was designed at least to support a few representations that have been found useful for many vessel analysis applications. We will proceed to describe these representations and introduce the node types involved.

Branch Vessel Graph Representation The *Branch Vessel Graph Representation* (BVG) is the simplest representation of a vessel network in VKR. It consists of a graph of interconnected nodes of type *BranchNode*. This type of node is the most conspicuous in VKR models, since it represents the geometry and properties of vessel branches, which are the main constituents of physical vessel networks. The rest of the vessel network is in fact an abstraction of the relationship of vessel branches (such as bifurcations), related features, groupings of branches, etc. The most important part

---

[2] This differs from other works where nodes are modelled as graph edges [134]

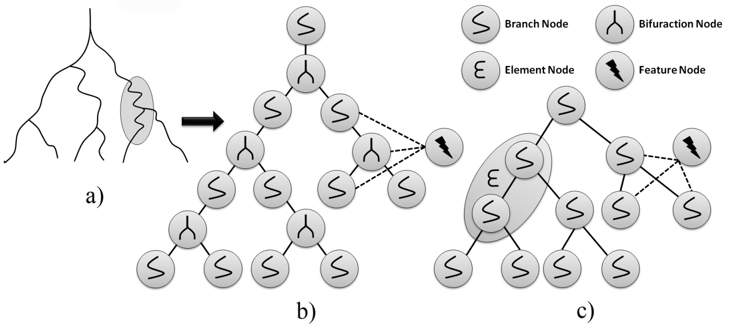

Figure 3.2: Vessel Graph Representations. a) Symbolic depiction of a vessel tree b) BVG rep. c) BBVG Rep and OEVG after incorporating an *Element* supernode.

of a *BranchNode* is the *Centerline Model* that is described in section 3.3.2.3. Several *BranchNode* instances can be connected in series, in order to divide a branch into different segments. This might be useful to model parts of a branch which require special attention, such as stenotic or aneurysmal regions, and separate them from the healthy regions.

Branch-bifurcation Vessel Graph Representation The *Branch-bifurcation Vessel Graph Representation* (BBVG) explicitly models the bifurcations using a *BifurcationNode*. In this case, the parent and children of a *BifurcationNode* need to be a *BranchNode* or any subclass of it.

Ordered Element Vessel Graph Representation The *Ordered Element Vessel Graph Representation* (OEVG) is most suited for morphometric and haemodynamic studies, since serial branches of the same order, with the order defined according to the *Diameter-defined Strahler Ordering System* [70], are grouped into a *CompositeNode* called *ElementNode*. In an OEVG representation, *BranchNodes* that are not grouped can also be considered as *ElementNodes* since they also represent an element in Strahler's system. In haemodynamic circuits, a series of vessel branches of the same order are the equivalent to an electric circuit composed of resistances in series.

3.3.2.2 Vessel Branch

A virtual vessel branch is represented in VKR by a *BranchNode,* and it corresponds to the vessel segment that extends between consecutive bifurcations. A physical vessel branch may also be represented by several concatenated *BranchNode* instances. This would be useful when the user wants to make a difference between different parts along the length of a physical branch, for example by indicating that part of a branch is stenosed. This is performed by associating corresponding accident node representations, such as the *StenosisModel*, to the *BranchNode*. This will be better described in section 3.3.2.7. The core of a vessel branch in our model is represented by the *Centerline Model* described next.

3.3.2.3 Centerline Model

The vessel centerline or medial loci [17] is an important part of our model, since it is a good descriptor of elongated objects. Compared to other descriptors, such as boundary descriptors, the centerline captures better the vessel shape and provides a straightforward way of obtaining the relationships between the different branches of the vessel tree [153], since the centerline can be easily converted into a graph structure. Furthermore, it serves as a reference for calculating and storing local properties, both inside and on the boundaries of vessels. For example, the vessel length is measured along the centerlines and diameters are measured over sections whose center is the centerline. Therefore, we provide an explicit, yet flexible and agile, representation of the centerline.

The *Centerline Model* is designed to provide several degrees of increasing representation complexity, as shown in Figure 3.3 left. The simplest level of representation complexity is to define a centerline by its point descriptors, where a point descriptor is anything that may identify the location of a geometrical point on the centerline. Examples of point descriptors may be geometrical points in physical coordinates, image pixel indexes, chain-codes, etc. The next level of complexity involves defining the vessel normal section that defines the cross-sectional planes. On a third level, we can define a section model, thus allowing further levels of flexibility and complexity.

Our point-based *Centerline Model* is independent from the mathematical model used to define the centerline curve, whose points need to be defined explicitly in our model. The reason is that the centerline curve needs to be discretized in order to store local quantitative properties of the vessel centerline and sections, and to localize vessel accidents or other features of interest that need to be referred to some point on the curve. However, this does not preclude the definition of an interpolation mathematical model that can be assumed as a curve point generator. Examples of this could be a centerline curve defined as a B-spline by using control points. This can be implemented either by subclassing *Centerline* class or, as will be described in section 3.3.3.6, by decoupling the curve generation from its defining points, by providing an external generator by subclassing the *CenterlineAlgorithm* class.

Finally, the *Centerline Model* provides a placeholder for optionally storing local centerline metrics which may provide valuable quantitative information about the local shape of the centerline. The most common and useful local centerline metrics, that can be defined at every point of the centerline, are the curvature, torsion (3D) and Frenet frame of reference, which includes the tangent, normal and binormal vectors (Figure 3.3 right). We contemplate an implementation (*LocalCurveMetrics* class) that generalizes this reference system to N-dimensions.

3.3.2.4 Section Model

Vessel Sections are localized at centerline points and they are assumed to vary along the vessel length. This variability is reflected in the parameters that define the section,

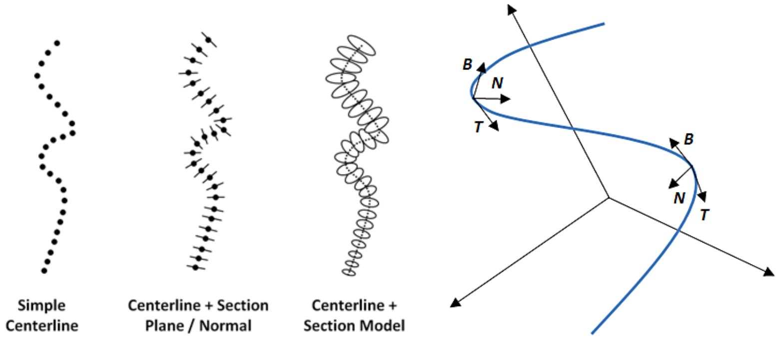

Figure 3.3: Centerline Models (left) and Frenet reference frame for a 3D curve (right).

for example, the diameter.

As we can see in Figure 3.4, vessel sections, like centerlines, can also be defined at increasing levels of complexity. The simplest level is to define the section as a circle, giving its center and radius/diameter. Since our sections are defined at explicit centerline points, the center is already given. The next level of complexity is an elliptical shape. More advanced mathematical models include radial functions and B-spline contours. The section can also be implicitly defined by a segmentation mask image or by level-sets of a higher dimensional function, that can be obtained by the level-sets method, based on evolution of implicit curves or surfaces [125]. Another possibility is that a section may define more than one contour. This is for example the case when we want to model the shape of the external and internal vessel wall or when we want to model the lumen and the aneurysm contour in abdominal aortic aneurysms). In the latter special case, the section is modelled in such a way that it can be shared by at least two different branches (*SharedVesselSection*) since a single aneurysm contour may extend to both iliac arteries.

These are just a few examples that demonstrate the versatility of the model. In this sense, our section model does not impose any shape model, the only condition is that it can be referred to centerline points.

3.3.2.5 3D Surface and Voxel Models of Vessels

So far we have dealt with explicit modelling of cross-sections. Another possibility, when dealing with 3D image data, is to directly generate a 3D surface mesh from the centerline. If the 3D mesh is generated for the complete vessel tree, it can be referred to branches or even to centerline points (and thus to sections) of the VKR model by proximity to the corresponding centerline. This reference can be direct, by splitting the model into surface patches and keeping references to them, or indirect, simply by associating a scalar value, acting as identifier, to the mesh points that corresponds to referred branches. This way a forth-and-back relationship may be kept between the VKR and surface models. Explicit sections may also be obtained by intersection with corresponding section planes.

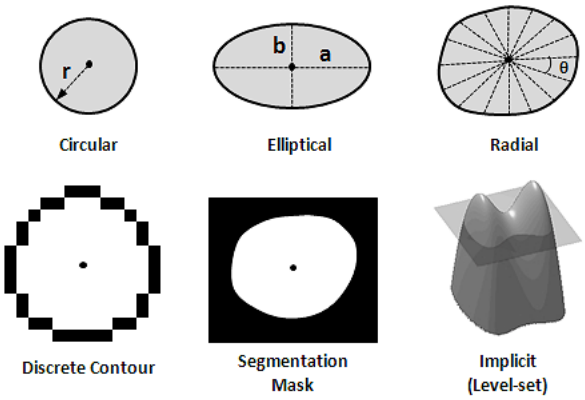

Figure 3.4: Section Models

If a segmentation is available, obtained either *a priori* or from the VKR model, it can be referred to corresponding branches by just labelling the mask pixels/voxels with corresponding branch identifiers. In this case, keeping references to separate volume "patches" seems to be more difficult to handle but it is a possibility that could be useful in cases where the source angiographic volumes are huge. The reason is that, in most software frameworks, only arrays corresponding to rectilinear volumes can be stored, and for sparse structures such as the vessels, sometimes many of these voxels are empty. Another possibility is to store these labelled voxels as sparse images, which is currently not implemented.

3.3.2.6 Vessel Bifurcations

Bifurcations may be represented explicitly in the VKR model by means of the *BifurcationNode* object that defined at graph level. The use of this node type is optional (see BBVG representation in section 3.3.2.1), and may be required when we want to model special features of the bifurcation, when (quantification) operations need to be assigned to the bifurcation, such as estimation of branch angles, and when there may exist more than one parent branch.

3.3.2.7 Vessel Features

In the VKR model, vessel "features" (*FeatureNode*) represent special characteristics of the vessels that need to be highlighted. Their definition may include models for vessel accidents or simply comments used for diagnostic. A feature may affect or may be associated to a part of a branch, a whole branch or a set of branches, entirely or partially. In order to make explicit these relationships, two mechanisms are devised:

1. *FeaturesNodes* are assigned as children (or alternatively as parents) of affected *BranchNodes*. This is illustrated in Figure 3.2.

2. *FeatureNodes* keep a *VesselRegion* structure that indicates which vessel branches are affected and to which extent. This is achieved by keeping a set of *VesselBranch* node identifiers, and for each identifier, the starting and end indexes of the points in corresponding centerlines that comprise the area affected by the feature.

Since a feature may affect more than one branch, *FeatureNodes* are treated in a special manner and are not even visited when performing many operations that require traversal of the graph. In this sense, FeatureNodes can be treated as “hypernodes” and their relationship with *VesselBranch* nodes (or possibly other nodes) is not that of a parent-child relationship but merely a reference.

An example of use of a *FeatureNode* is to perform an annotation, such as a diagnostic remark in a application for computer aided vascular diagnosis. The clinician would choose the branches affected by a given feature, for example, those feeding a tumor or included on it, and assign them the corresponding nodes comment. Another possibility is to assign specific models of vessel accidents or disease, such as a *StenosisModel*, to a *FeatureNode* which are described next.

3.3.2.8 Models of Vessel Accidents or Disease

The VKR model offers the possibility of providing representation models for vessel accident or disease. Examples of these models are the *StenosisModel* and *AneurysmModel*. These models contain the quantitative morphological measurements and other properties that are typical of a given vessel accident or related disease. We provide flexibility for defining application-specific models of this kind.

There are two main possibilities for incorporating these models in the vessel graph: in a *BranchNode* or in a *FeatureNode*. The first option is more suitable for cases in which the accident affects a whole branch or a part of it. In this case, the affected area is modelled by a subclass of BranchNode (for example *StenosisBranchNode* or *AneurysmBranchNode*) that is connected serially in both extremes either to other *BranchNodes* or to *BifurcationNodes*. This configuration can be seen in Figure 3.6 and is further commented in section 3.3.3.6. Another possibility is incorporating the model into a *FeatureNode* as explained in the previous section. This is more appropriate in cases in which the accident affects more than one branch.

3.3.3 Supported Operations

Operations that can be performed on the VKR model data structures can be classified by their nature or by the type of object they operate on. For example, quantification operations can be performed at graph, branch, centerline or section level, among others. Based on their nature we distinguish the following types:

- *Access Operations*: these are abstract access mechanisms that allows to perform other types of operations. For example, graph traversal is an operation that allows to access nodes on the vessel graph and perform other operations on them.
- *Edition Operations*: allows to change the internal structure and properties of the model.

- *Quantification Operations*: evaluation of quantitative measurements over different elements of the model.
- *Input/Output Operations*: used to load and save the model data.
- *Data Transformation Operations*: include generation of the VKR model and transformation into another representation that can be useful for intended applications.
- *Model-specific Operations*: these are internal operations that are specific to certain elements of the model, such as the centerlines or sections.

3.3.3.1 Access Operations

Graph Traversal The most important access operation is graph traversal. Graph traversal operations can be performed efficiently by using the *Visitor Pattern [51]* object-oriented technique (*GraphVisitor*). This pattern allows to decouple the structure of the graph and corresponding nodes from the operations performed of them. This is desirable because it constitutes and efficient manner of extending the framework with new operations. The visitor abstracts the mechanism of traversing the graph according to a set of rules that are defined by the user. For example the user may choose to visit only some specific type of nodes, such as bifurcations or may use node masks to enable/disable visiting specific nodes. Subclasses define specific traversal rules and the operation to be performed. Operations at any depth level that need to be performed on the whole vessel tree are implemented this way.

Model Picking Picking operations are those that allow to access structures of the VKR model by selecting them from a derived representation, either symbolic or geometric. They constitute the random access means to any part of the VKR.

Picking operations are based on established relationships between the target structures of the model (nodes, branches or sections) and their representation. This can be performed directly, by keeping references (pointers) to the structures on the model, or by assigning corresponding identifiers . Another possibility to establish this relationship is by proximity in terms of Euclidean distance. For example, a user could pick a point on the surface and the closest centerline point or section could be selected and its properties displayed.

3.3.3.2 Model Editing Operations

Most edition operations can be implemented in a straightforward manner by exposing the internal structure of the data after a picking operation. Of particular interest are graph editing operations, which alter the structure of the graph by changing the relationships between nodes and insert or delete nodes on demand. Graph editing operations can be performed interactively by the user, i.e. to correct artifacts in VKR models produced during its extraction, or by autonomous algorithms, i.e. deleting noisy branches based on their absolute length or underlying image values.

3.3.3.3 Quantification Operations

Quantification operations can be performed once the initial graph structure of the vessels has been created. Some of these quantitative measures are calculated and stored in the model on-the-fly, when they are part of the necessary calculations performed by the vessel extraction algorithms. Some other quantification operations are only performed on demand, on the whole vessel tree or on a part of it, since they may be computationally expensive. Whole tree calculations are performed via specific graph visitors. These visitors may incorporate other specific objects to perform quantification at deeper levels. For example, a *CenterlineMetricsCalculatorVisitor* object traverses the tree searching for centerlines of *BranchNodes*. At each centerline, a *CenterlineMetricsCalculator* object calculates local centerline metrics. If we want to calculate metrics for a single centerline, we can access it directly and use this latter object instead of using the visitor object.

Quantification can be performed at almost every level in the VKR model. A reference diagram of some of the attributes that can be measured is shown in Figure 3.5. The diagram shows the data model on which the operations are performed and the locality and type of measurement (i.e. geometrical, topological, image-based...) in a hierarchical manner. Some of the measurements are directly stored in the corresponding data structures or placeholders of the VKR model. Others can be obtained from the object that performs the operations.

3.3.3.4 Input/Output Operations

Input/Output (I/O) operations are intended to store/recover instances of the VKR model data structures. Two main types of I/O operations are initially considered: file and database I/O operations. The chosen format for file operations has been *GraphML* [22]. It is an XML-based format specifically designed for serializing graph information and that can be extended for custom needs. It allows to explicitly define the graph nodes, its relationships as edges[3]. Attributes can also be assigned to nodes and edges, allowing to store properties. Input/output of structures such as images or meshes is out of the scope of the model. As it may easily integrate with other toolkits, these operations are should be performed by third-party libraries. Other types of data may require the design of custom I/O routines, sometimes application specific. On the other hand, application-specific relational databases can be designed, mimicking the data structures of the VKR model, and allowing operations such as performing queries or keyword search of semantic qualitative attributes [129], or advances multimodal interfaces such as those described in [75].

3.3.3.5 Data Transformation Operations

Data transformation operations involve conversions between high-order vessel representations and are summarized in the VKR workflow diagram in Figure 3.1. Except for graph-to-graph operations, they consist of generation of the VKR model from external

---

[3] In our model, graph edges are implicitly defined as references or pointer to nodes

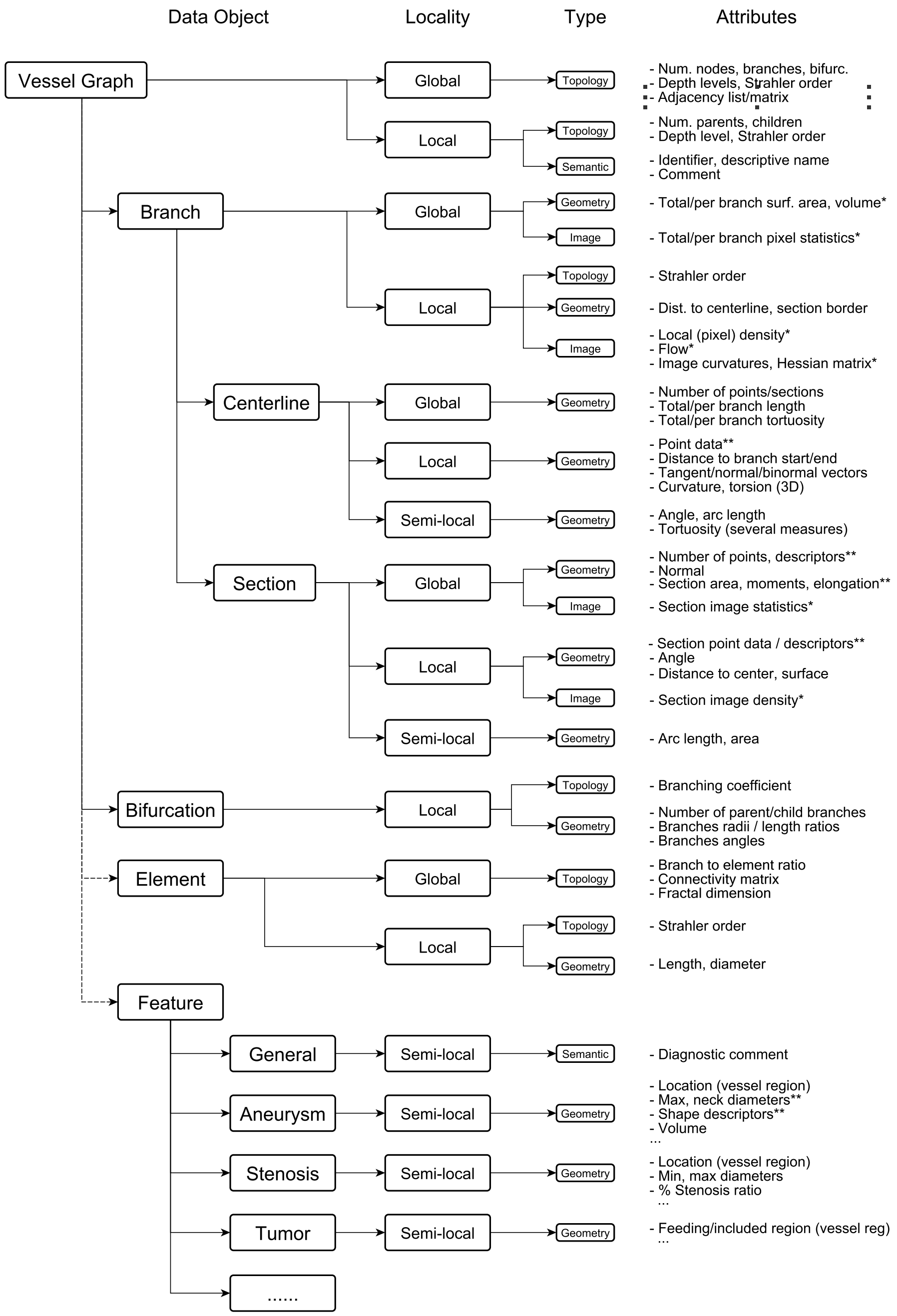

* Properties that require a reference to external data source (image, surface mesh, velocity field) to be calculated

** Definition of these measures is very open and not imposed by the model

Figure 3.5: Quantitative and qualitative attributes

image data and transformations to other types of data representations used in corresponding applications. Many of these external operations are not yet implemented, but for the sake of completeness, we describe some of these operations and important considerations here.

Graph-to-graph Operations These operations convert a vessel graph into another vessel graph in which the configuration of the nodes has changed. This is possible because the nature and openness of the graph representation in the VKR model allows the definition of different types of graphs and nodes, and thus, conversion operations between graph types. We do not include here operations that transform inner data structures only, such as the centerlines. Typical graph operations are conversions between vessel graphs representations.

Another operation of this type is converting a disconnected set of branches obtained by global detection algorithms into a vessel graph (see Figure 3.1). This is the equivalent of having a container of disconnected nodes which are organized into a complete graph by establishing the links.

Image-to-graph Operations These correspond to the VKR model construction from the image/volume by using vessel extraction schemes. Some schemes may use intermediate representations, such as a segmentation mask or a disconnected set of nodes (see Figure 3.1).

Graph-to-image Operations Sometimes it is necessary to convert the graph into a voxel representation (segmentation) that also involves branch labelling. This can be used, for example, for overlaying and blending this labelled segmentation on top of the original image and assigning a color to each label. These labels can also be used as region of interests, to limit further processing operations on the source image to corresponding branches.

Another set of graph to image operations is projection on 2D images (see Figure 3.1). A typical example is when we have a VKR model obtained from a 3D angiography (such as CTA or MRA) and we want to project part of the model, such as the centerline on a 2D X-ray angiography, in order to visualize the real paths of some vessels that may be occluded.

Graph-to-mesh Operations These operations convert a vessel graph into a surface mesh. The conversion depends on the actual representation of the graph. It can be obtained by contour sweeping or by using a predefined mesh model either explicitly or implicitly as described in section 2.4.1 among other techniques.

3.3.3.6 Model-specific Operations

We describe some model-specific operations that are not included in the previous classes of operations and that are exclusive of the corresponding representations.

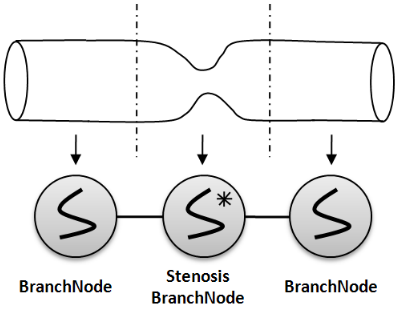

Figure 3.6: Example of branch splitting operation to indicate an stenosis. A single *BranchNode* is split into three serial nodes, where the middle node incorporates a *StenosisModel*.

Graph Operations We consider here operations that modify the attributes of common nodes only, because graph operations will be specified in terms of node operations and visitor patterns.

Graph Labelling is a straightforward operation that assigns unique labels to nodes. *Node Wrapping/Unwrapping* are operations that transform a vessel graph into another vessel graph in which some nodes are wrapped into a supernode (subclass of *CompositeNode*) and viceversa. Node wrapping may require specific rules by which nodes are merged into a single supernode. On the other hand, node unwrapping may work without setting any rules by simply restoring the underlying nodes. A specific wrapping operation is defined in order to convert a (B)BVG rep. into a OEVG rep. (see section 3.3.2.1) as defined in [62].

Branch Operations Operations that affect the branches as a whole are included here. A specific operation for branches is assigning them an *order* in the (modified) Strahler ordering system (see section **??**). This involves traversing all branches from the leaves to the roots. If the diameter-defined method is used, this requires iteratively assigning orders and calculating diameters.

Branch splitting is the operation of dividing a branch into several branches. This operation (see Figure 3.6) may be performed, for example, to mark a region of a branch as having a specific accident or disease model. *Branch merging* is the contrary operation, where several branch patches are merged into a single branch node. They can be also considered as edition operations (see section 3.3.3.2).

Section interpolation is an operation that needs to be considered at branch level, since it involves both, generation of new intermediate centerline points, that define the section location, and estimation of section normal and boundary according to the corresponding model.

Centerline Operations Centerline operations involve modification of the points that define a centerline. Centerline generation operations, such as centerline tracking or skeletonization (see section 2.4.2and 2.4.2), lie in this group, but they are usually part of the vessel extraction schemes that explicitly deal with centerlines and are not considered here.

Centerline interpolation is the process of resampling an existing centerline, or one that is being created, following a given mathematical model of curve. For example, if the distance between centerline points is not uniform, a linear resampling may produce uniform sampling. Another possibility is to fit the centerline curve to a set of connected B-spline curves.

Centerline filtering may also be used to convert a rough, noisy centerline into a smoother centerline, by removal of points or by several types of smoothing filters, such as average, median or anisotropic diffusion filters that operate on centerline points.

Centerline registration is the process of converting a centerline into another centerline by applying a rigid or elastic transform to the points of the centerline. This transform is obtained by minimization of a cost function, that is usually based on image-values. Examples of centerline registration applications are comparison of vessel geometrical features between different patients [138] or quantification of aneurysms and stenosis [67].

Section Operations Section operations involve generally modification of the geometry of the section, or reestimation of the section normal[4]. As in the previous case, these operations can be performed after or during the vessel extraction procedure. In the second case, section generation can be considered as an inherent part of the extraction schemes described in 2.4.2 but, like in the case of the centerline, some of the algorithms can be applied at a post-processing stage.

Section interpolation can be performed in two ways, either by interpolating the section geometry according to its mathematical representation (resampling of points, etc.) or by interpolating sections by creating new intermediate sections. In the later case, it also involves a modification of the centerline and as such, can be considered a branch operation (see section 3.3.3.6).

Section filtering involves geometric filtering of noisy boundaries. It is similar to centerline filtering and depends greatly on the section model.

3.4 Implementation Details

3.4.1 Programming Languages and Tools

The current implementation of the ideas presented in the paper is being developed in cross-platform C++, and is fully compatible with ITK[187] from which the lowest level structures are borrowed. We want to remark this compatibility since ITK is becoming a *de-facto* standard for developing research and commercial applications based on medical image analysis. The implementation is also fully compatible with CMake [111], a cross-platform build tool that facilitates the use of a broad range of platforms and compilers, increasing the potential number of users.

---

[4] reestimation of the section center corresponds to a centerline operation

3.4.2 Data Structures

In Figure 3.7 an Unified Modeling Language (UML) diagram of the most important objects in the VKR model is depicted. We give an overview of the main object definitions and their relationships. According to their function, we can distinguish two main types of objects: data representation objects (left), that describe the vascular structure, and algorithmic objects (right), that implement operations on the data representation objects. As can be seen, there is almost a one-to-one correspondence between data objects and algorithms. This separation between data objects and algorithmic objects provides more flexibility, since it makes easy to define new algorithms without affecting the data representations. Other more straightforward operations are implemented as methods of the corresponding data objects. In Figure 3.7 we have set a horizontal line that separates the depth level of the objects: data structures and algorithms above this line correspond to graph level whereas those below the line operate at underlying modelling levels.

The highest level data structure is the *VesselGraph* which may contain one or several root nodes. All vessel graph nodes are subclasses of the *GraphNode* abstract class, which provides generic node-handling operations and metadata such as node identifiers, and *VesselNode* which is an abstract class specific for nodes of vessel graphs. We chose not to model explicitly the edges of the graph. Thus, the graph consists of nodes, that are connected by virtual links, which are implemented as references (pointers) to the corresponding nodes. *GraphNodes* contain a set of children nodes, as strong references, and a set of parent nodes, as weak references [5].

Due to their importance, we provide a brief description of some salient implemented node types:

- *BranchNode*: is the most important node type, which represents the physical vessel segment that extends between two bifurcations. A *BranchNode* contains a *Centerline.* We decided to implement the centerline as a placeholder of *Section* objects, where the simplest section model is a point that represents the centerline, instead of keeping a list of points on the centerline model itself. This forces a one-to-one mapping and provides the flexibility for a non-explicit centerline definition. Centerline points are thus the centers of *Section* objects, and can be defined with any descriptor that identifies their geometrical position, such as euclidan coordinates, image indexes, chain-codes, etc.. The same applies for the points that define the section boundaries. This provides much flexibility in defining the centerline and section for a wide range of applications. In general, this type of flexibility is provided in the VKR model by using *Generic Programming* techniques [39].

- *BifurcationNodes* are more simple in their definition. They explicitly reference confluent branches as parent/child nodes and their use is optional (see Figure 3.2). Algorithms may be devised to operate on bifurcation nodes to take advantage of the direct access to confluent branches.

---

[5] Strong references imply a composition relationship and weak references an aggregation

- *CompositeNodes* are nodes obtained by wrapping other nodes and exposing the internal links only. The information about internal nodes and links is kept when wrapping is performed, so the situation can be reversed easily. This ability may provide several types of simultaneous representations of the vessel graph, as can be seen in Figure 3.2 (right). One direct application is converting the branch nodes of the same (modified) Strahler order into a single element using the node type *ElementNode*.

- *FeatureNodes* indicate relevant features in vessels and incorporate an optional feature model that describes the corresponding feature such as an stenosis (*StenosisModel*) or aneurysm (*AneurysmModel*). They incorporate a *VesselRegion* structure that indicates the area affected by the feature in corresponding branches.

With respect to the algorithms, those that operate at graph level are subclasses of *GraphNodeVisitor* and *VesselGraphNodeVisitor*. The use of the *Visitor Pattern* [51], allows to separate the node definition from the operations on the graph by decoupling the graph traversal from the node operations. These graph-level algorithms can be classified according to the objects they ultimately operate on. An algorithm may operate at graph level because only graph elements are involved in the corresponding algorithms. An example is calculating the number of nodes in the branch, or computing the (modified) Strahler order of *BranchNodes*. Another possibility is that they encapsulate algorithms that operate at deeper levels (such as the level of centerline or section) but are applied to the corresponding structures on the whole graph and not only locally. In this sense, the level of encapsulation of the data structure finds a correspondence in the level of encapsulation of the algorithms. This makes possible to reuse local algorithms and apply them to the whole graph. An example is the family of *CenterlineAlgorithm* classes, which perform operations on a single centerline. These operations can be performed for all the centerlines of the *BranchNodes* of a vessel graph by defining a specific visitor (*CenterlineAlgorithmVisitor*) which encapsulates the former.

In Figure 3.8 we can see a representation of the external operations (we call them "filters" here) that can be performed in order to create the VKR Model and to convert it to other (3D) representations, such as surface meshes or segmentation masks. Objects of type correspond to the vessel extraction schemes commented in section 2.4.2. Such an extraction scheme, may use the VKR Model as an intermediate representation and then use an algorithms of type *VesselGraphToImageFilter* to obtain the final segmentation or a *VesselGraphToSurfaceFilter* object to obtain a surface mesh.

Finally, most high-level objects, such as filters, nodes, centerlines or sections are implemented using reference counting, so they can be shared by many objects without unnecessary copies and additional overhead.

Needless to say, implementation is an on-going never-ending process, evolving as applications, imaging resources and computational algorithms evolve. Therefore, the description given of current state and trends of our implementation must be assumed as a core implementation aiming at a continuing incremental process incorporating new algorithms, accepting new imaging resources and addressing innovative applications.

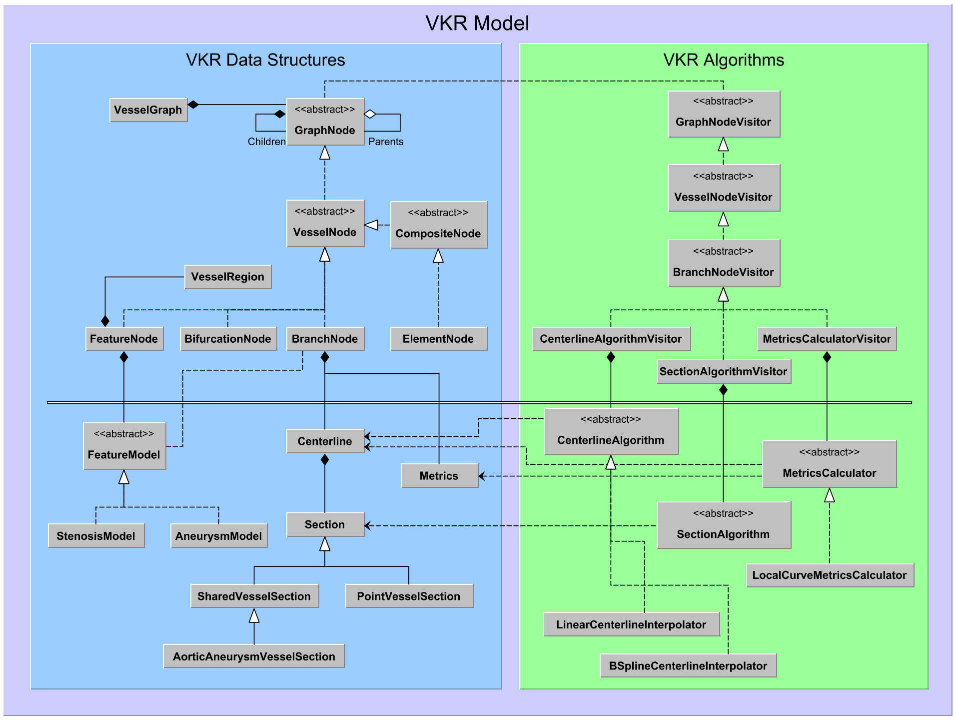

Figure 3.7: VKR Model. Internal Implementation

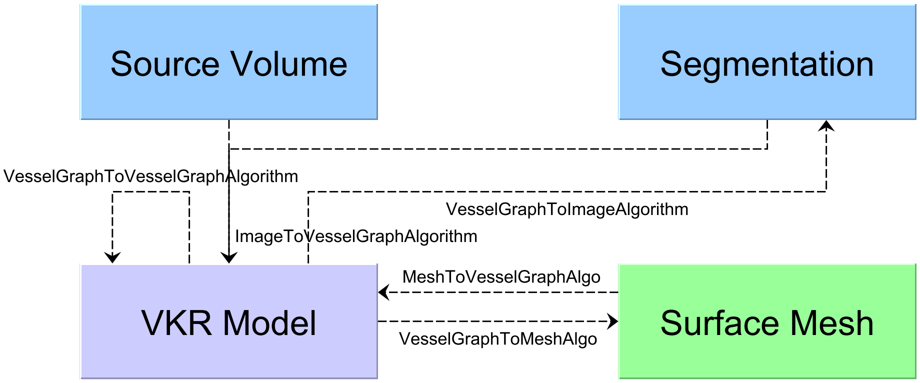

Figure 3.8: VKR Model. External Implementation

3.4.3 Prototype Execution Example

We are currently developing several vascular applications that make use of our VKR model. As an example, a prototype is being developed to demonstrate some of the capabilities of the model. Once a 3D image is loaded, the user may trace the corresponding centerlines, branch by branch, by means of a set of control points. These points are interpolated by using a BSpline curve model by means of a Centerline operation (see 3.3.3.6). The integration of our model with the model/view framework of the user interface tookit (Nokia Qt) is straightforward, and allows displaying several views of the defined model, being the tree view the most intuitive for exploration. Once a branch is selected in the tree, the properties of the corresponding sections may be displayed also.

In figure 3.9 we can see an interactive definition of the hepatic vein branches in a 3D contrast-enhanced MRI of the liver. The projections of the resulting centerlines are displayed in 2D orthogonal views (the vessel segments in green lie on the current slice) and the corresponding 3D renderings are overlaid on a volumen rendering of the dataset. This allows an intuitive exploration and visualization, by displaying branches in their real position and selecting them directly in the corresponding visualizations via picking operations. Local plane sections may be calculated from the centerline points, and the corresponding section images displayed. Furthermore, a curved planar reformatting may be obtained from the centerlines that displays the vessel along their whole length in a single plane. Obtained section images and curved reconstructions may be stored within the model if necessary by simply subclassing the section and centerline models, without modifying the existing algorithms, due to the adequate use of generic programming techniques.

Currently we are extending the capabilities of the prototype for allowing different types of sections and nodes, editing of branches and points, improved visualizations, etc. We are developing similar prototypes for other applications that require different models of sections, such as follow-up after aortic anerysm repair, which requires a delineation both of the aorta lumen and aneurysm thrombus. As mentioned before, combining the definition of several types of vessel sections is eased by the versatility of the model.

3.5 Conclusions

The evergrowing applications and techniques of Blood Vessel Analysis have produced a complex landscape of algorithms and data representations that hinders the composition of procedures, the reuse of software and the comparative analysis in terms of computational efficiency and quality of final results (visualization, measurement, edition, and others). We have detected the need of proposing a foundational Vessel Knowledge Representation (VKR) model that may allow the exchange of data among applications and users. One of the goals of VKR is the reuse of software pieces, providing a ground functional layer that may serve as the basis for new developments, thus alleviating development efforts. The model can be used as an intermediate representation between image-based extraction schemes and clinical and research applications, to perform quantitative measurements on extracted vessel structures and to provide the

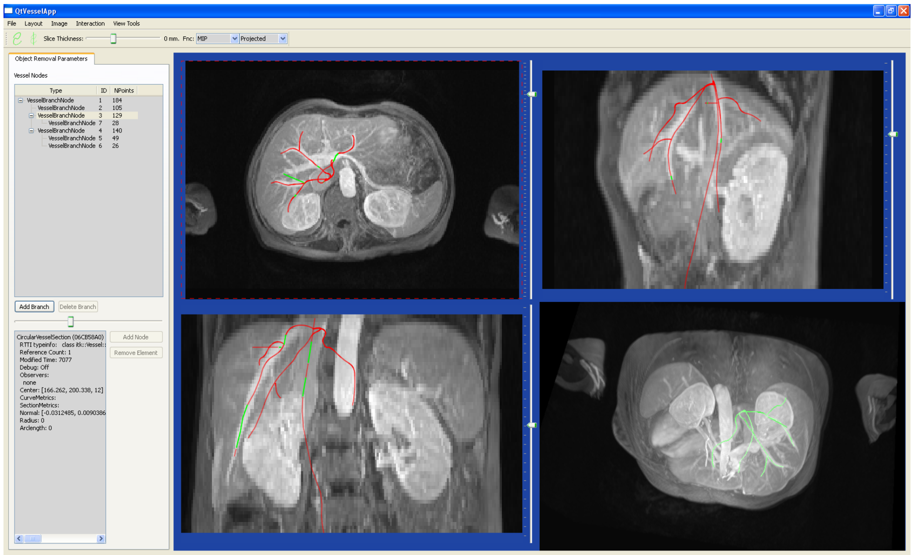

Slice Thickness: 0 mm. Fnc: MIP Projected

Vessel Nodes

Type	ID	NPoints
VesselBranchNode	1	184
VesselBranchNode	2	105
VesselBranchNode	3	129
VesselBranchNode	7	28
VesselBranchNode	4	140
VesselBranchNode	5	49
VesselBranchNode	6	26

```
CircularVesselSection (06CB58A0)
  RTTI typeinfo:   class itk::Vessel::
  Reference Count: 1
  Modified Time: 7077
  Debug: Off
  Observers:
    none
  Center: [166.262, 200.338, 12]
  CurveMetrics:
  SectionMetrics:
  Normal: [-0.0312485, 0.0090386
  Radius: 0
  Arclength: 0
```

Figure 3.9: Screen capture of the visualization given by the modeling application under development. Lines correspond to vessel centerlines created interactively by a user over a liver CTA.

necessary vessel representation and handling tools for the target applications. In this paper we have identified, from the literature and our own research work, the key knowledge representation items, as well as the key operations that are the building blocks for nowadays and future vessel analysis processes and applications.

VKR provides a versatile and efficient object-oriented representation of vessel structures and associated algorithms and quantitative data. It contemplates flexible data representations for the vascular tree, underlying structures such as branches, bifurcations, centerlines and sections, as well as vessel features such as stenosis, aneurysms, etc. It also contemplates operations and algorithms that operate efficiently on corresponding data structures. Furthermore, the model is designed so it can be easily integrated with pre-existing frameworks. We are already applying the VKR model in vessel-related applications related to our current research areas [85, 108, 107, 106, 105, 104].

Chapter 4

Ideal Shape Models for Vascular Analysis

4.1 Introduction

Most of the existing methods for the detection and extraction of vessels or tubular structures in images[1], requires some assumption or model of the local image intensity distribution of the vessels to be detected or extracted. A common model used by its simplicity is that the vessel is a thin, elongated and oriented structure whose intensity distribution resembles locally an oriented cylinder, with a circular section of constant intensity higher that the background[2] . This implies that the vessel can be described locally by an oriented section, in the same orientation as the local cylinder and whose center coindices with the local position of the axis or centerline. Then, the problem of vascular extraction consist of trying to estimate these parameters, namely the section center and orientation, for every section of the vessel of interest.

More advanced and realistic models, consider a generalized cylinder, where some of the previous assumptions are relaxed. The following properties may be considered when trying to model vascular structures that :

- A non-constant *radius* along the axis. The most basic assumption is to consider a constant radius but this is not very realistic since real vascular structures do not have a uniform radius or average radius for the sections along its axis. Thus, when assuming a local cylinder model it is very common to consider the radius as a parameter to estimate for the local section.

- An intensity distribution for the vessel *section profile*. Assuming that the section is radially symmetric, the section profile corresponds to the intensity found along

---

[1] To avoid redundancy, from now on we will talk in terms of vessels, but the analysis can be applied to other types of tubular structures to be detected in 3D (medical) images.

[2] unless told otherwise and without loss of generalization, we will assume that the vessels or tubes of interesest are hyperintense structures. Sometimes, the structures to detect are hypointense, but usually the analysis can be extended easily to these structures, for example by inverting the source image(s).

a diametral line contained in the section that crosses the cylinder axis. Apart from the ideal top hat, constant intensity profile inside the bounds of the cylinders other profiles are commonly used such as roof or Gaussian section profiles

- A *geometric shape* for the section intensity distribution. Some models assume that the section may not be perfectly circular and thus radially symmetric. For example, by generalizing the circular shape it can be assumed that the section intensity distribution is elliptical or corresponds to a radial function, with origin in the section center and where the radius is a function of the angle that covers 360º. For each geometric shape, the intensity profile may vary differently as commented in the previous point. Thus we may have for a example an elliptical cross-section with constant or Gaussian profile.

- A non-constant *intensity along the axis*. A given intensity distribution in the section can vary along the axis, for example by scaling the intensities by a given quantity that depends on the position or other variable such as the radius. This may be useful in some situations, for example in contrast-enhanced imaging, where the contrast may not be distributed evenly.

- A non-constant *curvature and/or torsion*. A basic assumption in the cylinder model is that the vessel is locally straight and in many circumstances this is valid for obtaining accurate results in the analysis. However, there are circumstances in which vessels tend to be very tortuous, for example in some specific parts of the human body or in the vecinity of tumors.

When assuming a simple model for the analysis of real vessels, different shape models of vessels can be used in order to test the validity of the assumptions and to understand the implications and limitations of the model under controled conditions. It is important to distinguish clearly that we are talking about two different types of models and we will introduce here some notation that will be used for distinction:

- *Hypothesis model:* this is the model that will be used for the real analysis and consist of the assumptions or hypothesis used for this analysis. Detection and extraction methods are devised based on these assumptions. An example of such a model is to assume that the vessel is locally a cylinder with an oriented circular section of given radius.

- *Shape model*: this is a mathematical model that emulates the intensity distribution of the vessel in a real section. resemble as much as possible the real properties displayed on the corresponding (medical) images. This model can be purely mathematical, consisting of formulas for the intensity distribution (i.e. a Gaussian circular cross-section) or can be a discrete realization of the mathematical model in the form of a digital (3D) image. An example of such a model is a procedural, discrete, volumetric tube.

Previously, Krissian *et al.* and Sato *et al.* have used different shape models in order to test the validity of several assumptions of the basic cylinder hypothesis model, taking into account considerations, such as the effect of non-circular section shape or the effect of curvature. The use of shape models, together with the introduction of other effects that difficult the analysis and that may appear in real images, such as simulated noise or artifacts, allows to test the performance of the detection and extraction methods under controlled but quite realistic conditions, and to extract both qualitative and quantitative information useful for the analysis.

The current chapter pretends to extend these analysis both, by incorporating new shape models and by studying some of the existing models more deeply or from a different point of view, such as that obtained by incorporating alternative spatial reference systems in the analysis (i.e. curvilinear coordinates). The objective is to further test the validity of the assumptions of some existing methods and to gain more insight in understanding the problem of vessel analysis. This will help to develop new, alternative detection and extraction methods that may be more efficient or more specific and valid in some circumstances.

As we have seen in the previous chapter using differential operators, the neighborhood of an image point can be described by its local derivatives. We cannot make any analysis based on first-order derivatives, since these are zero in the centerlines of vessels being extremal points. Thus, our analysis will be focused on studying the behaviour of second derivatives on these ideal shape models, since they provide crucial information on the local structure of images, that can be used to distinguish tubular structures from other types of structures. Moreover, many of the existing methods of vascular detection and extraction, are based on a local study of second derivatives, using mathematical tools such as the Hessian matrix and its corresponding eigenvalues and vectors. Hence, our analysis tries to analyze in depth the influence of several parameters of the imaged vessels in the detection.

4.2 Basic Shape Models

4.2.1 Ideal Cylinder

The basic cylinder model represents an ideal, infinitely long, straight cylinder with Gaussian cross-section that represents an ideal straight vessel of fixed diameter. In the following, we will use mainly Gaussian cross-sections, since they are a good approximation to partial volume effects in small vessels, which are the most difficult to detect and extract. In practice, the discrete realization of this cylinder model in the form of a volume cannot be infinitely long, but we create a cylinder long enough so there are no boundary effects when discrete derivatives are calculated in its central zone. By using this model, we can find theoretical values of derivatives and vessel detection functions for ideal vessels of different size.

The equation of a such a volumetric cylinder model, in cartesian coordinates, is given by:

$$I_{cyl}(x,y,z) = K \exp\left(-\frac{x^2+y^2}{2\sigma_0^2}\right) \tag{4.1}$$

where $\sigma_0$is the deviation of the Gaussian section which defines the apparent radius of the cylinder and K is a constant defining the intensity at the center of the cylinder[3]. If $K = 1/2\pi\sigma_0^2$ we obtain the unit area integral for the 2D Gaussian section, but in general we will assume $K = 1$in most of the following calculations unless told otherwise. This will allow us to compare values for different choices of radius.

Now we will proceed to calculate the analytical derivatives of this model. It is important to emphasize that, in a discrete realization of this model (a volumetric image of the cylinder) these derivatives should be calculated at the proper scale by convolution with a Gaussian. However, in this analytical analysis, we can assume continuous derivatives.

The first order derivatives correspond to:

$$\frac{\partial I_{cyl}}{\partial x} = -\frac{x}{\sigma_0^2} I_{cyl} \tag{4.2}$$

$$\frac{\partial I_{cyl}}{\partial y} = -\frac{y}{\sigma_0^2} I_{cyl} \tag{4.3}$$

$$\frac{\partial I_{cyl}}{\partial z} = 0 \tag{4.4}$$

which are zero at the center of the tube.

We are interested in the second order derivatives:

$$\frac{\partial^2 I_{cyl}}{\partial x^2} = -\frac{1}{\sigma_0^2} I_{cyl} + \left(-\frac{x}{\sigma_0^2}\right)\left(-\frac{x}{\sigma_0^2}\right) I_{cyl} = \frac{x^2 - \sigma_0^2}{\sigma_0^4} I_{cyl} \tag{4.5}$$

Similarly we can calculate the rest of derivatives. The resulting Hessian matrix is:

$$H = \frac{1}{\sigma_0^4} I_{cyl} H' \tag{4.6}$$

with

$$H' = \begin{bmatrix} x^2 - \sigma_0^2 & xy & 0 \\ xy & y^2 - \sigma_0^2 & 0 \\ 0 & 0 & 0 \end{bmatrix} \tag{4.7}$$

Lemma 1. *The Hessian matrix of an ideal cylinder with Gaussian cross-section has three different eigenvalues. The eigenvalue corresponding to the axial direction is identically zero for all values of the radius* $r = \sqrt{x^2 + y^2}$. *The remaining eigenvalues correspond to derivatives of the Gaussian function of odd order with respect to r multiplied by some constant.*

Proof. The characteristic equation of $H'$is: □

---

[3] Do not confuse this standard deviation with the scale corresponding to the standard deviation σ of the Gaussians used for derivative calculations. Here, $\sigma_0$is the real diameter of the tube, which is usually unknown at the detection stage in real datasets.

$$\left(x^2-\sigma_0^2-\lambda'\right)\left(y^2-\sigma_0^2-\lambda'\right)\left(-\lambda'\right)+x^2y^2\lambda'=0 \tag{4.8}$$

The first eigenvalue, corresponding to the z direction is:

$$\lambda_3=0 \tag{4.9}$$

The other two eigenvalues are the solution to the equation:

$$\left(x^2-\sigma_0^2-\lambda'\right)\left(y^2-\sigma_0^2-\lambda'\right)-x^2y^2=0$$

By multiplying and reordering terms we obtain the second order equation:

$$\lambda'^2+\left(-x^2+2\sigma_0^2-y^2\right)\lambda'+\left[\sigma_0^4-\left(x^2+y^2\right)\sigma_0^2\right]=0$$

The solution can be obtained analytically:

$$\lambda'=\frac{1}{2}\left(x^2-2\sigma_0^2+y^2\right)\pm\frac{1}{2}\sqrt{\left(-x^2+2\sigma_0^2-y^2\right)^2-4\left[\sigma_0^4-(x^2+y^2)\,\sigma_0^2\right]}=0$$

$$\lambda'=\frac{1}{2}\left(x^2-2\sigma_0^2+y^2\right)\pm\frac{1}{2}\sqrt{x^4+4\sigma_0^4+y^4-4\,(x^2+y^2)\,\sigma_0^2+2x^2y^2+4\,(x^2+y^2)\,\sigma_0^2-4\sigma_0^4}=0$$

$$\lambda'=\frac{1}{2}\left(x^2-2\sigma_0^2+y^2\right)\pm\frac{1}{2}\sqrt{x^4+2x^2y^2+y^4}=0$$

$$\lambda'=\frac{1}{2}\left(x^2-2\sigma_0^2+y^2\right)\pm\frac{1}{2}\left(x^2+y^2\right)=0$$

which results in the eigenvalues:

$$\lambda_1=\frac{x^2+y^2-\sigma_0^2}{\sigma_0^4}I_{cyl} \tag{4.10}$$

$$\lambda_2=\frac{-1}{\sigma_0^2}I_{cyl} \tag{4.11}$$

The third eigenvalue is zero for all values of r. The second eigenvalue is the inverted cylinder function, which can be considered a zero order derivative. The third eigenvalue correspond to the second derivative of the Gaussian function with respect to r.

Now we can proceed to obtain the corresponding eigenvectors, which are the solutions of the equation:

$$H\mathbf{x}=\lambda\mathbf{x} \tag{4.12}$$

or equivalently:

$$H'\mathbf{x} = \lambda'\mathbf{x} \tag{4.13}$$

and

$$\left(H' - \lambda' I\right)\mathbf{x} = 0 \tag{4.14}$$

Lemma 2. *The Hessian matrix of the ideal cylinder with Gaussian cross-section has three different eigenvectors, one in the axial direction and the rest in radial directions perpendicular to each other.*

Proof. For the first eigenvector we have the set of equations:

$$-y^2 v_x + xy v_y = 0$$

$$xy v_x - x^2 v_y = 0$$

$$\left(-x^2 - y^2 + \sigma_0^2\right) v_z = 0$$

The first two equations are the same equation yielding the relationship:

$$v_x = \frac{x}{y} v_y$$

From the last equation we obtain:

$$v_z = 0$$

Since any multiple of an eigenvector is also an eigenvector, we can arbitrarily choose $v_y = y$ obtaining the eigenvector:

$$x_1 = \begin{bmatrix} x \\ y \\ 0 \end{bmatrix} \tag{4.15}$$

which is in the radial direction.

For the second eigenvector the set of equations is:

$$x^2 v_x + xy v_y = 0$$

$$xy v_x + y^2 v_y = 0$$

$$\sigma_0^2 v_z = 0$$

Then, the second eigenvector is:

$$x_2 = \begin{bmatrix} -y \\ x \\ 0 \end{bmatrix} \tag{4.16}$$

$\lambda_1 = \frac{x^2+y^2-\sigma_0^2}{\sigma_0^4} I_{cyl}$	$\lambda_2 = \frac{-1}{\sigma_0^2} I_{cyl}$	$\lambda_3 = 0$
$x_1 = \begin{bmatrix} x & y & 0 \end{bmatrix}$	$x_2 = \begin{bmatrix} -y & x & 0 \end{bmatrix}$	$x_3 = \begin{bmatrix} 0 & 0 & 1 \end{bmatrix}$

Table 4.1: Eigenvalues and vectors for the ideal Gaussian cylinder

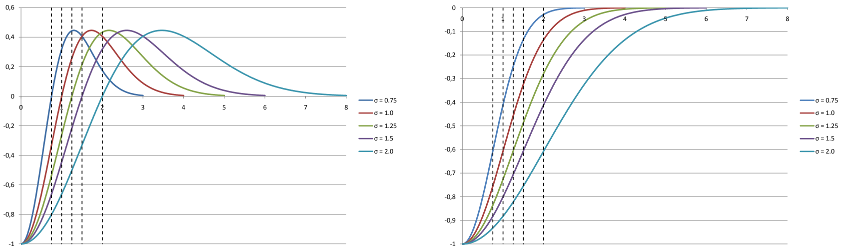

Figure 4.1: Analytical values of the scale-normalized eigenvalues λ_1(left) and λ_2(right) as a function of the distance to the center obtained for the ideal cylinder model at different scales.

which is also in the radial direction.

Finally, for the third eigenvector the set of equation is:

$$\left(x^2 - \sigma_0^2\right) v_x + xyv_y = 0$$

$$xyv_x + \left(y^2 - \sigma_0^2\right) v_y = 0$$

$$0v_z = 0$$

The first two equations give $v_x = 0$ and $v_y = 0$ whereas $v_z$can take any value. We arbitrarily choose $v_z = 1$ obtaining:

$$x_3 = \begin{bmatrix} 0 \\ 0 \\ 1 \end{bmatrix} \tag{4.17}$$

which is in the axial direction. □

Table 4.8 summarizes the eigenvalues and vectors for the ideal cylinder. As we can see the eigenvalue λ_3 is ideally zero at any point of the cylinder, not only at the center. The reason is that there is no intensity change in the direction of the cylinder axis. We can see that λ_2 is strictly negative and λ_1 is negative inside the cylinder, that is when the distance to the center $r^2 = x^2 + y^2$ is smaller than the radius, that is $r < \sigma_0$.

Figure 4.1shows the values of λ_1 and $\lambda_2$as a function of the distance to the cylinder axis for different cylinder radius, where the apparent radius is the standard deviation of the Gaussian section. In order to be able to compare the absolute values they have been normalized across-scale by multiplying by σ_0^2.[4]

We can see that both eigenvalues take a value of zero at the center of the cylinder. The first eigenvalue $\lambda_1$is exactly zero at the cylinder radius, and starts increasing until it reaches a maximum value outside the cylinder, as it corresponds to the second-order derivative of the Gaussian function as described in and as such it is a good ridge detector. This maximum value can be obtained analytically by the condition:

$$\frac{\partial \lambda_1(r)}{\partial r} = 0$$

for $r \neq 0$. This yields:

$$\frac{\partial \lambda_1(r)}{\partial r} = \frac{2r}{\sigma_0^2} I_{cyl} - \frac{r}{\sigma_0^2} \frac{r^2 - \sigma_0^2}{\sigma_0^2} I_{cyl} = 0$$

$$\frac{\partial \lambda_1(r)}{\partial r} = \frac{3\sigma_0^2 r - r^3}{\sigma_0^4} I_{cyl} = 0$$

$$r(\lambda_{1MAX}) = \sqrt{3}\sigma_0 \tag{4.18}$$

and the corresponding maximum value is:

$$\lambda_{1MAX} = 2\Pr\exp(-1.5) = 0.4463 \tag{4.19}$$

Thus, for any cylinder radius, λ_1 gives a positive response with a peak of 44,63% of the maximum negative response at a distance of approximately $0.732\sigma_0$ from the radius outside the cylinder. The signal recays rapidly from the center, and crosses zero exactly at the cylinder radius.

The second eigenvalue λ_2 corresponds exactly to an inverted Gaussian function, which is negative for any value of r and tends to zero at some distance outside the cylinder. It is easy to calculate the decay of this signal. For example, the normalized 97% decay of the signal can be calculated as:

$$0,03 = \exp\left(-\frac{r^2}{2\sigma_0^2}\right)$$

By taking logarithms on both sides we obtain:

---

[4] Note that the derivatives calculated here are not scaled derivatives but analytical exact derivatives. However, by multiplying by σ^2 the values of the derivatives are normalized with respect to the cylinder radius as if we were computing derivatives in scale-space. This way values can be compared in a straightforward manner.

$$r(\lambda_2 = 0.03) = 2.2648\sigma_0 \tag{4.20}$$

For the 50% decay, we obtain:

$$r(\lambda_2 = 0.5) = 1.1774\sigma_0 \tag{4.21}$$

That is, the signal of λ_2 is still quite powerful in the close neighborhood of the tube, and decays rapidly until being close two zero at more than twice the radius distance.

From the plots we can also visualize another property of the response of λ_2 that can be demostrated analytically.

Proposition 3. *The second eigenvalue of the Hessian matrix of the ideal cylinder with Gaussian cross-section, has an inflection point exactly at the location of the radius, that is for* $r = \sigma_0$

Proof. The condition for the inflection point is:

$$\lambda_2''(r) = \frac{\partial^2 \lambda_2}{\partial r^2} = 0 \tag{4.22}$$

The second derivative is:

$$\lambda_2''(r) = \frac{\sigma_0^2 - r^2}{\sigma_0^4} exp\left(-\frac{r^2}{2\sigma_0^2}\right) = -\lambda_1 \tag{4.23}$$

resulting in:

$$r\left(\lambda_2'' = 0\right) = \sigma_0$$

The value at this inflection point is:

$$\lambda_2\left(r\left(\lambda_2'' = 0\right)\right) \tag{4.24}$$

□

We have seen that the eigenvalues of the ideal cylinder have interesting properties for the detection of tubular structures, but these properties must be constrasted with the response in other types of structures.

4.2.2 Cartesian vs Cylindrical Coordinates for the Ideal Cylinder

The expressions for the ideal cylinder can be simplified by taking cylindrical coordinates as a reference system which, due to its cylindrical symmetry are the most natural way of describing the model. The change from cartesian (x,y,z) to cylindrical (r,θ,z) coordinates is:

$$\begin{aligned} r &= \sqrt{x^2+y^2} \\ \theta &= atan\left(\tfrac{y}{x}\right) \\ z &= z \end{aligned} \tag{4.25}$$

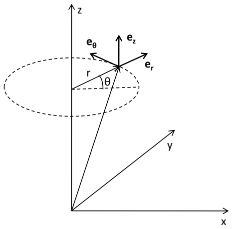

Figure 4.2: Cylindrical coordinates and corresponding orthogonal basis vectors

The inverse coordinate transformation is:

$$\begin{aligned} x &= r\cos\theta \\ y &= r\sin\theta \\ z &= z \end{aligned} \tag{4.26}$$

For any curvilinear coordinate system, orthogonal basis vectors are obtained by taking the tangent to the curve resulting from varying one coordinate while keeping the rest constant. The vectors obtained in this case are:

$$\begin{aligned} e_r &= r\cos\theta i + r\sin\theta j \\ e_\theta &= -r\sin\theta i + r\cos\theta j \\ e_z &= k \end{aligned} \tag{4.27}$$

These vectors are not constant and are depicted in 4.2 together with the corresponding cylindrical coordinates.

The change of coordinates results in the following expression for the ideal cylinder:

$$I_{cyl}(r,\theta,z) = K \exp\left(-\frac{r^2}{2\sigma_0^2}\right) \tag{4.28}$$

We can see that this expression only depends on the variable r. Now we can proceed to calculate the first-order derivatives:

$$\frac{\partial I_{cyl}}{\partial r} = -\frac{r}{\sigma_0^2} I_{cyl} \tag{4.29}$$

$$\frac{\partial I_{cyl}}{\partial \theta} = \frac{\partial I_{cyl}}{\partial z} = 0 \tag{4.30}$$

The calculation of the Hessian matrix is also straightforward:

$$H = \frac{1}{\sigma_0^4} I_{cyl} \begin{bmatrix} r^2 - \sigma_0^2 & 0 & 0 \\ 0 & 0 & 0 \\ 0 & 0 & 0 \end{bmatrix} \tag{4.31}$$

Proposition 4. *The Hessian matrix of the ideal cylinder with Gaussian crosss-section expressed in cylindrical coordinates has a single non-zero eigenvalue corresponding to a function of the second-derivative of the Gaussian with respecto to r. This main curvature occurs in the radial direction.*

Proof. From the above matrix we have the characteristic equation:

$$\left(r^2 - \sigma_0^2 - \lambda\right)\lambda^2 = 0 \tag{4.32}$$

The eigenvalues are:

$$\lambda_1 = \frac{r^2 - \sigma_0^2}{\sigma_0^4} I_{cyl} \tag{4.33}$$

$$\lambda_2 = 0 \quad (m = 2) \tag{4.34}$$

The eigenvector corresponding to the eigenvalue in the radial direction is obtained by the equations:

$$\begin{gathered} \left(r^2 - \sigma_0^2 - r^2 + \sigma_0^2\right) r_1 = 0 \\ \left(\sigma_0^2 - r^2\right)\theta_1 = 0 \\ \left(\sigma_0^2 - r^2\right) z_1 = 0 \end{gathered}$$

From the last two expressions $\theta_1 = z_1 = 0$ The first expression is true for any r_1 and we can take arbitrarily $r_1 = 1$. In order to obtain a vector in cartesian coordinates we can replace these values in equation 4.2.2:

$$x_1 = \begin{bmatrix} 1 \\ 0 \\ 0 \end{bmatrix} \tag{4.35}$$

which points in the direction of x. In fact, the condition that $r = 1$ means that $\sqrt{x^2 + y^2} = 1$ so we could take any eigenvector that satisfies the conditions:

$$\begin{aligned} &\sqrt{x^2 + y^2} = 1 \\ &z = 0 \end{aligned} \tag{4.36}$$

which is any radial direction.

□

Note that the condition that $r = 1$ was taken arbitrarily, so instead a section circle of unit radius, the eigenvector degenerates to the section plane passing by the origin at $z = 0$. Thus, we can rewrite the first eigenvector as[5]:

---

[5] Note that for the unit eigenvector we would need to divide by $r = \sqrt{x^2 + y^2}$ but we avoid this for simplicity.

$\lambda_1 = \frac{r^2-\sigma_0^2}{\sigma_0^4} I$	$\lambda_2 = 0 \quad (m=2)$
$x_1 = \begin{bmatrix} x & y & 0 \end{bmatrix}$	$x_2 = \begin{bmatrix} 0 & 0 & 1 \end{bmatrix}$

Table 4.2: Eigenvalues and vectors for the ideal Gaussian cylinder in polar coordinates

$$x_1 = \begin{bmatrix} x \\ y \\ 0 \end{bmatrix} \tag{4.37}$$

The second eigenvector corresponds to:

$$\begin{aligned} \left(r^2 - \sigma_0^2\right) r_2 &= 0 \\ 0\,\theta_2 &= 0 \\ 0\,z_2 &= 0 \end{aligned}$$

The first expression yields $r_2 = 0$ and the other two expressions are valid for any θ_2, z_2. By replacing these values in eq. 4.2.2 we obtein the z axis as eigenvector:

$$x_2 = \begin{bmatrix} 0 \\ 0 \\ 1 \end{bmatrix} \tag{4.38}$$

The eigenvalues and vectors reflect the fact that the intensity only varies on the radial direction and the surface defined by any r value is an iso-surface with value:

$$I_{cyl}(r = R, \theta, z) = K \exp\left(-\frac{R^2}{2\sigma_0^2}\right) \tag{4.39}$$

To sum up, we have obtained the following eigenvalues and eigenvectors for the ideal cylinder with Gaussian cross-section:

The eigenvalues and vectors reflect that one the principal curvatures occurs in the z direction (cylinder axis) and the other two curvatures occur in any two orthogonal directions in cross-section plane containing the origin. Hence the double multiplicity of the second eigenvalue.

4.2.3 Ideal Flat Structure

The ideal flat structure represents a thin, planar structure of infinite extension. The intensity variation occurs only in a principal direction corresponding to the normal to the surface. We can model the intensity profile accross the surface by a Gaussian function. If we make this direction coincide with the z axis, as shown in Figure the corrsponding equation is:

$$I_{flat}(x, y, z) = K \exp\left(-\frac{z^2}{2\sigma_0^2}\right) \tag{4.40}$$

$\lambda_1 = \frac{z^2-\sigma_0^2}{\sigma_0^4} I$	$\lambda_2 = 0 \quad (m = 2)$
$x_1 = \begin{bmatrix} 0 & 0 & 1 \end{bmatrix}$	$x_2 = \begin{bmatrix} x & y & 0 \end{bmatrix}$

Table 4.3: Eigenvalues and vectors for the ideal Gaussian flat structure in polar coordinates

Note that the equation coincides with that of the Gaussian cylinder in polar coordinates as in equation 4.2.2, but replacing r by z. Thus, the eigenvalues are the same but, due to the different nature of the coordinates, the interpretation of the second eigenvector varies. In this case, for the second eigenvector we have $z_2 = 0$ and x_2 and $y_2$can take any value yielding:

$$x_2 = \begin{bmatrix} x \\ y \\ 0 \end{bmatrix} \tag{4.41}$$

This is in fact not a vector but the plane $z = 0$. The eigenvalues and vector are then:

In this case the eigenvalues and vectors reflect that the principal curvature is in the z direction. If we want to find the other two orthogonal directions for the principal curvatures any other two directions in the plane $z = 0$ would be valid, due to the symmetry of the problem. Again this explains the double multiplicity of the second eigenvalue.

4.2.4 Ideal Blob Structure

A blob structure is an structure with no preferred direction for the intensity variation and can be modelled as a Gaussian sphere corresponding to the equation:

$$I_{blob}(x,y,z) = K \exp\left(-\frac{x^2+y^2+z^2}{2\sigma_0^2}\right) \tag{4.42}$$

We can take into account the symmetry of the problem an analyze it in spherical coordinates, using the following coordinate transformation:

$$\begin{array}{ll} r = \sqrt{x^2+y^2+z^2} & \\ \theta = a\tan\left(\frac{y}{x}\right) & 0 \leq \theta < 2\pi \\ \varphi = a\cos\left(\frac{z}{r}\right) & 0 \leq \varphi < \pi \end{array} \tag{4.43}$$

The inverse coordinate transformation is:

$$\begin{array}{l} x = r\cos\theta\sin\varphi \\ y = r\cos\theta\sin\varphi \\ z = r\cos\varphi \end{array} \tag{4.44}$$

The resulting equation in spherical coordinates is straightforward:

$$I_{blob}(r,\theta,\varphi) = K \exp\left(-\frac{r^2}{2\sigma_0^2}\right) \tag{4.45}$$

$\lambda_1 = \frac{r^2-\sigma_0^2}{\sigma_0^4} I$	$\lambda_2 = 0 \quad (m=2)$
$x_1 = \begin{bmatrix} 1 & 0 & 0 \end{bmatrix}$	$x_2 = \begin{bmatrix} 0 & 0 & 0 \end{bmatrix}$

Table 4.4: Eigenvalues and vectors for the ideal Gaussian blob structure (sphere) in polar coordinates

which again coincides with the equation of the Gaussian cylinder in polar coordinates (see eq. 4.2.2). In this case, when $r = 0$ the second eigenvector degenerates to the null vector. Thus, the eigenvalues and vector are in this case:

In this case the eigenvalues and vectors reflect that we can take any radial direction for the principal curvature. If we want to find the other two orthogonal directions for the principal curvatures any other two directions in the normal plane containing the origin would be valid, due to the symmetry of the problem. Once again, this explains the double multiplicity of the second eigenvalue.

4.2.5 Ideal....

4.3 Toroid

In the previous section we have studied the properties of the second-order derivatives for the ideal cylinder and other basic shape models. Next, we will introduce a more complicated model, the volumetric toroid, in order to study the effect of curvature and the behaviour of second-order derivatives with respect to the case of the ideal cylinder.

The toroid model was already introduced by Krissian *et al.* but here we will analyze it in more detail and provide more general expressions.

4.3.1 Centerline Definition

A *toroid* is a volumetric solid generated by the revolution of a circle around a coplanar axis. The resulting shape is that of a doughnut, assuming that the circle do not intersects the axis. If we just take the external surface, the shape is called *torus*.

We will assume that the circle revolves around the axis at a constant distance R which is the radius of the toroid, and that the radius of the circle is constant during the revolution. The centerline of such a toroid is a circle whose equation is given by:

$$\begin{aligned} x_C(\theta) &= R\cos\theta \\ y_C(\theta) &= 0 \\ z_C(\theta) &= R\sin\theta \end{aligned} \tag{4.46}$$

where we assume that the centerline lies in the plane $y = 0$, or, in other words, that the axis of revolution coincides with the y-axis. This orientation (see Figure 4.3) is more suitable for a comparison with the ideal cylinder model.

Figure 4.3: Curvilinear coordinates for the toroid model

4.3.2 Curvilinear Coordinates

In order to describe the equation of the volumetric toroid, it is convenient to describe it in terms of a set of curvilinear coordinates that take into account the geometry of the solid. This way we will obtain simpler expressions that can be analyzed easily.

Figure 4.3 shows the curvilinear coordinates that we will use for the toroid. The position of a point P in the volumetric toroid is given by the vectorial equation:

$$x_P(x,y,z) = x_C + r\cos\varphi e_1 + r\sin\varphi e_2 \tag{4.47}$$

The position vector x_C of the center of the cross-section in which P lies corresponds to the centerline defined in equation 4.3.1. We need to find an expression for e_1 and e_2, the basis vectors for the section that contains points P and C, in terms of the global reference system. Since $e_1$follows the direction of the segment $\overline{OC}$ we have that:

$$e_1 = \cos\theta i + \sin\theta k \tag{4.48}$$

On the other hand, the section normal n is tangent to the centerline circumference and thus:

$$n = -\sin\theta i \;\; + \cos\theta k + \tag{4.49}$$

Finally, from the figure, it is easy to see that

$$e_2 = j \tag{4.50}$$

which can also be derived from the cross-product

$$e_2 = n \times e_1 = \begin{vmatrix} i & j & k \\ -\sin\theta & 0 & \cos\theta \\ \cos\theta & 0 & \sin\theta \end{vmatrix} = \left(\cos^2\theta + \sin^2\theta\right) j = j$$

Replacing in equation 4.3.2 we obtain the inverse coordinate transformation from the curvilinear coordinates (r,φ,θ) to the cartesian coordinates:

$$\begin{array}{ll} x(r,\varphi,\theta) = R\cos\theta + r\cos\varphi\cos\theta & (1) \\ y(r,\varphi,\theta) = r\sin\varphi & (2) \\ z(r,\varphi,\theta) = R\sin\theta + r\cos\varphi\sin\theta & (3) \end{array} \tag{4.51}$$

We will proceed to find the direct coordinate transformation that takes the form:

$$\begin{array}{l} r = r(x,y,z) \\ \varphi = \varphi(x,y,z) \\ \theta = \theta(x,y,z) \end{array} \tag{4.52}$$

Combining equations 4.3.2 (1) and (3):

$$r\cos\varphi = \frac{x - R\cos\theta}{\cos\theta} = \frac{z - R\sin\theta}{\sin\theta}$$

From here we obtain[6]:

$$\begin{array}{ll} \tan\theta = \frac{z}{x} & (1) \\ \cos\theta = \frac{x}{\sqrt{x^2+z^2}} & (2) \\ \sin\theta = \frac{z}{\sqrt{x^2+z^2}} & (3) \end{array} \tag{4.53}$$

For the curvilinear coordinate r we know that

$$r^2 = (x - x_C)^2 + (y - y_C)^2 + (z - z_C)^2$$

$$r^2 = (x - R\cos\theta)^2 + y^2 + (z - R\sin\theta)^2$$

$$r^2 = x^2 + y^2 + z^2 + R^2 - 2R(x\cos\theta + z\sin\theta)$$

$$r^2 = x^2 + y^2 + z^2 + R^2 - 2R\sqrt{x^2+z^2}$$

Finally we obtain:

$$r = \sqrt{y^2 + \left(\sqrt{x^2+z^2} - R\right)^2} \tag{4.54}$$

From equation 4.3.2 (2):

$$\sin\varphi = \frac{y}{r} = \frac{y}{\sqrt{y^2 + \left(\sqrt{x^2+z^2} - R\right)^2}} \tag{4.55}$$

On the other hand:

$$\cos\varphi = \sqrt{1 - \sin^2\varphi} = \sqrt{1 - \frac{y^2}{y^2 + \left(\sqrt{x^2+z^2} - R\right)^2}}$$

$$\cos\varphi = \frac{\sqrt{x^2+z^2} - R}{\sqrt{y^2 + \left(\sqrt{x^2+z^2} - R\right)^2}} = \frac{\sqrt{x^2+z^2} - R}{r} = \frac{\sqrt{r^2 - y^2}}{r} \tag{4.56}$$

Finally:

$$\tan\varphi = \frac{y}{\sqrt{r^2 - y^2}} = \frac{y}{\sqrt{x^2+z^2} - R} \tag{4.57}$$

---

[6] Note that P is not necessarily on the centerline so in general $\sqrt{x^2+z^2} \neq R$

A possible expression for the direct coordinate transformation is thus:

$$\begin{aligned} r &= \sqrt{y^2+\left(\sqrt{x^2+z^2}-R\right)^2} && (1) \\ \theta &= \arctan\left(\tfrac{z}{x}\right) && (2) \\ \varphi &= \arctan\left(\frac{y}{\sqrt{x^2+z^2}-R}\right) && (3) \end{aligned} \tag{4.58}$$

Alternatively we can use any of the expressions derived above.

Now we will proceed to obtain some derivatives that we will use for our future analyses. By differentiating both sides of equation 4.3.2 (1):

$$dr = \frac{1}{2r}2\left(\sqrt{x^2+z^2}-R\right)\frac{2x}{2\sqrt{x^2+z^2}}dx$$

Replacing from equation 4.56 and 4.3.2 (2):

$$\frac{dr}{dx} = \cos\varphi\cos\theta \tag{4.59}$$

Similarly we obtain:

$$\frac{dr}{dy} = \frac{y}{r} = \sin\varphi \tag{4.60}$$

$$\frac{dr}{dz} = \cos\varphi\sin\theta \tag{4.61}$$

By taking derivatives on both sides of 4.3.2 (1):

$$\frac{d\theta}{\cos^2\theta} = -\frac{z}{x^2}dx = -\frac{\tan\theta}{x}dx$$

$$\frac{d\theta}{dx} = -\frac{\cos^2\theta\frac{\sin\theta}{\cos\theta}}{\cos\theta\left(R+r\cos\varphi\right)}$$

$$\frac{d\theta}{dx} = -\frac{\sin\theta}{R+r\cos\varphi} \tag{4.62}$$

Similarly:

$$\frac{d\theta}{\cos^2\theta} = \frac{dz}{x}$$

$$\frac{d\theta}{dz} = \frac{\cos^2\theta}{x} = \frac{\cos^2\theta}{R\cos\theta+r\cos\varphi\cos\theta}$$

$$\frac{d\theta}{dz} = \frac{\cos\theta}{R+r\cos\varphi} \tag{4.63}$$

And since y does not depend on θ and they are both independent variables:

$$\frac{d\theta}{dy} = 0 \tag{4.64}$$

To obtain similar relationships for the coordinate φ we can differentiate both sides of equation 4.57 and use the chain rule:

$$\frac{d\varphi}{\cos^2\varphi} = \frac{-y\frac{x}{\sqrt{x^2+z^2}}}{\left(\sqrt{x^2+z^2}-R\right)^2}dx$$

$$\frac{d\varphi}{dx} = -\frac{r\sin\varphi\cos\theta}{r^2\cos^2\varphi}\cos^2\varphi$$

$$\frac{d\varphi}{dx} = -\frac{1}{r}\sin\varphi\cos\theta \tag{4.65}$$

Similarly

$$\frac{d\varphi}{dy} = \frac{1}{r}\cos\varphi \tag{4.66}$$

$$\frac{d\varphi}{dz} = -\frac{1}{r}\sin\varphi\sin\theta \tag{4.67}$$

Now we can proceed to study the derivatives of the toroid model.

4.3.3 Gaussian Toroid and Derivatives

So far, we have just described the centerline of the toroid, which is in fact a circumference in 3D space, and a curvilinear coordinate system that takes into account the symmetry of the problem. We will proceed to introduce the equation of the volumetric toroid model.

At any point on the centerline, we will consider the section to have a constant intensity distribution. Our ultimate goal is to be able to detect vessels in volumetric datasets and tortuous vessels are typically small and tend to present partial volume effects. Hence, we will use a 2D Gaussian circular section as the intensity distribution for our volumetric helix section, which is more representative for small vessels. The equation of such a section in the plane is:

$$G(x_s, y_s) = K\exp\left(-\frac{x_s^2+y_s^2}{2\sigma_0^2}\right) \tag{4.68}$$

where we assume that the origin is at the center of the curent section.

If we want to describe the spatial intensity distribution of the toroid $I_{tor}(x,y,z)$ in a global 3D coordinate system, we need to express the position $C(x,y,z)$ of the current section centerline point in terms of this global coordinate system. However, this is straightforward if we use the curvilinear coordinate system just introduced, since the intensity only depends on the distance to the centerline and we know that:

$$r^2 = x_s^2 + y_s^2 \tag{4.69}$$

Thus, the resulting equation for the volumetric toroid with Gaussian cross-section, in terms of our curvilinear coordinate system is:

$$I_{tor}(r, \theta, \varphi) = K \exp\left(-\frac{r^2}{2\sigma_0^2}\right) \tag{4.70}$$

We can also express the volumetric toroid in cartesian coordinates by using the direct coordinate transformation of equation 4.3.2:

$$I_{tor}(x, y, z) = K \exp\left(-\frac{y^2 + \left(\sqrt{x^2+z^2} - R\right)^2}{2\sigma_0^2}\right)$$

where we have conveniently chosen the centerline of the toroid to lie on the plane $y = 0$.

Note that equation 4.3.3 is exactly the expression we had for the cylinder in cylindrical coordinates 4.28. However, the curvilinear coordinate system chosen here is different and does not correspond to the cylindrical coordinates. Our objective now is to calculate the expression of the derivatives in cartesian coordinates and compare them with the cylinder ideal model, in order to check how the curvature affects the value of the derivatives.

First, we need to calculate the first-order derivatives. We may use the chain rule for obtaining the *total* (not partial) first-order derivative[7] with respect to x:

$$\frac{dI}{dx} = \frac{\partial I}{\partial r}\frac{\partial r}{\partial x} = -\frac{r}{\sigma_0^2} I \cos\varphi \cos\theta$$

$$\frac{dI}{dx} = -\frac{r}{\sigma_0^2} \cos\varphi \cos\theta I \tag{4.71}$$

where the value of $\partial r/\partial x$ is taken from equation 4.127. In a similar fashion we obtain:

$$\frac{dI}{dy} = -\frac{r}{\sigma_0^2} \sin\varphi I \tag{4.72}$$

$$\frac{dI}{dz} = -\frac{r}{\sigma_0^2} \cos\varphi \sin\theta I \tag{4.73}$$

---

[7] When we use here the concept of total derivative of I with respect to x, y or z, we take into account all the indirect dependencies with respect to the variable we are obtaining the derivative for. When we use the partials derivatives, we do not take into account these dependencies. Note that in fact if $I = I(x, y, z)$ and if we didn't not have these intermediate dependencies, we would be talking about partial derivatives only since I depends on several variables, as we do in other parts of this thesis. Here we need a way to establish a difference and so we use the notation for total derivatives.

Now we can proceed to obtain the second-order partial derivatives. We start with the second derivative with respect to x. By the chain rule[8]:

$$\frac{d^2I}{dx^2} = \frac{\partial}{\partial r}\left(\frac{dI}{dx}\right)\frac{\partial r}{\partial x} + \frac{\partial}{\partial \theta}\left(\frac{dI}{dx}\right)\frac{\partial \theta}{\partial x} + \frac{\partial}{\partial \varphi}\left(\frac{dI}{dx}\right)\frac{\partial \varphi}{\partial x} \tag{4.74}$$

$$\frac{d^2I}{dx^2} = \frac{I}{\sigma_0^2}\left[\frac{r^2-\sigma_0^2}{\sigma_0^2}\cos^2\varphi\cos^2\theta - \frac{\sin^2\theta}{1+\frac{R}{r\cos\varphi}} - \sin^2\varphi\cos^2\theta\right]$$

Similarly we obtain:

$$\frac{d^2I}{dy^2} = \frac{I}{\sigma_0^2}\left[\frac{r^2-\sigma_0^2}{\sigma_0^2}\sin^2\varphi - \cos^2\varphi\right] \tag{4.75}$$

$$\frac{d^2I}{dz^2} = \frac{I}{\sigma_0^2}\left[\frac{r^2-\sigma_0^2}{\sigma_0^2}\cos^2\varphi\sin^2\theta - \frac{\cos^2\theta}{1+\frac{R}{r\cos\varphi}} - \sin^2\varphi\sin^2\theta\right] \tag{4.76}$$

$$\frac{d^2I}{dxdy} = \frac{I}{\sigma_0^2}\left[\frac{r^2}{\sigma_0^2}\cos\theta\sin\varphi\cos\varphi\right] \tag{4.77}$$

$$\frac{d^2I}{dxdz} = \frac{I}{\sigma_0^2}\sin\theta\cos\theta\left[\frac{r^2-\sigma_0^2}{\sigma_0^2}\cos^2\varphi - \frac{1}{1+\frac{R}{r\cos\varphi}} - \sin^2\varphi\right] \tag{4.78}$$

$$\frac{d^2I}{dydz} = \frac{I}{\sigma_0^2}\left[\frac{r^2}{\sigma_0^2}\sin\theta\sin\varphi\cos\varphi\right] \tag{4.79}$$

Due to the symmetry of the problem we can choose the values of the angles to be $\theta = 0$ (origin of the toroid centerline) and $\varphi = 0$ (zero polar angle for the section). This yields the following simplified Hessian matrix:

$$H = \frac{I}{\sigma_0^2}H' \tag{4.80}$$

$$H'(\theta = 0, \varphi = 0) = \begin{bmatrix} \frac{r^2-\sigma_0^2}{\sigma_0^2} & 0 & 0 \\ 0 & -1 & 0 \\ 0 & 0 & -\frac{1}{1+\frac{R}{r}} \end{bmatrix} \tag{4.81}$$

However, the previous expression is only valid for values of r from the centerline to the external boundary of the toroid ($\varphi = 0°$). If we choose values of r towards the internal part of the toroid, then $\varphi = 180°$ and the expression becomes

$$H'(\theta = 0, \varphi = 180) = \begin{bmatrix} \frac{r^2-\sigma_0^2}{\sigma_0^2} & 0 & 0 \\ 0 & -1 & 0 \\ 0 & 0 & -\frac{1}{1-\frac{R}{r}} \end{bmatrix} \tag{4.82}$$

This is the same as considering that the expression 4.81 can take both positive and negative values for r.

---

[8] Note that we must also take into account that $I = I(r)$when calculating derivatives with respect to r.

4.3.4 Eigenvalues and Eigenvectors

We proceed to calculate the eigenvalues and vectors of the Hessian matrix which correspond to the roots of the characteristic equation[9]:

$$\left|H - \lambda' I\right| = 0 \tag{4.83}$$

which yields the characteristic polynomial:

$$\left(\frac{r^2-\sigma_0^2}{\sigma_0^2} - \lambda'\right)\left(-1-\lambda'\right)\left(-\frac{1}{1+\frac{R}{r}} - \lambda'\right) = 0 \tag{4.84}$$

Since the Hessian matrix is a diagonal matrix, the eigenvalues are directly the diagonal elements. After multiplying by $\frac{I}{\sigma^2}$ we obtain:

$$\lambda_1 = \frac{r^2-\sigma_0^2}{\sigma_0^4} I \qquad \lambda_2 = -\frac{1}{\sigma_0^2} I \qquad \lambda_3 = -\frac{1}{1+\frac{R}{r}}\frac{1}{\sigma_0^2} I \tag{4.85}$$

Lemma 5. *The radius of curvature R of the ideal toroid model with Gaussian cross-section has only influence in the principal curvature corresponding to a direction perpendicular to the local toroid section.*

Proof. We can see that, for $\theta = 0$ and $\varphi = 0$, the first and second principal curvatures λ_1 and λ_2 for $\theta = 0$ and $\varphi = 0$ coincide with the first two principal curvatures of the ideal cylinder in cartesian coordinates (see equations 4.2.1 and 4.2.1) and are not influenced by the radius of curvature R of the toroid. However, we can see that, compared with the cylinder model, the third eigenvalue, corresponding to the z direction at the origin is not zero anymore and depends on the distance r to the centerline and the radius of curvature R of the toroid. Due to the symmetry of the problem, the same holds for other angles other than $\theta = 0$ and $\varphi = 0$. ☐

Now we can proceed to obtain the corresponding eigenvectors, which are the solutions of the equation 4.14. For the first eigenvalue we have the equations:

$$\left(\frac{r^2-\sigma_0^2}{\sigma_0^2} - \frac{r^2-\sigma_0^2}{\sigma_0^2}\right) v_x = 0$$

$$\left(-1 - \frac{r^2-\sigma_0^2}{\sigma_0^2}\right) v_y = 0$$

$$\left(-\frac{1}{1+\frac{R}{r}} - \frac{r^2-\sigma_0^2}{\sigma_0^2}\right) v_z = 0$$

The first equation is zero for all v_x. From the second and third equation we obtain $v_y = 0$ and $v_z = 0$. We can choose $x = 1$ in order to obtain a unit vector. Thus, the first eigenvalue is:

---

[9] Here I is the identity matrix, not the toroid equation.

$\lambda_1 = \frac{r^2-\sigma_0^2}{\sigma_0^4} I$	$\lambda_2 = -\frac{1}{\sigma_0^2} I$	$\lambda_3 = -\frac{1}{\sigma_0^2} \frac{1}{1+\frac{R}{r}} I$
$x_1 = \begin{bmatrix} 1 & 0 & 0 \end{bmatrix}$	$x_2 = \begin{bmatrix} 0 & 1 & 0 \end{bmatrix}$	$x_3 = \begin{bmatrix} 0 & 0 & 1 \end{bmatrix}$

Table 4.5: Eigenvalues and vectors for the ideal Gaussian toroid with $\theta = 0$, $\varphi = 0$.

$\lambda_1 = \frac{r^2-\sigma_0^2}{\sigma_0^4} I$	$\lambda_2 = -\frac{1}{\sigma_0^2} I$	$\lambda_3 = -\frac{1}{\sigma_0^2} \frac{1}{1-\frac{R}{r}} I$
$x_1 = \begin{bmatrix} 1 & 0 & 0 \end{bmatrix}$	$x_2 = \begin{bmatrix} 0 & -\tau & \kappa \end{bmatrix}$	$x_3 = \begin{bmatrix} 0 & \kappa & \tau \end{bmatrix}$

Table 4.6: Eigenvalues and vectors for the ideal Gaussian toroid with $\theta = 0$, $\varphi = 180$. Note that in these expressions $r > 0$.

$$x_1 = \begin{bmatrix} 1 \\ 0 \\ 0 \end{bmatrix} \tag{4.86}$$

which goes in the x direction (remember that this is for $\theta = 0$ and $\varphi = 0$).

It is easy to see, that being the Hessian a diagonal matrix, the remaining eigenvectors are:

$$x_2 = \begin{bmatrix} 0 \\ 1 \\ 0 \end{bmatrix} \tag{4.87}$$

$$x_3 = \begin{bmatrix} 0 \\ 0 \\ 1 \end{bmatrix} \tag{4.88}$$

which correspond to the y and z directions.

To sum up, we have obtained the following eigenvalues and corresponding eigenvectors for the regular toroid with Gaussian cross-section at the starting point of the helix ($\theta = 0, \varphi = 0$):
where I is defined in eq. 4.3.3.

Using a similar procedure, we can obtain the eigenvalues and vectors for ($\theta = 0, \varphi = 180$), that is, for points in the internal part of the toroid with respect to the centerline. The resulting eigenvalues and vectors are:

We can get a single combined expression by considering that r can take both positive and negative values in the expressions of Table 4.5. In fact what we change is the value of the angle φ by 180º and not the sign of the radius but the effect is the same.

4.3.5 Effect of curvature

4.3.5.1 Theoretical Model

We can already draw some conclusions on the effect of curvature as compared with a straight ideal cylinder from the simplified expressions of the eigenvalue λ_3:

Lemma 6. *Let $\overline{OC}$ be a line that connects the center of the toroid O with any point C on the centerline of the toroid with $d\left(\overline{OC}\right) \equiv R$. Let $P_1$and P_2 be symmetrical points on that line with respect to C at a distance r with P_1 the closest to O. Then, $|\lambda_3(P_1)| \geq |\lambda_3(P_2)| \forall r$.*

Proof. From the simplified expression of λ_3

$$\lambda_3 = -\frac{1}{\sigma_0^2}\frac{1}{1+\frac{R}{r}}I$$

where r can take positive or negative values depending if we are in the external ($\varphi = 0$) or internal ($\varphi = 180$) part of the cylinder we can see that, for the same absolute value of r we obtain two points P_1, P_2 in the line with respective values

$$\lambda_3^- = \lambda_3(P_1) = -\frac{1}{\sigma_0^2}\frac{1}{1-\frac{R}{|r|}}I \tag{4.89}$$

$$\lambda_3^+ = \lambda_3(P_2) = -\frac{1}{\sigma_0^2}\frac{1}{1+\frac{R}{|r|}}I \tag{4.90}$$

Comparing the quotient in the middle we can distinguish three cases for r. If $\frac{R}{|r|} < 1$ then the denominator in eq. 4.89 is always positive and the total value negative. If $\frac{R}{|r|} < 1$ the denominator in eq. 4.89 is always negative and the total value positive. If $\frac{R}{|r|} < 1$ then the denominator is zero in the same equation and the total value infinite. In all three cases the denominator in eq. 4.89 is smaller in absolute value than in 4.90 and thus $|\lambda_3(P_1)| \geq |\lambda_3(P_2)| \forall r$.

□

Thus, in the presence of curvature, the internal part of the toroid presents larger absolute values of λ_3 obtaining an assymetrical response. We can see that there is also asymmetry in the sign in the most typical case where $|r| < R$[10] , since in the internal part of the toroid (P_1), the value of $\lambda_3$becomes positive in this case whereas in the external part is always negative. From the formula we can see also that the assymetry in values is more noticeable when R is smaller, that is, which higher curvatures, since the effect of adding 1 in the denominator becomes more important and viceversa.

Figure 4.4 shows the ideal values of λ_3 as a function of r (distance to the closest toroid centerline point, for different values of σ_0 (which determines the apparent radius of the Gaussian section) and R (the radius of the toroid that determines the curvature) when $\theta = 0$ and $\varphi = 0$ (or $\varphi = 180^o$ for negative values of r). Increasing positive values of r imply moving towards the external boundary of the toroid whereas increasing negative values imply moving towards the internal boundary.

We can see that the eigenvalueλ_3 is always zero at the center of the section as in the case of the ideal cylinder. However, this eigenvalue starts increasing negatively as r increases positively and reaches a negative maximum at the vicinity of the toroid

---

[10] If $|r| < R$ either we are in places of very little influence or R is very small and the internal radius σ_0 of similar size which barely occurs in practice.

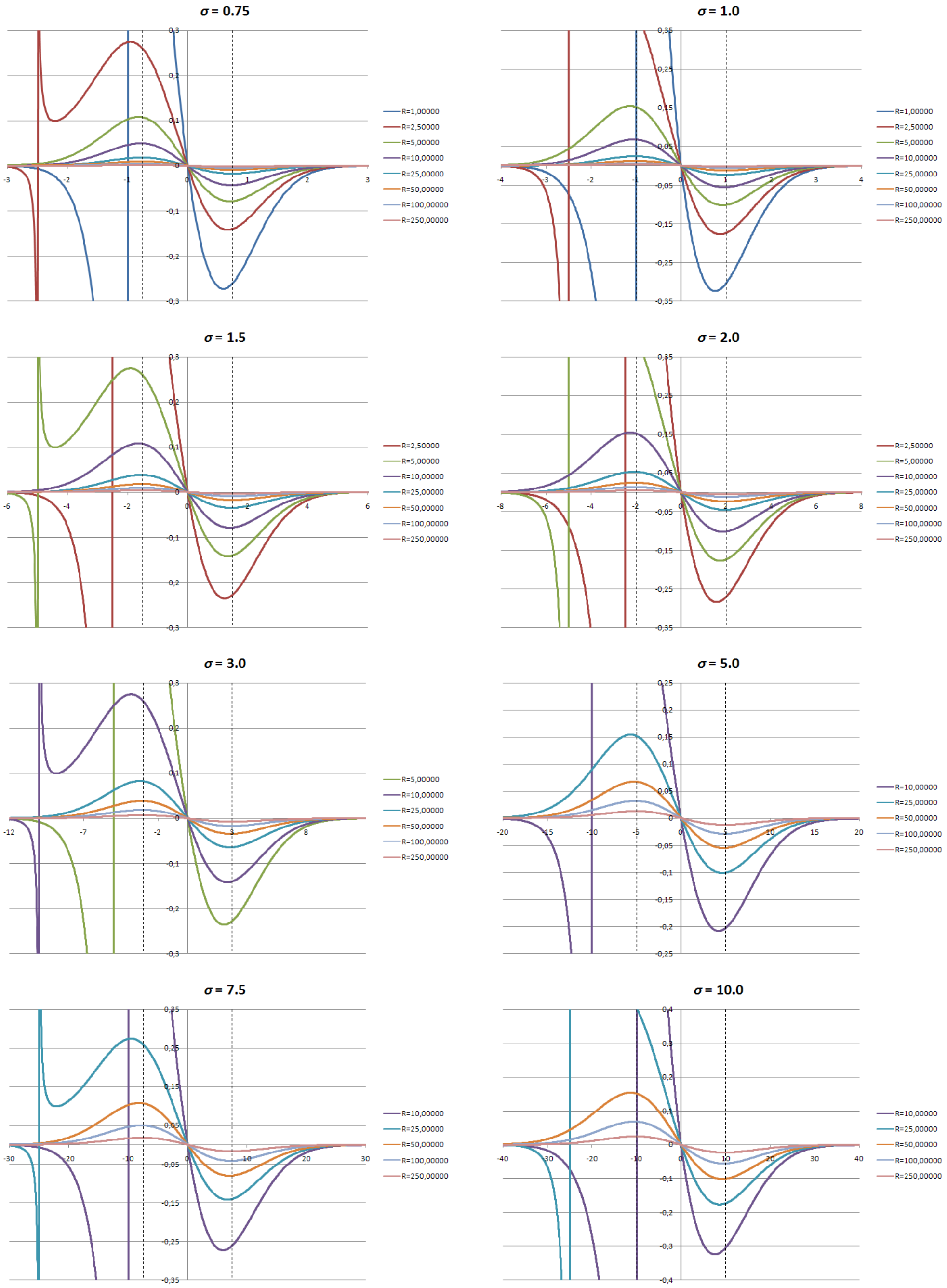

Figure 4.4: Values of λ_3 as a function of r with $\theta = 0$ and $\varphi = 0$ (or $\varphi = 180$ºfor $r < 0$) for different toroid centerline R and section σ_0 radius. Dashed vertical lines correspond to section (apparent) boundaries $(\sigma, -\sigma)$.

external section boundary, and viceversa, the eigenvalue starts increasing positively as r increases negatively and reaches a maximum at the vicinity of the internal boundary. We can also notice the asymmetrical response in absolute values with respect to the center, the values being larger in the inner part of the toroid (negative r).

Some other things are noteworthy:

- As the curvature increases (smaller R), both maximum positive and negative values tends to be larger. This was expected, since with the more the curvature increases the more the situation differs from the ideal tube in which the curvature is zero.

- As the curvature increases, the location of the negative maximum ($\sigma > 0$) is closer to the centerline, and the location of the positive maximum ($\sigma < 0$) is further from the centerline. We can theoretically derive the location of this maximum by calculating:

  $$\frac{\partial \lambda_3}{\partial r} = 0 \tag{4.91}$$

  $$\frac{\partial \lambda_3}{\partial r} = \frac{1}{\sigma_0^2} \exp\left(-\frac{r^2}{2\sigma_0^2}\right) \left[\frac{r^2}{(R+r)\,\sigma_0^2} - \frac{R}{(R+r)^2}\right]$$

  $$\frac{\partial \lambda_3}{\partial r} = \frac{1}{\sigma_0^2} \exp\left(-\frac{r^2}{2\sigma_0^2}\right) \left[\frac{r^2\,(R+r) - R\sigma_0^2}{(R+r)^2\,\sigma_0^2}\right] \tag{4.92}$$

  The exponential term is not zero except for $r = \pm\infty$. Then

  $$\left[\frac{r^2\,(R+r) - R\sigma_0^2}{(R+r)^2\,\sigma_0^2}\right] = 0$$

  $$r^3 + Rr^2 - R\sigma_0^2 = 0 \tag{4.93}$$

  If we think of R as a factor of the internal radius $R = k\sigma_0$we have

  $$r^3 + k\sigma_0 r^2 - k\sigma_0^3 = 0 \tag{4.94}$$

  We can also think of the solution r as $r = a\sigma_0$resulting in the equation:

  $$a^3 + ka^2 - k = 0 \tag{4.95}$$

  which does not depend on σ_0.

- For large curvatures, there is a discontinuity which corresponds to $|r| = R$ in equation 4.159. However, this theoretical situation does not occur in practice since it implies obtaining values of λ_3 in situations of large curvature and in places where the influence of the tube is negligible or minimal (very far from the centerline).

Figures 4.5 to 4.7 show the compared value of the three eigenvalues for different internal radius σ_0 and toroid centerline radius R. Note that as R increases, that is, as the curvature decreases, the third eigenvalue corresponding to the tubular direction becomes less significant and approaches the ideal cylinder. On the other hand, for the same curvature, the third eigenvalue becomes more significant with larger σ_0. The rest of eigenvalues remain the same (assuming σ-normalized Gaussian derivatives).

The conclusion is that, as pointed out by Krissian *et al.* if the point to be analyzed is in the vessel but not in the centerline, the values of λ_3 in the presence of curvature may not be negligible compared to the other eigenvalues. Moreover, this effect is more important in the internal part of the curve closest to the curvature center, that in the external part. This is important since, as we will see in Section a family of vessel detection methods assume that at vessel points λ_3 is almost zero and λ_1 and λ_2 are large and of similar value, which locally describes the principal curvatures of a cylindrical image structure.

4.3.5.2 Experimental Model

In order to compare the theoritecal conclusions in discrete models we designed a set of synthetic volumetric toroids with varying section σ_0 and centerline R radius. The procedure we used to create such a toroid is the following:

3. Create a discrete centerline for the given R and the limiting angles θ_{min} and θ_{max} which allow to create a toroid sector instead of a full toroid. In order to have enough precision[11], the number of centerline points is chosen as:

$$N = 2\left\lfloor \frac{(\theta_{max} - \theta_{min})R}{\delta} \right\rfloor \quad \{\theta_{min}, \theta_{max}\}\,\varepsilon\,[0, 2\pi] \tag{4.96}$$

where δ is spatial resolution of the volumetric image in which the toroid will lie, assuming the same spacing in all three directions. Note the *floor* function notation $\lfloor\rfloor$. In turn, we choose δ to depend on σ_0 in order to provide and appropiate sampling of the discrete Gaussian functions as follows:

$$\delta = \begin{cases} 0.2\sigma_0 & \sigma_0 \geq 1.25 \\ 0.25 & \text{otherwise} \end{cases} \tag{4.97}$$

The second condition is introduced to limit the computation time for small σ_0 since this computation time increases as σ_0 decreases, because N becomes larger. The resulting number of points for a full circle is:

We can see that for large values of R the number of samples may be considerably large.

4. Create and empty volumetric image to hold the toroid with the calculated spatial resolution δ. Assuming that the toroid is centered on the volume lying on the xy plane, the physical dimensions of the image will be approximately[12]:

---

[11] Note that the method is not optimized for speed but for precision since we are interested in building a realistic model. The number of points can be reduced to obtain a less precise model in less time.

[12] It is approximate because we need an integer number of equispaced samples to create a discrete image grid.

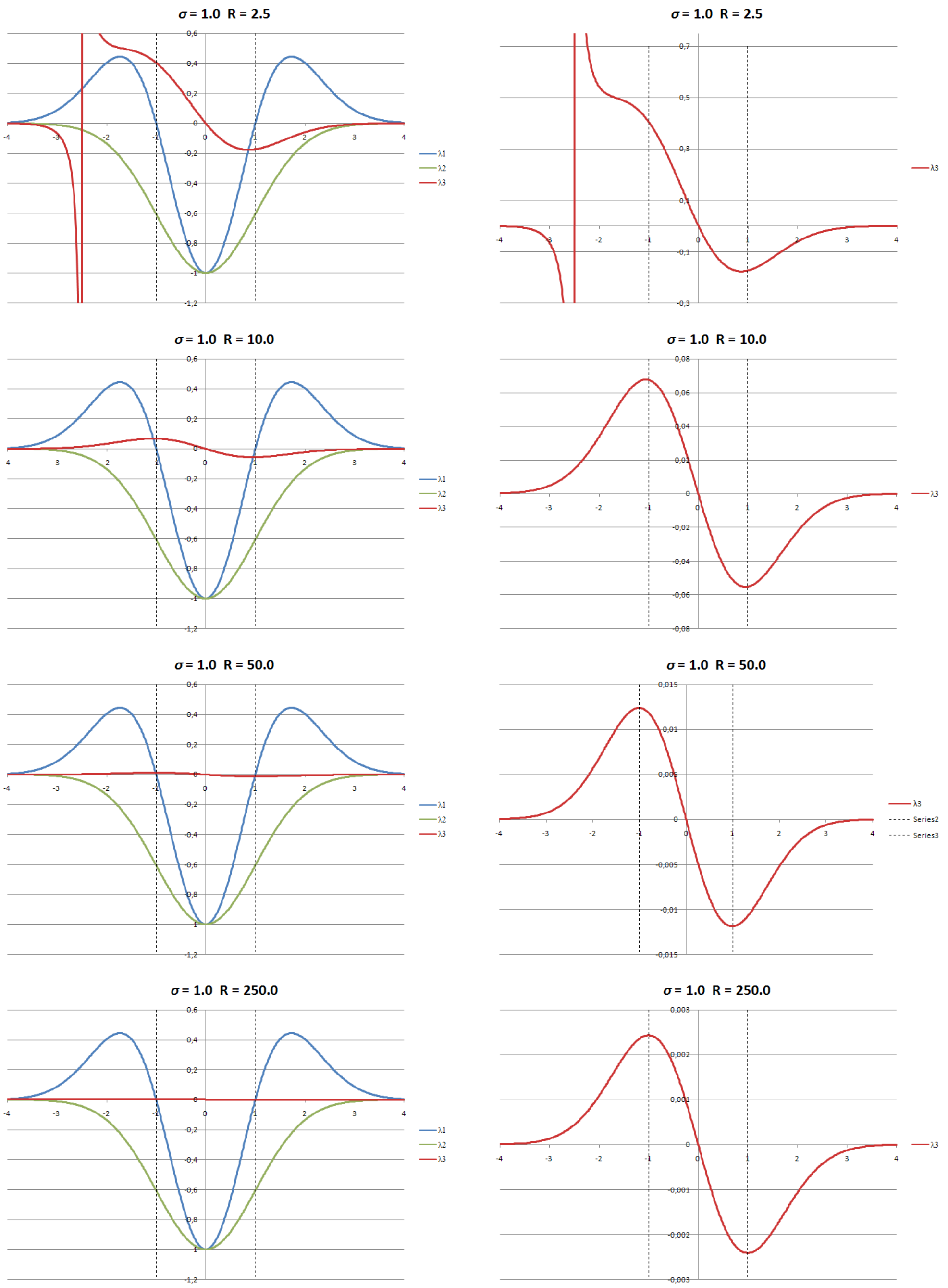

Figure 4.5: Toroid eigenvalues as a function of r with $\theta = 0$ and $\varphi = 0$ (or $\varphi = 180$ºfor $r < 0$), $\sigma_0 = 1.0$ and varying R. Left: three eigenvalues compared. Right: detail of third eigenvalue.

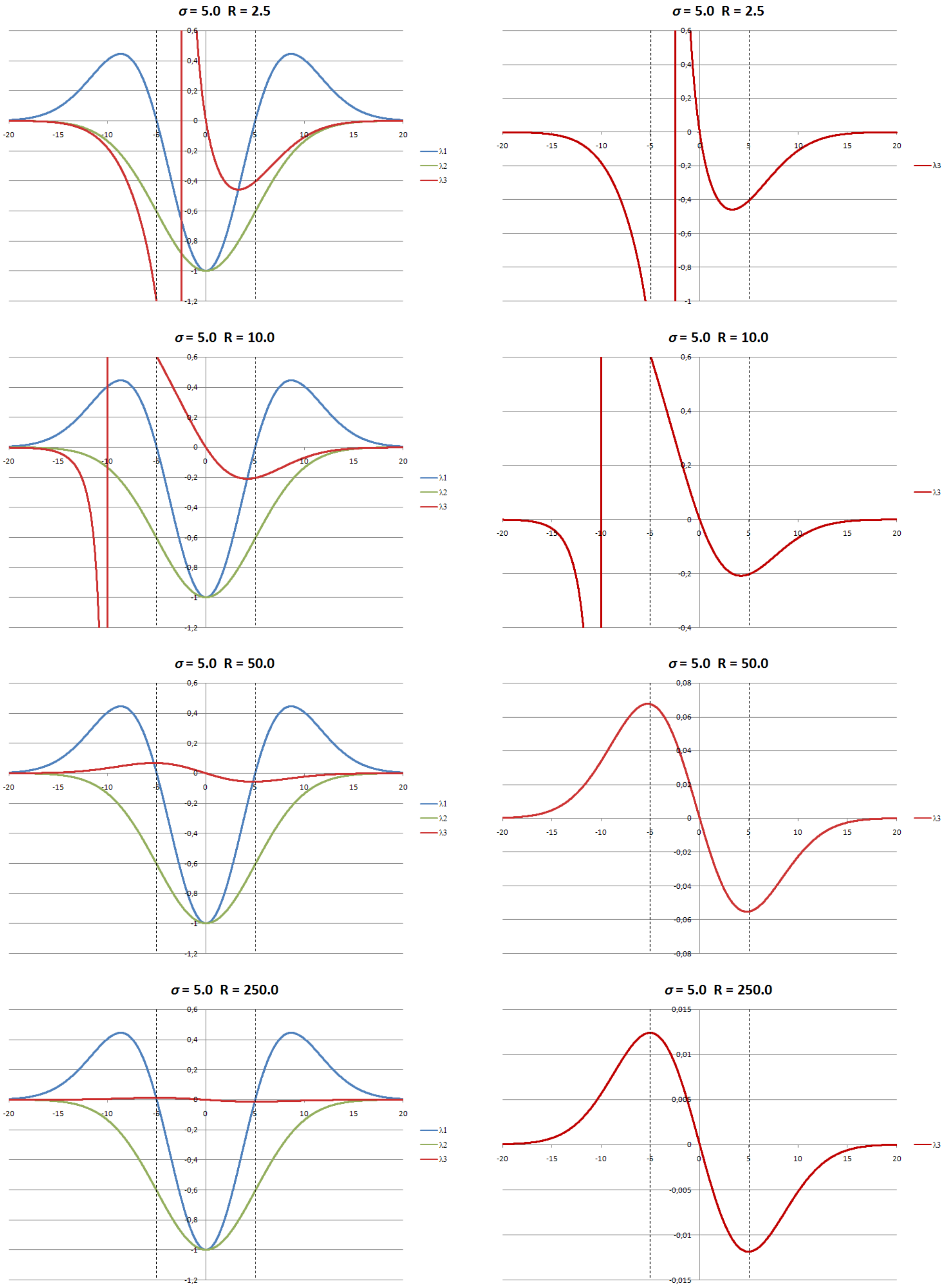

Figure 4.6: Toroid eigenvalues as a function of r with $\theta = 0$ and $\varphi = 0$ (or $\varphi = 180$ºfor $r < 0$), $\sigma_0 = 5.0$ and varying R. Left: three eigenvalues compared. Right: detail of third eigenvalue.

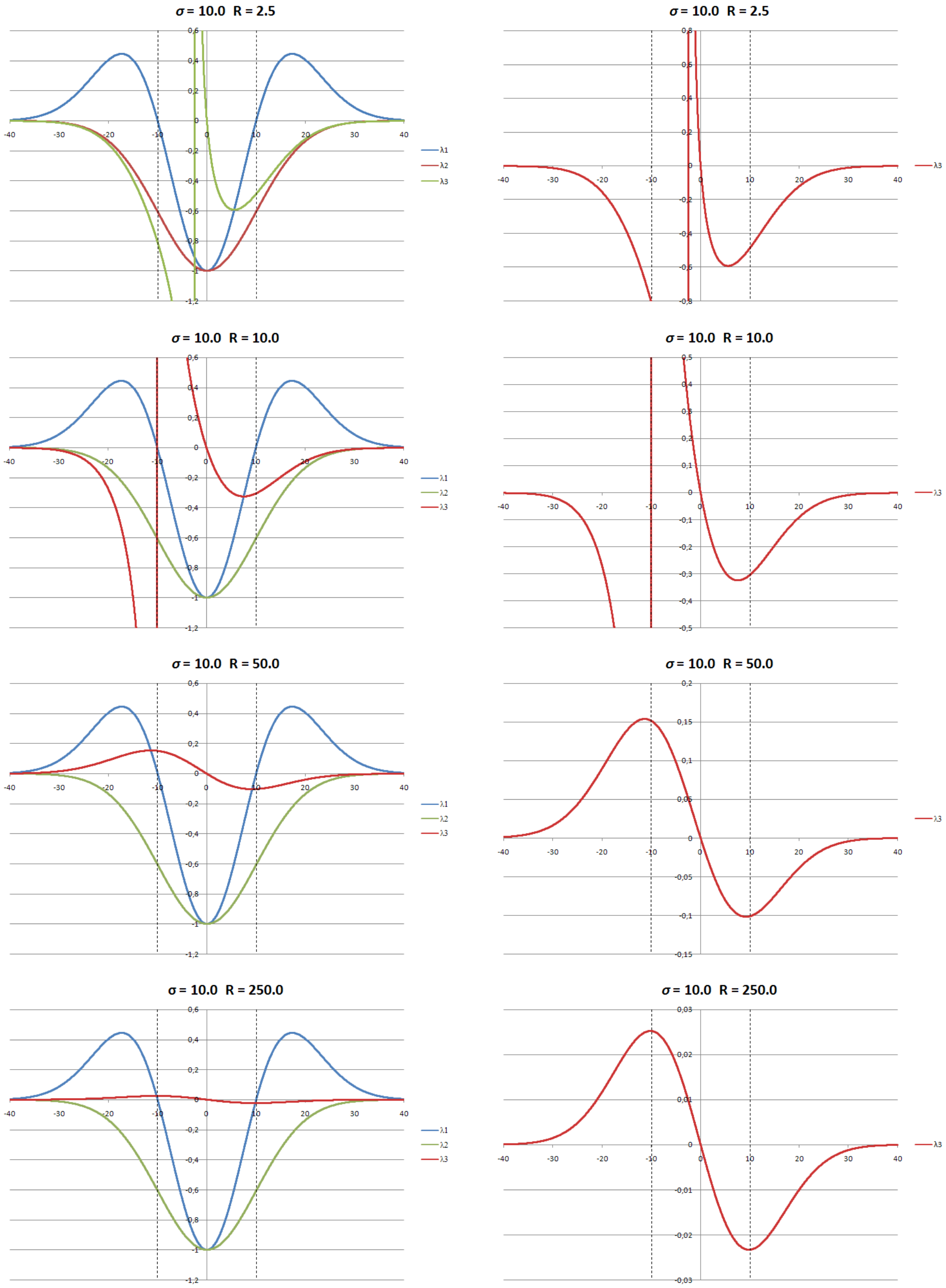

Figure 4.7: Toroid eigenvalues as a function of r with $\theta = 0$ and $\varphi = 0$ (or $\varphi = 180$ºfor $r < 0$), $\sigma_0 = 10.0$ and varying R. Left: three eigenvalues compared. Right: detail of third eigenvalue.

σ_0	$R = 2.5$	$R = 10.0$	$R = 50.0$	$R = 250.0$
0.75	125	502	2513	12566
1.0	125	502	2513	12566
1.25	125	502	2513	12566
2.0	78	314	1570	7853
3.0	52	209	1047	5235
5.0	31	125	628	3141
7.5	20	83	418	2094
10.0	15	62	314	1570

Table 4.7: Centerline sampling points depending on internal and external toroid radius.

$$\begin{aligned} S_x' &= S_y' = 2\,(R + 4\sigma_0 + a) \\ S_z' &= 2\,(4\sigma_0 + a) \end{aligned} \tag{4.98}$$

where, a is the desired additional offset. For the calculations we have taken the value $4\sigma_0$ as the external boundary of the Gaussian function, where it is attenuated from respect to the maximum by a factor of 3.3546×10^{-4}[13] which can be considered as zero for our purposes and provides us with more than enough precision. The resulting image dimensions are:

$$\begin{aligned} N_x &= N_y = \lfloor 2\,(R + 4\sigma_0 + a)/\delta \rfloor \\ N_z &= \lfloor 2\,(4\sigma_0 + a)/\delta \rfloor \end{aligned} \tag{4.99}$$

The resulting final physical dimensions are

$$\begin{aligned} S_x &= S_y = N_x\delta = N_y\delta \\ S_z &= N_z\delta \end{aligned} \tag{4.100}$$

5. Iterate through all points on the image. For each point:

6. Find the closest centerline point.

7. Calculate the Gaussian value by taking the distance to the centerline as r.

8. Set this value if is larger than the current image value.

Axial slices of toroid models lying on the xy plane can be seen on Figure 4.8.

Once the images are prepared, we can proceed to obtain the corresponding response profiles by sampling the toroid values and corresponding Hessian matrix eigenvalues, whose derivatives are calculated at the corresponding scales, that is with $\sigma = \sigma_0$, where σ is the scale or aperture of the derivative calculation and σ_0 defines the size of the Gaussian section of the toroid (internal radius). Values are obtained by linearly interpolating at continuous locations in the interval $[-4\sigma_0, 4\sigma_0]$ around the centerline point $x_0 = x_C(\theta = 0)$ obtaining the set of sampling locations:

---

[13] To obtain this value simply replace $r = 4\sigma$ in the exponential of the Gaussian function

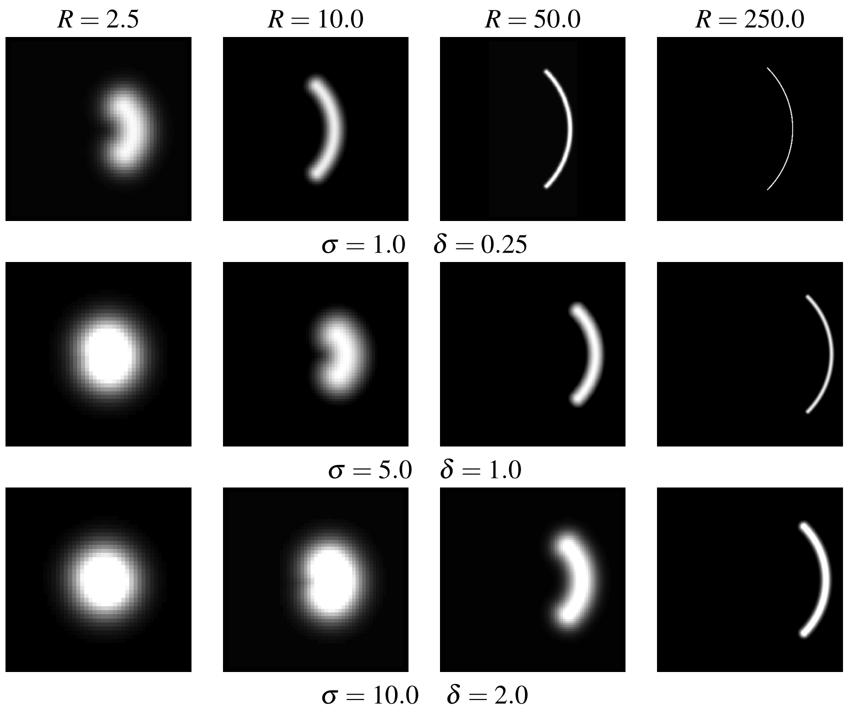

Figure 4.8: Gaussian toroid experimental models with varying $\sigma_0$and R represented as axial slices in the xy plane.

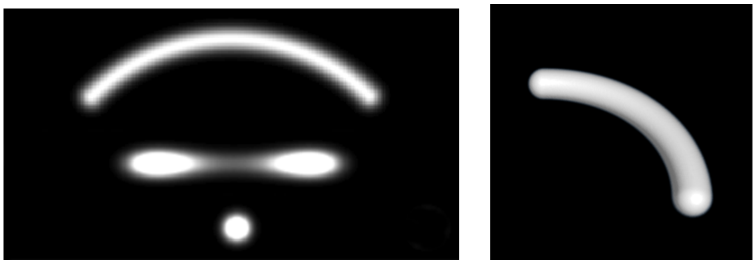

Figure 4.9: Gaussian toroid experimental model for $\sigma_0 = 10.0$ and $R = 250.0$. Left: axial rotated (top), sagittal (middle) and coronal (bottom) slices. Right: 3D volume rendering.

$$X_i = \{(x_i, y_0, z_0) : x_0 = x_C(0), (\exists i \in \mathbb{N} : x_i = x_0 + i\Delta x, x_i \in [-4\sigma_0, 4\sigma_0])\} \quad (4.101)$$

where we assume that the toroid centerline lies in the xy plane. In all of our experiments we used as sampling distance $\Delta x = 0.25\delta$ which provides an appropiate sampling in relation with the discrete image grid. The obtained results are depicted in Figure XXX.

We can see that, for small values of σ_0 and R the eigenvalue in the tube direction λ_3 differs considerably from zero, although in the proximity of the central zone ($r = 0$), it is still smaller than the other two eigenvalues. As R increases the eigenvalue also becomes closer to zero. We can also see that there are two peaks in the eigenvalue one positive on the left and one negative on the right at locations close to $r = -\sigma_0$ and $r = \sigma_0$ respectively. In these situations is where the theoretical values became discontinuous at some points close to the center.

On the other hand, when the ratio R/σ_0becomes small the eigenvalue λ_3 becomes more negative and closer to the values of λ_2. This is because the toroid becomes very thick but with a small perimeter and then resembles more like a blob which has all three eigenvalues large and negative . In intermediate cases, for example with $\sigma = 5.0$ and $R = 10.0$ we can see an evident assymetry which is an intermediate stage between the local structure of a tube and a blob. The assymetry occurs toward the internal side of the toroid curve ($r < 0$) which makes values more negative at the center and is a situation more likely to occur in practice.

The case $\sigma = 5.0$ and $R = 50.0$ is an exemplary case in which we can see the expected theoretical assymetry for λ_3 both in sign and peak values (larger positive peak on the left) with respect to the center. However, the values of λ_3 are already considerably small with respect to the other eigenvalues.

Finally, as the ratio R/σ_0becomes larger, the value of $\lambda_3$get closer to zero as the situation resembles an ideal cylinder.

4.4 Helix

The volumetric helix is a very interesting shape model, because it allows us to study both the effect of curvature and torsion in the derivative-based detection of curvilinear structures.

4.4.1 Centerline Definition

A helix is a smooth curve in three-dimensional space. Its main characteristic is that the tangent line at any point makes a constant angle with the helix axis. The helix revolves around the axis as it ascends (or descends). Helices can be left-handed or right handed, depending on the direction of ascension. The ratio of ascension per angle unit is usually a constant H for regular helices. We will call this constant here helix *unit pitch*. Usually the *pitch* is defined as $2\pi H$, that is, the amount the helix ascends (in the axial direction) in a complete 360° turn.

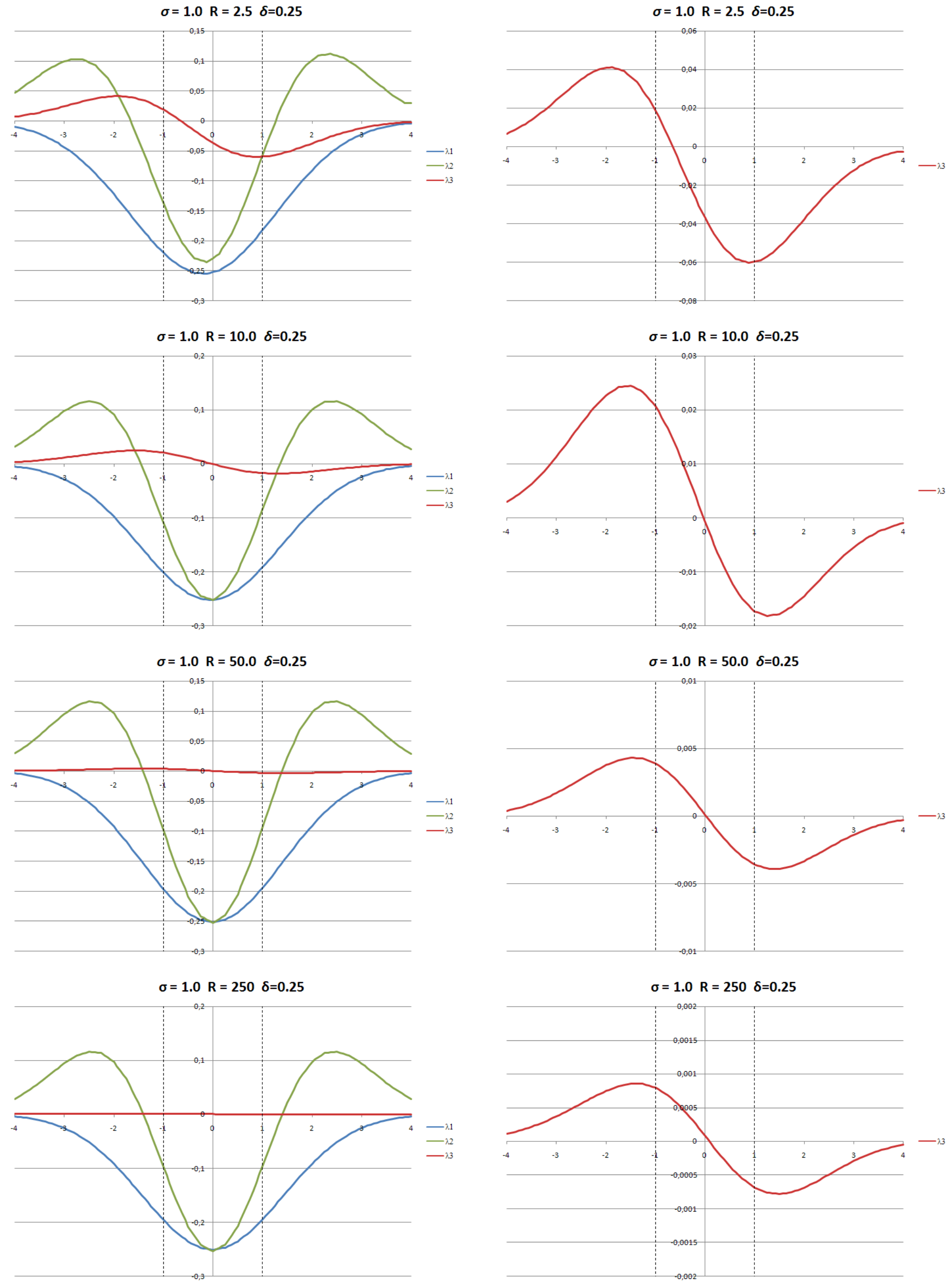

σ = 1.0 R = 2.5 δ=0.25

σ = 1.0 R = 2.5 δ=0.25

σ = 1.0 R = 10.0 δ=0.25

σ = 1.0 R = 10.0 δ=0.25

σ = 1.0 R = 50.0 δ=0.25

σ = 1.0 R = 50.0 δ=0.25

σ = 1.0 R = 250 δ=0.25

σ = 1.0 R = 250 δ=0.25

Figure 4.10: Experimental discrete toroid eigenvalues for $\sigma_0 = 1.0$ and varying R. Left: three eigenvalues compared. Right: detail of third eigenvalue.

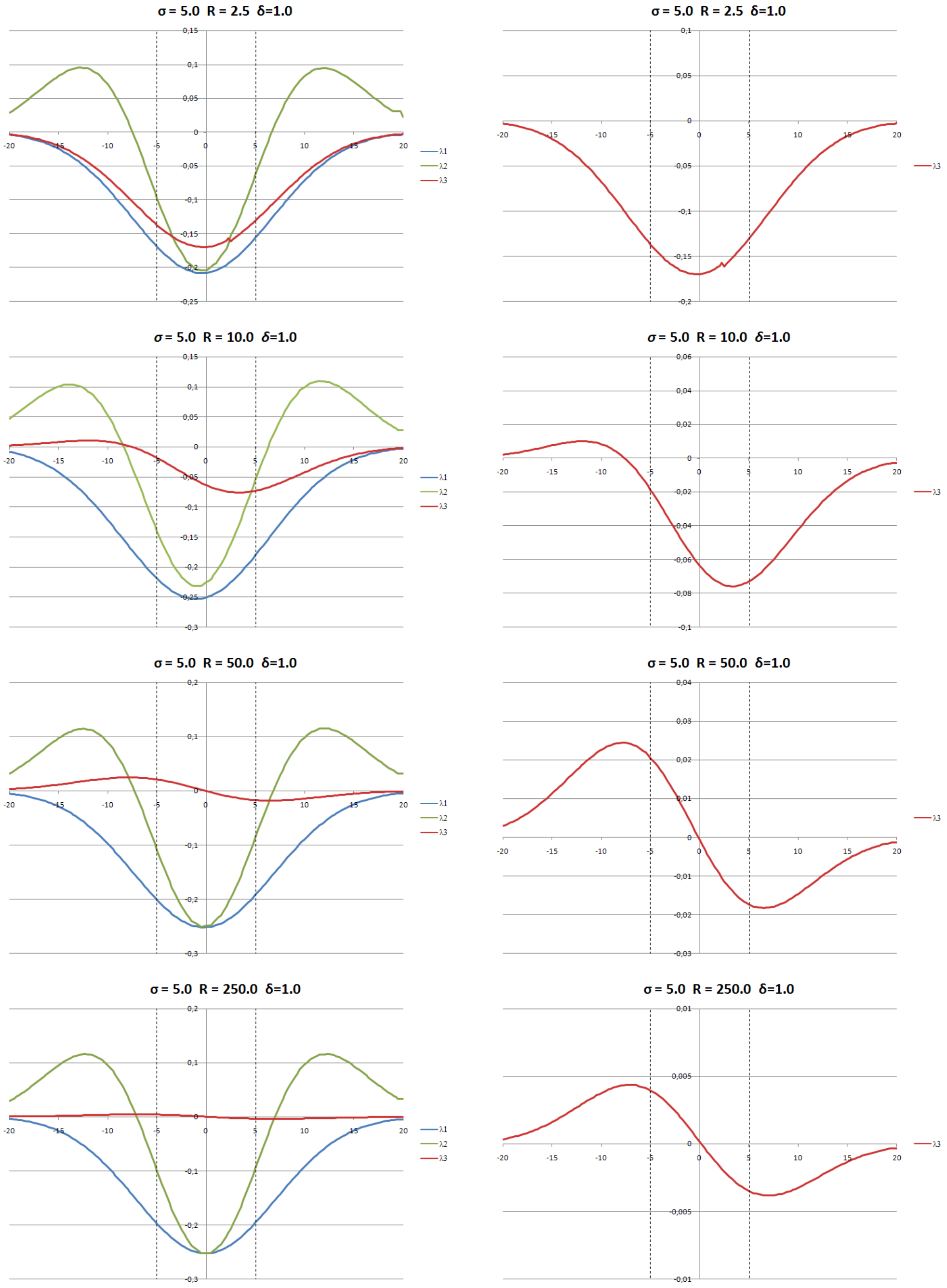

Figure 4.11: Experimental discrete toroid eigenvalues for $\sigma_0 = 5.0$ and varying R. Left: three eigenvalues compared. Right: detail of third eigenvalue.

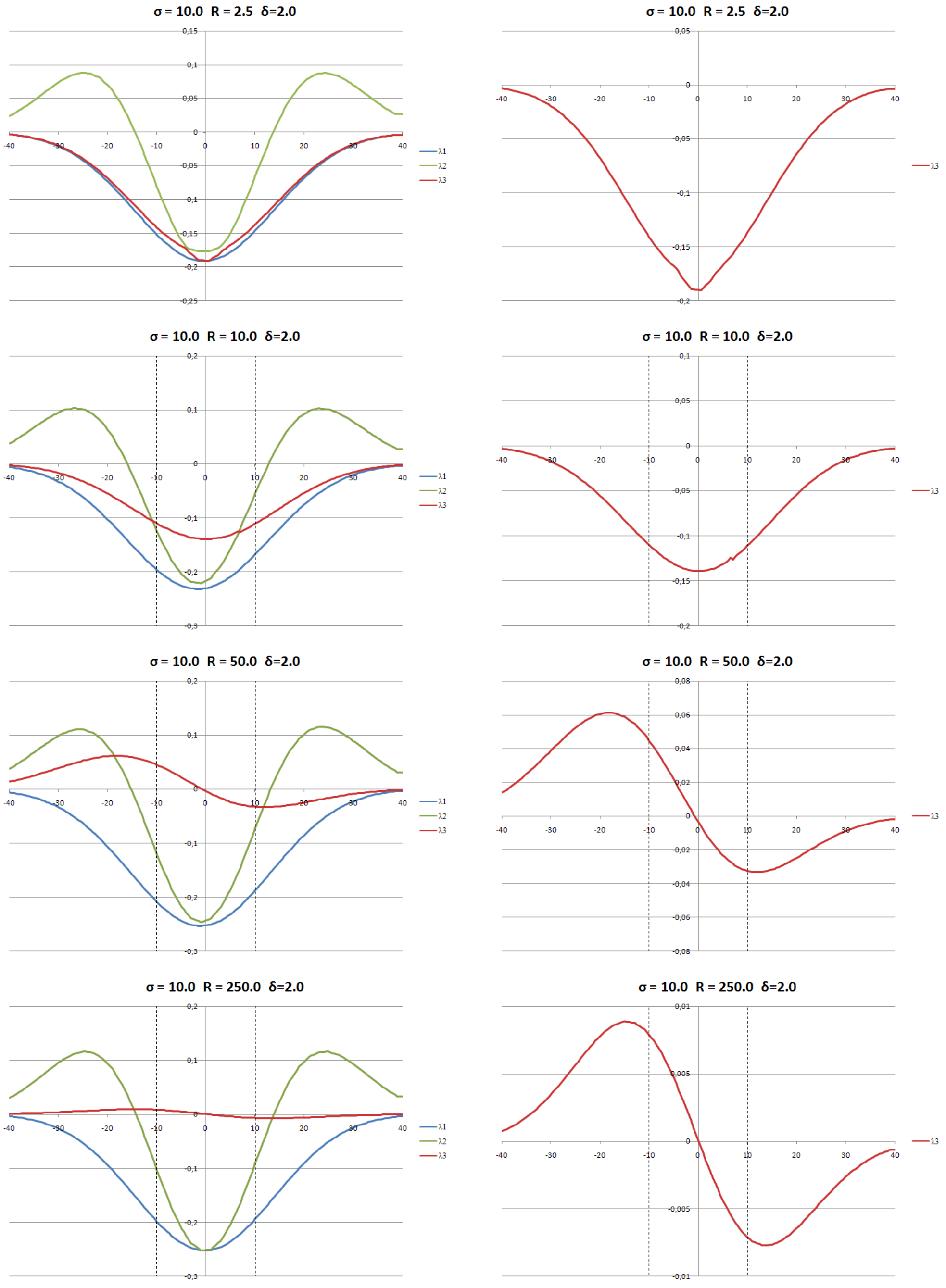

Figure 4.12: Experimental discrete toroid eigenvalues for $\sigma_0 = 10.0$ and varying R. Left: three eigenvalues compared. Right: detail of third eigenvalue.

The parametric equation of the centerline of an helix with constant radius and pitch is given by[14]:

$$\begin{aligned} x(\theta) &= R\cos\theta \\ y(\theta) &= R\sin\theta \\ z(\theta) &= H\,\theta \end{aligned} \tag{4.102}$$

where the parameter $\theta$is the angle depicted in Figure . Note that this is not the unit arc length parametrization. Such an helix with a constant radius R and constant unit pitch H is called a *circular helix* [64].

4.4.2 Frenet-Serret Frame

At every point of the helix, we can easily calculate the local coordinate system defined by the *Frenet-Serret frame*, consisting of three orthonormal vectors:

- T is the unit tangent vector to the curve at every point, in the ascending direction.
- N is the unit normal vector. It is normal to the tangent vector and in the direction of its derivative with respect to the arc-length parameter.B is the cross-product of T and N.

The unit tangent vector T has the direction of the derivative with respect to the arc length:

$$\alpha'(\theta) = \frac{\partial\alpha}{\partial\theta} = -R\sin\theta i + R\cos\theta j + Hk \tag{4.103}$$

and thus, the expresion of the unit tangent vector is:

$$T = \frac{\alpha'(\theta)}{|\alpha'(\theta)|} = \frac{1}{\sqrt{R^2+H^2}}(-R\sin\theta i + R\cos\theta j + Hk) \tag{4.104}$$

The unit arc-length parametrization of the helix can be obtained by dividing the vectorial expression in 4.102 by the modulus of the tangent vector $\sqrt{R^2+H^2}$.

The Frenet-Serret formulas for 1D curves in $\mathbb{R}^3$ express some relationships between the tangent, normal and binormal vectors and their derivatives with respect to the arc-length:

$$\begin{array}{rcccc} \frac{\partial T}{\partial s} & = & & \kappa N & \\ \frac{\partial N}{\partial s} & = & -\kappa T & & +\tau B \\ \frac{\partial B}{\partial s} & = & & -\tau N & \end{array} \tag{4.105}$$

where $\kappa$is the *curvature* and $\tau$is the *torsion* of the curve.

As can be seen in these formulas, the curvature expresses the magnitude of variation of the tangent vector with respect to the arc-length and the torsion the magnitude

---

[14] The standard notation for a parametric curve typically uses t for the curve parameter. However, we will use here θas the name of the parameter, since we want to emphasize that the parameter is an angle. Moreover, it can be confused with the t parameter in the scale-space representations.

of variation of the binormal vector with respect to the arc-length. We can use these formulas to calculate the normal and binormal vectors, as well as the curvature and torsion and proof the following proposition at the same time:

Proposition 7. Let $\widetilde{\gamma}: I \longrightarrow \mathbb{R}^3$ be a circular helix. Then, the curvature and torsion of the helix is constant.

Proof. First, we will try to find the value of the normal vector and the curvature. The value of these derivatives is independent of the chosen parametrization and thus, we can calculate the derivatives with respect to the angle parameter θ. For the tangent vector we have:

$$\frac{\partial T}{\partial \theta} = \frac{R}{\sqrt{R^2+H^2}}\left(-\cos\theta i - \sin\theta j\right) \tag{4.106}$$

$$N = \frac{\frac{\partial T}{\partial \theta}}{\left|\frac{\partial T}{\partial \theta}\right|} = -\cos\theta i - \sin\theta j \tag{4.107}$$

and thus the curvature is

$$\kappa = \left|\frac{\partial T}{\partial \theta}\right| = \frac{R}{\sqrt{R^2+H^2}} \tag{4.108}$$

which is a constant when both R and H are constants. Now we can obtain the binormal vector as:

$$B = T \times N = \frac{1}{\sqrt{R^2+H^2}} \begin{vmatrix} i & j & k \\ -R\sin\theta & R\cos\theta & H \\ -\cos\theta & -\sin\theta & 0 \end{vmatrix} \tag{4.109}$$

$$B = \frac{1}{\sqrt{R^2+H^2}}\left(H\sin\theta i - H\cos\theta j + Rk\right) \tag{4.110}$$

and its derivative with respect to the arc-length:

$$\frac{\partial B}{\partial \theta} = \frac{H}{\sqrt{R^2+H^2}}\left(\cos\theta i + \sin\theta j\right) \tag{4.111}$$

and thus the the torsion is

$$\tau = \left|\frac{\partial B}{\partial \theta}\right| = \frac{H}{\sqrt{R^2+H^2}} \tag{4.112}$$

which is a constant when both R and H are constants. □

Then, the binormal vector can also be expressed as:

$$B = \tau\sin\theta i - \tau\cos\theta j + \kappa k \tag{4.113}$$

4.4.3 Curvilinear Coordinates

The parametric equation described in equation 4.102 represents a 1D helix whose points are at a distance R from the helix axis. However, we are interested in a volumetric helix, that is, an helix that has a section with a given intensity distribution an radius. As in the previous models, we will use a 2D Gaussian function as the intensity distribution for our volumetric helix section, which is more representative for small vessels.

In order to obtain the equation of the volumetric helix with Gaussian cross-section we will use a curvilinear coordinate system with three coordinates (see Figure):

r = distance to the closest point on the helix centerline as defined by the equation .

φ= angle formed by the line of shortest distance to the centerline with the cross-section horizontal axis. This line is where r is measured.

θ= angle formed by the closest point of the centerline with the origin of the centerline as measured in a plane normal to the axis.

Note that the helix cross-section does not contain the helix axis as it happened with the torus model. In we can see that the cross-section is defined by the tangent plane to the helix at every point, and the normal and binormal planes are the base vectors in this section plane.

The position of a point $\vec{x} \in \mathbb{R}^3$ in a volumeteric helix can be defined in terms of the center $\vec{x_C} \in \mathbb{R}^3$ of the section where the point is defined and the normal and binormal vectors. The basis vectors of the section are:

$$\begin{aligned} e_1 &= -N \\ e_2 &= B \end{aligned}$$

and thus we have the vectorial equation:

$$x = x_C - r\cos\varphi N + r\sin\varphi B \tag{4.114}$$

where r is the distance to the closest point on the helix centerline. Thus, by combining eq. 4.102and 4.114and replacing the expressions of the normal and binormal vectors, we obtain a relationship between the curvilinear coordinates we have chosen for the helix and cartesian coordinates:

$$\begin{aligned} x(r,\varphi,\theta) &= R\cos\theta + r\cos\varphi\cos\theta + \tau r\sin\varphi\sin\theta \quad (1) \\ y(r,\varphi,\theta) &= R\sin\theta + r\cos\varphi\sin\theta - \tau r\sin\varphi\cos\theta \quad (2) \\ z(r,\varphi,\theta) &= H\theta + \kappa r\sin\varphi \quad (3) \end{aligned} \tag{4.115}$$

The equation 4.115 represents a direct transformation from curvilinear to cartesian coordinates. Ideally, from these equations we could obtain an inverse transformation in the form of equation 4.52. However, obtaining such a transformation is not always possible or practical.

In the case of the helix, instead of an explicit expression for the inverse transformation, we obtain a set of implicit equations that involve both, the curvilinear and cartesian coordinates and that will be useful for our derivative calculations. By combining eq. (1) and (2) from the vectorial eq. 4.115 we have:

$$r\cos\varphi = \frac{x - R\cos\theta - r\tau\sin\varphi\sin\theta}{\cos\theta} = \frac{x - R\sin\theta - r\tau\sin\varphi\cos\theta}{\sin\theta}$$

$$x\sin\theta - y\cos\theta = \tau r\sin\varphi$$

and replacing the value of $r\sin\varphi$in eq. 4.115 (3) we obtain the implicit relationship:

$$z - H\theta = \frac{\kappa}{\tau}\left(x\sin\theta - y\cos\theta\right) \tag{4.116}$$

or equivalently

$$z - H\theta = \frac{R}{H}\left(x\sin\theta - y\cos\theta\right) \tag{4.117}$$

which corresponds to an explicit expression of the type $f(\theta, x, y, z) = 0$ which is also useful.

Combining equations 4.115(1) and (3):

$$r\cos\varphi\cos\theta = x - R\cos\theta - \frac{\tau}{\kappa}\sin\theta\left(z - H\theta\right)$$

$$r\cos\varphi = \frac{1}{\cos\theta}\left[x - R\cos\theta - \sin\theta\left(x\sin\theta - y\cos\theta\right)\right] \tag{4.118}$$

Similarly:

$$r\cos\varphi\sin\theta = y - R\sin\theta + \frac{\tau}{\kappa}\cos\theta\left(z - H\theta\right)$$

$$r\cos\varphi = \frac{1}{\sin\theta}\left[y - R\sin\theta + \cos\theta\left(x\sin\theta - y\cos\theta\right)\right] \tag{4.119}$$

Finally we obtain two expressions for φ:

$$\tan\varphi = \frac{r\sin\varphi}{r\cos\varphi} = \frac{1}{\tau}\frac{\cos\theta\left(x\sin\theta - y\cos\theta\right)}{x - R\cos\theta - \sin\theta\left(x\sin\theta - y\cos\theta\right)} \tag{4.120}$$

$$\tan\varphi = \frac{r\sin\varphi}{r\cos\varphi} = \frac{1}{\tau}\frac{\sin\theta\left(x\sin\theta - y\cos\theta\right)}{y - R\sin\theta + \cos\theta\left(x\sin\theta - y\cos\theta\right)} \tag{4.121}$$

which is an expression in the form $\varphi = \varphi(\theta) = \varphi\left[\theta(x, y, z)\right]$

An expression for r can be obtained if we take into account that r is the distance from the current point to the closest centerline point, whose coordinates are given by the helix centerline equation 4.102. Thus, this distance is:

$$r^2 = (x - R\cos\theta)^2 + (y - R\sin\theta)^2 + (z - H\theta)^2 \tag{4.122}$$

which is an expression in the form $r = r(x, y, z, \theta) = r\left[x, y, z, \theta(x, y, z)\right]$

By differentiating the expressions above, we can obtain some derivatives of the curvilinear coordinates with respect to the cartesian coordinates that are useful for future calculations. From the expression 4.116 by differentiation with respect to θ and x we obtain:

$$-Hd\theta = \frac{\kappa}{\tau}(\sin\theta dx + x\cos\theta d\theta + y\sin\theta d\theta)$$

$$\frac{d\theta}{dx} = \frac{-\sin\theta}{\frac{\tau}{\kappa}H + x\cos\theta + y\sin\theta} \tag{4.123}$$

Similarly we obtain:

$$\frac{d\theta}{dy} = \frac{\cos\theta}{\frac{\tau}{\kappa}H + x\cos\theta + y\sin\theta} \tag{4.124}$$

$$\frac{d\theta}{dy} = \frac{\tau/\kappa}{\frac{\tau}{\kappa}H + x\cos\theta + y\sin\theta} \tag{4.125}$$

For the r curvilinear coordinate we can differentiate equation 4.122 with respect to r and x. However, in this expression, the curvilinear coordinate θalso appears. By the chain rule we know that:

$$dr = \frac{\partial r}{\partial x}dx + \frac{\partial r}{\partial \theta}\frac{\partial \theta}{\partial x}dx \tag{4.126}$$

but $\partial r/\partial\theta = 0$ since they are independent variables. This can be easily seen by differentiating equation 4.122 with respect to r and θ:

$$2rdr = 2(x - R\cos\theta)R\sin\theta d\theta - 2(y - R\sin\theta)R\cos\theta - 2H(z - H\theta)$$

Combining with equation 4.117:

$$\frac{dr}{d\theta} = (x - R\cos\theta)R\sin\theta - 2(y - R\sin\theta)R\cos\theta - 2R(x\sin\theta - y\cos\theta) = 0$$

Then, from equation 4.122 we have:

$$2rdr = 2(x - R\cos\theta)dx$$

$$\frac{dr}{dx} = \frac{1}{r}(x - R\cos\theta) \tag{4.127}$$

Similarly we obtain:

$$\frac{dr}{dy} = \frac{1}{r}(y - R\sin\theta) \tag{4.128}$$

$$\frac{dr}{dz} = \frac{1}{r}(z - H\theta) \tag{4.129}$$

4.4.4 Gaussian Helix and Derivatives

After obtaining this relationship between coordinate systems, we can proceed to obtain the expression of the volumetric helix with Gaussian cross-section and its derivatives. The expression of the volumetric is very if we express it in our curvilinear coordinate system for the helix:

$$I_{helix}(r,\varphi,\theta) = K \exp\left(-\frac{r^2}{2\sigma_0^2}\right) \tag{4.130}$$

Note that, again, this is exactly the expression we had for the cylinder in cylindrical coordinates 4.28. The curvilinear coordinate system chosen here is also different and does not correspond to the cylindrical coordinates. Our objective in this case is to calculate how both, the curvature and torsion, affects the value of the second order derivatives as compared with the ideal cylinder model.

We may use the chain rule for obtaining the *total* (not partial) first-order derivative with respect to x:

$$\frac{dI}{dx} = \frac{\partial I}{\partial r}\frac{\partial r}{\partial x} = -\frac{r}{\sigma_0^2} I \frac{1}{r}(x - R\cos\theta)$$

$$\frac{dI}{dx} = -\frac{I}{\sigma_0^2}(x - R\cos\theta) \tag{4.131}$$

where the value of $\partial r/\partial x$ is taken from equation 4.127. In a similar fashion we obtain:

$$\frac{dI}{dy} = -\frac{I}{\sigma_0^2}(y - R\sin\theta) \tag{4.132}$$

$$\frac{dI}{dz} = -\frac{I}{\sigma_0^2}(z - H\theta) = -\frac{I}{\sigma_0^2}\frac{\kappa}{\tau}(x\sin\theta - y\cos\theta) \tag{4.133}$$

Obtaining the second-order partial derivatives is more complicated, since now we have to take into account the derivative with respect to θ. We start with the second derivative with respect to x. By the chain rule:

$$\frac{d^2I}{dx^2} = \frac{\partial^2 I}{\partial x^2} + \frac{\partial}{\partial r}\left(\frac{dI}{dx}\right)\frac{\partial r}{\partial x} + \frac{\partial}{\partial \theta}\left(\frac{dI}{dx}\right)\frac{\partial \theta}{\partial x} \tag{4.134}$$

$$\frac{d^2I}{dx^2} = -\frac{I}{\sigma_0^2} + \frac{r}{\sigma_0^2}\frac{I}{\sigma_0^2}(x - R\cos\theta)\frac{\partial r}{\partial x} + \left(-\frac{I}{\sigma_0^2}\right)R\sin\theta\frac{\partial \theta}{\partial x} \tag{4.135}$$

By replacing the values of the derivatives calculated in section 4.4.3 we obtain:

$$\frac{d^2I}{dx^2} = \frac{I}{\sigma_0^2}\left(-1 + \frac{1}{\sigma_0^2}(x - R\cos\theta)^2 + \frac{R\sin^2\theta}{\frac{\tau}{\kappa}H + x\cos\theta + y\sin\theta}\right) \tag{4.136}$$

We can obtain the values of the remaining derivatives in a similar way obtaining:

$$\frac{d^2I}{dy^2} = \frac{I}{\sigma_0^2}\left(-1 + \frac{1}{\sigma_0^2}(y - R\sin\theta)^2 + \frac{R\cos^2\theta}{\frac{\tau}{\kappa}H + x\cos\theta + y\sin\theta}\right) \tag{4.137}$$

$$\frac{d^2I}{dz^2} = \frac{I}{\sigma_0^2}\left(-1 + \frac{1}{\sigma_0^2}(z - H\theta)^2 + \frac{\frac{\tau}{\kappa}H}{\frac{\tau}{\kappa}H + x\cos\theta + y\sin\theta}\right) \tag{4.138}$$

$$\frac{d^2I}{dxdy} = \frac{I}{\sigma_0^2}\left(\frac{1}{\sigma_0^2}(x - R\cos\theta)(y - R\sin\theta) - \frac{R\sin\theta\cos\theta}{\frac{\tau}{\kappa}H + x\cos\theta + y\sin\theta}\right) \tag{4.139}$$

$$\frac{d^2I}{dxdz} = \frac{I}{\sigma_0^2}\left(\frac{1}{\sigma_0^2}(x - R\cos\theta)(z - H\theta) - \frac{\frac{\tau}{\kappa}R\sin\theta}{\frac{\tau}{\kappa}H + x\cos\theta + y\sin\theta}\right) \tag{4.140}$$

$$\frac{d^2I}{dydz} = \frac{I}{\sigma^2}\left(\frac{1}{\sigma^2}(y - R\sin\theta)(z - H\theta) + \frac{\frac{\tau}{\kappa}R\cos\theta}{\frac{\tau}{\kappa}H + x\cos\theta + y\sin\theta}\right) \tag{4.141}$$

Due to the symmetry of the problem and, without loss of generality, we can choose the values of the angles to be $\theta = 0$ (origin of the helix) and $\varphi = 0$ (zero polar angle for the section). This yields the following simplified Hessian matrix:

$$H = \frac{I}{\sigma_0^2}H' \tag{4.142}$$

$$H' = \begin{bmatrix} -1 + \frac{1}{\sigma_0^2}(x-R)^2 & \frac{1}{\sigma_0^2}(x-R)y & \frac{1}{\sigma_0^2}(x-R)z \\ \frac{1}{\sigma_0^2}(x-R)y & -1 + \frac{y^2}{\sigma_0^2} + \frac{R}{\frac{\tau}{\kappa}H+x} & \frac{1}{\sigma_0^2}yz + \frac{\frac{\tau}{\kappa}R}{\frac{\tau}{\kappa}H+x} \\ \frac{1}{\sigma_0^2}(x-R)z & \frac{1}{\sigma_0^2}yz + \frac{\frac{\tau}{\kappa}R}{\frac{\tau}{\kappa}H+x} & -1 + \frac{z^2}{\sigma_0^2} + \frac{\frac{\tau}{\kappa}H}{\frac{\tau}{\kappa}H+x} \end{bmatrix} \tag{4.143}$$

The values of x, y, z in equations 4.115 for $\varphi = 0$ and $\theta = 0$:

$$\begin{array}{ll} x(r, \theta = 0, \varphi = 0) = R + r & (1) \\ y(r, \theta = 0, \varphi = 0) = 0 & (2) \\ z(r, \theta = 0, \varphi = 0) = 0 & (3) \end{array} \tag{4.144}$$

and replacing them in the expression of H' we obtain a matrix that depends only on the curvilinear coordinate r:

$$H'(\theta = 0, \varphi = 0) = \begin{bmatrix} \frac{r^2-\sigma_0^2}{\sigma_0^2} & 0 & 0 \\ 0 & -1 + \frac{R}{\frac{\tau}{\kappa}H+R+r} & \frac{\frac{\tau}{\kappa}R}{\frac{\tau}{\kappa}H+R+r} \\ 0 & \frac{\frac{\tau}{\kappa}R}{\frac{\tau}{\kappa}H+R+r} & -1 + \frac{\frac{\tau}{\kappa}H}{\frac{\tau}{\kappa}H+R+r} \end{bmatrix} = \begin{bmatrix} \frac{r^2-\sigma_0^2}{\sigma_0^2} & 0 & 0 \\ 0 & -\frac{\frac{\tau}{\kappa}H+r}{\frac{\tau}{\kappa}H+R+r} & \frac{\frac{\tau}{\kappa}R}{\frac{\tau}{\kappa}H+R+r} \\ 0 & \frac{\frac{\tau}{\kappa}R}{\frac{\tau}{\kappa}H+R+r} & -\frac{R+r}{\frac{\tau}{\kappa}H+R+r} \end{bmatrix}$$

Moreover, we have that $\tau/\kappa = H/R$ so we obtain:

$$H'(\theta=0,\varphi=0)=\begin{bmatrix} \frac{r^2-\sigma_0^2}{\sigma_0^2} & 0 & 0 \\ 0 & -\frac{\frac{\tau^2}{\kappa^2}+\frac{r}{R}}{\frac{\tau^2}{\kappa^2}+\frac{r}{R}+1} & \frac{\frac{\tau}{\kappa}}{\frac{\tau^2}{\kappa^2}+\frac{r}{R}+1} \\ 0 & \frac{\frac{\tau}{\kappa}}{\frac{\tau^2}{\kappa^2}+\frac{r}{R}+1} & -\frac{\frac{r}{R}+1}{\frac{\tau^2}{\kappa^2}+\frac{r}{R}+1} \end{bmatrix} \tag{4.145}$$

However, the previous expression is only valid for values of r from the centerline to the external boundary of the toroid ($\varphi = 0^{\circ}$). If we choose values of r towards the internal part of the toroid, then $\varphi = 180^{\circ}$ and the expression becomes

$$H'(\theta=0,\varphi=180)=\begin{bmatrix} \frac{r^2-\sigma_0^2}{\sigma_0^2} & 0 & 0 \\ 0 & -\frac{\frac{\tau^2}{\kappa^2}-\frac{r}{R}}{\frac{\tau^2}{\kappa^2}-\frac{r}{R}+1} & \frac{\frac{\tau}{\kappa}}{\frac{\tau^2}{\kappa^2}-\frac{r}{R}+1} \\ 0 & \frac{\frac{\tau}{\kappa}}{\frac{\tau^2}{\kappa^2}-\frac{r}{R}+1} & -\frac{-\frac{r}{R}+1}{\frac{\tau^2}{\kappa^2}-\frac{r}{R}+1} \end{bmatrix} \tag{4.146}$$

This is the same as considering that the expression 4.145 can take both positive and negative values for r.

4.4.5 Eigenvalues and Eigenvectors

We proceed to calculate the eigenvalues and vectors of the Hessian matrix which correspond to the roots of the characteristic equation 4.3.4 which yields the characteristic polynomial:

$$\begin{gathered} \left(\frac{r^2-\sigma_0^2}{\sigma_0^2}-\lambda'\right)\left(-\frac{\frac{\tau^2}{\kappa^2}+\frac{r}{R}}{\frac{\tau^2}{\kappa^2}+\frac{r}{R}+1}-\lambda'\right)\left(-\frac{\frac{r}{R}+1}{\frac{\tau^2}{\kappa^2}+\frac{r}{R}+1}-\lambda'\right) \\ -\left(\frac{r^2-\sigma_0^2}{\sigma_0^2}-\lambda'\right)\frac{\frac{\tau^2}{\kappa^2}}{\left(\frac{\tau^2}{\kappa^2}+\frac{r}{R}+1\right)^2}=0 \end{gathered} \tag{4.147}$$

One root is trivial and corresponds to:

$$\lambda_1' = \frac{r^2-\sigma_0^2}{\sigma_0^2} \tag{4.148}$$

and then a second degree polynomial remains:

$$\left(-\frac{\frac{\tau^2}{\kappa^2}+\frac{r}{R}}{\frac{\tau^2}{\kappa^2}+\frac{r}{R}+1}-\lambda'\right)\left(-\frac{\frac{r}{R}+1}{\frac{\tau^2}{\kappa^2}+\frac{r}{R}+1}-\lambda'\right)-\frac{\frac{\tau^2}{\kappa^2}}{\left(\frac{\tau^2}{\kappa^2}+\frac{r}{R}+1\right)^2}=0 \tag{4.149}$$

Multiplying and reordering terms we obtain:

$$\lambda'^2+\frac{\frac{\tau^2}{\kappa^2}+2\frac{r}{R}+1}{\frac{\tau^2}{\kappa^2}+\frac{r}{R}+1}\lambda'+\frac{\left(\frac{\tau^2}{\kappa^2}+\frac{r}{R}+1\right)\frac{r}{R}}{\left(\frac{\tau^2}{\kappa^2}+\frac{r}{R}+1\right)^2}=0$$

$$\lambda'^2 + \frac{\frac{\tau^2}{\kappa^2}+2\frac{r}{R}+1}{\frac{\tau^2}{\kappa^2}+\frac{r}{R}+1}\lambda' + \frac{\frac{r}{R}}{\frac{\tau^2}{\kappa^2}+\frac{r}{R}+1} = 0 \tag{4.150}$$

The discriminant of this equation is:

$$\triangle = \frac{\frac{\tau^4}{\kappa^4}+4\frac{r^2}{R^2}+1+4\frac{\tau^2}{\kappa^2}\frac{r}{R}+4\frac{r}{R}+2\frac{\tau^2}{\kappa^2}}{\left(\frac{\tau^2}{\kappa^2}+\frac{r}{R}+1\right)^2} - \frac{4\frac{r}{R}}{\frac{\tau^2}{\kappa^2}+\frac{r}{R}+1}$$

$$\triangle = \frac{\left(\frac{\tau^2}{\kappa^2}+1\right)^2}{\left(\frac{\tau^2}{\kappa^2}+\frac{r}{R}+1\right)^2} \tag{4.151}$$

so it results in a clean expression for the remaining eigenvalues:

$$\lambda' = -\frac{1}{2}\frac{\frac{\tau^2}{\kappa^2}+2\frac{r}{R}+1}{\frac{\tau^2}{\kappa^2}+\frac{r}{R}+1} \pm \frac{1}{2}\frac{\frac{\tau^2}{\kappa^2}+1}{\frac{\tau^2}{\kappa^2}+\frac{r}{R}+1}$$

$$\lambda_2^{'} = -1 \tag{4.152}$$

$$\lambda_3^{'} = -\frac{\frac{r}{R}}{\frac{\tau^2}{\kappa^2}+\frac{r}{R}+1} \tag{4.153}$$

These are the eigenvalues for H'. The eigenvalues for H, according to equation 4.142 are:

$$\lambda = \frac{I}{\sigma_0^2}\lambda' \tag{4.154}$$

So finally we have:

$$\lambda_1 = \frac{r^2-\sigma_0^2}{\sigma_0^4}I \qquad \lambda_2 = -\frac{1}{\sigma_0^2}I \qquad \lambda_3 = -\frac{1}{\sigma_0^2}\frac{\frac{r}{R}}{\frac{\tau^2}{\kappa^2}+\frac{r}{R}+1}I \tag{4.155}$$

Now we can proceed to obtain the corresponding eigenvectors, which are the solutions of the equation 4.14. For the first eigenvalue we have the equations:

$$\left(\frac{r^2-\sigma_0^2}{\sigma_0^2} - \frac{r^2-\sigma_0^2}{\sigma_0^2}\right)v_x = 0$$

$$\left(-\frac{\frac{\tau^2}{\kappa^2}+\frac{r}{R}}{\frac{\tau^2}{\kappa^2}+\frac{r}{R}+1} - \frac{r^2-\sigma_0^2}{\sigma_0^2}\right)v_y + \frac{\frac{\tau}{\kappa}}{\frac{\tau^2}{\kappa^2}+\frac{r}{R}+1}v_z = 0$$

$$\frac{\frac{\tau}{\kappa}}{\frac{\tau^2}{\kappa^2}+\frac{r}{R}+1}v_y + \left(-\frac{\frac{r}{R}+1}{\frac{\tau^2}{\kappa^2}+\frac{r}{R}+1} - \frac{r^2-\sigma_0^2}{\sigma_0^2}\right)v_z = 0$$

The first equation is zero for all v_x. From the second equation we obtain $v_y = 0$ and $v_z = 0$. We can choose $x = 1$ in order to obtain a unit vector. Thus, the first eigenvector is:

$$x_1 = \begin{bmatrix} 1 \\ 0 \\ 0 \end{bmatrix} \tag{4.156}$$

which is a unit vector in the direction of the r curvilinear coordinate.

For the second eigenvalue we have:

$$\left(\frac{r^2-\sigma_0^2}{\sigma_0^2}+1\right)v_x = 0$$

$$\left(-\frac{\frac{\tau^2}{\kappa^2}+\frac{r}{R}}{\frac{\tau^2}{\kappa^2}+\frac{r}{R}+1}+1\right)v_y + \frac{\frac{\tau}{\kappa}}{\frac{\tau^2}{\kappa^2}+\frac{r}{R}+1}v_z = 0$$

$$\frac{\frac{\tau}{\kappa}}{\frac{\tau^2}{\kappa^2}+\frac{r}{R}+1}v_y + \left(-\frac{\frac{r}{R}+1}{\frac{\tau^2}{\kappa^2}+\frac{r}{R}+1}+1\right)v_z = 0$$

From the first equation we obtain again $v_x = 0$. The first and second equations are identical and can be reduced to the relationship:

$$v_y = -\frac{\tau}{\kappa}v_z$$

we can choose arbitrarily $v_z = \kappa$ and thus $v_y = -\tau$ which gives:

$$x_2 = \begin{bmatrix} 0 \\ -\tau \\ \kappa \end{bmatrix} \tag{4.157}$$

This is already a unit vector since:

$$|x_2| = \sqrt{\tau^2+\kappa^2} = \sqrt{\frac{H^2}{R^2+H^2}+\frac{R^2}{R^2+H^2}} = 1$$

And finally, for the third eigenvalue:

$$\left(\frac{r^2-\sigma_0^2}{\sigma_0^2}+\frac{\frac{r}{R}}{\frac{\tau^2}{\kappa^2}+\frac{r}{R}+1}\right)v_x = 0$$

$$\left(-\frac{\frac{\tau^2}{\kappa^2}+\frac{r}{R}}{\frac{\tau^2}{\kappa^2}+\frac{r}{R}+1}+\frac{\frac{r}{R}}{\frac{\tau^2}{\kappa^2}+\frac{r}{R}+1}\right)v_y + \frac{\frac{\tau}{\kappa}}{\frac{\tau^2}{\kappa^2}+\frac{r}{R}+1}v_z = 0$$

$$\frac{\frac{\tau}{\kappa}}{\frac{\tau^2}{\kappa^2}+\frac{r}{R}+1}v_y + \left(-\frac{\frac{r}{R}+1}{\frac{\tau^2}{\kappa^2}+\frac{r}{R}+1}+\frac{\frac{r}{R}}{\frac{\tau^2}{\kappa^2}+\frac{r}{R}+1}\right)v_z = 0$$

$\lambda_1 = \frac{r^2-\sigma_0^2}{\sigma_0^4} I$	$\lambda_2 = -\frac{1}{\sigma_0^2} I$	$\lambda_3 = -\frac{1}{\sigma_0^2} \frac{\frac{r}{R}}{\frac{\tau^2}{\kappa^2}+\frac{r}{R}+1} I$
$x_1 = \begin{bmatrix} 1 & 0 & 0 \end{bmatrix}$	$x_2 = \begin{bmatrix} 0 & -\tau & \kappa \end{bmatrix}$	$x_3 = \begin{bmatrix} 0 & \kappa & \tau \end{bmatrix}$

Table 4.8: Eigenvalues and vectors for the ideal Gaussian helix with $\theta = 0$, $\varphi = 0$.

$\lambda_1 = \frac{r^2-\sigma_0^2}{\sigma_0^4} I$	$\lambda_2 = -\frac{1}{\sigma_0^2} I$	$\lambda_3 = \frac{1}{\sigma_0^2} \frac{\frac{r}{R}}{\frac{\tau^2}{\kappa^2}-\frac{r}{R}+1} I$
$x_1 = \begin{bmatrix} 1 & 0 & 0 \end{bmatrix}$	$x_2 = \begin{bmatrix} 0 & -\tau & \kappa \end{bmatrix}$	$x_3 = \begin{bmatrix} 0 & \kappa & \tau \end{bmatrix}$

Table 4.9: Eigenvalues and vectors for the ideal Gaussian helix with $\theta = 0$, $\varphi = 180$. Note that in these expressions $r > 0$.

From the first equation we obtain $v_x = 0$. The first and second equations are identical and can be reduced to the relationship:

$$v_y = \frac{\kappa}{\tau} v_z$$

we can choose arbitrarily $v_z = \tau$ and thus $v_y = \kappa$ which gives:

$$x_3 = \begin{bmatrix} 0 \\ \kappa \\ \tau \end{bmatrix} \tag{4.158}$$

which is also a unit vector.

To sum up, we have obtained the following eigenvalues and corresponding eigenvectors for the regular helix with Gaussian cross-section at the starting point of the helix ($\theta = 0, \varphi = 0$):

where I is defined in eq. 4.130.

Using a similar procedure, we can obtain the eigenvalues and vectors for ($\theta = 0, \varphi = 180$), that is, for points in the internal part of the helix with respect to the centerline. The resulting eigenvalues and vectors are:

We can get a single combined expression by considering that r can take both positive and negative values in the expressions of Table 4.8.

As we can see, the first and second eigenvalues coincide with the ideal Gaussian cylinder (see Table 4.1) and with the ideal Gaussian toroid (see Table 4.5). This is due to the rotational symmetry of the helix and the choice of coordinate system. The helix with circular cross-section can be considered an special case of cylinder where the centerline has been twisted by adding constant curvature and torsion.

Now we can proceed to analyze how the third eigenvalue, corresponding to the z direction for $\theta = 0$, varies with the curvature and torsion of the ideal helix.

4.4.6 Effect of curvature and torsion

4.4.6.1 Theoretical Model

We can already draw some conclusions on the combined effect of curvature and torsion as compared with a straight ideal cylinder from the simplified expressions of the eigenvalue λ_3:

Lemma 8. *Let I_{helix} be a circular Gaussian helix with internal radius σ_0, external radius R and unit pitch H. Let $\overline{OC}$ be a line that connects the center O of the helix with any point C on the centerline of the helix with $d\left(\overline{OC}\right) \equiv \sqrt{R^2 + H^2\theta^2}$. Let $P_1$and P_2 be symmetrical points on that line with respect to C at a distance r with P_1 the closest to O. Then, $|\lambda_3(P_1)| \geq |\lambda_3(P_2)| \forall r$.*

Proof. From the simplified expression of λ_3

$$\lambda_3 = -\frac{1}{\sigma_0^2}\frac{\frac{r}{R}}{\frac{\tau^2}{\kappa^2} + \frac{r}{R} + 1}I$$

where r can take positive or negative values depending if we are in the external ($\varphi = 0$) or internal ($\varphi = 180$) part of the cylinder we can see that, for the same absolute value of r we obtain two points P_1, P_2 in the line with respective values

$$\lambda_3(P_1) = -\frac{1}{\sigma_0^2}\frac{-\frac{|r|}{R}}{\frac{\tau^2}{\kappa^2} - \frac{|r|}{R} + 1}I \tag{4.159}$$

$$\lambda_3(P_2) = -\frac{1}{\sigma_0^2}\frac{\frac{|r|}{R}}{\frac{\tau^2}{\kappa^2} + \frac{|r|}{R} + 1}I \tag{4.160}$$

Comparing the quotient in the middle we can distinguish three cases for r. If $\frac{\tau^2}{\kappa^2} + 1 > \frac{|r|}{R}$ then the denominator in eq. 4.159 is always positive and so is the total value. If $\frac{\tau^2}{\kappa^2} + 1 < \frac{|r|}{R}$the denominator in eq. 4.159 is always negative and so is the total value. If $\frac{\tau^2}{\kappa^2} + 1 = \frac{|r|}{R}$then the denominator is zero in the same equation and the total value infinite. In all three cases the denominator in eq. 4.159 is smaller in absolute value than in eq. 4.160 and thus $|\lambda_3(P_1)| \geq |\lambda_3(P_2)| \forall r$.

□

Lemma 9. *Let I_1 be a circular Gaussian helix with internal radius σ_{01}, unit pitch $H_1$and external radius $R_1 = \rho H_1$. Let I_2 be another circular Gaussian helix with same internal radius σ_{01}, same unit pitch H_1 and different external radius R_2 such that $R_2 = \frac{1}{\rho}H_1$. Then $\lambda_3(I_1(x)) = \lambda_3(I_2(x)) \forall x \in \mathbb{R}^3$.*

Proof. For the first helix

$$\lambda_3(I_1) = -\frac{1}{\sigma_0^2}\frac{\frac{r}{\rho H_1}}{\frac{H_1^2}{\rho^2 H_1^2} + \frac{r}{\rho H_1} + 1}\exp\left(-\frac{r^2}{2\sigma_0^2}\right) = -\frac{1}{\sigma_0^2}\frac{r\rho}{H_1 + r\rho + \rho^2 H_1}\exp\left(-\frac{r^2}{2\sigma_0^2}\right)$$

and for the second helix

$$\lambda_3(I_2) = -\frac{1}{\sigma_0^2}\frac{\frac{\rho r}{H_1}}{\frac{\rho^2 H_1^2}{H_1^2}+\frac{\rho r}{H_1}+1}\exp\left(-\frac{r^2}{2\sigma_0^2}\right) = -\frac{1}{\sigma_0^2}\frac{r\rho}{\rho^2 H_1 + r\rho + H_1}\exp\left(-\frac{r^2}{2\sigma_0^2}\right)$$

which are identical. □

Corollary 10. *If* $\rho = 1$ *then* $I_1 = I_2$ *and* $\lambda_3(I_1) = \lambda_3(I_2)$ is maximum $\forall r$.

Proof. The maximum for $\lambda_3(I_1) = \lambda_3(I_2)$ can be found by setting

$$\frac{d\lambda_3(I_1)}{d\rho} = \frac{d\lambda_3(I_2)}{d\rho} = 0$$

$$\frac{r\left(H_1 + r\rho + \rho^2 H_1\right) - r\rho\left(r + 2\rho H_1\right)}{\left(H_1 + r\rho + \rho^2 H_1\right)^2} = 0 \tag{4.161}$$

$$H_1 + r\rho + \rho^2 H_1 - \rho r - 2\rho^2 H_1 = 0$$

$$\rho^2 = 1$$

$$\rho = \pm 1 \tag{4.162}$$

Where the negative solution is an helix going downward. By derivating again we can check that this is indeed a maximum by calculating the second derivative.

$$\frac{d^2\lambda_3(I_1)}{d\rho^2} = \frac{d^2\lambda_3(I_2)}{d\rho^2} = \frac{-2r\rho H_1\left(H_1^2 + r^2\rho^2 + \rho^4 H_1^2 + 2r\rho H_1 + 2r\rho^3 H_1 + 2\rho^2 H_1^2\right)}{\left(H_1 + r\rho + \rho^2 H_1\right)^4}$$

$$-\frac{\left(rH_1 - r\rho^2 H_1\right)2\left(H_1 + r\rho + \rho^2 H_1\right)\left(r + 2\rho H_1\right)}{\left(H_1 + r\rho + \rho^2 H_1\right)^4}$$

The denominator is always positive. The second part of the numerator is zero for $\rho = 1$ due to the first term. Replacing $\rho = 1$ in the numerator for the rest of terms, multiplying and removing the common positive factors gives the following simplified numerator

$$-8H_1^2 - 8r^2H_1^2 - 2r^2 < 0 \quad \forall (r, H_1)$$

which denotes a relative maximum. □

Thus, in the presence of curvature, the internal part of the helix presents larger absolute values of λ_3 obtaining an assymetrical response. We can see that there is also asymmetry in the sign when $\frac{\tau^2}{\kappa^2} + 1 > \frac{|r|}{R}$, since in the internal part of the helix (P_1), the value of $\lambda_3$becomes positive whereas in the external part is always negative.

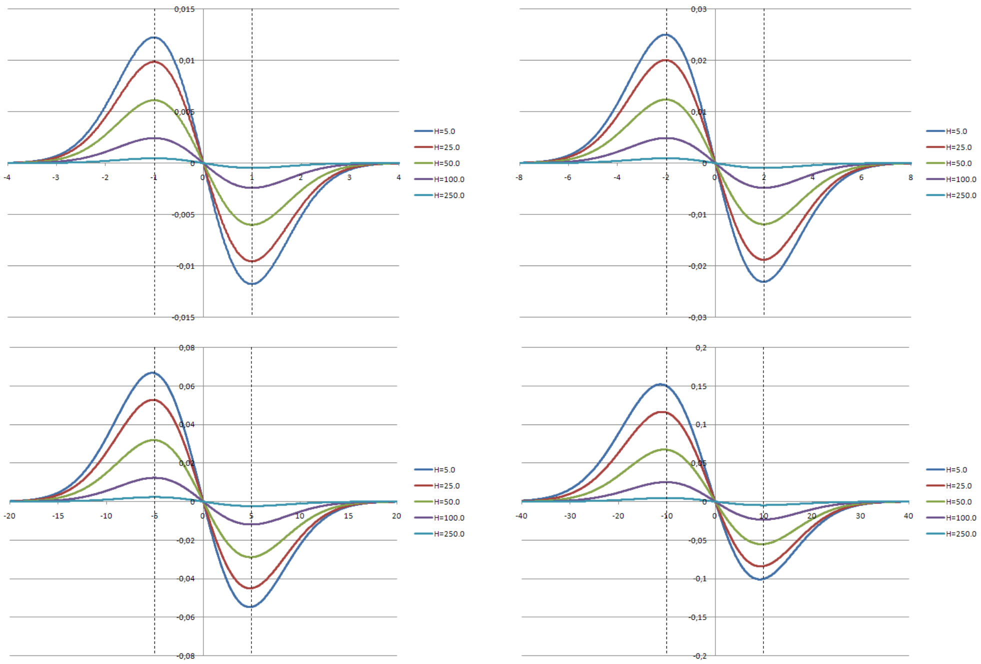

Figure 4.13: Values of λ_3 as a function of r with $\theta = 0$ and $\varphi = 0$ (or $\varphi = 180$ºfor $r < 0$) for different helix section radius σ_0 and pitch H and fixed centerline radius $R = 50.0$. Dashed vertical lines correspond to section (apparent) boundaries $(\sigma, -\sigma)$.

Figure 4.13 shows the ideal values of λ_3 as a function of r when $\theta = 0$ and $\varphi = 0$ (or $\varphi = 180$º for negative values of r), for different values of σ_0 and H and with fixed helix centerline radius $R = 50.0$. We can see that the eigenvalue is zero at the center, reaches maximum values at the vicinity of the helix section boundaries, positive on the left and negative on the right. The most important observation is that, when R is constant, the largest H leads to a zero eigenvalue at any position as in the ideal cylinder and when $H = 0$ we have the same expression λ_3 as in the toroid case.

Thus, *for the helix circular model with constant curvature, as the torsion increases,* λ_3*is more similar to an ideal cylinder*. The worst-case scenario is when $H = 0$ which is equivalent to the toroid model. This is because and increasing value of torsion under constant curvature straightens the cylinder and the third eigenvector gets more oriented towards the direction of the helix axis (see 4.8).

Figure 4.14 shows the ideal values of λ_3 as a function of r when $\theta = 0$ and $\varphi = 0$ (or $\varphi = 180$º for negative values of r), for different values of σ_0 and R and with fixed helix unit pitch $H = 50.0$. We can see that the worst situation is for $R = H = 50.0$ where the curve reaches maximum values as demonstrated in Corollary 10. We can also see that, as demonstrated in Lemma 9, the values for $R = 100.0$ and $R = 25.0$ are exactly the same (only the first curve can be seen) which corresponds to the case $\rho = 2$.

Thus, *for the helix circular model with constant torsion, as the curvature changes,*

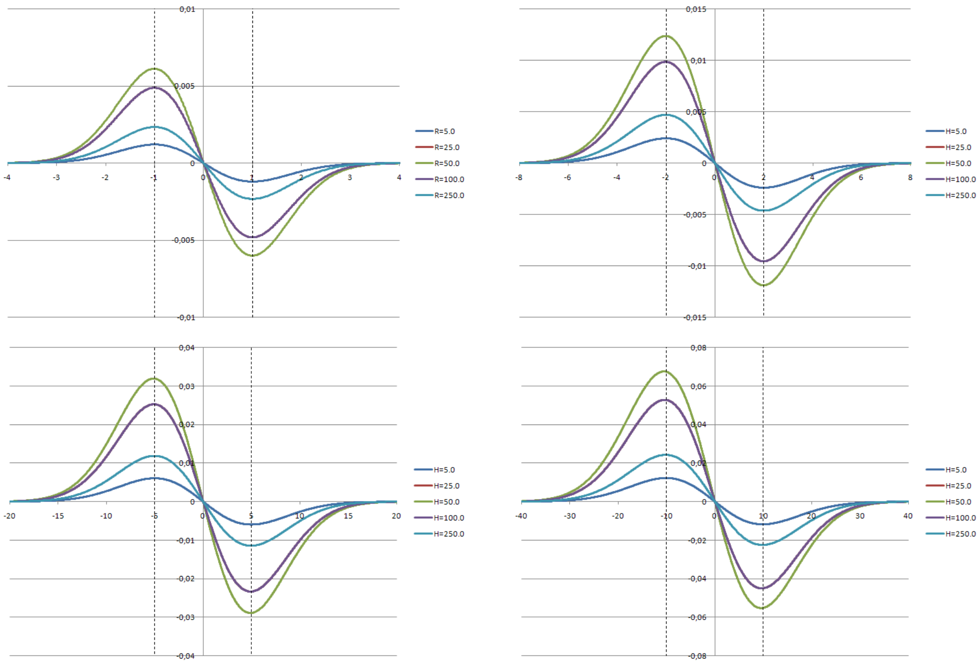

Figure 4.14: Values of λ_3 as a function of r with $\theta = 0$ and $\varphi = 0$ (or $\varphi = 180^{\circ}$for $r < 0$) for different helix centerline R and section σ_0 radius and fixed unit pitch $H = 50.0$. Dashed vertical lines correspond to section (apparent) boundaries $(\sigma, -\sigma)$.

λ_3 is more similar to an ideal cylinder when it deviates from $R = H$ which is the worst-case scenario for eigenvalue-based detection. In this case, the third eigenvector has a unit slope (see 4.8). The effect of increasing R is the same as in the toroid, decreasing the curvature and locally straightening the tube in the xy plane. On the other hand, the effect of decreasing R makes the vertical direction more dominant and straightens the tube in the axial direction.

In this case, it is not necessary to plot the remaining eigenvalues for comparison, since the other two eigenvalues are exactly the same as in the toroid model, and we have already seen what is the effect of varying H for a constant R. As we have seen, the third eigenvalue decreases its magnitude as H increases.

4.4.6.2 Experimental Model

In order to compare the theoritecal conclusions in discrete models we designed a set of synthetic volumetric helices with varying section radius σ_0, centerline radius R and unit pitch H. The procedure we used to create such a helix is very similar to the one used for the toroid model in 4.3.5.2. The only difference is the introduction of the pitch parameter in the centerline model and the estimation of the volumetric image size in the axial direction. We use the same sampling scheme used in the toroid model, that takes into account the section and centerline radius only, although in extreme cases, when the pitch differs much from the centerline radius, it would be better to consider also the pitch.

4.5 Section Profiles

So far we have dealt mostly with Gaussian cross-section intensity profiles, mostly due to their mathematical properties which allows us to draw conclusions analytically which can be then translated into practice. The Gaussian section profile may be used as a model for vascular analysis, specially for small vessels where the partial volume effect induces an smoothing in the profile. Moreover, most profiles of depicted vessels can be converted into a Gaussian profile by smoothing with a Gaussian kernel of the right aperture or some other mathematical operation [10]. More importantly, this Gaussian smoothing operation is usually performed as a part of a scale-space analysis of vessels as in .

However, the introduction of other section profiles may be important for more realistic analysis that try to simulate real situations of normal or pathological vessels. It can be demonstrated [78] that the size estimation based on a multiscale analysis is dependent on this intensity profile. For example, the Gaussian profile is not adequate for the study of vessels of medium or large size [183] whose profile is more like a plateau. Different types of alternative profiles have been proposed in the literature, such as bar [77], parabolic [156] or convolved bar [78, 183]. These intensity profiles can be combined with the above 3D shape models in order to create for complex models of vessels.

Due to its relevance as a realistic model for vessels, we will provide a more detailed analysis of the bar convolved model in the following, preceded by an introduction of the bar model.

4.5.1 Bar Section Profiles

The bar cross-section profile is studied for the scale-space analysis of curvilinear structures in [156]. It can be modelled as a pulse with height h and width 2ω, which corresponds to the equation:

$$f_b(x;h,\omega) = \begin{cases} h & |x| \leq \omega \\ 0 & |x| > \omega \end{cases} \tag{4.163}$$

It can also be expressed as the sum of two scaled and translated Heaviside functions:

$$f_b(x;h,\omega) = h\,[H(x+\omega) - H(x-\omega)] \tag{4.164}$$

with H being the Heaviside or step function

$$H(x) = \begin{cases} 1 & x \geq 0 \\ 0 & x < 0 \end{cases} \tag{4.165}$$

Here we will reproduce some of the analysis in [156] in order to provide additional proofs and concepts that may be useful for the convolved bar profile, which is used extensively in our experiements in chapters .

We are mostly interested in the behaviour of the second Gaussian derivative in the central point of the profile ($x = 0$). For the profile to be detected, the second derivative should show a clear minimum at this location for a given scale σ. Due to the symmetry of the problem, the analysis can be performed in 1D.

For the scale-space analysis, we need to convolve the bar profile f_b with a Gaussian function

$$g_\sigma(x) = \frac{1}{\sqrt{2\pi}\sigma} e^{-\frac{x^2}{2\sigma^2}} \tag{4.166}$$

This convolution can be calculated analytically as:

$$r_b(x;h,\omega,\sigma) = f_b(x) \star g_\sigma(x) = \int_{-\infty}^{\infty} f_b(x-\tau)\, g_\sigma(\tau)\, d\tau$$

which can be split as the sum of two integrals

$$r_b(x;h,\omega,\sigma) = h\int_{-\infty}^{\infty} H(x+\omega-\tau)\, g_\sigma(\tau)\, d\tau + h\int_{-\infty}^{\infty} H(x-\omega-\tau)\, g_\sigma(\tau)\, d\tau \tag{4.167}$$

resulting in[15]

$$r_b(x;h,\omega,\sigma) = \frac{h}{\sqrt{2\pi}\sigma}\left(\phi_\sigma(x+\omega) - \phi_\sigma(x-\omega)\right) \tag{4.168}$$

where $\phi_\sigma(x)$ is the Gaussian integral function

$$\phi_\sigma(x) = \int_{-\infty}^{x} e^{-\frac{x^2}{2\sigma^2}}\, dx \tag{4.169}$$

Since the derivative of the Gaussian integral is simply the Gaussian function, it is very easy to obtain the first and second order Gaussian derivatives of the bar profile with respect to the spatial variable x which results in:

$$r_b^{'}(x;h,\omega,\sigma) = h\left[g_\sigma(x+\omega) - g_\sigma(x-\omega)\right] \tag{4.170}$$

$$r_b^{''}(x;h,\omega,\sigma) = h\left[g_\sigma^{'}(x+\omega) - g_\sigma^{'}(x-\omega)\right] \tag{4.171}$$

where the first derivative of Gaussian is

---

[15] Note that here we do not omit the normalization factor of the Gaussian as in [156].

$$g'_{\sigma}(x) = -\frac{x}{\sigma^2}\, g_{\sigma}(x) \tag{4.172}$$

Now, we can proceed to analyze the behaviour of this second order derivative.

Lemma 11. *Given a bar profile* $f_b(x;h,\omega)$*, its second-order Gaussian derivative* $r''_b(x;h,\omega,\sigma)$ *has a critical point at* $x = 0$ *for all positive values of the parameters* h, ω *and scale* σ*.*

Proof. The third derivative of the bar profile is:

$$r'''_b(x;h,\omega,\sigma) = h\left[g''_{\sigma}(x+\omega) - g''_{\sigma}(x-\omega)\right] \tag{4.173}$$

$$r'''_b(x;h,\omega,\sigma) = \frac{h}{\sqrt{2\pi}\sigma^5}\left\{\left[(x+\omega)^2 - \sigma^2\right]e^{-\frac{(x+\omega)^2}{2\sigma^2}} + \left[\sigma^2 - (x-\omega)^2\right]e^{-\frac{(x-\omega)^2}{2\sigma^2}}\right\} \tag{4.174}$$

which is zero at $x = 0\ \forall (h,\omega,\sigma) \in \mathbb{R} : h > 0, \omega > 0, \sigma > 0$.

□

For a given bar profile with parameters (h,ω) the selection of the scale parameter σ will determine if this point will be a maximum, a minimum or an inflection point with respect to x. The following two lemmas are already formulated in [156].

Lemma 12. *Given a bar profile* $f_b(x;h,\omega)$*, its second-order Gaussian derivative* $r''_b(x;h,\omega,\sigma)$ *has a minimum with respect to the spatial variable x at* $x = 0$ *if and only if* $\sigma \geq \omega/\sqrt{3}$*.*

Proof. The derivative of $r''_b(x;h,\omega,\sigma)$ is

$$r''_b(x;h,\omega,\sigma) = \frac{h}{\sqrt{2\pi}\sigma}\left[-\frac{x+\omega}{\sigma^2}e^{-\frac{(x+\omega)^2}{2\sigma^2}} + \frac{x-\omega}{\sigma^2}e^{-\frac{(x-\omega)^2}{2\sigma^2}}\right] \tag{4.175}$$

The conditions for a minimum point at $x = 0$ with respect to the spatial variable x are

$$r'''_b(x=0;h,\omega,\sigma) = 0 \tag{4.176}$$

$$\frac{\partial^4 r_b}{\partial x^4}(x=0;h,\omega,\sigma) > 0 \tag{4.177}$$

The condition in 4.176 is demonstrated in Lemma 11. The fourth order derivative is:

$$\frac{\partial^4 r_b}{\partial x^4}(x;h,\omega,\sigma) = \frac{h}{\sqrt{2\pi}\sigma^7}\left\{\left[3(x+\omega)\sigma^2 - (x+\omega)^3\right]e^{-\frac{(x+\omega)^2}{2\sigma^2}} - \left[3(x-\omega)\sigma^2 - (x-\omega)^3\right]e^{-\frac{(x-\omega)^2}{2\sigma^2}}\right\} \tag{4.178}$$

The value at $x = 0$ is

$$\frac{\partial^4 r_b}{\partial x^4}(x=0;h,\omega,\sigma) = \frac{h}{\sqrt{2\pi}\sigma^7}\left(6\omega\sigma^2 - 2\omega^3\right)e^{-\frac{\omega^2}{2\sigma^2}} \tag{4.179}$$

which is positive for positive values of the parameters if and only if $\sigma \geq \omega/\sqrt{3}$.

□

Lemma 13. *Given a bar profile $f_b(x;h,\omega)$, its second-order Gaussian derivative $r_b^{''}(x;h,\omega,\sigma)$ has a minimum in scale-space at $x=0$ for $\sigma=\omega/\sqrt{3}$.*

Proof. The derivative of $r_b^{''}(x;h,\omega,\sigma)$ at $x=0$ is

$$r_b^{''}(x=0;h,\omega,\sigma) = -\frac{2\omega h}{\sqrt{2\pi}}\frac{1}{\sigma^3}e^{-\frac{\omega^2}{2\sigma^2}} \tag{4.180}$$

The derivative with respect to the scale parameter is

$$\frac{\partial r_b^{''}(x=0;h,\omega,\sigma)}{\partial\sigma} = -\frac{2\omega h}{\sqrt{2\pi}}\left(\frac{\omega^2-3\sigma^2}{\sigma^6}\right)e^{-\frac{\omega^2}{2\sigma^2}} \tag{4.181}$$

which has a critical point at $\sigma=\omega/\sqrt{3}$. This will be a minimum if and only if

$$\frac{\partial^2 r_b^{'''}}{\partial\sigma^2}(x=0;h\omega,\sigma=\omega/\sqrt{3})>0 \tag{4.182}$$

Calculating the derivative

$$\frac{\partial^2 r_b^{'''}}{\partial\sigma^2}(x=0;h,\omega,\sigma) = -\frac{2\omega h}{\sqrt{2\pi}}\left(\frac{12\sigma^4-9\omega^2\sigma^2+\omega^4}{\sigma^9}\right)e^{-\frac{\omega^2}{2\sigma^2}} \tag{4.183}$$

The expression in the parenthesis is negative for $\sigma=\omega/\sqrt{3}$ which makes all the expression positive $\forall\,(\sigma>0,\omega>0)$. □

The above proofs provide a means of selecting the correct scale for detecting the tube using the second derivative at the center location as a measure of strength. However, one problem found in [156] is that no normalization of derivatives is performed as described in [94] which allows finding a maximum (minimum) across scales that is best suited for the entity we want to detect.

Lemma 14. *Given a bar profile $f_b(x;h,\omega)$, its second-order γ-normalized Gaussian derivative $r_b^{''}(x;h,\omega,\sigma)_{\gamma-norm}=\sigma^{2\gamma}r_b^{''}(x;h,\omega,\sigma)$ has a minimum in scale-space at $x=0$ for $\sigma=\omega$ when $\gamma=1$.*

Proof. The γ-normalized strength measure at the center location would be:

$$r_b^{''}(x=0;h,\omega,\sigma)_{\gamma-norm} = -\frac{2\omega h}{\sqrt{2\pi}}\sigma^{2\gamma-3}e^{-\frac{\omega^2}{2\sigma^2}} \tag{4.184}$$

Calculating the derivative with respect to the scale:

$$\frac{\partial r_b^{''}(x=0;h,\omega,\sigma)_{\gamma-norm}}{\partial\sigma} = -\frac{2\omega h}{\sqrt{2\pi}}\sigma^{2\gamma-4}\left[(2\gamma-3)\,\sigma^2+\omega^2\right]e^{-\frac{\omega^2}{2\sigma^2}} \tag{4.185}$$

which has a critical point for $\sigma = \omega$ which, as in Lemma 13 corresponds to a minimum.

$\square$

By an appropiate selection of the normalization parameter γ we have obtained a normalized measure of strength, such that, the scale selected estimates the section half-width or radius.

4.5.2 Convolved-Bar Section Profiles

The convolved-bar section profile is obtained as a bar profile that is convolved with a Gaussian function with small aperture. It is a more realistic profile than the Gaussian for most vessel sizes [78]:

- For small vessels it resembles a Gaussian-like profile, since the aperture of the Gaussian is in the scale of the vessel width. It simulates the partial volume effect decreasing the intensity of the vessel.
- For medium and large vessels it shows a plateau in the area around the vessel axis, which is typical for most images of contrasted vessels. The small Gaussian represents the partial volume effect in the vessel boundaries.

Chapter 5

Basic Differential Feature Detection

In this chapter we will present the main algorithms used to detect tubular structures in images in general. As a particular case of tubular structures, the focus will be oriented towards our objective of detecting blood vessels in medical images.

5.1 Introduction

Curvilinear structures, also known as line or tubular structures are small width elongated structures present in both 2D and 3D medical images[1]corresponding to either anatomical structures, such as blood vessels, bronchi, nerves, biliary ducts, etc. or artificial structures, such as catheters, electrodes, stents, etc..

The basic geometrical property describing a line structure is that its length exceeds by far its diameter, thus it can be considered as a 1D manifold in the 2D/3D embedding image space,. At every point of the line structure (with the exception of the end and bifurcation or branching points) we can associate a direction, corresponding to the direction of the centerline (also known as medial axis/line) of the line structure, and a section line (in 2D images) or plane (in 3D images), that is normal to the axis direction. The geometry of the line structure's section is almost circular for small vessels, tending to differ from the ideal circle for larger vessels or when clinical or anatomical anomalies are present, such as stenoses or aneurysms..

The typical intensity profile of a tubular structure measured on its section shows a central elevation. The 2D or 3D shape of this elevation may be modeled as a Gaussian, bar-like (also known as rectangular or boxcar), parabolic or roof cross-section . On the other hand, the intensity profile variation along the line direction is small, assuming that there is no blockage that prevents the diffusion of the contrast media. These hyperintensity properties are exploited by most detection methods.

---

[1]. The term line structure or line filtering is more used in the literature in the context of detection and the term tubular structure is more used in volumetric image analysis.

The main goal of the vessel detection process is to detect curvilinear structures of, within some limits, arbitrary shape and size, regardless of the section intensity profiles [76].

Vessel detection methods are generally based on a '*vesselness*' measure, which can be calculated either locally or globally, estimating for each voxel the likelihood that it belongs to a blood vessel . If the vesselness measure is specially designed to detect the vessel centerlines, we call it *medialness* measure, as it refers to the medial line or medial axis of the curvilinear structure .

5.2 Edges, Ridges and Curvilinear Structures in Images

One approach to curvilinear structures detection is to consider their cross-sectional profiles as *double-sided edges* building detectors based on the image local derivatives.

Consider the image of an ideal step edge along the y direction in Fig. 5.1 (a). Its cross-sectional profile in the x direction (shown in Fig. 5.1(d)) corresponds to an ideal unit step or Heaviside function[2]:

$$u(x) = \begin{cases} 1 & x > 0 \\ 0 & x \leq 0 \end{cases} \tag{5.1}$$

A double-sided edge can be represented ideally with a rectangular function, aka normalized boxcar function, which can be expressed in terms of the ideal step edge or bar profile as follows:

$$f_b(x) = u(x + \frac{\omega}{2}) - u(x - \frac{\omega}{2}), \tag{5.2}$$

where ω is the width of the pulse. An image with a rectangular pulse is represented in Fig. 5.1 (b) with its corresponding x profile (Fig.5.1 (e)). If we make the pulse narrower, by decreasing the value of w we obtain an ideal line-like structure with a rectangular cross-sectional profile (Fig. 5.1(f)). In the limit, when $\omega \to 0$, we would obtain an ideal delta or Dirac pulse.

In real images, edge profiles are not sharp. Sometimes they can be approximated by Gaussian or other functions, with some kind of noise added. Let us consider the convolution of the previous ideal step functions with a Gaussian kernel in the x direction (Eq. 5.3). The effect of Gaussian convolution is to smooth the profiles so as to obtain an smooth transition as can be seen in Fig. 5.2. In the case of the ideal line with rectangular profile, the line in the middle corresponding to the maxima in the x direction is known as an *intensity ridge*.

An intensity ridge [40] corresponds to local maxima of N-dimensional functions in N-1 principal directions [40]. If we think of a 2D image as a 3D surface map, where the height correspond to intensity, ridges correspond to the surface crests. On the other

---

[2] an alternative definition is $u(x) = \int_x^{\infty} \delta(x)dx$ where $\delta(x)$ is the Dirac or delta function

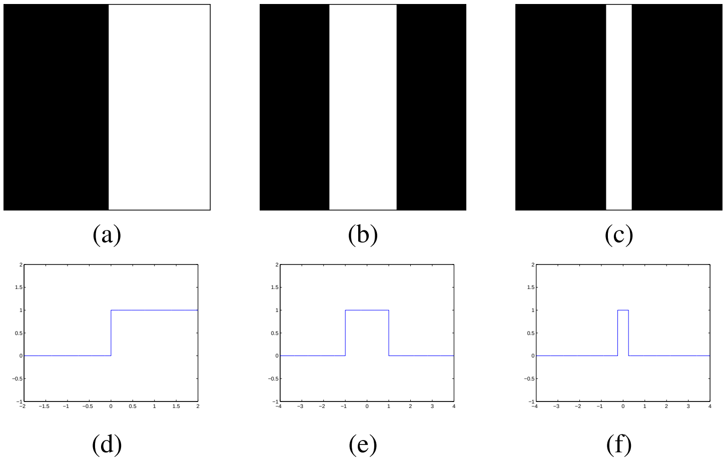
(a) (b) (c)

(d) (e) (f)

Figure 5.1: Different ideal edge images (top row) and profiles along x direction (bottom row). Columns correspond to ideal unit step (left), rectangular function (center) and line-like profile (right)

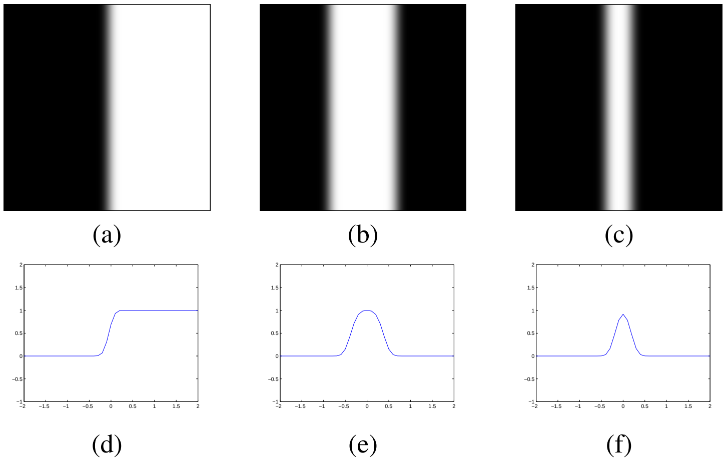
(a) (b) (c)

(d) (e) (f)

Figure 5.2: Different ideal edge images (top row) and profiles along x direction (bottom row) after smoothing with Gaussian convolution. Columns correspond to ideal unit step (left), rectangular function (center) and line-like profile (right)

hand, valleys follow the dual definition considering local minima instead of maxima. [3]. Intensity ridges are important both in edge and linear structure detection, since they may be used for the detection and localization of the corresponding structures.

The concept of edges and ridges can easily be extended to 3D images. The case of the step edge is trivial and less interesting for our analysis and is simply a transition in one direction of a volume. For the case of the double-sided edge or ridge, a 3D ideal line can be represented by an ideal cylinder with rectangular, Gaussian or other types of cross-section. In this case, the profiles are obtained diametrally in the cross-sections and the planes that contain the axis correspond to the images in center and right of Figures 5.1 and 5.2.

Let us consider a ramp edge profile as depicted in Fig. 5.3 (a) and the corresponding first and second order derivatives in Figs. 5.3 (b) and 5.3 (c), respectively. The first derivative of this ramp is a pulse. Narrowing the ramp (Fig. 5.3, second row), we approximately have a line structure for the first derivative. Performing a Gaussian convolution on the ramp edge (Fig. 5.3 bottom row), we approximately obtain an intensity ridge for the first derivative.

From the previous analysis we can conclude that *the analysis of line structures corresponds to the analysis of the first derivative of standard single-sided edges of various profiles*. Thus, from the review of the main edge detection techniques, we can draw some conclusions important for the task of line detection.

5.3 Principles of Edge Detection

5.3.1 The Problem of Edge Detection

The goal of edge detection methods is to find a set of curves that define the significant image edges that represent the boundaries of the objects of interest and reduce the amount of information to be processed [28]. Edge detection is affected by noise, illumination conditions, image resolution, contrast. etc.

One of the most common approaches for edge detection is to use detectors based on the local derivatives of the image, usually first- and second-order derivatives. In order to compare first- and second-order derivative methods, let us consider a ramp edge profile as depicted in Fig. 5.3 (top row). The corresponding first and second order derivatives are represented in Fig. 5.3 (top center and right respectively).

The first derivative (center) is positive and constant in the ramp segment and shows two discontinuities in the transition. The second derivative (left) is zero in all areas except the start and end points of the rampwhere it shows two peaks, one positive and one negative. We can see similar results for narrower edges and Gaussian smoothed edges (Fig. 5.3 center and bottom row, respectively). The following conclusions can be made from this simple 1D analysis[53]:

- Edges can be detected by the magnitude of the first derivative.

---

[3] (sometimes curvilinear structures are called ridge-like structures or simply ridges which may lead to confusion)

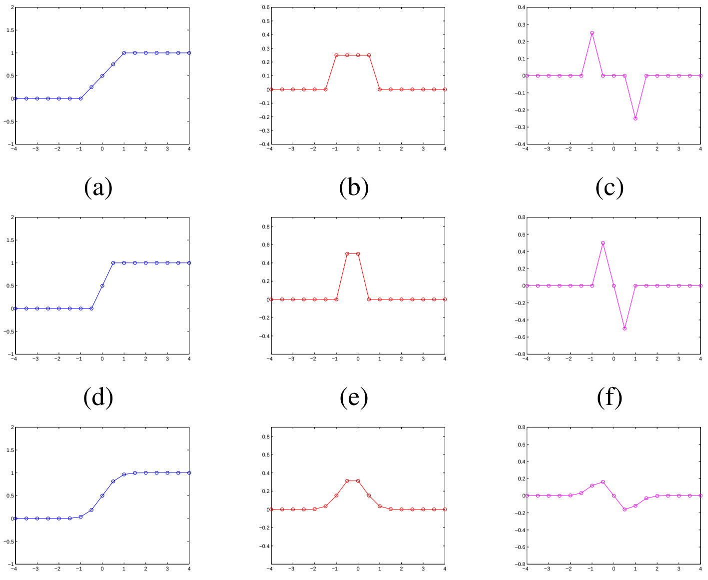

(a) (b) (c)

(d) (e) (f)

(g) (h) (i)

Figure 5.3: Several models of an ideal ramp edge (left column) and corresponding first (center column) and second (right column) derivatives. The first row corresponds to a wide edge, the second row to a narrow edge and the third row correspond to the narrow edge after Gaussian convolution (smoothing).

- The second derivative gives two responses for a single peak, corresponding to the positive and negative image curvatures at each side of the edge. This is initially an undesiderable property since we would like a single signed response.

- The second derivative gives two responses of different sign. Thus the edge can be detected by considering the zero-crossing of the second derivative.

Derivative-based detection is very sensitive to noise. Consider the ideal ramp with added white Gaussian noise decreasing its signal-to-noise ratio (SNR) as depicted in Fig. 5.4. With SNR = 100 (top row) the noise is imperceptible in the ramp; however, some noise appears in the first and second derivatives (top center and right respectively). With SNR = 65 (middle row) the situation degenerates evidently. The noise in the ramp is still hardly visible but, in the first derivative important noise peaks appear . whereas in the second derivative the peaks can hardly be seen. Finally, with SNR = 45.0 the ramp is still clearly visible, but we can barely see the pulse in the first derivative and the peaks in the second derivative cannot be distinguished from noise. As we can see, there is a limit or scale of noise, from which the derivative values start degenerating considerably. The effect of noise amplification is more evident with the second derivative, since it is more sensitive to small variations in the signal.

In the example shown in Figure 5.4 we see that there is a limit or scale of noise, from which the derivative values start degenerating considerably. When calculating derivatives we are not comparing any more the source, uncorrupted signal with noise, which gives us the SNR value. Instead, we are comparing local differences in signal with noise, and these differences may be small with gradual and long intensity transitions, so they may become close to the magnitude of noise.

This leads to think that some sort of scaling in the derivative calculations is necessary, so differences are only taken into account only at the appropiate *scale or aperture* at which differences are meaningful. On the other hand, scale-selection implies removal of structures at coarser scales without introducing new spurious details so scale-selection must performed via some sort of smoothing which also removes noise. Conversely, by blurring images to remove noise what we do is to make measurements at larger scales above the scale of noise, where image entities are more meaningful.

To sum up, *in order to calculate derivatives robustly and coherently we must devise a way to calculate smoothed and scaled image derivatives*. This is performed by using

some sort of noise removal or smoothing algorithm which performs scale selection, reducing the range of scales over which intensity changes take place [110], and removes noisy high frequency components.

Gaussian filtering is widely used as a pre-processing step while calculating derivatives and also for *scale-space* image analysis (see Section 5.4). In image processing, it is achieved by convolution with discrete approximations of the continuous, normalized (unit integral) Gaussian function:

$$g(x) = \frac{1}{\sqrt{2\pi}\sigma} e^{-\frac{x^2}{2\sigma^2}} \qquad (1D) \tag{5.3}$$

$$g(x,y) = \frac{1}{2\pi\sigma^2} e^{-\frac{x^2+y^2}{2\sigma^2}} \qquad (2D) \tag{5.4}$$

$$g(x_1, x_2 \ldots x_N) = \frac{1}{\left(\sqrt{2\pi}\sigma\right)^N} e^{-\frac{\Sigma_{i=1}^N x_i}{2\sigma^2}} \qquad (ND) \tag{5.5}$$

The degree of smoothing is controlled by the standard deviation σ of the Gaussian (the larger, the smoother). It has several important properties that makes it specially adequate in many circumstances. We can mention here a few:

- The Fourier transform of a Gaussian function in spatial domain is a Gaussian function in the frequency domain, usually centered at zero and with standard deviation $1/\sigma$, which corresponds to a low-pass filter . For a normalized 1D Gaussian function, its Fourier transform is:

$$G(\varpi) = e^{-\frac{\varpi^2\sigma^2}{2}} \tag{5.6}$$

- The Gaussian is the function that optimizes the localization in both the spatial and frequency domains. In Section 5.4.1 we will see that these both localization requirements are desiderable for smoothing filters but are conflicting: localization in the spatial domain spreads the spectrum in the frequency domain and viceversa. This can easily be seen in formulas 5.3 and 5.6: if we decrease σ in the spatial domain it increases in the frequency domain. The Gaussian function optimizes this trade-off with respect to another types of filters.
- Gaussian convolution is linearly separable: this means that, instead of using one large 2D Gaussian kernel, one can use a 1D kernel and apply it sucessively in x and y direction, which is computationally much more efficient (unless applied for a single pixel). The same applies for a higher number of dimensions.
- Gaussian convolution has infinite support: theorically one would need the whole image to compute the smoothed value for every pixel. However, in practice, the contribution of pixels at a distance of more than 3σ is usually negligible and kernels can be designed in order to obtain the desired accuracy within some limits, for example in terms of the unit integral .
- The convolution of two Gaussians with standard deviations σ_1, σ_2 is another Gaussian with standard deviation $\sqrt{\sigma_1^2 + \sigma_2^2}$. This can be easily proven in the frequency domain:

$$G_1(\varpi)G_2(\varpi) = \exp\left(-\frac{\varpi^2\sigma_1^2}{2}\right)\exp\left(-\frac{\varpi^2\sigma_2^2}{2}\right) = \exp\left[-\frac{\varpi^2\left(\sigma_1^2+\sigma_2^2\right)}{2}\right] \tag{5.7}$$

An ideal edge detector should have the following properties [28]:

- Good detection: the algorithm should find most edges of the image avoiding false edge detection. This criterion corresponds to maximizing the signal-to-noise ratio.
- Good localization: the algorithm should obtain edges close enough to the center of the true edges.

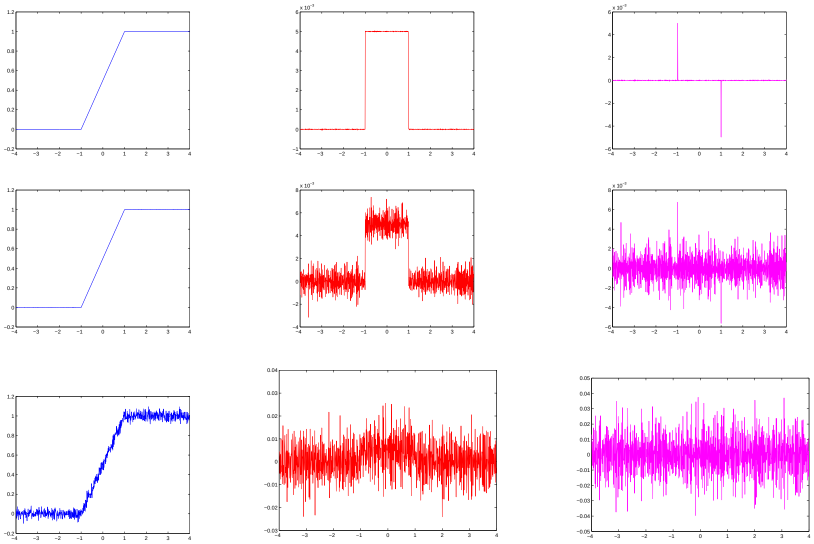

Figure 5.4: Ideal ramp edge (left column) and corresponding first (center column) and second (right colum) derivatives with increasing values of noise (from top to bottom SNR = 100, 65, 35).

- Single response: ideally we would like to obtain a single response per edge (important for ideal centerline detection).

Edge detection algorithms must find a compromise between the two first requirements. If we are going to suppress noise by smoothing in order not to detect false edges, which is equivalent to increasing the scale or aperture by increasing the support of the filter, then we will blur the real edges obtaining a poorer localization. On the other hand, if we deal with small scales preserving all the details, we will localize better the true edges but will also detect noisy spurious details. In most cases, a single scale of analysis is not sufficient to detect all edges of the image and one must devise a way to obtain responses at different scales and integrate them into a single, *multiscale* representation. The same applies for the detection of ridges and other features.

5.3.2 First-order Derivative Methods

Most of first-order derivative edge detection methods are *search-based* methods. The idea is to compute a measure of edge strength, such as the gradient magnitude, and of edge direction, such as the normal to the gradient vector. Then, the edge location can be found as the local maxima in the edge direction.

The components of the image gradient are the first order derivatives of the image f in each direction. For a 3D image:

$$\nabla f(x,y,z) = \frac{\partial f}{\partial x} i + \frac{\partial f}{\partial y} j + \frac{\partial f}{\partial z} k = f_x i + f_y j + f_z k \tag{5.8}$$

The *gradient magnitude* provides a measure of the edge strength:

$$|\nabla f(x,y,z)| = \sqrt{f_x^2 + f_y^2 + f_z^2} \tag{5.9}$$

and the unit vector in the direction of the gradient provides information about the edge orientation:

$$u_{\nabla f}(x) = \frac{\nabla f(x)}{|\nabla f(x)|} \tag{5.10}$$

where we have chosen the notation for the first derivatives $f_i = \frac{\partial f}{\partial x_i}$. When using higher order derivatives, we will use the notation $f_{ij} = \frac{\partial f}{\partial x_i \partial x_j}$. Derivatives in other directions can be calculated as the scalar product of gradient and the unit vector u in the desired direction:

$$f_u = \frac{\partial f}{\partial u} = \nabla f \cdot u \tag{5.11}$$

gauge coordinates is a local reference system aligned with the edge. The normal to the gradient vector and the gradient itself in 2D are denoted by the pair $\{v,w\}$ in the computer vision literature and constitute *first-order gauge coordinates* or *gradient gauge coordinates*. From this definition $f_w = |\nabla f|$ and $f_v = 0$

Since the gradient is a continous function and we are dealing with digital images, it is necessary to compute discrete approximations of the gradient. In one dimension, the derivative is defined as:

Discrete derivatives in one dimension are computed using finite differences. In order to compute discrete image gradients, we must devise convolution kernels that may calculate derivatives in all possible image dimensions. The basic properties that these kernels must meet are:

- The coefficients must sum to zero, in order to obtain zero response in constant regions (differently from smoothing kernels which must sum to one in order not to change constant regions).
- Obtain high absolute values in places of high contrast.
- Avoid the introduction of sampling artifacts and spurious details.

Numerous convolution kernels for derivative calculation can be found in the literature, such as the Prewitt, Sobel or Robert-Cross operators . These kernels can be thought of as a rough approximation to the first order derivative of a Gaussian function which presents interesting properties for edge detection [28]. However, these kernels perform poorly when edges are blurred and noisy . Convolution and derivative operations are commutative and associative. Take for example Gaussian filtering and derivative calculation on an image (we could have taken averaging instead of Gaussian):

$$\frac{\partial}{\partial x}(f * g) = f * \frac{\partial g}{\partial x} \tag{5.12}$$

Then, instead of Gaussian filtering the whole image and then calculating derivatives, for example with central differences, we might precompute Gaussian derivative kernels that could be convolved with the image. Due to the separability of Gaussian kernels this may speed up calculations greatly. Different kernels can be computed for different orders of Gaussian derivatives too.

For our scaled derivative calculations used in tubular structure detection we have developed discrete implementations of the Gaussian derivatives using 1D kernels in different directions as explained in [102] where 1D kernels are calculated for desired order of derivatives and apertures and then applied in the corresponding directions.

5.3.3 Second-order Derivative Methods

Second-order derivative methods try to find the maxima of the gradient magnitude directly, since they correspond to local maxima in the direction of the edge's normal, looking for points where the second derivative of the image becomes zero. As we have seen in 5.3.1, in the presence of an edge, the second derivative gives two responses of different sign and the *zero-crossing* of the second derivative is located, approximately, on the center of the edge. The problem of edge detection is stated as the problem of *finding the zero-crossings of the second derivative in the appropiate direction*. The advantages of finding zero-crossings is that they are easier to estimate that the maxima of the gradient magnitude and they always form closed contours (REF).

In 2D/3D images, edges are not necessarily oriented in the main axes directions, and we need detectors that can cope with different edge orientations. One idea is to try to estimate the edge direction locally (corresponds to the orientation of the zero crossing) and then calculate the derivative of the gradient magnitude in that direction (directional second derivative). The orientation of the zero-crossing will have maximum slope under the asumption of *linear variation*, that is, when the intensity variation near and parallel to the line of zero-crossings is locally linear, which is approximately true for smoothed images [110].

The disadvantage of this approach is that it would require either multiple convolutions in different orientations, in order to search for the maximum response, or alternatively, an optimal estimation of the direction.

Another approach is to use some sort of detector valid for different edge orientations. The only rotationally-invariant second-order operator is the *Laplacian*, which is the scalar product of the gradient vector by itself:

$$\triangle f = \nabla^2 f = \nabla \cdot \nabla f = \frac{\partial^2 f}{\partial x^2} + \frac{\partial^2 f}{\partial y^2} + \frac{\partial^2 f}{\partial z^2} \tag{5.13}$$

Two different convolution kernels may be used typically to calculate the Laplacian:

The Laplacian operator is usually used in conjunction with a Gaussian operator for smoothing and scale selection because Laplacian zero-crossings are only effective in a band-limited situation. Again, due to the associative and commutative properties of the convolution, we can combine both operators

$$\frac{1}{8}\begin{array}{|c|c|c|}\hline 0 & -1 & 0 \\ \hline -1 & 4 & -1 \\ \hline 0 & -1 & 0 \\ \hline \end{array} \quad \frac{1}{16}\begin{array}{|c|c|c|}\hline -1 & -1 & -1 \\ \hline -1 & 8 & -1 \\ \hline -1 & -1 & -1 \\ \hline \end{array}$$

Figure 5.5: Laplacian convolution kernels in 2D.

$$g_\sigma(x,y) = \frac{1}{2\pi\sigma^2} e^{-\frac{x^2+y^2}{2\sigma^2}} \tag{5.14}$$

$$\triangle\left[g_\sigma(x,y) * f(x,y)\right] = \triangle\left[g_\sigma(x,y)\right] * f(x,y) = LoG * f(x,y) \tag{5.15}$$

and obtain an expression for the new operator

$$LoG \triangleq \triangle\left[g_\sigma(x,y)\right] = \frac{\partial^2 g}{\partial x^2} + \frac{\partial^2 g}{\partial y^2} = \frac{x^2+y^2-2\sigma^2}{\sigma^4} g_\sigma \tag{5.16}$$

The resulting *LoG* operator, that depends on theσscale parameter, is known as the *Laplacian of Gaussian* or *Marr-Hildreth* operator [110]and can be seen in Fig. 5.6, where we can also see the corresponding second derivative components. The scale, corresponding to the σ value of the Gaussian, should be chosen according to the size of the edge features to be detected. Discrete approximations may be obtained for each scale value by several methods, for example by approximating and truncating the Gaussian function (sampled Gaussian kernel) or by discrete derivative approximations using the *discrete Gaussian kernel*, which preserves scale-space properties [91].

Another second order approach is the *Difference of Gaussians (DoG)* operator [100]. From the fact that scale-space representation of an image $L(x,y;t)$ satisfies the diffusion equation [74]

$$\frac{\partial L(x,y;t)}{\partial t} = \triangle L(x,y;t) = L_x^2(x,y;t) + L_y^2(x,y;t) \tag{5.17}$$

also called Laplace equation, it follows that the *LoG* operator can be found as the limit of the difference between two Gaussian smoothed images:

$$\triangle L(x,y;t) = \lim_{\triangle t \to 0} \frac{2}{\triangle t}\left(L(x,y;t+\triangle t) - L(x,y;t)\right) \tag{5.18}$$

where $L(x,y;t) = f(x,y) * g(x,y;t)$ and $t = \sigma^2$.

Hence, subtracting two Gaussian smoothed images with different apertures we obtain an edge detector. The *DoG* operator is an approximation of the Laplacian of Gaussians but does not require complex second order derivative calculations which made its use quite popular.

Once the zero-crossings have been calculated, a magnitude can be assigned to them at each scale, as the slope of the second directional derivative taken perpendicular to the zero-crossing segment [110]. Another possibility is to simply use the gradient magnitude at the zero-crossing location.

The use of the Laplacian operator requires that the intensity variation along, but not necessarily near, the line of zero-crossings is approximately linear. Then the Laplacian zero-crossings will coincide with the local orientation line zero-crossings. However, the *Marr-Hildreth* operator exhibits severe localization errors in curved edges and other places where the intensity varies in a non-linear way [110, 149].

Moreover, it detects false edges corresponding to local minima of the gradient magnitude and it is difficult to combine the information obtained from the zero-crossings at different scales so it is not currently used in practice.

Extensive local second-order derivative information may be obtained by calculatingthe *Hessian matrix* at an image point. Its components are the image second-order spatial derivatives. A second-order Taylor expansion of a 2D image around a point x_0 is:

$$f(x_0+\triangle x, y_0+\triangle y) = f(x_0,y_0) + \begin{bmatrix} \triangle x & \triangle y \end{bmatrix} \begin{bmatrix} f_x(x_0,y_0) \\ f_y(x_0,y_0) \end{bmatrix} +$$

$$+\frac{1}{2}\begin{bmatrix} \triangle x & \triangle y \end{bmatrix} \begin{bmatrix} f_{xx}(x_0,y_0) & f_{xy}(x_0,y_0) \\ f_{xy}(x_0,y_0) & f_{yy}(x_0,y_0) \end{bmatrix} \begin{bmatrix} \triangle x \\ \triangle y \end{bmatrix}$$

We obtain an expression which is valid for N-dimensional scalar images

$$f(x_0+\triangle x) = f(x_0) + \triangle x^T \cdot \nabla f(x_0,y_0) + \frac{1}{2}\triangle x^T \mathscr{H}(x_0,y_0)\triangle x \tag{5.19}$$

where $\mathscr{H}$is the symmetric Hessian matrix, which captures the second order local structure of the image in the vecinity of x_0, corresponding to the local image curvatures.

Different features may be obtained from the Hessian matrix. The Laplacian in eq. **??** corresponds to the trace of the Hessian matrix:

$$\triangle f = \nabla^2 f = \operatorname{tr}(\mathscr{H}(x)) \tag{5.20}$$

A more in-depth analysis of the Hessian matrix properties is performed in in the context of line structure detection.

5.3.4 Advanced Edge Detection

Marr and Hildreth introduced important concepts such as some notion of scale, that was later conceptualized in the framework of *scale-space*, first introduced by [178], and Gaussian filtering as a means of scale selection. However, early edge detectors such as the Marr-Hildreth operator exhibited several problems which led researchers to develop new strategies such as optimal edge detection, integration of information at multiple scales and non-linear filters. It is not our intention to make an extensive review on the subject of edge detection (see for example [126] or [13]) but rather focus on some interesting concept useful for tubular structure detection.

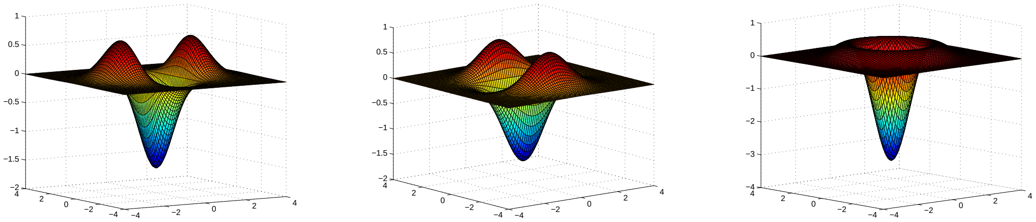

Figure 5.6: Surface plots of $\partial^2 g/\partial x^2$ (left) and $\partial^2 g/\partial y^2$ (center) and Laplacian of Gaussian (right). All surfaces are calculated for $\sigma = 1.0$.

5.3.4.1 Canny-like Edge Detectors

Canny [28] developed a computational theory of edge detection in order to find the optimal edge detector which maximized the criteria of detection, localization and single responseness (see Section 5.3.1). He showed that there is an uncertainty principle regarding detection and localization of noisy edges and that one must find a trade-off between these. He then derived an optimal detector which is the sum of four complex exponentials, but which can be approximated in practice by the first derivative of Gaussian functions, which is much more efficient to compute. Compared to the Marr-Hildreth operator, its 2D performance is better in terms of detection and localization due to its directional properties. Moreover, the amplitude of the response is a good estimate of edge strength and compared with the zero-crossings of the Laplacian, it can be thresholded adaptatively to find local maxima.

Canny's edge detector finds the zero-crossings of the second-order image derivative in the edge direction n:

$$\frac{\partial^2}{\partial n^2} g * f \tag{5.21}$$

which correspond to the maxima of the derivative in the edge direction. First, an estimate of the local edge direction is computed using the gradient:

$$n = \frac{\nabla (g * f)}{|\nabla (g * f)|}$$

In practice, the direction can be rounded to one of four edge directions at angles of 0°,45°,90 and 135°.

Often the Canny algorthm computes the first directional derivative of Gaussian filtered image

$$\frac{\partial}{\partial n} g * f \tag{5.22}$$

performing later the non-maximum suppression in the gradient direction in order to compute single edge responses. Due to the separability of the Gaussian functions, the above scheme can be implemented efficiently by first convolving the image with a 1D Gaussian in each dimension and then computing the derivative in the edge direction only.

Compared to the Laplacian, the latter can be decomposed into second derivative components in two arbitrary orthogonal directions. If we choose as directions the gradient direction and its normal, then we will have a contribution in the gradient direction which is esentially the same as the operator described by Canny, and another contribution which does not contribute to detection and localization but to noise only.

The last stage of the Canny algorithm is to threshold the edges in order to remove the response for false edges by using *hysteresis thresholding*, which is a sort of adaptative thresholding. The algorithm is sensitive to weak edges but the problem is that this also makes it sensitive to spurious or unstable edges .

Canny also devised a way to combine the output from multiple scales in what is known as *feature shynthesis*. In a similar approach Schunk [145] also performed scale integration by combining ridge information obtained from detected edges accross scales.

One recurrent problem in multi-scale approximation is that sometimes there are no indications on how to choose the number and range of scales. Jeong and Kim tried to find the optimal scale for every pixel by minimizing the following energy function on the filter width domain σ:

$$E(\sigma) = \int\int \left[(I * g)^2 + \lambda \left| \nabla \sigma^{-1} \right|^2 \right] \tag{5.23}$$

designed for large apertures in flat areas and small apertures in places of high intensity variation and smoothnes in the resulting scale map. It is slow , but its performance could be greatly improved with a preselection of candidate points. A similar adaptative idea by Deng and Cahill uses the following formula for scale selection:

$$\sigma^2(x) = \frac{k\sigma_n^2}{\sigma_f^2(x) + \sigma_n^2} \tag{5.24}$$

where σ_f is the local variance and σ_n is the standard deviation of the image noise, assumed Gaussian.

Lindeberg [95] proposed, within the scale-space framework (see Section 5.4) a method for edge detection based on the maximization of two γ-normalized edge strength measures:

$$\mathcal{G}_{\gamma-norm} L = \sigma^{\gamma} \left(L_x^2 + L_y^2 \right) \tag{5.25}$$

$$\mathcal{T}_{\gamma-norm} L = \sigma^{3\gamma} \left(L_x^3 L_{xxx} + L_y^3 L_{yyy} + 3L_x^2 L_y L_{xxy} + 3L_x L_y^2 L_{xyy} \right) \tag{5.26}$$

where L is the scale-space representation of the image and γ is a parameter that makes the scale selection dependent on the edge diffuseness. The first equation corresponds to gradient magnitude and the second equation takes into account that the edge is located at a maximum of gradient magnitude, that is, with zero second derivative and negative third derivative. The problem with this approach is that the user has to provide a set of desired scales in a range and the use of high order derivatives may be problematic and not justified by the results, which are similar to other existing methods . However, the edge diffuseness is an interesting concept that allows to select finer scales for sharp edges and coarser scales for diffused edges.

5.3.4.2 Steerable Filters

Freeman and Adelson [48] proposed an alternative approach to Canny-like filters, that use optimal 1D operators in the gradient direction and smoothing in the orthogonal direction(s), is to use a set of directional filter banks for predefined orientations, what is known as *steerable filters*. In this approach, detectors for arbitrary orientation can be generated by linear combination using these oriented filters as basis functions. They demonstrate that all functions that can be expressed as a Fourier series in angle or as a polynomial multiplying a radially symmetric window function are steerable in orientation. Hence, derivatives of Gaussian of all orders are steerable since they consist of polynomials (here the Hermite polynomials) multiplying a Gaussian which is rotationally symmetric (see section 5.4.2). In order to synthetize filters with arbitrary phase response, they use filters in quadrature (same frequency response but with a phase difference of 90º) which can be found using a Hilbert transform, that may be approximated via polynomial fit. Thus, a set of steerable filters is combined with another set whose originating functions (the non-rotated versions) are in quadrature.

One example of such combination of filters is to combine the second derivative of Gaussian $f(x,y) = G_2^{0^\circ} = \left(4x^2-2\right)\exp(x^2+y^2)^4$, with rotated versions for 0º, 60º and 120º:

$$G_2^{\theta} = k_1(\theta)G_2^{0^\circ} + k_2(\theta)G_2^{60^\circ} + k_3(\theta)G_2^{120^\circ}$$

where the k_i can be found solving a set of equations for the steering conditions yielding

$$k_i(\theta) = \frac{1}{3}\left[1+2\cos\left(2(\theta-\theta_j)\right)\right]$$

Then, the Hilbert transform of G_2 can be approximated by a third order polynomial, namely H_2 with four rotated versions that are used as basis functions. Thus the seven basis functions ofG_2 and H_2 are sufficient to shift G_2 to the desired phase and orientation. Similar approximations can be found for other orders of derivatives.

---

[4] We follow here the notation from Freeman and Adelson with the subscript for the derivative order and the superscript for the angle

Steerable filters can be used, among other things, to estimate local feature orientation and strength. The squared magnitude of the quadrature pair filter can be used to estimate the orientation θ_d with largest strength:

$$E_2(\theta_d) = \left[G_2^{\theta_d}\right]^2 + \left[H_2^{\theta_d}\right]^2 \tag{5.27}$$

Using an scheme similar to Canny's but replacing the feature detector with this energy, one obtains single responses to different features, as compared with Canny's method that gives spurious responses to non-edge features, such as double responses for lines. One major drawback is that the process of obtaining the Hilbert transform in order to design quadrature filter pairs is very difficult and tedious. Weiping and Huazhong propose an alternative to the Hilbert transform that uses dyadic B-spline wavelets [169].

Canny applied its optimal 1D operator orthogonal to the local feature while smoothing in the normal direction. Jacob and Unser [65] developed a set of tryly 2D feature detectors following Canny-like optimization criteria but obtaining explicit expressions. Moreover, they used the ideas of Freeman and Adelson in order to design optimal 2D detectors which were steerable. The resulting detectors achieved good performance in terms of accuracy and speed and showed better orientation selectivity. They considered matched filters of the form:

$$h(x,y) = \sum_{k=1}^{M}\sum_{i=0}^{k} \alpha_{k,i} g_{k,i}(x,y) = \sum_{k=1}^{M}\sum_{i=0}^{k} \alpha_{k,i} \frac{\partial^{k-i}}{\partial x^{k-i}} \frac{\partial^{i}}{\partial y^{i}} g(x,y) \tag{5.28}$$

where $g(x,y)$ is an isotropic window function, and M is the order of the detector. Following the theory of Freeman and Adelson, the idea is to find a rotated version of the filter $h(\mathrm{R}_\theta x)$for an angle θ where the magnitude $r(x) = f(x) * h(\mathrm{R}_\theta x)$is maximum. They demonstrated that the filters in eq. 5.28 are steerable. That is, the convolution of the image with a rotation version of the filter can be expressed as:

$$f(x) * h(\mathrm{R}_\theta x) = \sum_{k=1}^{M}\sum_{i=0}^{k} b_{k,i}(\theta)\left(f(x,y) * g_{k,i}(x,y)\right) \tag{5.29}$$

with

$$b_{k,i}(\theta) = \left(\sum_{j=0}^{k} \alpha_{k,j} \sum_{l,m \in S(k,j,i)} \begin{pmatrix} k-j \\ l \end{pmatrix} \begin{pmatrix} j \\ m \end{pmatrix} (-1)^m \cos(\theta)^{j+(l-m)} \sin(\theta)^{(k-j)+(l-m)}\right) \tag{5.30}$$

where $S(k,i,j)$ is the set

$$S(k,i,j) = \{l,m | 0 \le l \le k-i; 0 \le m \le i; k-(l+m) = j\}$$

Note that the steering coefficients $b_{k,i}(\theta)$ which build the rotated version of the filter for the angle θ have one part that does not depend on the angle, which corresponds to the $\alpha_{k,j}$ for the derivative coefficients. The most interesting case is $g(x,y)$ being the Gaussian function, which is optimal in terms of detection versus localization and is separable. The resulting filters are similar, but not identical to those in [48].

By using Canny-like optimization criteria, the coefficient vector a which contains the $\alpha_{k,i}$ is an eigenvector a_{λ_i} of the matrix[5]:

$$-\mathbf{P}^{-1}\left[\mathbf{Q}-\mu\mathbf{R}\right] \tag{5.31}$$

appropiately scaled to meet the condition

$$a_{\lambda_i}^{\mathbf{T}}\mathbf{P}a_{\lambda_i}=1 \tag{5.32}$$

where

$$\mathbf{Q}=sq^{\mathrm{T}}$$

$$[s]_i=\langle f(x),g(-x)_i\rangle$$

$$[q]_i=\langle f(x),g(-x)_i\rangle$$

$$[\mathbf{P}]_{i,j}=\left\langle [g]_i,[g]_j\right\rangle$$

$$[\mathbf{R}]_{i,j}=\left\langle ([g]_i)_{yy},\left([g]_j\right)_{yy}\right\rangle+\left\langle ([g]_i)_{xx},\left([g]_j\right)_{xx}\right\rangle$$

and the inner product of two functions *f,g* is defined as

$$\langle f,g\rangle=\int_{\mathbb{R}^{\in}} f(x,y)g(x,y)dxdy \tag{5.33}$$

Among the (two) eigenvectors, the optimal solution $\overline{a}$ is the one that satisfies the condition

$$\overline{a}=\max\left\{a_{\lambda_i}^{\mathbf{T}}\left[\mathbf{Q}-\mu\mathbf{R}\right]a_{\lambda_i};i=0\ldots M(M+3)/2\right\} \tag{5.34}$$

The optimal angle $\theta^*$is obtained for every point as the solution to

$$\frac{\partial}{\partial\theta}\left(f(x)*h(R_{\theta^*}x)\right)=\sum_{k=1}^{M}\sum_{i=0}^{k}f_{k,i}(x,y)\frac{\partial}{\partial\theta}\left(b_{k,i}(\theta)\right)|_{\theta=\theta^*}=0 \tag{5.35}$$

---

[5] The formulas are expressed for the 2D case only

which is a polynomial of order M in $\cos(\theta)$ and $\sin(\theta)$. This has an analytic solution if M<=3 or can be solved numerically for higher orders. When M=2 this can be solved as the well-known eigendecomposition of the Hessian. The use of this framework is demonstrated by developing specific detectors for edge, ridge and wedge features that outperform Canny's detector without any relevant additional computational cost.

5.4 Image Analysis in Scale-space

5.4.1 Concept of Scale-space

When faced with the problem of image analysis, one important consideration is that an image is a *physical observable* that represents the reality as measured by some apparatus that is able to register some physical measure (typically illumination, but may be any other physical observable phenomenon such as X-ray attenuation, magnetic resonance, etc.) in a regular discrete grid and with a certain dynamic range. This implies that there exist a finite scale range at which observations are made [43]. The lower bound of this scale range, often referred to as the *inner scale*, is determined by the sampling characteristics of the device and it refers to the size of the finest possible feature that can be detected. The *upper scale* bound is limited by the scope of the field of view and refers to the coarsest features that can be observed on the image. Moreover, objects, illumination changes, details and other features represented in digital images have different sizes and some of them are only meaningful at a certain range of scale(s). This finite scale range and multi-scale image nature must be taken into account when performing any image analysis task in order to fix the proper scale(s) at which calculations are meaningful.

Sometimes, calculations performed at a single scale may miss some information. No single filter can be optimal simultaneosly at all scales and a multi-scale approach is necessary, which deals with every relevant scale separately. This happens for example when trying to detect some objects or entities whose coarse and fine details span a variable range of scales and all the information is relevant. This is the case for example of images of the human vasculature. A complex vascular network is comprised of multiple vessels of varying length and diameter and multi-scale approaches are required in most cases for the detection and extraction of the whole vascular tree.

The basic idea of multi-scale analysis is to take local averages of the image at various resolutions and detect changes in intensity that occur at each one. Then, this information at each scale is translated into a set of primitive features such as edges, bars, blobs and corners obtaining what is known as a *raw primal sketch*. Finally the information from all scales is organized and integrated, translating it into more meaningful, higher-level features and descriptions, in order to obtain what is called the *full primal sketch* of the image.

When faced with the problem of multi-scale analysis of digital images, it is necessary to find a way to convert the images into a multi-scale representation and deal with each scale separately. This leads to the basic idea of taking local averages at various resolutions, in a sort of smoothing filter, and detecting changes of intensity that occur at each one. To achieve this, it is necessary to:

- Find the optimal smoothing filter in order to obtain image representations at different scales, which is known as a *scale-space image representation*.
- Detect the intensity changes at each scale.
- Integrate the information obtained at different scales.

When designing the optimal smoothing filter two important considerations must be taken into account [110]:

- Filtering should reduce the range of scales over which intensity changes take place. This implies that the frequency spectrum of the filter must be smooth and roughly band-limited with a small variance $\Delta\varpi$.
- Features at each scale should be spatially localized. This implies that the contributions to each point in the filtered image should be obtained from a smoothed average of nearby points, so the filter must be smooth and localized in the spatial domain with a small variance Δx.

The problem is that these two localization requirements, one in the spatial and the other in the frequency domain, are conflicting and related by the uncertainty principle that states that $\Delta\varpi\Delta x \geq \pi/4$ [21]. This means that it is impossible to concentrate a function both in the spatial and frequency domain. The more concentrated it is in the spatial domain, the more spread it is in the frequency domain. The best trade-off is achieved with the use of Gaussian functions.

The structure of images, the properties that a scale-space representation of an image should have and the way to accommodate such a scale-space representation in a mathematical theory was studied in depth by several authors [178, 74, 188, 93, 43] inspired on some work of the behaviour of the human visual system . Their basic idea for a scale-space representation of an image is that it should consist of a one-parameter family of derived signals from fine to coarse scales as the *scale* parameter t increases, where the fine details are suppressed sucesively at coarser scales. The original signal will be the one with the finest details, that is, the one at the lowest scale. Mathematically, for an N-dimensional signal $f : \mathbb{R}^N \to \mathbb{R}$, its scale-space representation $L : \mathbb{R}^N \times \mathbb{R}_+ \to \mathbb{R}$ is defined as the convolution:

$$L(x;t) = (T_t f)(x) \int_{\vec{\xi}\in\mathbb{R}^N} f(x-\xi)\, g(\xi;t)\, d\xi = g(x;t) * I(x) \tag{5.36}$$

where $g : \mathbb{R}^N \times \mathbb{R}_+ \to \mathbb{R}$ is a family of functions in the scale parameter t. These functions act as *operators* that interact with the data in order to extract relevant information and generate the corresponding representations. The scale parameter t is equivalent to the *aperture* of the physical observation device. Sometimes g is called the *aperture function*.

A key requirement for obtaining this scale-space representation, is that structures obtained at coarser scales, should be a simplification of the structures at lower scales, and that no new structures should be generated when going from a fine to coarse scale.

Instead, the fine details should be "flattened" when moving to coarse scales. This idea was formalized by several authors in order to arrive at similar conclusions, by taking also in consideration some *scale-space axioms*. These axioms that take into account some desired properties of the scale-space representation as well as some practical issues and reduce the number of possible scale-space representations to a smaller class.

The scale-space axioms can be summarized then in the following properties (we only cite here the most important):

- *linearity,* meaning that we want no particular knowledge or model involved

  $$T_t(af(x) + bh(x)) = aT_t f(x) + bT_t h(x) \tag{5.37}$$

  with a, b constants

- *spatial shift invariance,* implies the convolution in 5.36, that is, we scan the aperture over any possible location of the signal (image).

- *existence of an infinitesimal generator A*

  $$\partial_t L(x;t) = (AL)(x;t) \tag{5.38}$$

- *non-creation of local extrema* (zero-crossings) in one dimension, meaning that no new information or spurious details should be generated when going from fine to coarse scales.

- *non-enhancement of local extrema* (zero-crossings) with increasing scale in multiple dimensions, meaning that fine details should not be enhanced at larger scales. For spatial maxima and minima respectively:

  $$\partial_t L(x;t) \leq 0 \tag{5.39}$$

  $$\partial_t L(x;t) \geq 0 \tag{5.40}$$

- *rotational symmetry / isotropy*, meaning that there is no preferred orientation. Mathematically, for some function h

  $$g(x;t) = h(\sum_i^N x_i^2; t) \tag{5.41}$$

- *scale invariance*, meaning that there is no preferred scale

- *semi-group structure,* meaning that the action of two operators is equivalent to the same action done by a single operator. That is a concatenation of two rescalings, should be a third rescaling in the form

  $$g(x;t_1) * g(x;t_2) = g(x;t_1 + t_2) \tag{5.42}$$

- *cascade smoothing property*, related to the previous

$$L(x;t_2) = g(x;t_2 - t_1) * L(x;t_1) \tag{5.43}$$

It can be demonstrated [11, 74, 178, 188] that the Gaussian kernel[6]

$$g(x;t) = \frac{1}{(2\pi t^2)^{N/2}} \, e^{-\Sigma^N x_i^2/(2t)} \tag{5.44}$$

is the only family of functions that meet all these requirements. From these, the "non-creation / non-enhacement of local extrema" are the crucial axioms which relate scale-space to smoothing, hence the selection of the Gaussian.

Thus, one can obtain a multi-scale representation $L(x;t)$ of the image $f(x)$ by convolving the original image with a Gaussian kernel $g(x;t)$ for different values of the scale parameter t.

Equivalently, this family of functions can be obtained as the solution of the diffusion equation

$$\partial_t L = \frac{1}{2}\nabla^2 L = \frac{1}{2}\sum_i^N \partial_{ii} L \tag{5.45}$$

with initial condition $L(x;0) = f(x) \; \forall x \in \mathbb{R}^N$ [91].

5.4.2 Scale-space and Derivatives

The scale-space representation provides a consistent way of calculating scaled, smoothed derivatives. Spatial derivatives of the smoothed intensity function L can be calculated at each level of scale, the so called *Gaussian derivatives*. For example, for 2D images, these partial derivatives would be

$$L_{x^i y^j}(x,y;t) = \left(\partial_{x^i y^j} L\right)(x,y;t) = \frac{\partial^{i+j} L}{\partial x^i \partial y^j} \tag{5.46}$$

We have already seen how some methods, such as the Marr-Hildreth operator, incorporated implicitly this concept of Gaussian derivatives as a method for scale selection. As Florack states [43] disregarding the intrinsic dinlensionality of an image or, in other words, the scaling degree of freedom, is the cause of the failure of naively applying differential methods in image analysis. Hence, equation 5.46 provides a way of appropiately computing scaled, smoothed derivatives that take into account the scale of the different features and that deals at the same time with noise.

Since the derivative operator commutes with the Gaussian operator we have that

$$L_{x^i y^j}(x,y;t) = \partial_{x^i y^j}(g * I) = g * \partial_{x^i y^j} I = \partial_{x^i y^j} g * I \tag{5.47}$$

This means that we can smooth the whole image and then compute its derivatives, or compute derivatives and then smooth the image or even generate a derivative of Gaussian kernel which is convolve with the image. Depending on the situation this

---

[6] Note the change of variable $t = \sigma^2$ with respect to the standard representation of the Gaussian function. This notation using the scale parameter t is typically used in the scale-space framework.

may lead to a reduced number of operations. If several derivatives must be computed, it is sometimes easy to convolve the image with the Gaussian first, and then compute the desired derivatives. However, if a single derivative must be calculated, or derivatives are calculated in a few points only, it may be better to use Gaussian derivative kernels.

When computing scaled derivatives, we must take into account that the whole image should be scaled for consistency using the Gaussian kernel, even if in some directions the derivative order is zero. Take for example the case of computing the second derivative in the x direction of a 2D image. We would precompute a 1D kernel for the second derivative of Gaussian at the desired scale t and then apply it in the x direction. However, this would be inconsistent with filtering the image with a Gaussian and calculating the second derivative in the x direction, since the y direction remains unscaled, and is not affected by the smoothing. Unless we explicitly want an anisotropic behaviour, we should also convolve the image in the y direction with a (zero-order) Gaussian kernel with the same aperture.

Another related property is that the derivative of a Gaussian is another Gaussian multiplied by a polynomial of the same order as the derivative. Calculating the derivatives analytically we obtain:

$$G_x = \frac{\partial G}{\delta x} = -\frac{x}{\sigma^2}G, \tag{5.48}$$

$$G_{xx} = \frac{\partial^2 G}{\partial x^2} = \frac{x^2 - \sigma^2}{\sigma^4}G, \tag{5.49}$$

$$G_{xxx} = \frac{\partial^3 G}{\partial x^3} = \frac{-x^3 + 3\sigma^2 x}{\sigma^6}G, \tag{5.50}$$

$$G_{4x} = \frac{\partial^4 G}{\partial x^4} = \frac{x^4 - 6\sigma^2 x^2 + 3\sigma^4}{\sigma^8}G, \tag{5.51}$$

$$G_{5x} = \frac{\partial^5 G}{\partial x^5} = \frac{-x^5 + 10\sigma^2 x^3 - 15\sigma^4 x}{\sigma^{10}}G. \tag{5.52}$$

Thus, the derivatives take the form:

$$G_{nx} = \frac{(-1)^n}{\sigma^{2n}}H_n(x,\sigma)\,G \tag{5.53}$$

where $H_n(x)$ are the classical *Hermite polynomials*[7] modified by the introduction of the sigma parameter (they are derived from the derivatives of $e^{-x/2\sigma^2}$ instead of $e^{-x/2^2}$) but the properties are the same. These polynomials form an *orthogonal polynomial sequence* which means that the Hermite polynomials are orthogonal in the interval $[-\infty,\infty]$ with respect to the weigth function $W(x) = e^{-x^2/2}$. Mathematically:

$$\forall\{m,n \in N\,|\,m \neq n\} \Rightarrow \int_{-\infty}^{\infty} H_m(x)H_n(x)\,e^{-x^2/2}dx = 0 \tag{5.54}$$

---

[7] We use the probabilistic definition of Hermite polynomials. The physics definition is slightly different in the coefficients and derived recursion and explicit formulas.

Hermite polynomials of any order can be obtained using recursive and explicit formulas. We can easily find a recursive formula for these modified polynomials.

$$\frac{\partial^n G}{\partial x^n} = \frac{\partial}{\partial x}\left(\frac{\partial^{n-1} G}{\partial x}\right) = \frac{\partial}{\partial x}\left(\frac{(-1)^{n-1}}{\sigma^{2(n-1)}} H_{n-1}(x,\sigma) G(x)\right)$$

$$= \frac{(-1)^{n-1}}{\sigma^{2(n-1)}}\left(\frac{\partial}{\partial x}\left(H_{n-1}(x,\sigma)\right) G(x) + H_{n-1}(x,\sigma)\frac{\partial G}{\partial x}\right)$$

It can be proven[7] that :

$$H_n^{'}(x) = \frac{\partial}{\partial x}\left(H_n(x,\sigma)\right) = nH_{n-1}(x,\sigma)$$

and hence we obtain

$$\frac{\partial^n G}{\partial x^n} = \frac{(-1)^{n-1}}{\sigma^{2(n-1)}}\Big((n-1)\, H_{n-2}(x,\sigma)G(x) - \frac{x}{\sigma^2} H_{n-1}(x,\sigma)G(x)\Big)$$

$$G_{nx} = \frac{\partial^n G}{\partial x^n} = \frac{(-1)^{n-1}}{\sigma^{2n}}\left((n-1)\,\sigma^2 H_{n-2}(x,\sigma) - xH_{n-1}(x,\sigma)\right) G(x) \tag{5.55}$$

and thus, comparing with equation 5.53 we obtain the recursive relationship:

$$H_n(x,\sigma) = (n-1)\,\sigma^2 H_{n-2}(x,\sigma) - xH_{n-1}(x,\sigma) \tag{5.56}$$

that allows to calculate polynomials up to any order easily.

5.4.3 Scale-space and Discrete Signals

In order to implement the scale-space representation for discrete signals, one must think of discretizing the Gaussian function and its derivatives. Derivatives are usually discretized using finite difference approximations as in eq. **??** to **??**. However, discretization of the Gaussian function is more complicated since it has theorically infinite support. A direct way is to compute a *sampled Gaussian kernel*, by sampling the Gaussian function at discrete intervals and truncating it at the ends to obtain a filter with finite impulse response. Suppose we obtain a sampled Gaussian kernel with $2M+1$ terms that is convolved with the input signal

$$L(x;t) = \sum_{n=-M}^{M} f(x-n)g(n;t) \tag{5.57}$$

where

$$g(n;t) = \frac{1}{\sqrt{2\pi t^2}} e^{-n^2/2t} \tag{5.58}$$

For an normalized Gaussian we can find a reasonable value for M on the basis of the unit integral, by adding the generated coefficients up to a desired error:

$$1 - \sum_{n=-M}^{M} g(n;t) < \varepsilon \tag{5.59}$$

However, the sampled Gaussian kernels may lead to implementation problems, in particular for small scales or when calculating higher order derivatives. Moreover, scale-space properties are not preserved.

Lindeberg [90][91] studied how the scale-space framework in the continuous domain should be discretized so the scale-space properties hold also in the discrete domain, developing a scale-space theory for discrete signals. This included the conception of a *discrete Gaussian kernel*, and a way of calculating *discrete Gaussian derivative approximations* with scale-space properties. The discretization, however, allowed for a continuous scale parameter t, so discrete kernels could be generated for virtually any scale if needed.

Starting from the a set of scale-space axioms, the scale-space representation of a discrete image is obtained as a convolution with a family of kernels T on the continuous scale parameter t. For a one-dimensional signal f:

$$L(x;t) = \sum_{n=-\infty}^{\infty} T(n;t) f(x-n) \tag{5.60}$$

Such kernels take the form

$$T(n;t) = e^{-\alpha t} I_n(\alpha t)$$

where I_n are the modified Bessel functions of integer order [1]

$$I_n(x) = \sum_{m=0}^{\infty} \frac{1}{m!\,\Gamma(m+n+1)} \left(\frac{x}{2}\right)^{2m+n} \tag{5.61}$$

and the scaling paramater α is usually set to 1. The kernel $T(n;t)$ is called the discrete analogue of the Gaussian kernel or simply the *discrete Gaussian kernel*. We can see that we can obtain a kernel for every desired value of the continuous scale parameter t. In practice, the kernel may be truncated on the basis of the unit integral error as with the sampled Gaussian kernel.

5.5 Ridge Detection

5.5.1 Ridge Definition

In section 5.2 we have already introduced the concepts of edges and ridges which are some of the most important low-level features in images. Others include blobs, corners or other types of interest points which are not so important for our purpose of detecting vascular line-like structures[8]. Now we will focus on ridges since they are closely related to line-like structures. Most of the times, line-like structures in medical images present intensity ridges with maxima in their medial axes or centerlines. If the centerlines don't present an intensity maximum at the centerlines, such as with MR Time-of-Flight (TOF) images [58], image processing methods, such as Gaussian filtering, could be applied in order to create an intensity ridge so as to create a maximum in the central part of the tubular section [10].

We have already commented that there is a close relationship between edges and ridges. From the analysis in section 5.3 we can now state that finding the maximum of gradient magnitude in the gradient direction, as in the method of Canny, is equivalent to finding the ridges of gradient magnitude, since this corresponds to the definition of a ridge. As Eberly states [40], the method of edge detection consists of following ridges of edgeness. Hence, though not exclusively, *both edge detection and line-like structure detection can be both approached as a problem of ridge detection using differential calculus*, applied to the gradient magnitude in the first case and to the source intensity image in the second case (probably with some pre-processing). Ridges are also related to the notion of a medial axis of an object [143] and thus may provide regional information complementary to edge information.

Ridges could be considered as a generalization of a function maximum. Intuitively if a maximum is the highest value of a function in a local neighborhood in all N space directions, assuming the function is locally smooth, a ridge is a *maximum in N-1 principal directions*. Conversely, the notion of *valley* can be considered as a generalization of the minimum of the function and we indistincly will talk of ridges when referring to both ridges and valleys[9]. Note that we the ridge is defined in terms of the principal directions or image (surface) curvatures, which corresponds to the eigenvectors of the local Hessian matrix.

We will now provide a formal definition of *height ridges* from Eberly[10] [40]. Let $f : \mathbb{R}^n \rightarrow \mathbb{R}$ be a $\mathscr{C}^2$smooth function. Let $\lambda_i \quad 1 \leq i \leq n$ be the eigenvalues of the Hessian matrix $\mathscr{H}$ of f with $\lambda_1 \leq \ldots \leq \lambda_n$. Let $v_i \quad 1 \leq i \leq n$ be the corresponding eigenvectors. Let V be a $(n-d) \times (n-d)$ matrix, whose columns are the $n-d$ first eigenvectors, corresponding to the negative eigenvalues. A point x_0 is a d-dimensional ridge point if

$$V^T \nabla f(x_0) = 0 \tag{5.62}$$

and

$$\lambda_{n-d}(x_0) < 0 \tag{5.63}$$

The first condition is a set of $n-d$ equations in the form $v_i \cdot \nabla f(x_0) = 0$ which means that the directional derivatives in the direction of those eigenvectors must be zero and, hence, the point is a local extremum in that direction.

---

[8] There are some exceptions to this. For example bifurcation points in vessel branches resemble more a blob-like structure than a line-like structure.

[9] Sometimes these are collectively referred to as *crease points*.

[10] The *height definition* of ridges is more useful for image analysis but some other definitions exist.

The second condition implies that there are $n-d$ negative eigenvalues (since these are ordered in the definition). These eigenvalues represent the curvature in the direction of the corresponding eigenvectors. Negative eigenvalues imply that the local extrema defined by the first condition are maxima, and not minima, of local curvature. This second condition is obtained from a more general condition that $V^T \mathscr{H} V$ must be negative definite and this corresponds to a diagonal matrix whose non-zero values are the eigenvectors. For finding local minima and valleys we just have to change the sign of the second condition.

When $d = 0$ we have a *local maximum* and $\mathscr{H}$ is a negative definite matrix. We are mostly interested in one-dimensional ridges, corresponding to curves, so in our case $d = 1$. This means that the function is a local maximum, except in one direction, of the set of linearly independent directions defined by the eigenvectors. In other words, a ridge point is a maximum in the subspace defined by the $n-d$ eigenvectors corresponding to negative eigenvalues.

If this concept is applied to the detection and extraction of vascular structures in medical images, this intensity ridge will aproximately correspond to the centerline or medial axis of the vessel[11], assuming that the image of the vessel presents such a peak along its path. Specially interesting is the case where a *medialness* filter is applied to the vascular image for vessel detection and/or enhancement. The response of such a filter is designed to be maximum in the medial axis of the vascular structures or very close to it and thus, extracting ridges of the medialness response will provide the centerlines of the filter.

5.6 Second-order Local Structure

The local structure of images can be intuitively described as the apparent shape taken by the local intensity distribution in the images. The Hessian Matrix, was introduced previously (see 5.3.3) as a tool that could be used to obtain different second-order differential features of images. In section 5.5, the eigenvalues and eigenvectors of the Hessian matrix where used to detect ridge points. Now, we will see how the eigenvalue analysis can be used to distinguish between different types of local structure, according to the sign and value of the eigenvalues or principal curvatures.

5.6.1 Eigenvalue Analysis of the Hessian Matrix

The eigenvalues and eigenvectors of the Hessian matrix of second derivatives can be used as local shape descriptors describing the local structure of images. The eigenvalues correspond to the principal image curvatures and the eigenvectors correspond to the direction of those curvatures. These principal curvatures correspond to the second-order derivatives of the image in the directions of the reference system described by the eigenvectors, which are called the principal directions. Thus the eigenvalue analysis of the Hessian matrix provides two types of information at every point of the image:

---

[11] We say approximately because the medial axis is defined in terms of the real object boundaries, which are usually unknown, and not in terms of the intensity peaks in the sections. However, in practice, in most vascular images, the loci of medial axis and the ridges are close to each other.

2D		3D			local shape
λ_1	λ_2	λ_1	λ_2	λ_3	
N	N	N	N	N	noisy (blob-like)
		L	L	H-	plate-like (bright)
		L	L	H+	plate-like (dark)
L	H-	L	H-	H-	tubular (bright)
L	H+	L	H+	H+	tubular (dark)
H-	H-	H-	H-	H-	blob-like (bright)
H+	H+	H+	H+	H+	blob-like (dark)

Table 5.1: Basic local structure shapes in terms of eigenvalues of the Hessian matrix according to [47]. H=high, L=low, N=noisy, usually small, +/- indicate sign.

- It describes the local distribution of intensities in the image in terms of three curvatures corresponding to three main orthogonal directions. These are the eigenvalues.

- It describes the reference system that best fits the local structure of the image, in which the principal curvatures are measured. In other words, it describes the orientation of the local shape. This local reference system, defined by the eigenvectors, constitute the principal directions of curvature. Somehow, obtaining the eigenvectors, we find the orthogonal directions that are more suitable for describing the local shape.

As stated previously (see Section 5.4.1), discrete derivative calculations always imply obtaining scaled calculations and therefore the corresponding Hessian matrix and eigenvalue analysis must be performed at each point at the appropriate scale, which depends on the size of the structures of interest to be analyzed in the image.

Frangi *et al.* [47] classified the local structure of a 3D image in several basic shapes, according to the values of the eigenvalues (in magnitude and sign) of the local Hessian matrix, ordered by magnitude ($|\lambda_1| < |\lambda_2| < |\lambda_3|$) as follows:

Danielsson and Lin [34] extended this analysis to other types of shapes, but for our purpose, it is enough to distinguish between these three main types of local shape in 3D:

- *Tubular structures*: also called line-like structures, they present low curvature in one of the principal directions and high curvature in the other two directions. The low curvature corresponds to the axial direction of the local tube-like shape, since the intensity hardly varies in this directions. In the other directions, the curvature is high, since they correspond to the radial directions of the tube, where the intensity varies rapidly from the center to the external part of a tube-like shape. In medical images, they may corresponds to local shapes of vessels or other line-like structures.

- *Plate-like structures*: also called shee-like structures or flat structures, their intensity varies wildly in a single direction and hardly varies in the other two directions. Here, the structure is locally flat, as if forming a plane. This is typical of some organs appearing in medical images, that are not vessels or tubes.

- *Blob-like structures*: they represent symmetrical spherical-like structures, with no preferred direction, where the intensity varies wildly from its center. Noisy structures are also tipically blob-like, since they eigenvalues are usually of similar magnitude, with no preferred asymmetrical shape.

As we can see, by measuring the eigenvalues at points of interest of the images, we can obtain a local shape description at those points and distinguish between tubular, plate-like and blob-like structures at a local level. This is the basis of some of eigenvalue filters commonly used in vessel detection, such as those from Sato et al. [140], Frangi et al. [47]. These methods try to discriminate points that are locally tubular from the rest of points in the images by building a *vesselness* function, based on these eigenvalues, that is maximum for tubular structures and yields low values for other types of structures.

5.6.2 The Structure Tensor

Chapter 6

Vascular Detection

In this chapter we will present the main algorithms used to detect tubular structures in images in general. As a particular case of tubular structures, the focus will be oriented towards our objective of detecting vascular structures in 3D medical images. However, most of the methods can be applied without major modifications for the detection of other similar structures such as bronchii, pulmonary trees, liver ducts, nerves, etc.

6.1 Introduction

Curvilinear structures, also called line or tubular structures[1], are of particular interest for medical image analysis where they appear in different forms, both in anatomical structures, such as blood vessels, bronchi, nerves, biliary ducts, etc. as well as in artificial structures, such as catheters, electrodes, stents, etc. that may be of clinical interest. Since we are interested in the detection of vascular structures, it is of crucial interest defining methods that allow us to detect these structures and distinguish them from other types of structures and tissues, artifacts or background noise.

The detection of vascular structures in medical imaging is particularly challenging. We

- Complexity: vascular structures may be highly ramificated structures creating complex networks of connected branches. In general, these branches are curved and sometimes very tortuous.

- Multi-scale structures: a high variation in diameters may be observed from the root to the visible endpoints of a vascular network which makes necessary to define detectors that operate a multiple scales in order to detect vessels of all sizes expected. Moreover, different sizes may require different approaches due to considerations such as accuracy or computation time. Some methods are best

---

[1] We will use indistinctly both terms for referring to elongated structures of small width represented in medical images both in 2D and 3D. The term line structure or line filtering is more used in the literature in the context of detection and the term tubular structure is more used in volumetric image analysis.

suited for the smallest scales, even close to the inner scale of the data. Others are specific for the largest of vessels such as the aorta.

- Presence of bifurcations or anomalies such as stenoses and aneurysms: even if the main local shape of vessels resemble a linear structures, along the paths of a vessel network some structures may be found whose local shape may differ to some extent from that of a linear structure. Examples of these are branching points or vascular accidents such as stenoses or aneurysms.

- Volume of information: the volumetric nature of 3D angiographic images, which may consist of hundreds of slices in the case of CTA, implies a very large search space in which vascular structures have to be detected, even if the structures themselves do not occupy a high percentage of this volume.

- Non-uniformity of contrast: many angiographic modalities make use of a contrast agent injected in the blood stream in order to enhance the visualization of vascular structures. Failure to adequately inject the contrast agent at the time of the scan may result in non-uniformities of the contrast agent distribution and hence of the image intensities along the vessel paths. Even if the contrast was correctly injected, distances are sometimes too large for the contrast bolus to reach all the vascular structures of interest.

A line or tubular structure has the basic geometrical property that its length exceeds by far its diameter and thus, it can be considered as a 1D manifold in the embedding space, which is typically 2D or 3D. At every point of the line structure (with the exception of the end and bifurcation or branching points) we can associate a direction, corresponding to direction of the centerline or central axis of the tubular structure, and a section line (2D) or plane (3D), that is normal to the axis direction. The geometry of the section can be considered almost circular for small vessels, and tends to differ from the ideal circle when the vessels are larger.

The typical intensity profile of a line structure shows an elevation across the longitudinal direction. The shape of this elevation may vary but typically can be modeled as a Gaussian, boxcar (also known as rectangular or bar-like) or roof cross-section, both in their 2D and 3D modalities. On the other hand, the intensity profile along the tube direction varies only slowly, if we assume that there is no blockage that prevents the diffusion of the contrast media. These hyperintensity properties are exploited by many detection methods.

The main goal of the process is to detect curvilinear structures in medical images of, within some limits, arbitrary shape, size (in diameter and length) and section profile (bar, roof, Gaussian-like...). Furthermore, if possible, we would like to obtain during the detection process[2]at least three types of information:

- *Geometric Information*: such as an estimation of the diameters, lengths or curvatures.

---

[2] We refer here only to basic low-level information, and not higher level information that may be infered from this, such as the presence of an aneurysm or stenoses.

- *Topological Information*: such as the number of total branches and the number of bifurcations at a branch point.
- *Luminance Information*: it may be used for posterior image analysis processes or as low-level information for the detection of blockages, time and extension of contrast arrival etc.

The same requirements of detection and localization expressed in the previous chapter are also appliable here: we would like to detect if possible all vessels, discard noisy branches or other spurious structures and locate the vessel position with the maximum precision. As we have seen, these requirements are conflicting.

The accuracy of the analysis of vascular structures is determined greatly by the accuracy of the vessel detection or enhancement technique used. If the method is not accurate enough or presents limitations, for example at branching points or in the presence of some features such as stenoses and aneurysms, it may result in incorrect vessel extraction results . If the algorithm fails it may require user interaction but depending on the application this process can be very cumbersome and, if the target vascular network is very dense and its vessels small or tortuos practically impossible. In this sense, manual vascular extraction is general, a more cumbersome process than manual segmentation of organs, unless we just need to mark a few points on the centerline of a vessel of medium or large size.

Many vessel or tube detection methods are generally based on the calculation, either locally or globally, of a vascular measure or feature which is usually known as '*vesselness*'. By *vesselness* measure, we refer to a function that assigns to each voxel a value, usually a floating point scalar, that is proportional to the likelihood that the voxel belongs to a blood vessel in the original image . If the vesselness measure is specially designed to detect the vessel centerlines, we call it *medialness* measure as it refers to the medial line or medial axis of the curvilinear structure .

6.2 Differential Features

6.2.1 Koller

6.2.2 Features based on Hessian Matrix Eigenvalues

6.2.2.1 Definitions

Applying non-linear combinations of finite difference operatorsin a set of orientations is computationally very expensive, specially when we are dealing with 3D detection of line-like (tube-like) structures. In order to overcome this problem, the eigenvalue analysis of the Hessian matrix was first introduced in [76]. They extended their non-linear line structure detector to 3D by finding the optimal orientation in which to apply their non-linear filtering scheme.

The Hessian matrix is an important tool for vascular detection based on differential operators. For a three dimensional image $I : \mathbb{R}^3 \to \mathbb{R}$ the Hessian matrix $\mathscr{H}$ is defined as the matrix of (scaled) second order derivatives of the image

$$\mathscr{H}(x,\sigma) = \begin{bmatrix} I_{xx} & I_{xy} & I_{xz} \\ I_{xy} & I_{yy} & I_{yz} \\ I_{xz} & I_{yz} & I_{zz} \end{bmatrix} \tag{6.1}$$

which describes the second order local image structure, that is, local image curvatures. The parameter σ is the scaling parameter and corresponds to the Gaussian smoothing, assuming that the derivatives are calculated in scale-space .

The three ordered eigenvalues λ_i, $\lambda_3 \leq \lambda_2 \leq \lambda_1$ of this Hessian matrix describe the principal image curvatures which best describe the local image second-order variations. The corresponding eigenvectors v_i describe the directions in which the principal curvatures occur. When the point x is close to the centerline or medial axis of a vessel and an appropriate scaling parameter is chosen, the local structure of the image is that of a bright (or dark) tubular structure, and the eigenvalues exhibit the following properties :

$$\lambda_2 \approx \lambda_3 \tag{6.2}$$

$$\lambda_2, \lambda_3 \ll 0 \tag{6.3}$$

$$\lambda_1 \approx 0 \tag{6.4}$$

This assumes that the local curvature of the vessel is not too high and that the section shows radial symmetry. If these conditions are not met, the eigenvalues differ from this ideal situation.

The eigenvector v_1 corresponds to the direction of the local vessel/tube axis where the curvature barely varies, hence λ_1 is almost zero. The other two principal curvatures, λ_2 and λ_3 occur in directions that go from the center of the tube to the external part of the vessel, where the curvature varies highly. Hence these eigenvalues are negative and of high absolute value (positive for a dark vessel in a bright background). The associated eigenvectors v_2, v_3 are estimators of the local vessel section plane, since they are aligned with the directions of maximum curvature. Thus, they constitute a *section estimator*.

Several detectors or filters may be designed using these second-order local structure properties. One approach is to take non-linear combination of the eigenvalues, trying to distinguish tube-like local structures from other shapes, such as plate-like or blob-like structures, which exhibit different relationships between the eigenvalues. For example, for plate-like structures two eigenvalues are similar to zero, and blob-like structures show three eigenvalues of the same relatively large value .The filters are designed to enhance even the smallest vessels and remove the effects of non-linear structures and noise.

Sato *et al.* [140] propose a filter based on a non-linear combination of eigenvalues, ordered as $\lambda_3 \leq \lambda_2 \leq \lambda_1$, which consists of two terms:

$$\lambda_{23} = \begin{cases} |\lambda_3| \left(\frac{\lambda_2}{\lambda_3}\right)^{\gamma_{23}} & \lambda_2 < 0 \quad \text{and} \quad \lambda_3 < 0 \\ 0 & \text{otherwise} \end{cases} \tag{6.5}$$

$$\lambda_{12} = \begin{cases} \left(1 + \frac{\lambda_1}{|\lambda_2|}\right)^{\gamma_{12}} & \lambda_1 \leq 0 \\ \left(1 - \alpha \frac{\lambda_1}{|\lambda_2|}\right) & \frac{|\lambda_2|}{\alpha} > \lambda_1 > 0 \\ 0 & \text{otherwise} \end{cases} \tag{6.6}$$

The term λ_{23} corresponds to the conditions 6.2and 6.3 enhancing structures with two large negative eigenvalues of similar magnitude. This distinguishes line-like from sheet-like structures, since for the later $\lambda_3 \ll 0$ but $\lambda_2 \approx 0$. The parameter γ_{23} controls the cross-section anisotropy. Note that due to the ordering of eigenvalues $\lambda_2/\lambda_3 < 0$. If strong sheet-like structures are expected $\gamma_{23} = 1$ is a good choice. More assymetrical values are more tolerated when γ_{23} is closer to zero, for example γ_{23}=0.5 allows some degree of anisotropy. $\gamma_{23} = 0$ is a limit case where sheet-like structures would also be enhanced.

The term λ_{12} is introduced in order to accomplish the condition 6.4 and the condition $\lambda_2 \ll 0$ in 6.3. This distinguishes line-like from blob-like structures with the parameter γ_{12}.

Combining both conditions, the following single-scale filter response is obtained:

$$\lambda_{123} = \begin{cases} |\lambda_3| \left(\frac{\lambda_2}{\lambda_3}\right)^{\gamma_{23}} \left(1 + \frac{\lambda_1}{|\lambda_2|}\right)^{\gamma_{12}} & \lambda_1 \leq 0,\ \lambda_2 < 0,\ \lambda_3 < 0 \\ |\lambda_3| \left(\frac{\lambda_2}{\lambda_3}\right)^{\gamma_{23}} \left(1 - \alpha \frac{\lambda_1}{|\lambda_2|}\right)^{\gamma_{12}} & \frac{|\lambda_2|}{\alpha} > \lambda_1 > 0,\ \lambda_2 < 0,\ \lambda_3 < 0,\ 0 \leq \alpha \leq 1 \\ 0 & \text{otherwise} \end{cases} \tag{6.7}$$

Experiments performed on ideal curved tubes show that this filter gives high response at lower slopes of the profiles in the opposite side of the center of curvature with the curvature κ increasing. The introduction of the α provides an assymetrical response depending on the sign of λ_1 which helps to mitigate this effect. However, selecting $\alpha = 0$ results in some lines broken, so $\alpha = 0.25$ is shown to be a good compromise. On the other hand, in experiments with branch models, the authors show that, at bifurcation or branch points, there is a trade-off between obtaining spurious branches in the response (reduce γ_{12} and increase α) and fragmentation of the line, due to a different eigenvalue becoming dominant at the edge of the line. Moreover, spurious holes may appear on the branch point.

Finally, single-scale filter responses are combined in order to obtain a multi-scale filter response. This is described in .

Almost simultaneously, Frangi et al. [47] proposed a similar filter based on a nonlinear combination of eigenvalues. They ordered the eigenvalues according to their magnitude $|\lambda_3| \leq |\lambda_2| \leq |\lambda_1|$and interpreted geometrically as describing a second order ellipsoid. They proposed the following single-scale vesselness measure:

$$\mathcal{V}_0(s) = \begin{cases} 0 & \text{if}\, \lambda_2 > 0 \,\text{or}\, \lambda_3 > 0 \\ \left(1 - \exp\left(-\frac{R_A^2}{2\alpha^2}\right)\right) \exp\left(-\frac{R_B^2}{2\beta^2}\right) \left(1 - \exp\left(-\frac{S^2}{2c^2}\right)\right) & \text{otherwise} \end{cases} \tag{6.8}$$

with

$$R_A = \frac{|\lambda_2|}{|\lambda_3|} \quad R_B = \frac{|\lambda_1|}{\sqrt{|\lambda_2 \lambda_3|}} \quad S = \|H\|_F = \sqrt{\sum_{j \leq D} \lambda_j^2} \tag{6.9}$$

Here R_A is interpreted as the largest cross-section area of the ellipsoid (normal to v_1) and similarly to λ_{23}in the approach of Sato *el al.* distinguishes between tube-like and sheet-like structures. On the other hand R_B represents the volume divided by the largest cross-section area of the ellipsoid and accounts for the deviation from a blob-like structure as in λ_{12} in the approach of Sato *et al.* Moreover, the Frobenius norm S of the Hessian matrix is incorporated, in order to distinguish real tubular structures from background noise. The parametersα, β, c control the sensitivity of each term. The authors use $\alpha = \beta = 0.5$ in their experiments, whereas c is used as a threshold that depends on the grey-scale range of the image. A multi-scale line measure is obtained by computing the maximum value over a range of discrete user-selected scales.

Another similar vesselness feature is the one proposed by Erdt *et al.* [41]. They devised a filter based on a linear combinatoin of the Hessian matrix components in the form:

$$\mathscr{V}(x) = \sum_{i=1}^{3} \sum_{j=1}^{i} \alpha_{ij} h_{ij} \tag{6.10}$$

By optimization via Lagrange multipliers of the convolution of a filter in this form, with an ideal model with Gaussian cross-section they obtain that the best response is obtained for a filter with the form:

$$\mathscr{V}(x) = c \left(\frac{2}{3} h_{xx} - h_{yy} - h_{zz} \right) \tag{6.11}$$

where

$$c = \sqrt{\frac{3\sigma_0}{5\pi^{3/2}}} \tag{6.12}$$

and $\sigma_0$is the standard deviation of the Gaussian section of the tube. Generalizing to an arbitrary vascular direction by using the Hessian eigenvalues they obtain:

$$\mathscr{V}(x) = c\kappa \left(\frac{2}{3} \lambda_1 - \lambda_2 - \lambda_3 \right) \tag{6.13}$$

with $\lambda_1 \geq \lambda_2 \geq \lambda_3$. The factor κ is incorporated in order to distinguish tube-like from sheet-like structures by penalizing anisotropy in the smallest (most negative) eigenvalues:

$$\kappa = 1 - \frac{||\lambda_2| - |\lambda_3||}{|\lambda_2| + |\lambda_3|} \quad \in [0, 1] \tag{6.14}$$

This factor takes a maximum value of 1 when $\lambda_2 = \lambda_3$. However, note that this factor also would give a value of 1 for $\lambda_2 = -\lambda_3$ assuming that $\lambda_1 > \lambda_2$ and hence we propose the modified factor:

$$\kappa_{mod} = 1 - \frac{|\lambda_2 - \lambda_3|}{|\lambda_2| + |\lambda_3|} \quad \in [0,1] \tag{6.15}$$

Note that this method is parameterless, as compared with the previous one that had three parameters each in order to control each aspect of the vessel enhancement.

6.2.2.2 Scale Considerations

The scale selection mechanism for the methods described above consists of choosing the maxima over scales of a combination of the discrete, second-order, Gaussian derivatives used in the Hessian matrix [96], where the scale is changed by varying the aperture of the Gaussian in the derivative calculations.

One idea would be to test the methods separatedly against ideal tubes in order to see how they perform with different tube sizes and detection scales, but this is a very cumbersome analysis. However, scale selection criteria may be established on the basis of the interpretation of the eigenvalues of the Hessian matrix for the detection of tubular structures corresponding to conditions 6.2 to 6.4. These eigenvalues represent the principal curvatures which are second derivatives oriented in the local spatial orientation that best describes the shape. If we restrict our analysis to ideal circular tubes with radial symmetry, these curvatures will be oriented with the tube axis and the conditions described will hold almost exactly. Since in this case $\lambda_1 \simeq 0$ and $\lambda_2 \simeq \lambda_3 \ll 0$ it is sufficient to analyze the behaviour of λ_3 to obtain criteria for scale selection. Moreover, if the ideal tube images are aligned with the z-axis, this eigenvalue will coincide with the second derivatives on the x or y-axis, which does not even require the calculation of the Hessian matrix for this analysis. However, in the following experiments we will calculate the eigenvalus in order to test the described ideal conditions for the eigenvalues.

Following this idea, we performed experiments on radially symmetric ideal cylinders of different sizes whose axis is aligned with the image z-axis . We created two sets of cylinders, one set with Gaussian cross-sections and another set with flat sections convolved with a Gaussian with a small value of aperture (we used $\sigma = 1.0$). The radii were chosen as:

$$R_i = s^i R_0 \quad i = 1 \ldots N_R \tag{6.16}$$

where $R_0$is the initial radius and s the scale factor and N_r is the number of cylinders. We chose $R_0 = 0.75$, $s = 1.225$ and $N_R = 10$.

For each cylinder, we calculated the Hessian matrix and corresponding eigenvalues in a discrete set of scales and observed the behaviour of the most negative eigenvalue λ_3. The set of discrete scales for the Gaussian derivatives where chosen as:

$$\sigma_{hj} = s_h^j \sigma_{h0} \quad j = 1 \ldots N_h \tag{6.17}$$

where we used $\sigma_{h0} = 0.5$, $s_h = 1.025$, $N_h = 110$ for both types of cross-sections.

As expected, we observed a perfect match in the values of λ_2 and λ_3 whereas λ_1 was zero or practically zero (in the order of between -1.0×10^{-12} and -1.0×10^{-16}). Figure 6.1 (left) shows the plots of the values obtained for λ_3 for different scales for both tube profiles. A visible minimum is found for all tube sizes, where the peak tends to flatten for larger scales and is more prominent for small scales, specially for the tubes with Gaussian section. In these, the minimum value is quite similar and tend to stabilize for larger scales, whereas in tubes with flat convolved section the minimum is smaller (in absolute value) for small scales. Figure 6.1 (right) shows the relationship between the maxima accross scales for each tube size with respect to the tube size itself. An almost linear relationship is found between the scale and the radius ($R^2 = 0.998$ and $R^2 = 0.995$ for Gaussian and flat convolved tubes respectively). For tubes with Gaussian section this relationship is:

$$\sigma_{rmax} = 0.973R + 0.117 \tag{6.18}$$

And for tubes with flat convolved section:

$$\sigma_{rmax} = 0.662R + 0.578 \tag{6.19}$$

Compared to the ideal line $\sigma_h = R$ we can observe that for Gaussian tubes the best scale is slightly over the radius value. For flat convolved tubes, however, the scale should be smaller than the radius for small scales and larger for large scales. From the formulas of the straight lines, the cross-point is found at $\sigma_h = R = 1.71$. For practical applications and in the context of vascular analysis, this may help us to select a correct range of scales knowing the possible range of vessel sizes present in our images.

6.3 Integral Features

6.3.1 Offset Medialness

6.3.1.1 Definition

The *offset medialness* measure is an integral measure defined in the section plane as:

$$\mathscr{M}_\sigma^+(x,r) = \frac{1}{2\pi}\int_{\alpha=0}^{2\pi} -\nabla I_\sigma\left(x + r v_{\alpha_i}\right) \cdot v_{\alpha_i} d\alpha \tag{6.20}$$

where v_α is a rotating vector, or phasor given by

$$v_\alpha = v_1 \cos\alpha + v_2 \sin\alpha \tag{6.21}$$

Equation 6.20 is the integral of the projection of the negate of the gradient vector in the radial direction of a circle of radius r around the considered point. This circle is located in the estimated section plane formed by eigenvectors v_1 and v_2. In fact, any other section estimator could be used. As we can see, by tuning r we have an estimate of the local vessel radius.

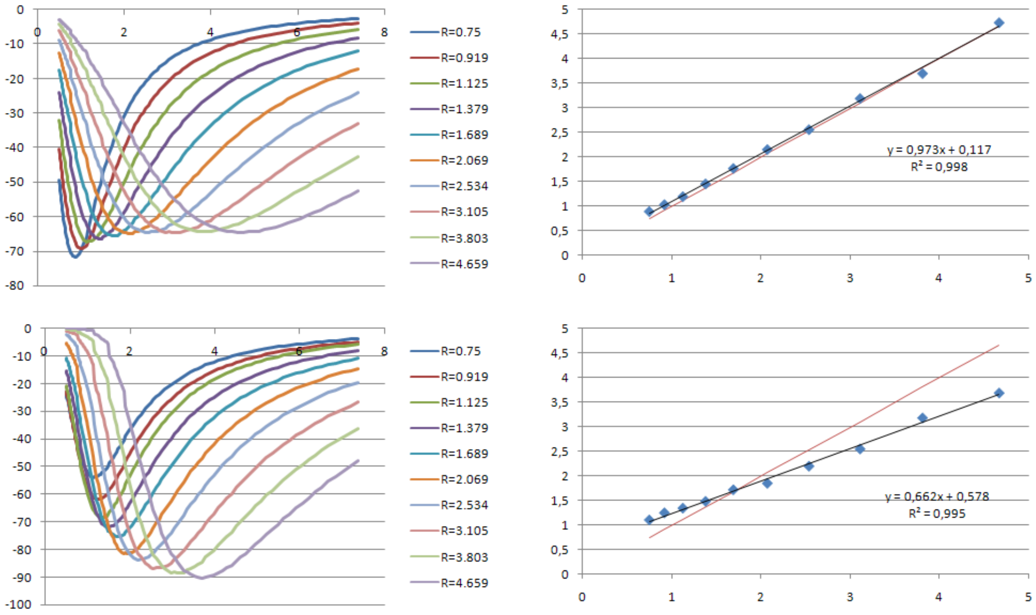

Figure 6.1: Values of the most negative eigenvalue λ_3 obtained in the center of the tube for different tube sizes for different Hessian scales σ_h and for tubes with Gaussian (top row) and flat convolved (bottom row) section profile. Left column shows all values obtained varying σ_h. Right column shows the relationship between the tube radius (x-axis) and radius scale for the maximum values obtained for each radius. Here, the black line shows the obtained linear trend line and the red line represents the line $\sigma_h = R$.

The corresponding discrete implementation samples the circle points in which the gradient is calculated and corresponds to:

$$\mathscr{M}_{\sigma}^{+}(x,r) = \frac{1}{N}\sum_{i=0}^{N-1} -\nabla I_{\sigma}\left(x + r v_{\alpha_i}\right)\cdot v_{\alpha_i}, \qquad \alpha = 2\pi i/N \tag{6.22}$$

Pock *et al.* use the gradient magnitude instead of the gradient projection. We believe that is better to use the projection in the radial direction determined by v_{α} rather than the gradient magnitude, since spurious or adjacent structures may have a greater undesired contribution in terms of gradient magnitude, which may lead to large values of medialness where it should not. On the other hand, as an improvement, they introduce the following symmetry coefficient:

$$\omega(b_i) = \exp\left[-\frac{1}{2\xi^2}\left(1 - \frac{b_i}{R_{\sigma}^{+}}\right)^2\right], \quad \xi \in (0,1] \subset \mathbb{R} \tag{6.23}$$

where

$$b_i = -\nabla I_{\sigma}\left(x + r v_{\alpha_i}\right)\cdot v_{\alpha_i} \tag{6.24}$$

is the contribution of each radial point, also called *boundariness* . Here, we have used the boundariness measure of Krissian *et al.* but other boundariness measures could be used. The resulting adaptive medialness function is:

$$\mathscr{M}_{\sigma}(x,r) = \frac{1}{N}\sum_{i=0}^{N-1} \omega(b_i)\, b_i \tag{6.25}$$

The symmetry coefficient ξ penalizes asymmetry in the radial distribution of gradient values. When $\xi = 1$ no penalization is performed. The lower the value the more the asymmetry is penalized. There is a trade-off between the asymmetry of the section and the detection rate. If very asymmetrical sections are expected, the value should be one or close to one. Otherwise, $\xi = 0.5$ gives good results in most situations. We also divide the resulting medialness by one plus the gradient magnitude at the center point, since it should be low in a centerline point. This last step was also used by Pock *et al.* but they substracted this value instead of dividing it.

The original implementation of Krissian *et al.* makes the radius r dependent on the scale in the form $r = \tau\sigma$. In practice, it is not necessary to change r linearly with the scale. Additionally, with large diameters, we would need large scales with increased computational costs. A better approach is to choose a single or a few scales valid enough for the range of diameters to be considered and then adjust r to obtain a maximum response.

6.3.1.2 Scale Selection

The calculation of the Offset Medialness measure requires the definition of at least three scales: the scale for the Hessian derivatives: the radius of the section circle and the scale of the gradients calculated at the circle locations.

- The *Hessian scale* σ_h corresponds to the scale for the second order Gaussian derivatives of the Hessian matrix. It is used to estimate the section normal as the eigenvector corresponding to the lowest eigenvalue (close to zero) of the Hessian which, for points on the centerline, coincides with the tube axis. In Chapter we analyze this estimation in detail in the contect of vascular extraction using centerline tracking. The ideal scale for the Hessian should be proportional to the radius tube and usually a bit larger.
- The *radius scale* σ_r is the most critical scale and should be approximately equal to the tube radius. Failing to choose the appropiate radius scale will result in a poor estimation or even missing the tube at all.
- The *gradient scale* σ_g should be chosen according to the expected tube boundary width and thus should be smaller than σ_r. In general, for small and medium tube sizes, a small scale should be chosen, close to the inner scale of the image (resolution). However, for larger scales, increasing the gradient scale could improve the detection rate at the cost of a worse localization. This is specially important in multi-scale approaches when a small set of scales is used for detection.

In order to establish some criteria for scale selection, we performed some experiments on the same set of ideal cylinders described in 6.2.2.2. Testing the influence of the three types of scales in all tube sizes involves a very large parameter space in which maxima of medialness have to be found. However, as expected, we noticed that results were independent of the Hessian scale value and hence it will remain fixed in the following. The reason is that this scale is only used for the estimation of the section in which offset gradient values are calculated and, for ideal noiseless tubes, the result is always the tube axis but for very small or very large scales.

The first set of experiments used a fixed Hessian and gradient scale values of $\sigma_h = 2.25$ and $\sigma_g = 1.0$ with σ_r varying according to

$$\sigma_{rj} = s_r^j \sigma_{r0} \quad j = 1 \dots N_r \tag{6.26}$$

where we used $\sigma_{r0} = 0.5$, $s_r = 1.005$, $N_r = 550$. The idea is to set a criteria for the selection of the radius scale using fixed small gradient scale values.

Figure 6.2 (left) shows the medialness values obtained for this experiment for both tubes with Gaussian and flat convolved section profile. In all cases, there is a visible maximum for each tube size. This maximum is more prominent for small scales in the case of Gaussian tubes, but the plots tend to flatten for higher scales. The absolute values also reach a maximum for medium scales and tend to decrease. For flat convolved tubes, the prominence of the peak is similar in all scales and the maximum seems to increase and stabilize for larger scales, obtaining in general a better localization. This is expected, since, in the Gaussian tubes, the tube boundaries are more diffuse. Moreover, an increase in the signal seems to reflect that there is less uncertainty in the radius location when the scale increases, as long as the correct scales are chosen (a wrong scale selection may imply a lower detection rate). With small scales, the small smoothing of the boundary may be significant enough as compared to the tube radius to induce some uncertainty. Moreover, the peak seems to flatten with respect to the Gaussian tubes.

6.2 (right) shows the values of the gradient scale that resulted in maxima of medialness with respect to the tube size of that maxima. As we can see in the linear trend lines depicted in black, theres is almost a perfect linear relationship ($R^2 = 0.993$ and $R^2 = 0.988$ for Gaussian and flat convolved tubes respectively) between the gradient scale and the tube radius. For Gaussian tubes the relationship is approximately:

$$\sigma_{rmax} = 0.926R + 0.471 \tag{6.27}$$

And for flat convolved tubes:

$$\sigma_{rmax} = 0.946R + 0.506 \tag{6.28}$$

We can see that the best values are obtained aproximately for scales about 92-95% the tube radius plus 0.5 mm, which is a bit more than the expected 100% of the tube radius. From the plots we can also see that, even if the right scale is not chosen, there is still some margin for radius scale selection that provides reasonable medialness values. Tables 6.1 and 6.2 represent the range of radius scales between which the response decays less than 10% and 25%, for Gaussian and flat convolved tubes respectively.

Table 6.3 shows corresponding averages and minimum values. We can see that there is some margin for error in the scale selection that still gives reasonable responses. The margin is narrower for flat convolved tubes but these may represent better real vessels, specially for larger widths. Still, average errors of 37 and 45% are obtained. Note that these results are approximate, for the discrete set of tube sizes and scales used in our experiments. However, the radius scale discretization had enough resolution to give significant results for the chosen tube sizes. Similar analyses can be performed to set a criteria for discrete scale selection for a given application similar to that in [141].

Keeping the gradient scale fixed as in the previous experiment does not necessarily yield the best results. In order to test the influence of both, the radius and gradient scales, we computed the offset medialness value at the center of each cylinder i for a set of discrete scales, chosen as:

$$\begin{array}{ll} \sigma_{rj} = s_r^j \sigma_{r0} & j = 1 \ldots N_r \\ \sigma_{gj} = s_g^i \sigma_{g0} & j = 1 \ldots N_g \end{array} \tag{6.29}$$

A first set of experiments combining these scales used $\sigma_h = 2.25$, $\sigma_{r0} = 0.8R_i$, $s_r = 1.5$, $N_r = 11$, $\sigma_{g0} = 0.5$, $s_g = 1.25$, $N_g = 30$. Note that here, for every tube size, the first radius scale σ_{r0} depends on the tube size. For the gradients scale, the initial scale is fixed.

Figure 6.3 shows the offset medialness values obtained in the center of the Gaussian and flat convolved tubes depending on the gradient scale values σ_g. Since the Hessian scale is not relevant, we fixed $\sigma_h = 2.25$. For each tube radius, we selected the radius

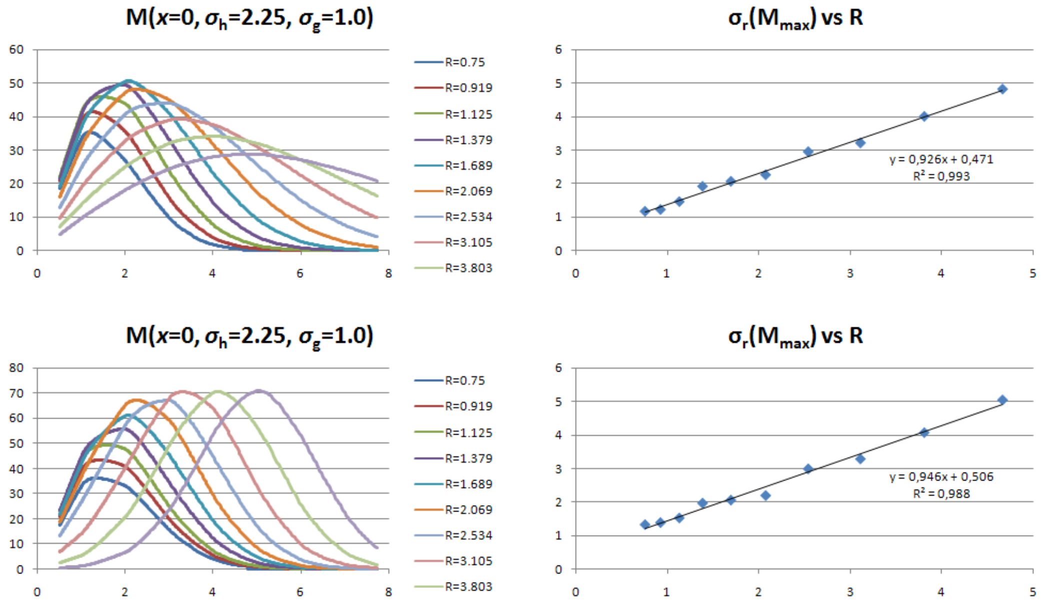

Figure 6.2: Offset medialness values obtained in the center of the tube for different tube sizes with $\sigma_h = 2.25$ and $\sigma_g = 1.0$ and varying σ_r (x-axis), for tubes with Gaussian (top row) and flat convolved (bottom row) section profile. Left column shows all values obtained varying σ_r. Right column shows the relationship between the tube radius (x-axis) and radius scale for the maximum values obtained for each radius.

$\mathscr{M}_{max}$		$\triangle\mathscr{M} = 10\%$				$\triangle\mathscr{M} = 25\%$			
R	σ_r	σ_{rmin}	σ_{rmax}	$\Delta\sigma_{rmin}$	$\Delta\sigma_{rmax}$	σ_{rmin}	σ_{rmax}	$\Delta\sigma_{rmin}$	$\Delta\sigma_{rmax}$
0.75	1.1791	0.9373	1.6063	20.50%	36.24%	0.7564	2.0105	35.85%	70.52%
0.919	1.2332	0.9610	1.8379	22.07%	49.03%	0.7794	2.2436	36.80%	81.94%
1.125	1.4684	1.0001	2.1667	31.89%	47.55%	0.8152	2.5038	44.49%	70.52%
1.379	1.9222	1.1500	2.3939	40.17%	24.54%	0.9007	2.7803	53.14%	44.64%
1.689	2.0716	1.4684	2.6451	29.12%	27.68%	1.0305	3.1653	50.25%	52.80%
2.069	2.2661	1.6801	3.1495	25.86%	38.98%	1.2149	3.6945	46.39%	63.03%
2.534	2.9518	1.9127	3.6945	35.20%	25.16%	1.4538	4.3555	50.75%	47.55%
3.105	3.2130	2.2889	4.3992	28.76%	36.92%	1.7311	5.1862	46.12%	61.41%
3.803	4.0015	2.7803	5.2907	30.52%	32.22%	2.0613	6.2063	48.49%	55.10%
4.659	4.8124	3.3272	6.3948	30.86%	32.88%	2.5038	7.5389	47.97%	56.66%

Table 6.1: Deviation in radius scale for offset medialness response decays of 10% and 25% for tubes with Gaussian cross-section. σ_{rmax} and σ_{rmin} represent respectively the minimum and maximum radius scales for the corresponding decay percentage.

$\mathscr{M}_{max}$		$\triangle\mathscr{M} = 10\%$				$\triangle\mathscr{M} = 25\%$			
R	σ_r	σ_{rmin}	σ_{rmax}	$\Delta\sigma_{rmin}$	$\Delta\sigma_{rmax}$	σ_{rmin}	σ_{rmax}	$\Delta\sigma_{rmin}$	$\Delta\sigma_{rmax}$
0.75	1.3290	0.9804	2.0408	26.23%	53.56%	0.7991	2.3702	39.87%	78.35%
0.919	1.3900	0.9902	2.1028	28.76%	51.28%	0.8111	2.4300	41.65%	74.82%
1.125	1.5282	1.0203	2.1993	33.23%	43.92%	0.8357	2.5164	45.31%	64.67%
1.379	1.9708	1.2028	2.3584	38.97%	19.67%	0.9234	2.6984	53.14%	36.92%
1.689	2.0613	1.5435	2.5416	25.12%	23.30%	1.1106	2.9666	46.12%	43.92%
2.069	2.1993	1.7926	2.9080	18.49%	32.22%	1.4180	3.3272	35.53%	51.28%
2.534	2.9963	2.1345	3.4112	28.76%	13.85%	1.7660	3.7878	41.06%	26.42%
3.105	3.2941	2.8082	4.0015	14.75%	21.47%	2.4179	4.3773	26.60%	32.88%
3.803	4.0821	3.5856	4.6939	12.16%	14.99%	3.1339	5.1092	23.23%	25.16%
4.659	5.0585	4.4433	5.5613	12.16%	9.94%	3.9815	5.9635	21.29%	17.89%

Table 6.2: Deviation in radius scale for offset medialness response decays of 10% and 25% for tubes with flat convolved cross-section.

	$\Delta\sigma_{rmin}$		$\Delta\sigma_{rmax}$	
	Avg.	Min.	Avg.	Min.
$\triangle\mathscr{M} = 10\%$				
Gaussian	$29.50 \pm 5.52\%$	20.50%	$35.12 \pm 8.48\%$	24.54%
Flat-conv.	$23.86 \pm 8.70\%$	12.16%	$28.42 \pm 15.97\%$	9.94%
$\triangle\mathscr{M} = 25\%$				
Gaussian	$46.03 \pm 5.70\%$	35.85%	$60.42 \pm 11.50\%$	44.64%
Flat-conv.	$37.38 \pm 10.57\%$	21.29%	$45.23 \pm 21.38\%$	17.89%

Table 6.3: Averages obtained for values in tables.

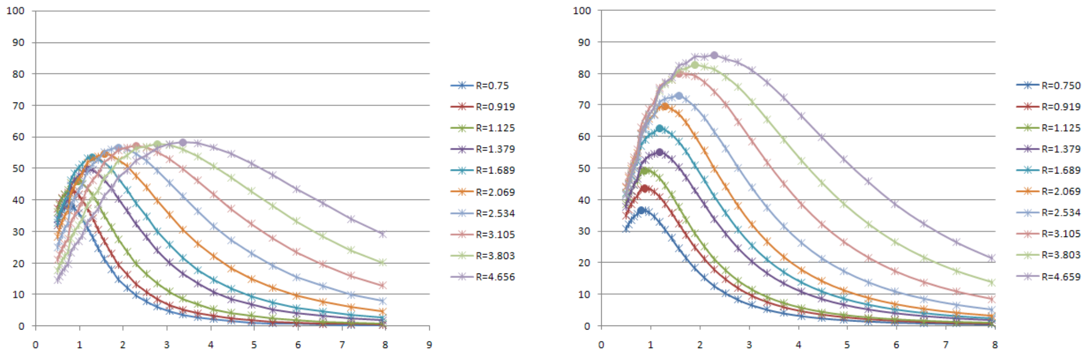

Figure 6.3: Offset medialness values obtained in the center of the tube for different tube sizes and gradient scales σ_g, with $\sigma_h = 2.25$ and the best radius scale σ_r obtained for each tube. Left: tubes with Gaussian section profile. Right: tubes with flat convolved section profile.

scale σ_r that gave the best medialness value. The plots obtained are assymetrycal with respect to the peak values, meaning that is worse underestimating than overestimating the scale. These peak values in the flat convolved tubes are stronger, since the tubes are less smooth, and the best values for σ_g are smaller than for Gaussian tubes. The selectivity of the response is also higher for the flat convolved tubes since the peaks are more prominent. With respect to the tube radius, responses are more selective for smaller radii whereas, for large radii, peaks tend to flatten, specially in the Gaussian tubes due to their smoothness.

In order to refine the results we performed a new set of experiments with a better scale resolution centered around the best values obtained in the previous experiment. For the Gaussian tubes we used $\sigma_{r0} = R_i/(s_r^{N_r/4})$, $s_r = 1.04$, $N_r = 40$, $\sigma_{g0} = 0.56\sigma_r/(s_g^{N_g/6})$, $s_g = 1.04$ and $N_g = 40$. For the flat convolved tubes we used $\sigma_{r0} = R_i/(s_r^{N_r/4})$, $s_r = 1.04$, $N_r = 40$, $\sigma_{g0} = 0.424\sigma_r/(s_g^{N_g/4})$, $s_g = 1.04$ and $N_g = 60$. The factors 0.56 and 0.454 were obtained as an approximate linear relationship between σ_r and σ_g for the maximum values obtained for each tube radius in the previous experiment.

Figure 6.4 shows the maximum values obtained for the offset medialness at the tube centers depending on the radius scale. For each radius scale, the maximum was chosen by varying the gradient scale. We can see that for Gaussian tubes the curves of maxima are more abrupt for small tube sizes, being more selective, and then to flatten for large tube sizes, increasing the detection rate but with less selectivity. For the flat convolved tubes we obtain a more uniform response for all tube sizes. With respect to the gradient scale corresponding to these maxima, they seem to be approximately piece-wise constant, giving the same value for a range of radius scales, except for high scales where some linearity is shown. The results for Gaussian tubes seem to be more stable. This means that results are not so dependent on the gradient scale for some reasonable values of the gradient scale.

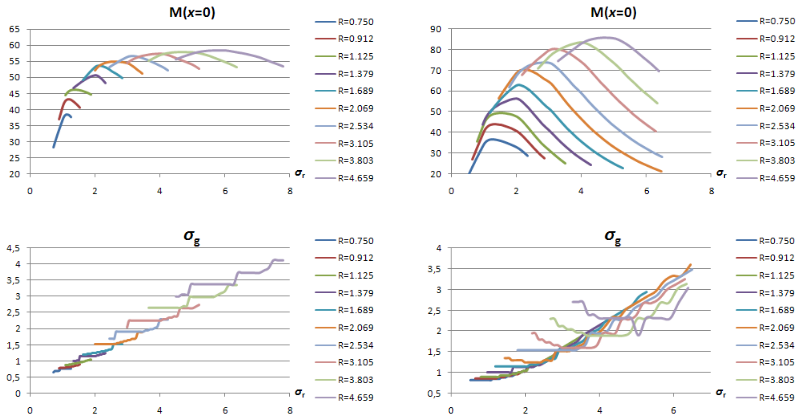

Figure 6.4: Maximum values of *offset medialness* obtained for each tube size and radius scale. Top row: medialness values obtained at the center of the tubes for each radius. Bottom row: corresponding gradient scales that give this maximum values. Left: tubes with Gaussian section. Right: tubes with flat convolved section.

Figure 6.5 represents the radius σ_{rmax} and gradient σ_{gmax} scales that yield the maximum value of medialness for each tube size. These corresponds to the maxima of each series in Figure 6.4. Note that for both section types, the relationship is almost linear as shown by the linear trend lines.

From these plots we can infer some criteria for scale selection as a result of our analyses. For tubes with Gaussian section the linear relationship between the radius and gradient scales for the maxima is approximately:

$$\sigma_{gmax} = 0.540\sigma_{rmax} + 0.150 \tag{6.30}$$

For tubes with flat convolved section, the linear relationship is approximately:

$$\sigma_{gmax} = 0.411\sigma_{rmax} + 0.316 \tag{6.31}$$

Then, in order to select the right scales, we just need to search for the maxima of medialness accross radius scales and select the gradient scales according to the these linear relationships depending on the expected tube profile.

6.3.2 Flux

6.3.3 Optimally Oriented Flux

6.3.3.1 Definition

A major criticism for features based on second derivatives, such as those described in 6.2.2, is that it computes the difference between the intensities outside and inside the object. In a kernel-based implementation, this means the kernel support extends beyond

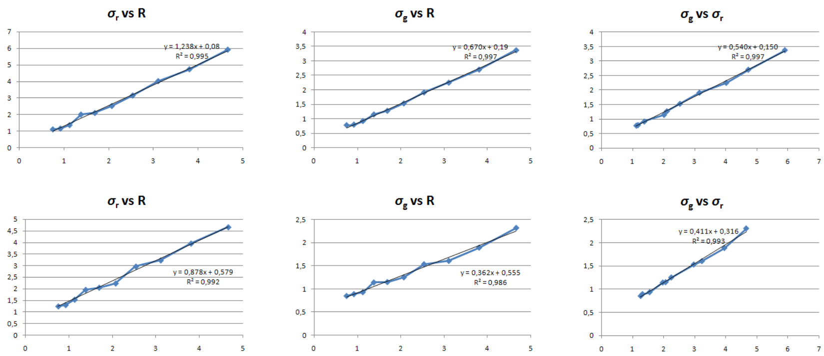

Figure 6.5: Radius and gradient scales that yield the maximum of *offset medialness* for each tube size with corresponding linear trend lines (in black). Top row: tubes with Gaussian section. Bottom row: tubes with flat convolved section.

the limits of the structures. Furthermore, a criticism for standard flux-based features is that they not take into account directionality. In order to overcome this problem, the concept of Optimally Oriented Flux (OOF) is presented in [82].

The OOF first calculates the flux of projected gradient that enters or leaves a sphere surface around the current point. The gradient is projected along a specific direction becoming and oriented flux. The OOF tries to find the optimal projection direction that minimizes this oriented flux. If the current point is in the center of a vessel, this direction will correspond to the vessel axis direction. The radius of the sphere acts as an scale parameter, which allows adapting the detector to different vessel sizes in a multi-scale fashion.

Given a sphere S_r with radius r and a projection direction v the oriented flux can be calculated as the sum:

$$\mathscr{F}(x;r,v) = \int_{\partial S_r} (\nabla I(x+rn)\cdot v)\, v \cdot n\, dA \tag{6.32}$$

where n is the normal to the surface on the infinitesimal surface area dA. The authors show that this expression can be converted into a quadratic form as follows:

$$\mathscr{F}(x;r,v) = \int_{\partial S_r} \left\{ \sum_{k=1}^{3} \sum_{l=1}^{3} (\nabla I_k(x+rn)\cdot v_k \cdot v_l \cdot n_l) \right\} dA = v^T Q_{r,x} v \tag{6.33}$$

where the component (i,j) of the matrix $Q_{r,x}$ is calculated as the integral

$$q_{r,x}^{i,j} = \int \nabla I_i(x+rn)\cdot n_j dA \tag{6.34}$$

which does not depend on the projection direction v but solely on the gradient image values and the sphere geometry. We will call the matrix $Q_{r,x}$ the *oriented flux matrix*, since it allows us to calculate the oriented flux along a given projection direction v.

Then, obtaining the direction v which minimizes eq. 6.32 can be considered as a generalized eigenvalue problem on the matrix Q. The analysis obtains a set of ordered eigenvalues $\lambda_i(x;r)$, $\lambda_3 \leq \lambda_2 \leq \lambda_1$ [3] with corresponding eigenvectors $v_{\lambda(i)}$.

A paralelism is found with the Hessian matrix features in 6.2.2. For a point x in the interior of a tubular structure brighter than the background the eigenvalues follow the relations described in eqs. 6.2 to 6.4. The eigenvectors $v_{\lambda_2}, v_{\lambda_3}$ corresponding to the most negative eigenvalues estimate the cross-section plane of the tube and the eigenvector v_{λ_1} estimates the optimal orientation that minimizes flux, which corresponds to the tube axis.

Once the eigenvalues and eigenvectors are estimated, several vesselness metrics may be devised, following again a paralelism with the features based on the Hessian matrix. The authors use the geometric mean of the two most negative eigenvalues:

$$\mathscr{M}(x;r) = \begin{cases} \sqrt{\lambda_2 \cdot \lambda_3} & \lambda_3 \leq \lambda_2 < 0 \\ 0 & \text{otherwise} \end{cases} \tag{6.35}$$

However, any other features based on eigenvalues, described in 6.2.2, could be used, with their calculation based on the oriented flux matrix instead of the Hessian matrix. Moreover, the estimation of the section plane and normal of the tube, allows to use any other feature that may be computed on the plane, such as the offset medialness measure in 6.3.1. In this case, we are replacing the estimation of the section plane, by another estimation based on oriented flux.

The authors...

6.3.3.2 Scale Selection

The calculation of an OOF-based measure requires the definition of at least two scales: the radius of the sphere in whose surface the flux is calculated, and the scale of the projected gradients whose flux is computed. The authors mention

- The *radius scale* σ_r, as in the offset medialness case (see 6.3.1.2) is the most critical scale and should be approximately equal to the tube radius. Failing to choose the appropiate radius scale will result in a poor estimation or even missing the tube at all. The idea is that the sphere surface should touch the vessel boundary in order to obtain enough signal for the flux-based calculations.

- The *gradient scale* σ_g, again as in 6.3.1.2, should be chosen according to the expected tube boundary width and thus should be smaller than σ_r. The authors in [82] propose using a fixed small scale factor (they use $\sigma_g = 1.0$) for all sphere radii. However, in our experiments we have seen that this is not always the best option since for large scales, such a small scale for the gradients may result in

---

[3] Note that, to be consistent with previous analysis, we named the eigenvalues differently from [82]

a good localization but poor detection rate, with the risk of missing the vessel boundaries when a small discrete set of scales is chosen.

Again, to establish some criteria for scale selection, we performed some experiments on ideal cylinders of different sizes. The set of cylinders used is the same as in section 6.3.1.2. The first set of experiments used a fixed gradient scale $\sigma_g = 1.0$ and σ_r varying according to

$$\sigma_{rj} = s_r^j \sigma_{r0} \quad j = 1 \ldots N_r \tag{6.36}$$

where we used $\sigma_{r0} = 0.5$, $s_r = 1.005$, $N_r = 600$. The idea is to set a criteria for the selection of the radius scale using fixed small gradient scale values as in [82].

Figure 6.6 (left) shows the medialness values obtained for both tubes with Gaussian and flat convolved section profile. Results are similar with respect to the equivalent experiment in section 6.3.1.2 with respect to the shape of the plots both types of tubes. However, the peaks seems to be less prominent and tend to flatten. Some irregularities may be observed for the smallest tube sizes, probably due to discretization effects, since the apparent tube radius is at the scale of the image resolution (here, we used a spacing of 1.0 in all tubes).

6.6 (right) shows the relationship obtained for the maximum radius scales versus the corresponding tube radii. Here, still a good linear relationship may be observed ($R^2 = 0.988$ and $R^2 = 0.969$ for Gaussian and flat convolved tubes respectively). For Gaussian tubes the relationship is approximately:

$$\sigma_{rmax} = 1.094R + 0.482 \tag{6.37}$$

And for flat convolved tubes:

$$\sigma_{rmax} = 0.947R + 0.887 \tag{6.38}$$

However, a better relationship may be obtained for the flat convolved tubes, since the scale values for small radii are very close to $\sigma_r = 2.0$ as can be seen in Table. Therefore, we provide an estimation using a linear piece-wise function:

$$\sigma_{rmax} = \begin{cases} 2.0 & R \leq 1.4 \\ 1.079R + 0.44 & R > 1.4 \end{cases} \tag{6.39}$$

As can be seen in 6.6 (right bottom) this gives a match of $R^2 = 0.990$ for the second linear stretch. Here, the best scales are obtained for values even larger than in the case of the offset medialness, approximately 110% plus 0.5 mm.

Tables 6.1 and 6.2 represent the range of radius scales between which the response decays less than 10% and 25%, for Gaussian and flat convolved tubes respectively.

Then, we tried to evaluate the joint influence of the radius and gradient scales. For this, we computed the OOF medialness value corresponding to equation 6.35 value at the center of each cylinder i for a set of discrete scales, chosen as:

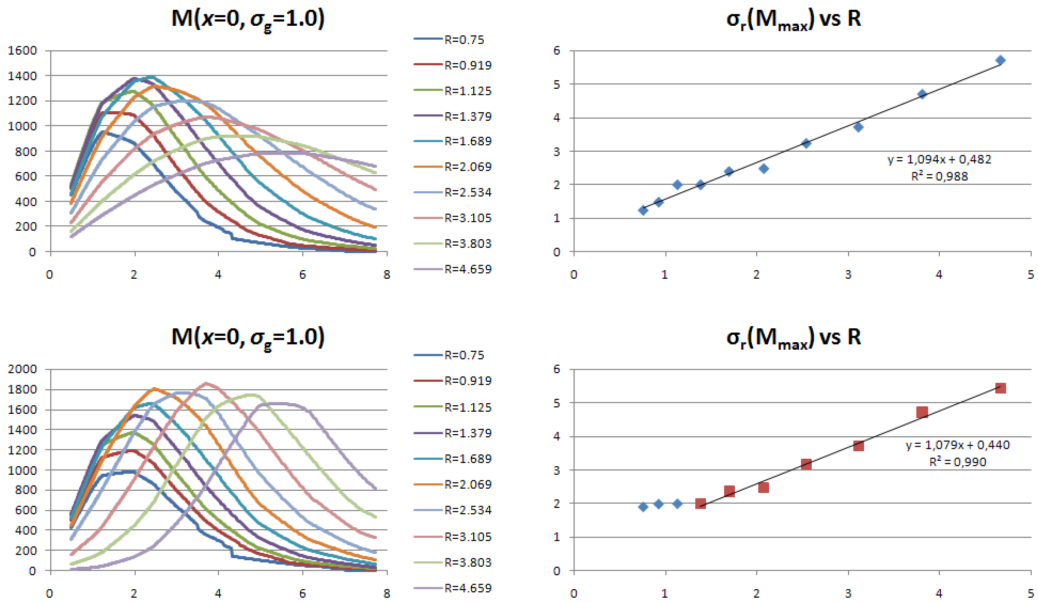

Figure 6.6: OOF medialness values obtained in the center of the tube for different tube sizes with $\sigma_g = 1.0$ and varying σ_r (x-axis), for tubes with Gaussian (top row) and flat convolved (bottom row) section profile. Left column shows all values obtained varying σ_r. Right column shows the relationship between the tube radius (x-axis) and radius scale for the maximum values obtained for each radius.

$\mathcal{M}_{max}$		$\triangle\mathcal{M} = 10\%$				$\triangle\mathcal{M} = 25\%$			
R	σ_r	σ_{rmin}	σ_{rmax}	$\Delta\sigma_{rmin}$	$\Delta\sigma_{rmax}$	σ_{rmin}	σ_{rmax}	$\Delta\sigma_{rmin}$	$\Delta\sigma_{rmax}$
0.75	1.23935	1.0305	2.01049	16.85%	62.22%	0.831588	2.39394	32.90%	93.16%
0.919	1.4831	1.05652	2.26614	28.76%	52.80%	0.852587	2.65828	42.51%	79.24%
1.125	2.00048	1.17319	2.479	41.35%	23.92%	0.932669	2.87911	53.38%	43.92%
1.379	2.00048	1.44658	2.68493	27.69%	34.21%	1.04604	3.213	47.71%	60.61%
1.689	2.39394	1.68845	3.04148	29.47%	27.05%	1.18495	3.69454	50.50%	54.33%
2.069	2.479	1.89369	3.63967	23.61%	46.82%	1.41095	4.29084	43.08%	73.09%
2.534	3.22907	2.15589	4.2695	33.23%	32.22%	1.64687	5.05851	49.00%	56.66%
3.105	3.71302	2.65828	5.0083	28.41%	34.88%	1.96097	5.99334	47.19%	61.41%
3.803	4.69388	3.11828	6.1754	33.57%	31.56%	2.3118	7.24401	50.75%	54.33%
4.659	5.70175	3.73158	7.38998	34.55%	29.61%	2.83635	8.75567	50.25%	53.56%

Table 6.4: Deviation in radius scale for OOF medialness response decays of 10% and 25% for tubes with Gaussian cross-section.

$\mathscr{M}_{max}$		$\triangle\mathscr{M} = 10\%$				$\triangle\mathscr{M} = 25\%$			
R	σ_r	σ_{rmin}	σ_{rmax}	$\Delta\sigma_{rmin}$	$\Delta\sigma_{rmax}$	σ_{rmin}	σ_{rmax}	$\Delta\sigma_{rmin}$	$\Delta\sigma_{rmax}$
0.75	1.90316	1.12169	2.38203	41.06%	25.16%	0.896188	2.75273	52.91%	44.64%
0.919	1.99053	1.15576	2.41794	41.94%	21.47%	0.923412	2.79422	53.61%	40.38%
1.125	2.00048	1.22094	2.49139	38.97%	24.54%	0.965807	2.86478	51.72%	43.20%
1.379	2.00048	1.49052	2.64505	25.49%	32.22%	1.07245	3.10276	46.39%	55.10%
1.689	2.35839	1.73974	2.8935	26.23%	22.69%	1.25803	3.42823	46.66%	45.36%
2.069	2.479	1.99053	3.26144	19.70%	31.56%	1.59832	3.82581	35.53%	54.33%
2.534	3.16529	2.34665	3.94203	25.86%	24.54%	1.93185	4.37731	38.97%	38.29%
3.105	3.71302	3.213	4.3123	13.47%	16.14%	2.71185	4.93392	26.96%	32.88%
3.803	4.71735	3.84494	5.29075	18.49%	12.16%	3.3942	5.81664	28.05%	23.30%
4.659	5.42435	4.69388	6.29984	13.47%	16.14%	4.3123	6.75545	20.50%	24.54%

Table 6.5: Deviation in radius scale for OOF medialness response decays of 10% and 25% for tubes with flat convolved cross-section.

	$\Delta\sigma_{rmin}$		$\Delta\sigma_{rmax}$	
	Avg.	Min.	Avg.	Min.
$\triangle\mathscr{M} = 10\%$				
Gaussian	$29.75 \pm 6.29\%$	16.85%	$37.53 \pm 12.33\%$	23.92%
Flat-conv.	$26.47 \pm 10.28\%$	13.47%	$22.66 \pm 6.50\%$	12.16%
$\triangle\mathscr{M} = 25\%$				
Gaussian	$40.13 \pm 11.96\%$	32.90%	$40.20 \pm 10.88\%$	43.92%
Flat-conv.	$37.38 \pm 10.57\%$	20.50%	$45.23 \pm 21.38\%$	23.30%

Table 6.6: Averages obtained for values in tables.

$$\begin{aligned} \sigma_{rj} &= s_r^j \sigma_{r0} \quad j = 1 \ldots N_r \\ \sigma_{gj} &= s_g^i \sigma_{g0} \quad j = 1 \ldots N_g \end{aligned} \tag{6.40}$$

Our experiments used $\sigma_{r0} = 0.5$, $s_r = 1.05$, $N_r = 60$, $\sigma_{g0} = 0.7R_i$, $s_g = 1.05$, $N_g = 30$ for Gaussian tubes and $\sigma_{r0} = 0.5$, $s_r = 1.05$, $N_r = 50$, $\sigma_{g0} = 0.7R_i$, $s_g = 1.05$, $N_g = 30$ for flat convolved tubes.

Figure 6.7 shows the maximum values obtained for the OOF medialness at the tube centers depending on the radius scale. For each radius scale, the maximum was chosen by varying the gradient scale. We can see that for Gaussian tubes the curves of maxima are more abrupt for small tube sizes, being more selective, and then to flatten for large tube sizes, increasing the detection rate but with less selectivity. For the flat convolved tubes, lower responses and less abrupt are observerd for small tube sizes. With respect to the gradient scale corresponding to these maxima, there is an approximate piece-wise constant behaviour for both tube types. For Gaussian tubes, the gradient scale remains fixed with respect to the radius scale until the maximum of medialness is reached for that tube size. Then, an approximate linear relationship holds as the medialness value decreases. For flat convolved tubes, there is an additional ascending ramp at the beginning of the plots at the lowest radius scales.

Figure 6.8 represents the radius σ_{rmax} and gradient σ_{gmax} scales that yield the maximum value of OOF medialness for each tube size. These corresponds to the maxima of each series in Figure 6.7. Again, for both section types, the relationship is almost linear as shown by the linear trend lines.

From these plots we can infer some criteria for scale selection as a result of our analyses. For tubes with Gaussian section the linear relationship between the radius and gradient scales for the maxima is approximately:

$$\sigma_{gmax} = 0.530\sigma_{rmax} + 0.040 \tag{6.41}$$

For tubes with flat convolved section, the linear relationship is approximately:

$$\sigma_{gmax} = 0.439\sigma_{rmax} + 0.115 \tag{6.42}$$

Then, in order to select the right scales, we just need to search for the maxima of medialness accross radius scales and select the gradient scales according to the these linear relationships depending on the expected tube profile.

6.4 Scale Integration of Filter Responses

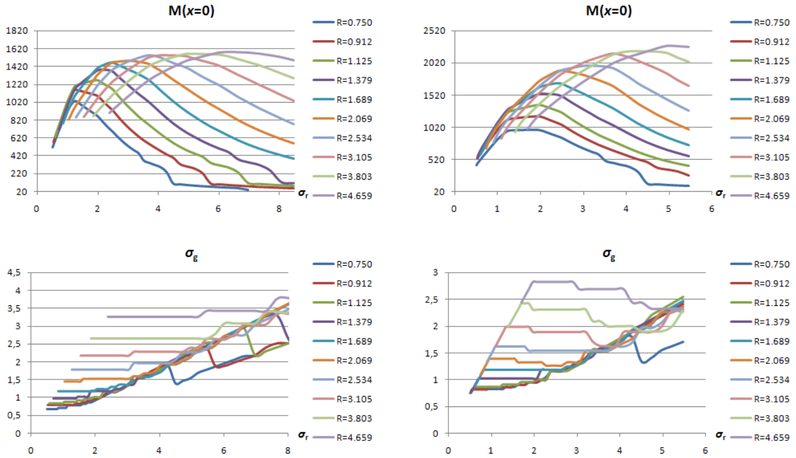

Figure 6.7: Maximum values of *OOF medialness* obtained for each tube size and radius scale. Top row: medialness values obtained at the center of the tubes for each radius. Bottom row: corresponding gradient scales that give this maximum values. Left: tubes with Gaussian section. Right: tubes with flat convolved section.

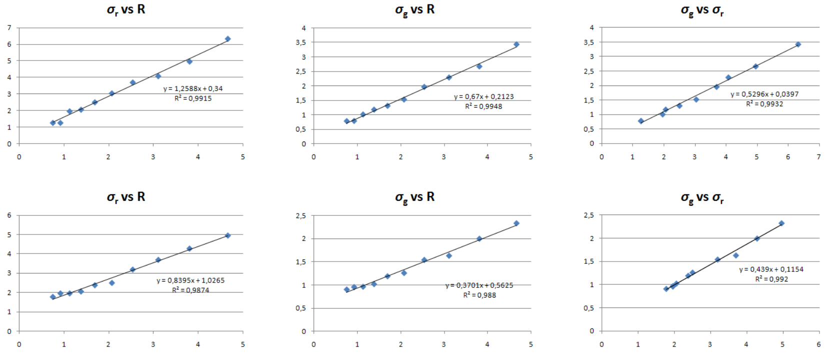

Figure 6.8: Radius and gradient scales that yield the maximum of *OOF medialness* for each tube size with corresponding linear trend lines (in black). Top row: tubes with Gaussian section. Bottom row: tubes with flat convolved section.

Chapter 7

Vascular Extraction

The focus on this Chapter is on *vascular tracking* methods which are a subset of *direct centerline extraction* methods [10]. These methods are more robust in many circumstances, specially for small vessels, and may be more appropiate for quantification or navigation purposes, since a full segmentation of the vessels is not required.

In Section 7.1 we propose an architecture for modelling vascular tracking processes called *Generalized Vascular Tracking (GVT) Framework*. In the following, we describe the different components and stages of the GVT process model, and provide a systematic approach to vascular tracking that incorporates different components into the system with increasing complexity.

In Section 7.2 we demonstrate how this approach is valid for vascular tracking performin experiments with synthetic and real datasets with increasing degree of complexity. We explore the influence of some components identified by using some of the most popular approaches in the literature and obtain qualitative and quatitative results on the accuracy of the centerline tracking using these approaches on ideal and real datasets.

Finally, in Section 7.3 we propose a novel method for vascular section estimation during tracking procedures. It incorporates an optimization stage that uses specific modified vascular detectors as cost functions in order to obtain accurate vascular sections when the direct detection approach fails. We demonstrate the validity of this new approach with experiments using real datasets. We also show that, for a family of medialness functions, the procedure can be performed at fixed small scales which is computationally efficient for local kernel-based estimators. We also demostrate how this novel method is easily accommodated within the proposed GVT Framework.

7.1 Generalized Vascular Tracking (GVT) Framework

7.1.1 Motivation

The literature on vascular structure detection and extraction from medical images is very extensive (see Lesage et al. [88] and Quek and Kirbas [135] for complete reviews)

. Many of the methods try to obtain better measures of vesselness for detection; other focus on innovatives approaches to extraction; it is also common to include different elements or components, which independently may influence the final extraction result. The most advanced methods include complex chains of components acting sequentially to obtain the final extraction result. In [88] there is an increasing need of taking into account the influence of the individual components, clarify their inter-dependencies and design inter-changeable components for the different stages and abstraction levels of the extraction.

From these facts and from our own experience, we conclude that here is a need for specific architectures for vascular extraction consisting of connected and interchangeable components, that allow to compare consistently existing methods, verify the influence of the different components and their relationship and allow for systematic studies and rapid prototyping of complex extraction schemes.

As a result, we propose in the context of vascular tracking, we propose a *Generalized Vascular Tracking (GVT) Framework* which is described next.

7.1.2 Description

The GVT Framework tries to model vascular tracking processes by identifying different *components* and *stages*. We model the tracking procedure as an iterative process with different sequential *stages*. The different interchangeable models, metrics and algorithmic cores [88] identified in these stages are called *components*.

7.1.2.1 Vascular Tracking Components

We identify and define the following common components for vascular tracking:

- *Section Estimator*: locally obtains for every point an estimate of the section normal and possibly of the local radius based on image content, previous estimations and section models. The Hessian Matrix and the Oriented Flux Matrix (OFM) may be considered simple section estimators in our framework, since they provide an estimate of the section normal and radius, obtained from the eigenvalue analysis of these matrices.

- *Vesselness Metric*: is a measure of the likelihood of point of being part of a vessel. If the measure refers to the likelihood of being part of the centerline or medial line we call it *Medialness*. The metric may be used in several parts of the extraction process, for example to estimate the correct scale as the one which gives a maximum value of the metric, or to search for the centerline point.

- *Centerline Model*: this defines which output extraction information is stored (see). It may be as simple as set of centerline points, but may also include an underlying mathematical model such as an interpolating B-spline curve. It also may include a section model for every point or the centerline, the simplest being an estimate of the radius, and other quantitative measurements.

- *End Condition*: stopping criterion for the algorithm. It may be as simple as maximum number of iterations. More practical end conditions may have into account the vesselness value in order to establish a minimum. Adaptive methods with variable step size may incorporate the step size as a stopping criterion.

- *Scale Estimator* (optional): used in multi-scale approaches. It estimates which scale is the best for performing calculations on the current point. In general, the scale is proportional to the relative size of the vascular structures to detect but its interpretation depends on the algorithm used. For example, in Hessian-based calculations, it determines the aperture of the Gaussian kernel used for scaled derivatives; in oriented flux calculations, it determined the radius of the sphere used to calculate the flux. The estimation of the scale is usually based on a (vesselness) metric. The simples rule is to take the scale which gives the maximum value of the metric accross-scales, but other more complex approaches may be taken, such as penalizing moving accross scales. The scale may also provide an estimate of the local section radius.

- *Bifurcation (Branch) Detector* (optional): used for detecting possible bifurcations or branching points. They may be based on the vesselness measures or other indicators which may alert of the presence of bifurcations. The detector may also estimate the number and orientation of the bifurcations. In the current thesis we do not deal deeply with the problem of bifurcations, but they must be taken into account in the extraction of complex networks or when the vesselness metrich behaves poorly at these locations.

- *Optimizer* (optional): methods which incorporate an optimization procedure may use different optimization algorithms. The most simple is to take the maximum (minimum) value between a set of sampled points in parameter space (exhaustive optimizer), but more complex optimization procedures may be used, with algorithms such as gradient descent, simplex, Levenberg-Marquardt or evolutionary approaches.

Most of these components, are used in every iteration but some may only be used once during the tracking procedure, for example at initialization. Some components are regarded as optional, depending on whether the tracking perform some kind of action, for example an optimization procedure.

These components have been identified for vascular extraction based on tracking procedures. However, some of them make also sense in other approaches to extraction. For example, the Section Estimator or the Vesselness Metric may also be used in minimum path search or global detection approaches.

7.1.2.2 Vascular Tracking Stages

A process diagram describing the different identified stages and their relationship is shown in Figure 7.1. Most of the stages are performed at every iteration. Other, such as the *Initialize* and *Post-process* stages are performed only onceWe proceed to describe the different stages shown:

- *Initialize*: the purpose of this stage, performed only once at the beginning, is to initialize the tracking procedure. The most simple initialization consists of providing a seed point in the vessel centerline. More advanced initialization may involve trying to find the closest centerline point from the seed point, assuming this point is not on the centerline. This may also be considered a *Search stage*.

- *Turn*: this stage tries to find the correct orientation and section of the vessel when a new (centerline) point is obtained, after advancing one step (*Step stage*) or after searching for the correct centerline point (*Search stage*). The process involves using a *Section Estimator* and possibly, in multi-scale approaches, a *Scale Estimator* and a *Vesselness Function*.
- *Search*: the point obtained after a *Step stage* may not lie on the real centerline, and therefore, the normal and section obtained in the *Turn stage* will not be correct. This stage aims to correct the trajectory in the vecinity of the new vessel candidate point. Several conditions may be imposed for the new point. For example, it may be the maximum value of the vesselness (medialness) in the previously estimated plane, or might be the closest ridge point, assuming that the intensity or vesselness function used has maxima at the centerline points. Once a new point is found, a *Turn stage* estimates a new orientation and section. This may be done once or in an iterative loop as can be seen in Figure 7.1. Note that the Turn and Search stages only involve calculations for the current point and do not involve estimating the new step direction (*Step stage*).
- *Measure*: once a new vessel (centerline) point is found, local or cummulative quantitative measurements may be performed, which are costly to calculate before the *Search stage* finishes and which are not needed in previous calculations. This may involve for example a detailed section shape or profiles, curvatures or cummulative lengths.
- *Step*: this stage estimates the new direction of advance and performs a step in the current direction. The most simple way of estimating the direction is to take the current section normal direction, but more advanced strategies may be used, such as filtering (i.e. averaging) the trajectory, extrapolating, etc. The process also involves setting the size of the current step. This may be fixed or adaptive, i.e. decreasing the step depending on curvature.
- *Check Branch* (optional): this stage uses a *Branch Detector* in order to verify if the current point is a branch point. If a bifurcation is found, the current branch extraction is finished and new extraction processes are spawned for each branch. The process can be seen on the diagram as an *Initialization stage* for each new branch.
- *Check End*: this stage checks if we have reached the end of the vessel. This may be as simple as checking a maximum number of iterations, or, more practically, checking the value of a *Vesselness Metric* or the step size for some adaptive approaches.
- *Post-process*: this stage performs any post-processing operation in the extracted branch or tree, such as quantification processes, filtering of centerlines and sections, etc.

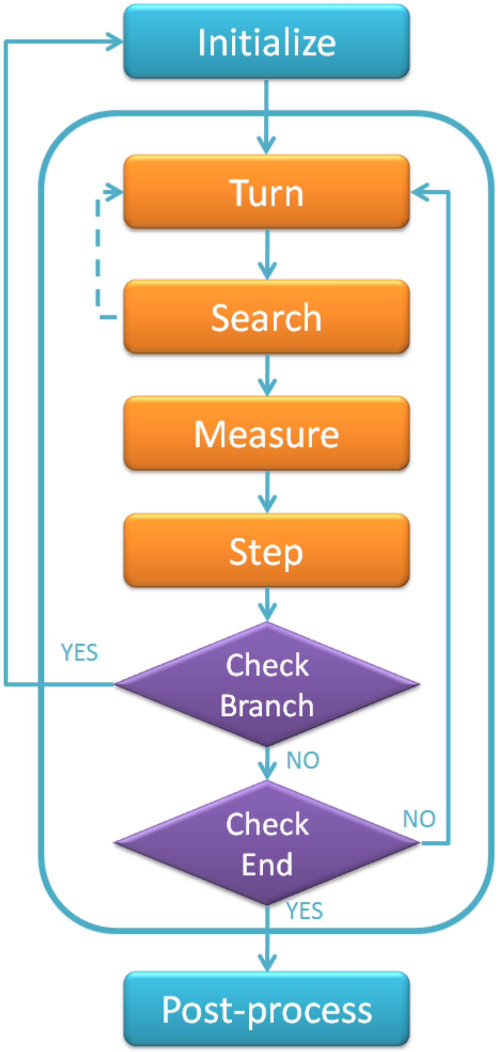

Figure 7.1: Process diagram of the GVT showing the different stages.

7.2 A Systematic Approach to Vascular Tracking Using GVT

Once we have defined the GVT Framework, it is now possible to test the influence of the different components, stages and corresponding parameters in the outcome of the extraction procedure. We do this by performing extraction experiments in synthetic and real datasets, with increasing complexity: from single-scale to multi-scale approaches; from methods with no search stage to exhaustive or optimized search based methods, etc.

Thus, by performing this set of experiments, we test the validity of the GVT framework in the design of new, complex extraction methods based on existing components and possibly with new algorithmic or heuristic approaches for some parts of the extraction procedure. We also provide some insight in which are the most important aspects in the definition of such custom algorithms.

As the number of combinations of components that may be covered is enormous, we provide some representative designs in increasing complexity. For each, we provide a list of components used and the corresponding stage.

7.2.1 Fixed-scale Extraction

Fixed-scale extraction performs extraction using components whose operators will perform at a single, user-provided scale. It is assumed that the size (diameter) of the vessels to extract is in the range of sizes that can be detected at the selected scale. Moreover, for simplicity, we do not provide initially any *Search* stage to correct the trajectory.

We performed some experiments on ideal tubes in order to test the accuracy of the section estimation and the influence of several parameters, such as the tube radius, scale of detection and noise level. We used the eigenvectors of the Hessian matrix and Oriented Flux (OF) Matrix in order to compare the accuracy and robustness of both *Section Estimators*.

We created a set of six ideal cylinders with maximum intensity of 255 and radius values according to:

$$R = sR_0 \tag{7.1}$$

where $R_0$is the initial radius and s the scale factor. We chose $R_0 = 1.0$ and $s = 1.5$. We also provided noisy versions with additive Gaussian noise of 10, 25, 50 and 75% with respect to the signal. We used two models of tubes: one with Gaussian cross-section and another with flat section convolved with a Gaussian with a small value of aperture (we used $\sigma = 1.0$). The second model better represents real vessels and partial volume effects, but the first model makes the tube boundary more diffuse.

Similarly, we selected a set of six discrete scales for calculations as in:

$$\sigma = s\sigma_0 \tag{7.2}$$

We chose $\sigma_0 = 0.7698$ and $s = 1.5$. The values where taken in a way that both the set of radii and detection scales used the same multiplying factor, and that, for the smaller radius values, there existed an optimal scale of detection in the discrete set. According to Krissian *et al.* , for Gaussian tubes, the scale that gives best response for their offset medialness function is $\sigma = \sqrt{3}R$. We used this relationship as a reference for the scale selection and thus $\sigma_2 = s^2\sigma_0 = 1.732 \backsimeq \sqrt{3}$. While this does not hold exactly true for all cases, we have observed that the best detection scale in most cases is a bit larger than the tube radius.

The extraction algorithm started from a seed point in the centerline of the tube, but not in the extrema in order to avoid boundary effects. The algorithm used a fixed step size of 1.0 advancing in the estimated direction for a fixed number of 40 iterations.

We analyze two different quantitative measures in these experiments, obtained for different radii of tubes and noise levels:

- *Mean (in section) centerline error* : corresponds to the mean error for the 40 sections (one for every iteration) calculated as the distance to the true centerline. We do not take into account here the error in the z direction, which accumulates with the deviation in the angle estimation. The reason is that we are more interested in the precision of the centerline estimation. The z error may accumulate with errors in the in-section centerline estimation, because less distance along the centerline will be travelled, but to travel more distance we just need a higher number of iterations in this case. This happens for example with oscillating centerline estimates. Other measures could be used, such as the maximum error or the standard deviation, but we saw a high correlation with the mean.
- *Mean angle error* : corresponds to the mean of the angle between the estimated and ground truth section normals, taking the z-axis as ground truth, as:

$$\theta = \arccos\left(v \cdot u_z\right) = \arccos\left(v_1 u_{z1} + v_2 u_{z2} + v_3 u_{z3}\right) = \arccos\left(v_3\right) \tag{7.3}$$

  where v is the estimated unit vector and $u_z$is the z-axis unit vector and $v \cdot u_z$is the cosine of the angle formed by both unit vectors, which corresponds to the z component of the v vector. This also takes into account the sign of the vector giving values from 0 to 180º (in the opposite direction) which is important in order to check that the tracking does not turn back pointing to the wrong direction.

However, these quantitative measures do not provide qualitative information about the quality of the tracking, that is whether the tracking was succesful or not or whether difficulties were found. We consider here five different situations:

- *Accurate tracking*: errors are minimal and the tracking proceeds without difficulties (Figure 7.2(a)).
- *Oscillating tracking*: centerline tracking is achieved, but tracking tends to oscillate around the true centerline position. It is typical of an overestimated scale (Figure 7.2(b)).

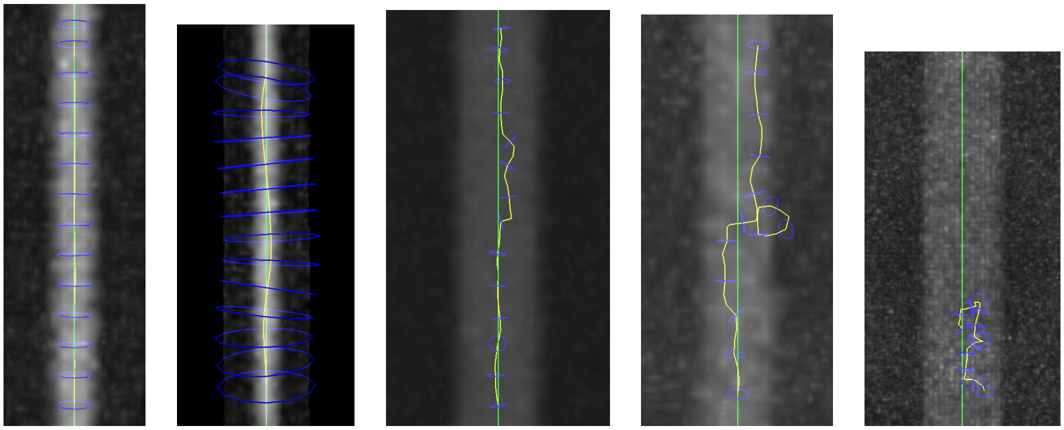
(a) (b) (c) (d) (e)

Figure 7.2: Different characteristic vessel tracking situations obtained in experiments with synthetic ideal cylinders with additive Gaussian noise. Examples use Hessian estimators. (a) *Accurate tracking* (Gaussian section, $R = 1.5$, 10% noise $\sigma = 1.73$), (b) *Oscillating tracking* (Gaussian section, $R = 1.0$, 10% noise $\sigma = 5.84$), (c) *Difficult tracking* (Gaussian section, $R = 3.37$, 10% noise $\sigma = 0.76$), (d) *Lost tracking with recovery* (Flat-convolved section, $R = 2.25$, 25% noise, $\sigma = 0.76$), (e) *No tracking* (Flat-convolved section, $R = 7.59$, 50% noise, $\sigma = 1.73$). Figures shows cylinders as volume render with adjusted contrast levels for better visualization. Yellow line shows estimated trajectory; green line shows ground truth centerline; blue circles represent scale used and estimated orientation.

- *Difficult tracking*: difficulties arise. Tracking is not totally lost but many centerline and angle estimates are incorrect. It results in a non-smooth centerline and, even the centerline location is quite accurate, local section angle estimations are poor (Figure 7.2(c)).

- *Lost tracking*: tracking is correct at the beginning but centerline is lost at some point. Some cases of lost tracking may end up in a partial recovery. When using small scales with large tubes, this may happen when the tracking progresses close to the external contour, as it partially finds some of the vessel boundary that gives a good enough response on the estimator (Figure 7.2(d)).

- *No tracking*: tracking is not achieved at all (Figure 7.2(e)).

Tables 7.1 to 7.4 show the values of the mean centerline and angle error for different radii of tubes, scales for the detectors and noise levels. Values are color coded according to the quality of tracking. We do not distinguish between correct and oscillating tracking, since sometimes this classification is not clear. Instead we classify the experiments as good when no difficulties are found and we also mark the best values with a different color (see Table 7.1).

From the tables we can see that scale selection is important to achieve a good or

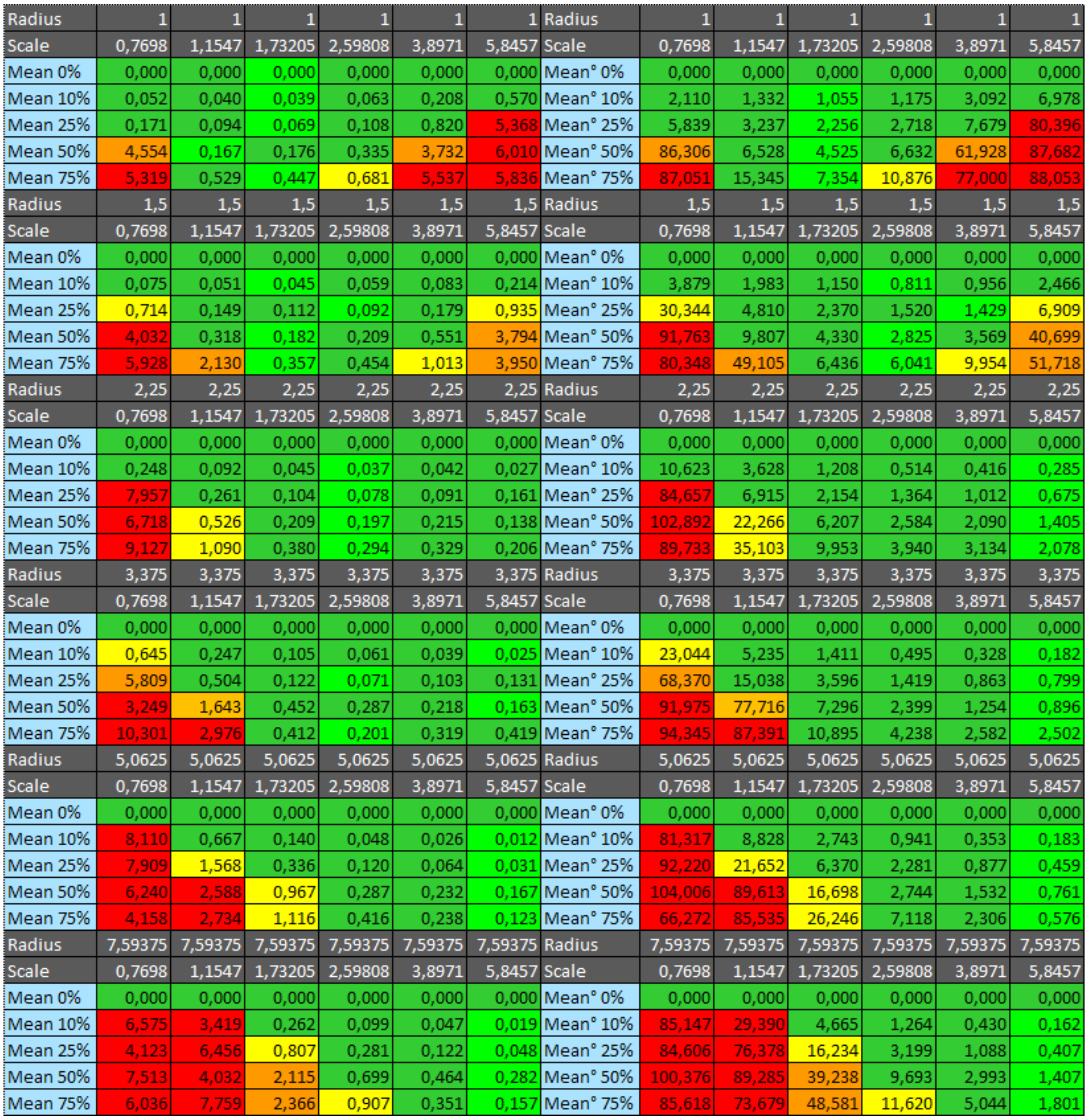

Radius	1	1	1	1	1	1	Radius	1	1	1	1	1	1
Scale	0,7698	1,1547	1,73205	2,59808	3,8971	5,8457	Scale	0,7698	1,1547	1,73205	2,59808	3,8971	5,8457
Mean 0%	0,000	0,000	0,000	0,000	0,000	0,000	Mean° 0%	0,000	0,000	0,000	0,000	0,000	0,000
Mean 10%	0,052	0,040	0,039	0,063	0,208	0,570	Mean° 10%	2,110	1,332	1,055	1,175	3,092	6,978
Mean 25%	0,171	0,094	0,069	0,108	0,820	5,368	Mean° 25%	5,839	3,237	2,256	2,718	7,679	80,396
Mean 50%	4,554	0,167	0,176	0,335	3,732	6,010	Mean° 50%	86,306	6,528	4,525	6,632	61,928	87,682
Mean 75%	5,319	0,529	0,447	0,681	5,537	5,836	Mean° 75%	87,051	15,345	7,354	10,876	77,000	88,053
Radius	1,5	1,5	1,5	1,5	1,5	1,5	Radius	1,5	1,5	1,5	1,5	1,5	1,5
Scale	0,7698	1,1547	1,73205	2,59808	3,8971	5,8457	Scale	0,7698	1,1547	1,73205	2,59808	3,8971	5,8457
Mean 0%	0,000	0,000	0,000	0,000	0,000	0,000	Mean° 0%	0,000	0,000	0,000	0,000	0,000	0,000
Mean 10%	0,075	0,051	0,045	0,059	0,083	0,214	Mean° 10%	3,879	1,983	1,150	0,811	0,956	2,466
Mean 25%	0,714	0,149	0,112	0,092	0,179	0,935	Mean° 25%	30,344	4,810	2,370	1,520	1,429	6,909
Mean 50%	4,032	0,318	0,182	0,209	0,551	3,794	Mean° 50%	91,763	9,807	4,330	2,825	3,569	40,699
Mean 75%	5,928	2,130	0,357	0,454	1,013	3,950	Mean° 75%	80,348	49,105	6,436	6,041	9,954	51,718
Radius	2,25	2,25	2,25	2,25	2,25	2,25	Radius	2,25	2,25	2,25	2,25	2,25	2,25
Scale	0,7698	1,1547	1,73205	2,59808	3,8971	5,8457	Scale	0,7698	1,1547	1,73205	2,59808	3,8971	5,8457
Mean 0%	0,000	0,000	0,000	0,000	0,000	0,000	Mean° 0%	0,000	0,000	0,000	0,000	0,000	0,000
Mean 10%	0,248	0,092	0,045	0,037	0,042	0,027	Mean° 10%	10,623	3,628	1,208	0,514	0,416	0,285
Mean 25%	7,957	0,261	0,104	0,078	0,091	0,161	Mean° 25%	84,657	6,915	2,154	1,364	1,012	0,675
Mean 50%	6,718	0,526	0,209	0,197	0,215	0,138	Mean° 50%	102,892	22,266	6,207	2,584	2,090	1,405
Mean 75%	9,127	1,090	0,380	0,294	0,329	0,206	Mean° 75%	89,733	35,103	9,953	3,940	3,134	2,078
Radius	3,375	3,375	3,375	3,375	3,375	3,375	Radius	3,375	3,375	3,375	3,375	3,375	3,375
Scale	0,7698	1,1547	1,73205	2,59808	3,8971	5,8457	Scale	0,7698	1,1547	1,73205	2,59808	3,8971	5,8457
Mean 0%	0,000	0,000	0,000	0,000	0,000	0,000	Mean° 0%	0,000	0,000	0,000	0,000	0,000	0,000
Mean 10%	0,645	0,247	0,105	0,061	0,039	0,025	Mean° 10%	23,044	5,235	1,411	0,495	0,328	0,182
Mean 25%	5,809	0,504	0,122	0,071	0,103	0,131	Mean° 25%	68,370	15,038	3,596	1,419	0,863	0,799
Mean 50%	3,249	1,643	0,452	0,287	0,218	0,163	Mean° 50%	91,975	77,716	7,296	2,399	1,254	0,896
Mean 75%	10,301	2,976	0,412	0,201	0,319	0,419	Mean° 75%	94,345	87,391	10,895	4,238	2,582	2,502
Radius	5,0625	5,0625	5,0625	5,0625	5,0625	5,0625	Radius	5,0625	5,0625	5,0625	5,0625	5,0625	5,0625
Scale	0,7698	1,1547	1,73205	2,59808	3,8971	5,8457	Scale	0,7698	1,1547	1,73205	2,59808	3,8971	5,8457
Mean 0%	0,000	0,000	0,000	0,000	0,000	0,000	Mean° 0%	0,000	0,000	0,000	0,000	0,000	0,000
Mean 10%	8,110	0,667	0,140	0,048	0,026	0,012	Mean° 10%	81,317	8,828	2,743	0,941	0,353	0,183
Mean 25%	7,909	1,568	0,336	0,120	0,064	0,031	Mean° 25%	92,220	21,652	6,370	2,281	0,877	0,459
Mean 50%	6,240	2,588	0,967	0,287	0,232	0,167	Mean° 50%	104,006	89,613	16,698	2,744	1,532	0,761
Mean 75%	4,158	2,734	1,116	0,416	0,238	0,123	Mean° 75%	66,272	85,535	26,246	7,118	2,306	0,576
Radius	7,59375	7,59375	7,59375	7,59375	7,59375	7,59375	Radius	7,59375	7,59375	7,59375	7,59375	7,59375	7,59375
Scale	0,7698	1,1547	1,73205	2,59808	3,8971	5,8457	Scale	0,7698	1,1547	1,73205	2,59808	3,8971	5,8457
Mean 0%	0,000	0,000	0,000	0,000	0,000	0,000	Mean° 0%	0,000	0,000	0,000	0,000	0,000	0,000
Mean 10%	6,575	3,419	0,262	0,099	0,047	0,019	Mean° 10%	85,147	29,390	4,665	1,264	0,430	0,162
Mean 25%	4,123	6,456	0,807	0,281	0,122	0,048	Mean° 25%	84,606	76,378	16,234	3,199	1,088	0,407
Mean 50%	7,513	4,032	2,115	0,699	0,464	0,282	Mean° 50%	100,376	89,285	39,238	9,693	2,993	1,407
Mean 75%	6,036	7,759	2,366	0,907	0,351	0,157	Mean° 75%	85,618	73,679	48,581	11,620	5,044	1,801

Table 7.1: Mean values for in-section center point estimation error for different detector scale values (x axis) along tubes of $R = 1.0$ and $R = 1.5$ as calculated for the Hessian (H) section estimator for tubes with Gaussian (G) cross-section. Results are shown for different levels of noise with respect to the signal (0, 10, 25, 50 and 75%). Color codes provide qualitative information (bright green: best values, green: good or fair estimates, yellow: evident difficulties in tracking, orange: centerline is lost during tracking, red: unable to track the vessel)

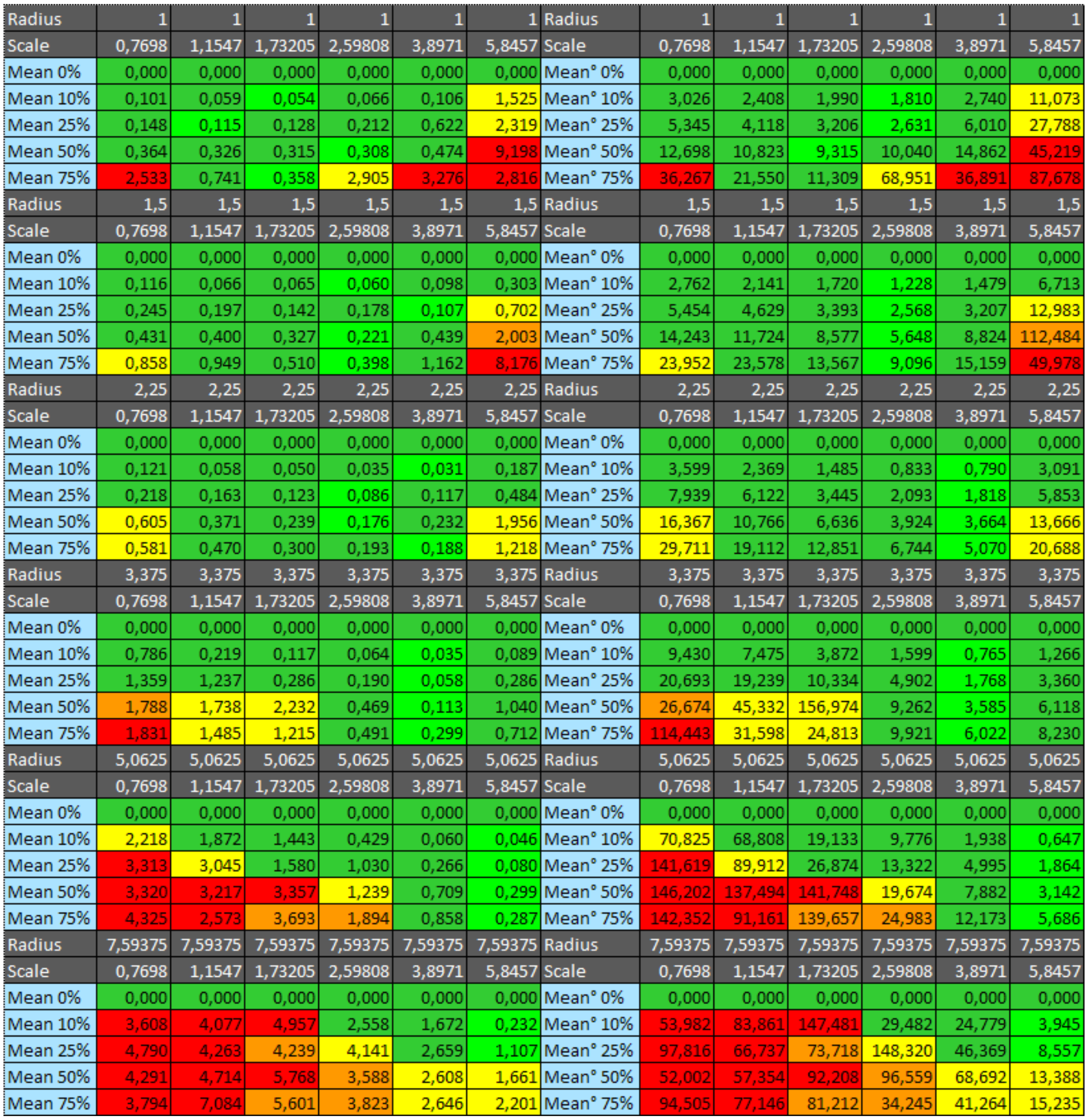

Radius	1	1	1	1	1	1	Radius	1	1	1	1	1	1
Scale	0,7698	1,1547	1,73205	2,59808	3,8971	5,8457	Scale	0,7698	1,1547	1,73205	2,59808	3,8971	5,8457
Mean 0%	0,000	0,000	0,000	0,000	0,000	0,000	Mean° 0%	0,000	0,000	0,000	0,000	0,000	0,000
Mean 10%	0,101	0,059	0,054	0,066	0,106	1,525	Mean° 10%	3,026	2,408	1,990	1,810	2,740	11,073
Mean 25%	0,148	0,115	0,128	0,212	0,622	2,319	Mean° 25%	5,345	4,118	3,206	2,631	6,010	27,788
Mean 50%	0,364	0,326	0,315	0,308	0,474	9,198	Mean° 50%	12,698	10,823	9,315	10,040	14,862	45,219
Mean 75%	2,533	0,741	0,358	2,905	3,276	2,816	Mean° 75%	36,267	21,550	11,309	68,951	36,891	87,678
Radius	1,5	1,5	1,5	1,5	1,5	1,5	Radius	1,5	1,5	1,5	1,5	1,5	1,5
Scale	0,7698	1,1547	1,73205	2,59808	3,8971	5,8457	Scale	0,7698	1,1547	1,73205	2,59808	3,8971	5,8457
Mean 0%	0,000	0,000	0,000	0,000	0,000	0,000	Mean° 0%	0,000	0,000	0,000	0,000	0,000	0,000
Mean 10%	0,116	0,066	0,065	0,060	0,098	0,303	Mean° 10%	2,762	2,141	1,720	1,228	1,479	6,713
Mean 25%	0,245	0,197	0,142	0,178	0,107	0,702	Mean° 25%	5,454	4,629	3,393	2,568	3,207	12,983
Mean 50%	0,431	0,400	0,327	0,221	0,439	2,003	Mean° 50%	14,243	11,724	8,577	5,648	8,824	112,484
Mean 75%	0,858	0,949	0,510	0,398	1,162	8,176	Mean° 75%	23,952	23,578	13,567	9,096	15,159	49,978
Radius	2,25	2,25	2,25	2,25	2,25	2,25	Radius	2,25	2,25	2,25	2,25	2,25	2,25
Scale	0,7698	1,1547	1,73205	2,59808	3,8971	5,8457	Scale	0,7698	1,1547	1,73205	2,59808	3,8971	5,8457
Mean 0%	0,000	0,000	0,000	0,000	0,000	0,000	Mean° 0%	0,000	0,000	0,000	0,000	0,000	0,000
Mean 10%	0,121	0,058	0,050	0,035	0,031	0,187	Mean° 10%	3,599	2,369	1,485	0,833	0,790	3,091
Mean 25%	0,218	0,163	0,123	0,086	0,117	0,484	Mean° 25%	7,939	6,122	3,445	2,093	1,818	5,853
Mean 50%	0,605	0,371	0,239	0,176	0,232	1,956	Mean° 50%	16,367	10,766	6,636	3,924	3,664	13,666
Mean 75%	0,581	0,470	0,300	0,193	0,188	1,218	Mean° 75%	29,711	19,112	12,851	6,744	5,070	20,688
Radius	3,375	3,375	3,375	3,375	3,375	3,375	Radius	3,375	3,375	3,375	3,375	3,375	3,375
Scale	0,7698	1,1547	1,73205	2,59808	3,8971	5,8457	Scale	0,7698	1,1547	1,73205	2,59808	3,8971	5,8457
Mean 0%	0,000	0,000	0,000	0,000	0,000	0,000	Mean° 0%	0,000	0,000	0,000	0,000	0,000	0,000
Mean 10%	0,786	0,219	0,117	0,064	0,035	0,089	Mean° 10%	9,430	7,475	3,872	1,599	0,765	1,266
Mean 25%	1,359	1,237	0,286	0,190	0,058	0,286	Mean° 25%	20,693	19,239	10,334	4,902	1,768	3,360
Mean 50%	1,788	1,738	2,232	0,469	0,113	1,040	Mean° 50%	26,674	45,332	156,974	9,262	3,585	6,118
Mean 75%	1,831	1,485	1,215	0,491	0,299	0,712	Mean° 75%	114,443	31,598	24,813	9,921	6,022	8,230
Radius	5,0625	5,0625	5,0625	5,0625	5,0625	5,0625	Radius	5,0625	5,0625	5,0625	5,0625	5,0625	5,0625
Scale	0,7698	1,1547	1,73205	2,59808	3,8971	5,8457	Scale	0,7698	1,1547	1,73205	2,59808	3,8971	5,8457
Mean 0%	0,000	0,000	0,000	0,000	0,000	0,000	Mean° 0%	0,000	0,000	0,000	0,000	0,000	0,000
Mean 10%	2,218	1,872	1,443	0,429	0,060	0,046	Mean° 10%	70,825	68,808	19,133	9,776	1,938	0,647
Mean 25%	3,313	3,045	1,580	1,030	0,266	0,080	Mean° 25%	141,619	89,912	26,874	13,322	4,995	1,864
Mean 50%	3,320	3,217	3,357	1,239	0,709	0,299	Mean° 50%	146,202	137,494	141,748	19,674	7,882	3,142
Mean 75%	4,325	2,573	3,693	1,894	0,858	0,287	Mean° 75%	142,352	91,161	139,657	24,983	12,173	5,686
Radius	7,59375	7,59375	7,59375	7,59375	7,59375	7,59375	Radius	7,59375	7,59375	7,59375	7,59375	7,59375	7,59375
Scale	0,7698	1,1547	1,73205	2,59808	3,8971	5,8457	Scale	0,7698	1,1547	1,73205	2,59808	3,8971	5,8457
Mean 0%	0,000	0,000	0,000	0,000	0,000	0,000	Mean° 0%	0,000	0,000	0,000	0,000	0,000	0,000
Mean 10%	3,608	4,077	4,957	2,558	1,672	0,232	Mean° 10%	53,982	83,861	147,481	29,482	24,779	3,945
Mean 25%	4,790	4,263	4,239	4,141	2,659	1,107	Mean° 25%	97,816	66,737	73,718	148,320	46,369	8,557
Mean 50%	4,291	4,714	5,768	3,588	2,608	1,661	Mean° 50%	52,002	57,354	92,208	96,559	68,692	13,388
Mean 75%	3,794	7,084	5,601	3,823	2,646	2,201	Mean° 75%	94,505	77,146	81,212	34,245	41,264	15,235

Table 7.2: Same as Table 7.1 for Hessian tubes with Optimally Oriented Flux as section estimator.

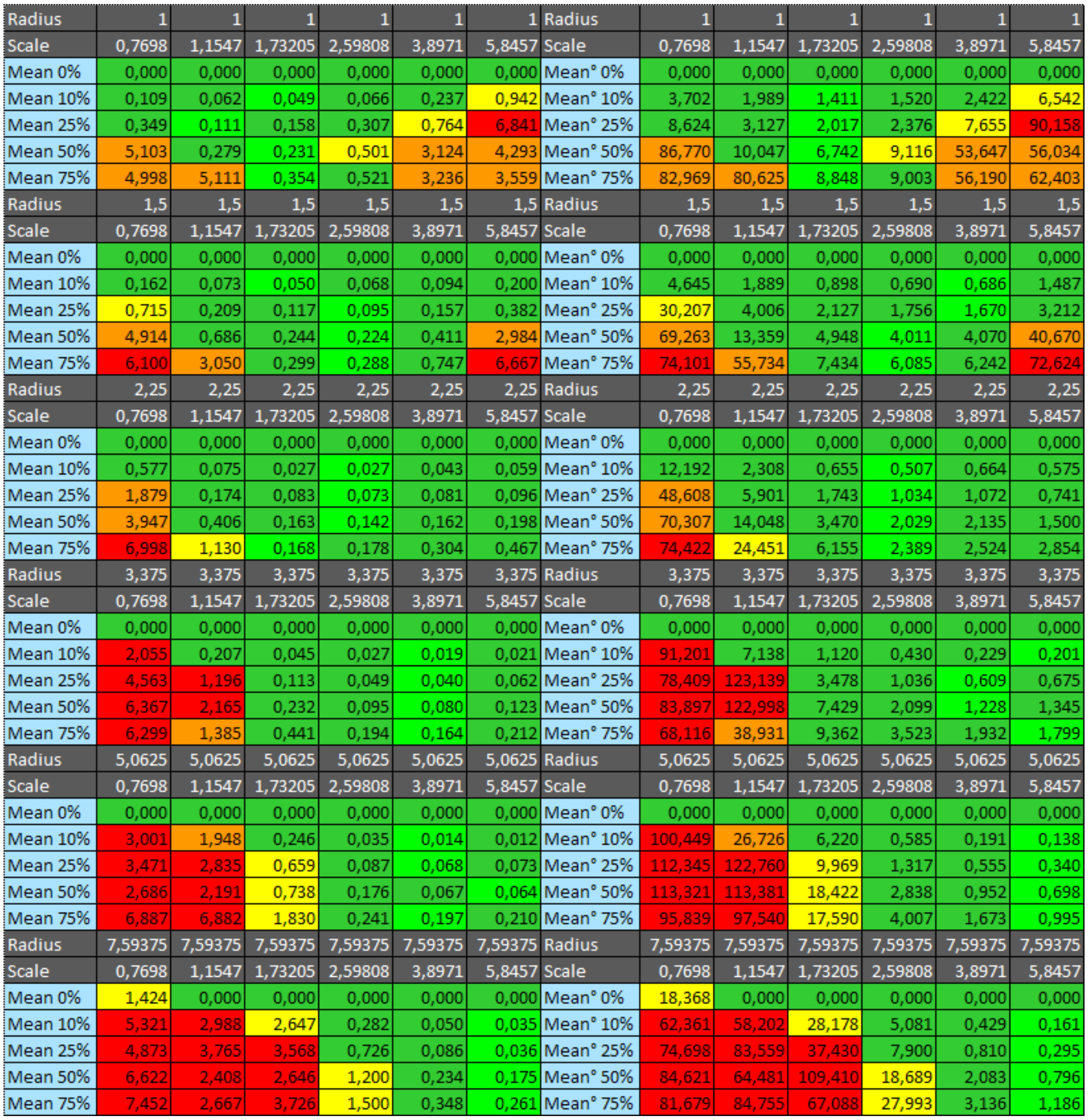

Radius	1	1	1	1	1	1	Radius	1	1	1	1	1	1
Scale	0,7698	1,1547	1,73205	2,59808	3,8971	5,8457	Scale	0,7698	1,1547	1,73205	2,59808	3,8971	5,8457
Mean 0%	0,000	0,000	0,000	0,000	0,000	0,000	Mean° 0%	0,000	0,000	0,000	0,000	0,000	0,000
Mean 10%	0,109	0,062	0,049	0,066	0,237	0,942	Mean° 10%	3,702	1,989	1,411	1,520	2,422	6,542
Mean 25%	0,349	0,111	0,158	0,307	0,764	6,841	Mean° 25%	8,624	3,127	2,017	2,376	7,655	90,158
Mean 50%	5,103	0,279	0,231	0,501	3,124	4,293	Mean° 50%	86,770	10,047	6,742	9,116	53,647	56,034
Mean 75%	4,998	5,111	0,354	0,521	3,236	3,559	Mean° 75%	82,969	80,625	8,848	9,003	56,190	62,403
Radius	1,5	1,5	1,5	1,5	1,5	1,5	Radius	1,5	1,5	1,5	1,5	1,5	1,5
Scale	0,7698	1,1547	1,73205	2,59808	3,8971	5,8457	Scale	0,7698	1,1547	1,73205	2,59808	3,8971	5,8457
Mean 0%	0,000	0,000	0,000	0,000	0,000	0,000	Mean° 0%	0,000	0,000	0,000	0,000	0,000	0,000
Mean 10%	0,162	0,073	0,050	0,068	0,094	0,200	Mean° 10%	4,645	1,889	0,898	0,690	0,686	1,487
Mean 25%	0,715	0,209	0,117	0,095	0,157	0,382	Mean° 25%	30,207	4,006	2,127	1,756	1,670	3,212
Mean 50%	4,914	0,686	0,244	0,224	0,411	2,984	Mean° 50%	69,263	13,359	4,948	4,011	4,070	40,670
Mean 75%	6,100	3,050	0,299	0,288	0,747	6,667	Mean° 75%	74,101	55,734	7,434	6,085	6,242	72,624
Radius	2,25	2,25	2,25	2,25	2,25	2,25	Radius	2,25	2,25	2,25	2,25	2,25	2,25
Scale	0,7698	1,1547	1,73205	2,59808	3,8971	5,8457	Scale	0,7698	1,1547	1,73205	2,59808	3,8971	5,8457
Mean 0%	0,000	0,000	0,000	0,000	0,000	0,000	Mean° 0%	0,000	0,000	0,000	0,000	0,000	0,000
Mean 10%	0,577	0,075	0,027	0,027	0,043	0,059	Mean° 10%	12,192	2,308	0,655	0,507	0,664	0,575
Mean 25%	1,879	0,174	0,083	0,073	0,081	0,096	Mean° 25%	48,608	5,901	1,743	1,034	1,072	0,741
Mean 50%	3,947	0,406	0,163	0,142	0,162	0,198	Mean° 50%	70,307	14,048	3,470	2,029	2,135	1,500
Mean 75%	6,998	1,130	0,168	0,178	0,304	0,467	Mean° 75%	74,422	24,451	6,155	2,389	2,524	2,854
Radius	3,375	3,375	3,375	3,375	3,375	3,375	Radius	3,375	3,375	3,375	3,375	3,375	3,375
Scale	0,7698	1,1547	1,73205	2,59808	3,8971	5,8457	Scale	0,7698	1,1547	1,73205	2,59808	3,8971	5,8457
Mean 0%	0,000	0,000	0,000	0,000	0,000	0,000	Mean° 0%	0,000	0,000	0,000	0,000	0,000	0,000
Mean 10%	2,055	0,207	0,045	0,027	0,019	0,021	Mean° 10%	91,201	7,138	1,120	0,430	0,229	0,201
Mean 25%	4,563	1,196	0,113	0,049	0,040	0,062	Mean° 25%	78,409	123,139	3,478	1,036	0,609	0,675
Mean 50%	6,367	2,165	0,232	0,095	0,080	0,123	Mean° 50%	83,897	122,998	7,429	2,099	1,228	1,345
Mean 75%	6,299	1,385	0,441	0,194	0,164	0,212	Mean° 75%	68,116	38,931	9,362	3,523	1,932	1,799
Radius	5,0625	5,0625	5,0625	5,0625	5,0625	5,0625	Radius	5,0625	5,0625	5,0625	5,0625	5,0625	5,0625
Scale	0,7698	1,1547	1,73205	2,59808	3,8971	5,8457	Scale	0,7698	1,1547	1,73205	2,59808	3,8971	5,8457
Mean 0%	0,000	0,000	0,000	0,000	0,000	0,000	Mean° 0%	0,000	0,000	0,000	0,000	0,000	0,000
Mean 10%	3,001	1,948	0,246	0,035	0,014	0,012	Mean° 10%	100,449	26,726	6,220	0,585	0,191	0,138
Mean 25%	3,471	2,835	0,659	0,087	0,068	0,073	Mean° 25%	112,345	122,760	9,969	1,317	0,555	0,340
Mean 50%	2,686	2,191	0,738	0,176	0,067	0,064	Mean° 50%	113,321	113,381	18,422	2,838	0,952	0,698
Mean 75%	6,887	6,882	1,830	0,241	0,197	0,210	Mean° 75%	95,839	97,540	17,590	4,007	1,673	0,995
Radius	7,59375	7,59375	7,59375	7,59375	7,59375	7,59375	Radius	7,59375	7,59375	7,59375	7,59375	7,59375	7,59375
Scale	0,7698	1,1547	1,73205	2,59808	3,8971	5,8457	Scale	0,7698	1,1547	1,73205	2,59808	3,8971	5,8457
Mean 0%	1,424	0,000	0,000	0,000	0,000	0,000	Mean° 0%	18,368	0,000	0,000	0,000	0,000	0,000
Mean 10%	5,321	2,988	2,647	0,282	0,050	0,035	Mean° 10%	62,361	58,202	28,178	5,081	0,429	0,161
Mean 25%	4,873	3,765	3,568	0,726	0,086	0,036	Mean° 25%	74,698	83,559	37,430	7,900	0,810	0,295
Mean 50%	6,622	2,408	2,646	1,200	0,234	0,175	Mean° 50%	84,621	64,481	109,410	18,689	2,083	0,796
Mean 75%	7,452	2,667	3,726	1,500	0,348	0,261	Mean° 75%	81,679	84,755	67,088	27,993	3,136	1,186

Table 7.3: Same as Table 7.1 for Flat Convolved tubes with Hessian as section estimator.

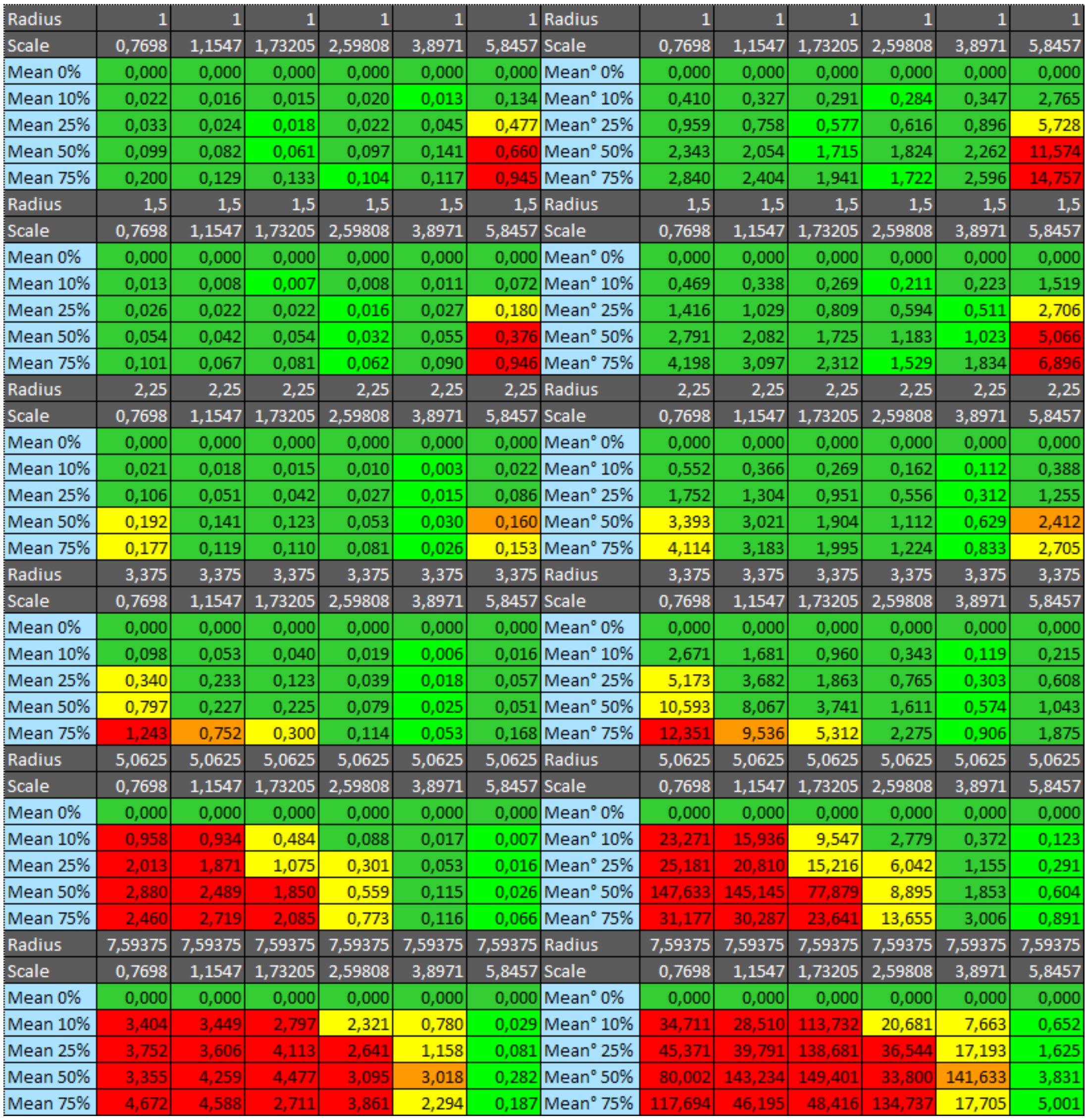

Radius	1	1	1	1	1	1	Radius	1	1	1	1	1	1
Scale	0,7698	1,1547	1,73205	2,59808	3,8971	5,8457	Scale	0,7698	1,1547	1,73205	2,59808	3,8971	5,8457
Mean 0%	0,000	0,000	0,000	0,000	0,000	0,000	Mean° 0%	0,000	0,000	0,000	0,000	0,000	0,000
Mean 10%	0,022	0,016	0,015	0,020	0,013	0,134	Mean° 10%	0,410	0,327	0,291	0,284	0,347	2,765
Mean 25%	0,033	0,024	0,018	0,022	0,045	0,477	Mean° 25%	0,959	0,758	0,577	0,616	0,896	5,728
Mean 50%	0,099	0,082	0,061	0,097	0,141	0,660	Mean° 50%	2,343	2,054	1,715	1,824	2,262	11,574
Mean 75%	0,200	0,129	0,133	0,104	0,117	0,945	Mean° 75%	2,840	2,404	1,941	1,722	2,596	14,757
Radius	1,5	1,5	1,5	1,5	1,5	1,5	Radius	1,5	1,5	1,5	1,5	1,5	1,5
Scale	0,7698	1,1547	1,73205	2,59808	3,8971	5,8457	Scale	0,7698	1,1547	1,73205	2,59808	3,8971	5,8457
Mean 0%	0,000	0,000	0,000	0,000	0,000	0,000	Mean° 0%	0,000	0,000	0,000	0,000	0,000	0,000
Mean 10%	0,013	0,008	0,007	0,008	0,011	0,072	Mean° 10%	0,469	0,338	0,269	0,211	0,223	1,519
Mean 25%	0,026	0,022	0,022	0,016	0,027	0,180	Mean° 25%	1,416	1,029	0,809	0,594	0,511	2,706
Mean 50%	0,054	0,042	0,054	0,032	0,055	0,376	Mean° 50%	2,791	2,082	1,725	1,183	1,023	5,066
Mean 75%	0,101	0,067	0,081	0,062	0,090	0,946	Mean° 75%	4,198	3,097	2,312	1,529	1,834	6,896
Radius	2,25	2,25	2,25	2,25	2,25	2,25	Radius	2,25	2,25	2,25	2,25	2,25	2,25
Scale	0,7698	1,1547	1,73205	2,59808	3,8971	5,8457	Scale	0,7698	1,1547	1,73205	2,59808	3,8971	5,8457
Mean 0%	0,000	0,000	0,000	0,000	0,000	0,000	Mean° 0%	0,000	0,000	0,000	0,000	0,000	0,000
Mean 10%	0,021	0,018	0,015	0,010	0,003	0,022	Mean° 10%	0,552	0,366	0,269	0,162	0,112	0,388
Mean 25%	0,106	0,051	0,042	0,027	0,015	0,086	Mean° 25%	1,752	1,304	0,951	0,556	0,312	1,255
Mean 50%	0,192	0,141	0,123	0,053	0,030	0,160	Mean° 50%	3,393	3,021	1,904	1,112	0,629	2,412
Mean 75%	0,177	0,119	0,110	0,081	0,026	0,153	Mean° 75%	4,114	3,183	1,995	1,224	0,833	2,705
Radius	3,375	3,375	3,375	3,375	3,375	3,375	Radius	3,375	3,375	3,375	3,375	3,375	3,375
Scale	0,7698	1,1547	1,73205	2,59808	3,8971	5,8457	Scale	0,7698	1,1547	1,73205	2,59808	3,8971	5,8457
Mean 0%	0,000	0,000	0,000	0,000	0,000	0,000	Mean° 0%	0,000	0,000	0,000	0,000	0,000	0,000
Mean 10%	0,098	0,053	0,040	0,019	0,006	0,016	Mean° 10%	2,671	1,681	0,960	0,343	0,119	0,215
Mean 25%	0,340	0,233	0,123	0,039	0,018	0,057	Mean° 25%	5,173	3,682	1,863	0,765	0,303	0,608
Mean 50%	0,797	0,227	0,225	0,079	0,025	0,051	Mean° 50%	10,593	8,067	3,741	1,611	0,574	1,043
Mean 75%	1,243	0,752	0,300	0,114	0,053	0,168	Mean° 75%	12,351	9,536	5,312	2,275	0,906	1,875
Radius	5,0625	5,0625	5,0625	5,0625	5,0625	5,0625	Radius	5,0625	5,0625	5,0625	5,0625	5,0625	5,0625
Scale	0,7698	1,1547	1,73205	2,59808	3,8971	5,8457	Scale	0,7698	1,1547	1,73205	2,59808	3,8971	5,8457
Mean 0%	0,000	0,000	0,000	0,000	0,000	0,000	Mean° 0%	0,000	0,000	0,000	0,000	0,000	0,000
Mean 10%	0,958	0,934	0,484	0,088	0,017	0,007	Mean° 10%	23,271	15,936	9,547	2,779	0,372	0,123
Mean 25%	2,013	1,871	1,075	0,301	0,053	0,016	Mean° 25%	25,181	20,810	15,216	6,042	1,155	0,291
Mean 50%	2,880	2,489	1,850	0,559	0,115	0,026	Mean° 50%	147,633	145,145	77,879	8,895	1,853	0,604
Mean 75%	2,460	2,719	2,085	0,773	0,116	0,066	Mean° 75%	31,177	30,287	23,641	13,655	3,006	0,891
Radius	7,59375	7,59375	7,59375	7,59375	7,59375	7,59375	Radius	7,59375	7,59375	7,59375	7,59375	7,59375	7,59375
Scale	0,7698	1,1547	1,73205	2,59808	3,8971	5,8457	Scale	0,7698	1,1547	1,73205	2,59808	3,8971	5,8457
Mean 0%	0,000	0,000	0,000	0,000	0,000	0,000	Mean° 0%	0,000	0,000	0,000	0,000	0,000	0,000
Mean 10%	3,404	3,449	2,797	2,321	0,780	0,029	Mean° 10%	34,711	28,510	113,732	20,681	7,663	0,652
Mean 25%	3,752	3,606	4,113	2,641	1,158	0,081	Mean° 25%	45,371	39,791	138,681	36,544	17,193	1,625
Mean 50%	3,355	4,259	4,477	3,095	3,018	0,282	Mean° 50%	80,002	143,234	149,401	33,800	141,633	3,831
Mean 75%	4,672	4,588	2,711	3,861	2,294	0,187	Mean° 75%	117,694	46,195	48,416	134,737	17,705	5,001

Table 7.4: Same as Table 7.1 for Flat Convolved tubes with Optimally Oriented Flux as section estimator.

Type	Centerline Error		Angle Error	
	Min	Max	Min	Max
Accurate	0.0	0.15-0.2	0.0	2.0-3.0
Not accurate/ Oscillating	0.15-0.2	0.4-0.5	2.0-3.0	5.0-7.5
Difficult	0.4-0.5	1.0	5.0-7.5	20.0-25.0
Lost / No tracking	1.0-2.0	...	20.0-25.0	180.0

Table 7.5: Approximate values obtained for each qualitative tracking type

optimal tracking. The scales that yield best values are in most cases larger than the radius. In Table 7.5 we provide approximate values obtained for the qualitative types of tracking described above.

say approximately that, for the mean centerline error, values under $0.15-0.2$ represent an *accurate tracking*, values between $0.15-0.2$ and $0.4-0.5$ represent correct trackings with some loss of accuracy, such as *oscillating tracking*, values between $0.4-0.5$ and 1.0 represent tracking with difficulties and

Here we can make some disctintions according to the tube size:

- For small radii ($R=1.0$ and $R=1.5$) the best values are found for scales around $\sqrt{3}R$ which is according to the theory of Krissian *et al.* for Gaussian tubes . Good tracking is achieved in most cases, except for the larger scale values due to a poor localization. There are sometimes problems with high levels of noise (50 and 75%) and the lowest scales, specially for the Hessian estimator, since the smoothing of the kernel is too small for the noise levels and scales are close to the inner scale of the data (sampling). The Oriented Flux estimator is more robust in these situations.

- For medium radii ($R=2.25$ and $R=3.375$) best values are mostly found for scales about $1.2R$. For small scales, the tracking start to fail since they are too small with respect to the size of the tube and, for the case of the Gaussian, the smoothing is not so strong, which is good against noise. Again the behaviour of the OF is better for small scales.

- For larger radii ($R=5.0625$ and $R=7.59385$) we can see that best scales are probably beyond the ones we used in our experiments and better results are obtained in general for the Hessian estimator. This is due to the large amount of smoothing with large Gaussian derivative kernels, which are very robust against noise and give response for a reasonable number of scales. On the other hand, the OF has a very good localization, since it uses gradient values at small scales in the sphere surface, but this makes the detection rate much worse at large scales. One solution to this problem is increasing the scale for the gradient calculations in the sphere, but keeping into account that it should not be according to the radius but to the width of the boundary of the tube. Regarding computation times, the Hessian is much slower due to the large kernels involved whereas, in the case of the OF, computation times are the same[1].

---

[1] Unless the sampling of the sphere where flux is calculated is increased with the radius.

Figures 7.3 to 7.5 show the plots for the mean centerline error for different values of tube radius and noise levels which allows to compare the numbers obtained. For the case of the datasets without noise, we can see that there is no error for all situations except one of the worst (largest radius, smallest scale and highest noise level). For the noisy datasets we can distinguish again three situations:

- For small radii ($R = 1.0$ and $R = 1.5$) the OF shows more precision, with an excellent behaviour for flat convolved (FC) tubes. This is normal since the OF adapts very well to this section profile in which there is a narrow transition for the boundary. The behaviour of the OF with the Gaussian tubes is similar to the Hessian but a bit better. Larger scales give the worse results and also small scales with high levels of noise in the case of the Hessian.
- For medium radii ($R = 2.25$ and $R = 3.375$) we can see a transition in behaviour. At $R = 2.25$ results are still very good for the OF, specially with FC tubes. However the Hessian starts to behave quite well except for the smallest scales. Its behaviour is quite similar at $R = 3.375$ but here the OF starts to give poor results for the Gaussian where there is no sharp edge involved. At this radius, results are good for the FC except for the smallest scales which is starting to be poor.
- For larger radii ($R = 5.0625$ and $R = 7.59385$) we can confirm that the Hessian gives more precise and consistent responses for a larger range of scales, and the error increases abruptly for some small scale values, which leaves them out of the plots. The behaviour of the OF is specially poor for the FC tubes when the scale chosen is too small. In these cases, the sphere used to calculate the flux lies completely inside the tube and since it is flat in most of its section, no boundary is detected and the section estimator is poor. In the case of the Hessian, the aperture of the derivative kernels extends beyond the expected boundaries and thus results are slightly better. Results are worse in this case for the FC tubes, since their boundary is less diffuse. The increased smoothness due to large Gaussian kernels also works against very noisy data. The OF definitely behaves poorly with Gaussian tubes. We can also see that the OF only gives good values for a few large scales, for the reasons mentioned above, and thus is more selective but may miss the tube if the right scale is not chosen. In all cases, the scale needed for optimal detection at $R = 7.59385$ seems to be larger than the ones used.

Figures 7.6 and 7.7 represent the plots of the mean angle error along the 40 calculated cross-sections obtained by the Hessian and OF section estimators for different scale values and noise levels. Again we compare results for Gaussian versus flat convolved (FC) tubes and distinguish three situations:

- For small radii ($R = 1.0$ and $R = 1.5$) we can see that the angle estimation is poor for high levels of noise due to the small sizes of the tubes to be detected with respect to the inner scale of the data (resolution). Best results are found again for FC tubes with OF detection. Here, the effect of noise in the angle estimated by the Hessian is more evident than in the center position. For larger scales, in the cases where the tube is still tracked successfully, the centerline

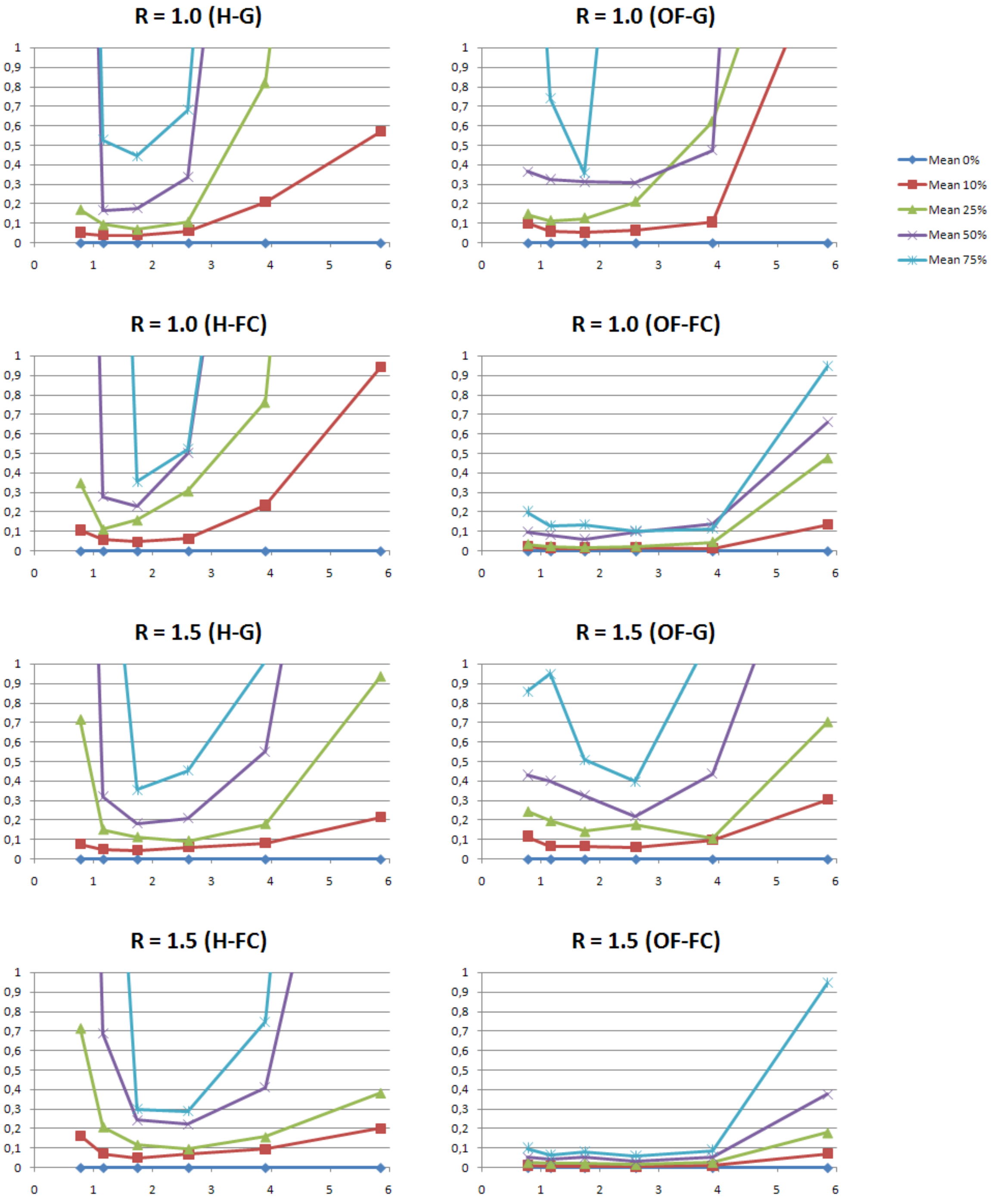
R = 1.0 (H-G)

R = 1.0 (OF-G)

R = 1.0 (H-FC)

R = 1.0 (OF-FC)

R = 1.5 (H-G)

R = 1.5 (OF-G)

R = 1.5 (H-FC)

R = 1.5 (OF-FC)

Figure 7.3: Mean values for in-section center point estimation error for different detector scale values (x axis) along tubes of $R = 1.0$ and $R = 1.5$ as calculated for the Hessian (H) and Oriented Flux (OF) section estimators and for tubes with Gaussian (G) and Flat Convolved (FC) cross-section. Series show results for different levels of noise with respect to the signal (0, 10, 25, 50 and 75%)

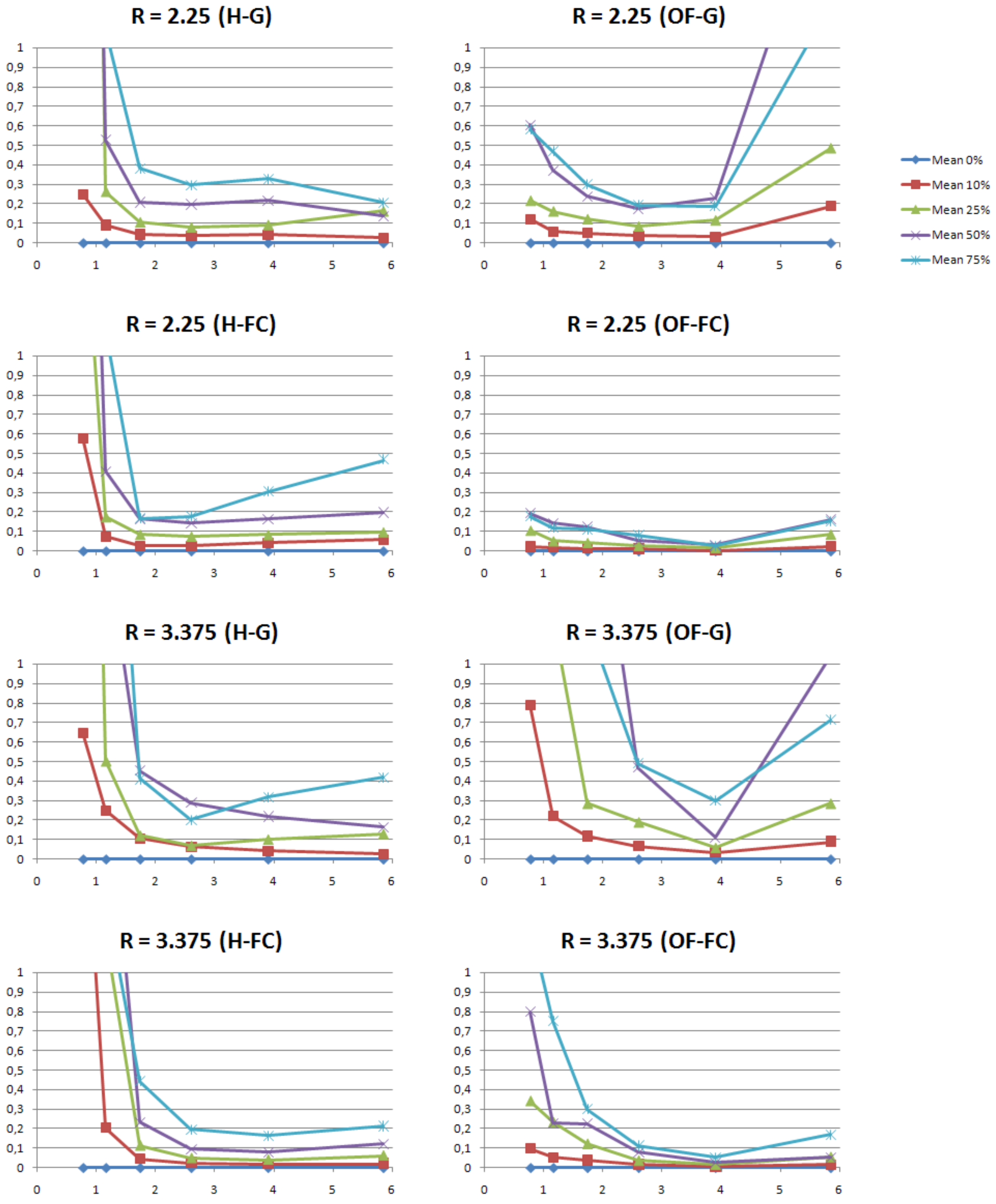

Figure 7.4: Same as Fig. 7.3 for $R = 2.25$ and $R = 3.375$

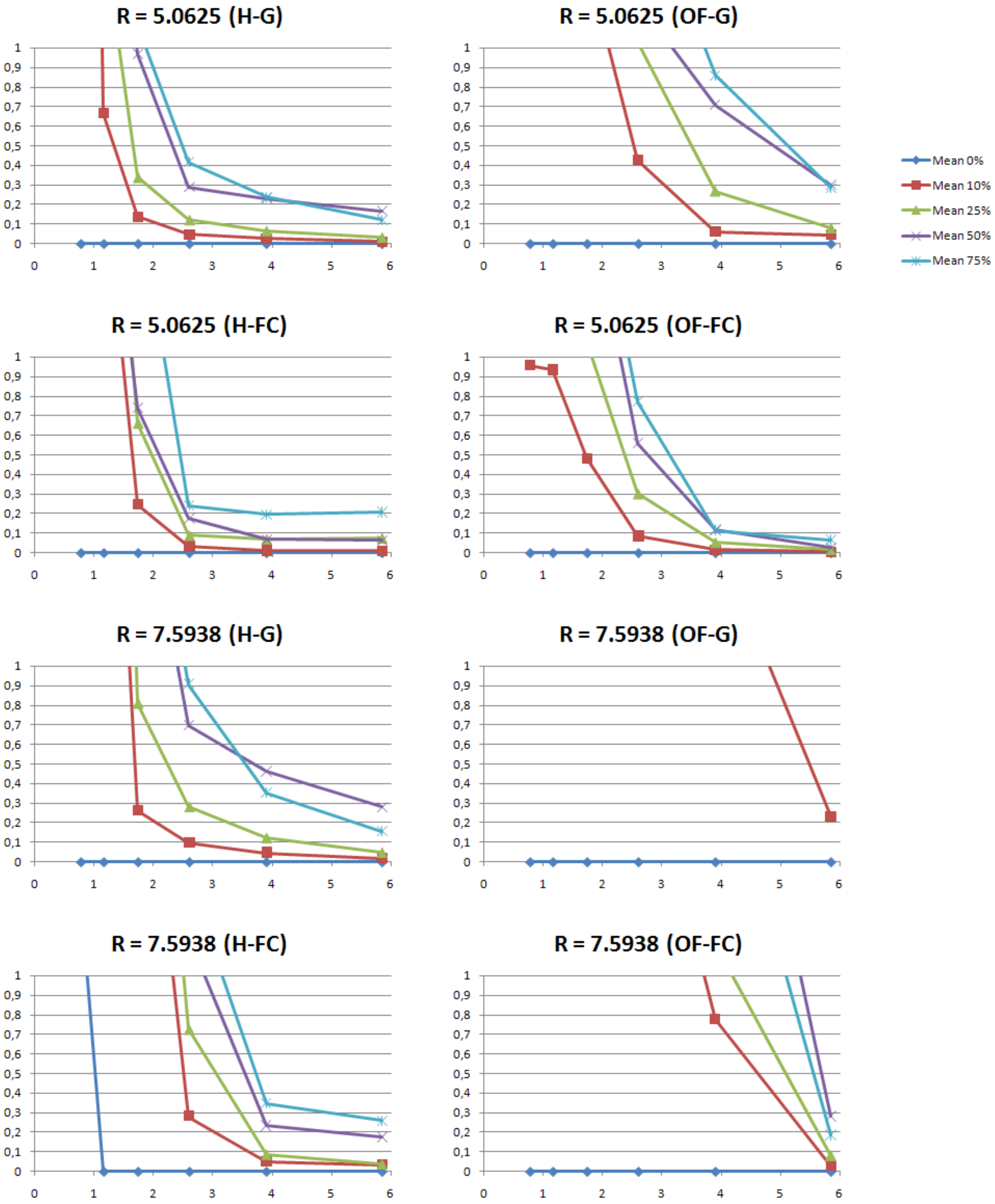

Figure 7.5: Same as Fig. 7.3 for $R = 5.0625$ and $R = 7.5938$

oscillates in a zig-zag pattern, since no correction of the trajectory is involved, yielding higher angular errors.

- For medium radii ($R = 2.25$ and $R = 3.375$) the behaviour is very similar for both detectors, except for the OF detector with FC tubes which shows very accurate results at all scales and noise levels. In most cases, at small scales either the tracking is lost or important difficulties are found, which some sections very poorly estimated.

- For larger radii ($R = 5.0625$ and $R = 7.59385$) the behaviour is also similar to the mean centerline error. Many values out of the plots represent unsuccessful tracking attempts. The OF is lost in most circumstances or shows lost of difficulties and for an appropiate behaviour of this estimator, larger scales should be selected and probably in larger number due to the selectivity of the estimator. The Hessian behaves better at large scales yielding acceptable angular errors.

As we have seen, the FC tube, in general, requires more precision in the scale selection, specially for large scales. One advantage of the OF estimator with respect to the Hessian, is that it requires smaller apertures and thus, calculations are faster. This allows us to test a wider range of scales in order to mitigate the problem of missing the border due to the selectivity of the filter. Again, there is a compromise between detection and accuracy. The Hessian seems to be less sensitive to the scale selection but also is less selective. In order to improve the detection rate of the OF for large scales, one may choose to increase the scale of the gradient calculations involved (which was fixed in our experiments to $\sigma = 1.0$ as were used in) but according to the expected transition width of the tube boundary, and not according to the whole tube radius.

The OF estimator is more selective in the scale selection, but at the cost of possibly failing to detect the tube with a wrong scale choice. On the other hand, the Hessian shows itself very robust against noise, specially with larger radius values and is able to detect the tubes at a wider range of scales. This is due to the large support of the Gaussian kernel at wide apertures, which increases the smoothing and the detection rate at the cost of poorer localization and slower calculations. Moreover, the support of the Gaussian derivative kernels at large scales tend to extend far beyond the tubes to be detected, resulting in an influence by external spurious structures which may hamper the detection. This was one of the main reasons for proposing the OF algorithm in .

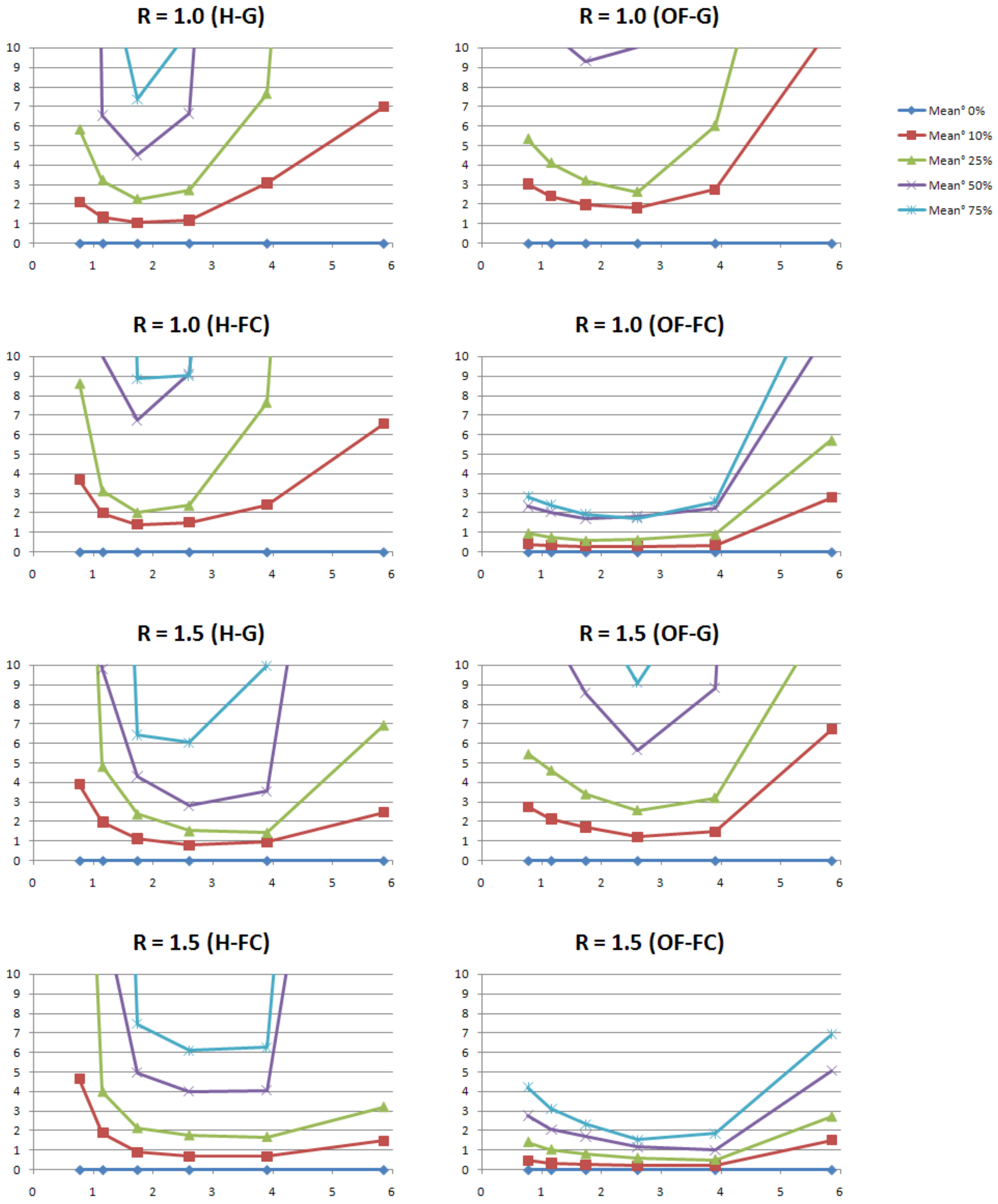

Figure 7.6: Mean values for section angle estimation error (with respect to the z-axis) for different detector scale values (x axis) along tubes of $R = 1.0$ and $R = 1.5$ as calculated for the Hessian (H) and Oriented Flux (OF) section estimators and for tubes with Gaussian (G) and Flat Convolved (FC) cross-section. Series show results for different levels of noise with respect to the signal (0, 10, 25, 50 and 75%)

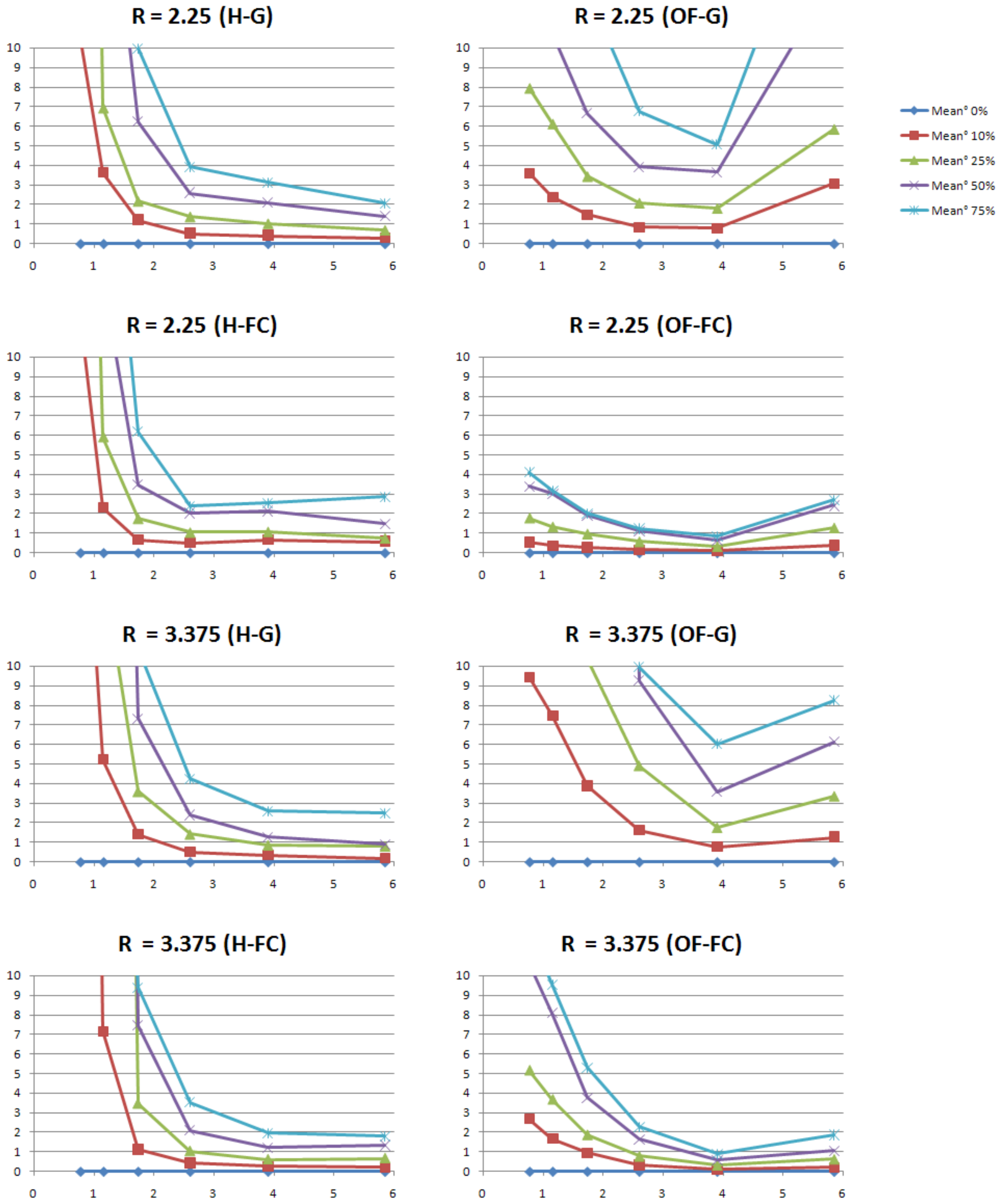
R = 2.25 (H-G)

R = 2.25 (OF-G)

R = 2.25 (H-FC)

R = 2.25 (OF-FC)

R = 3.375 (H-G)

R = 3.375 (OF-G)

R = 3.375 (H-FC)

R = 3.375 (OF-FC)

Figure 7.7: Same as Fig. 7.6 for $R = 2.25$ and $R = 3.375$

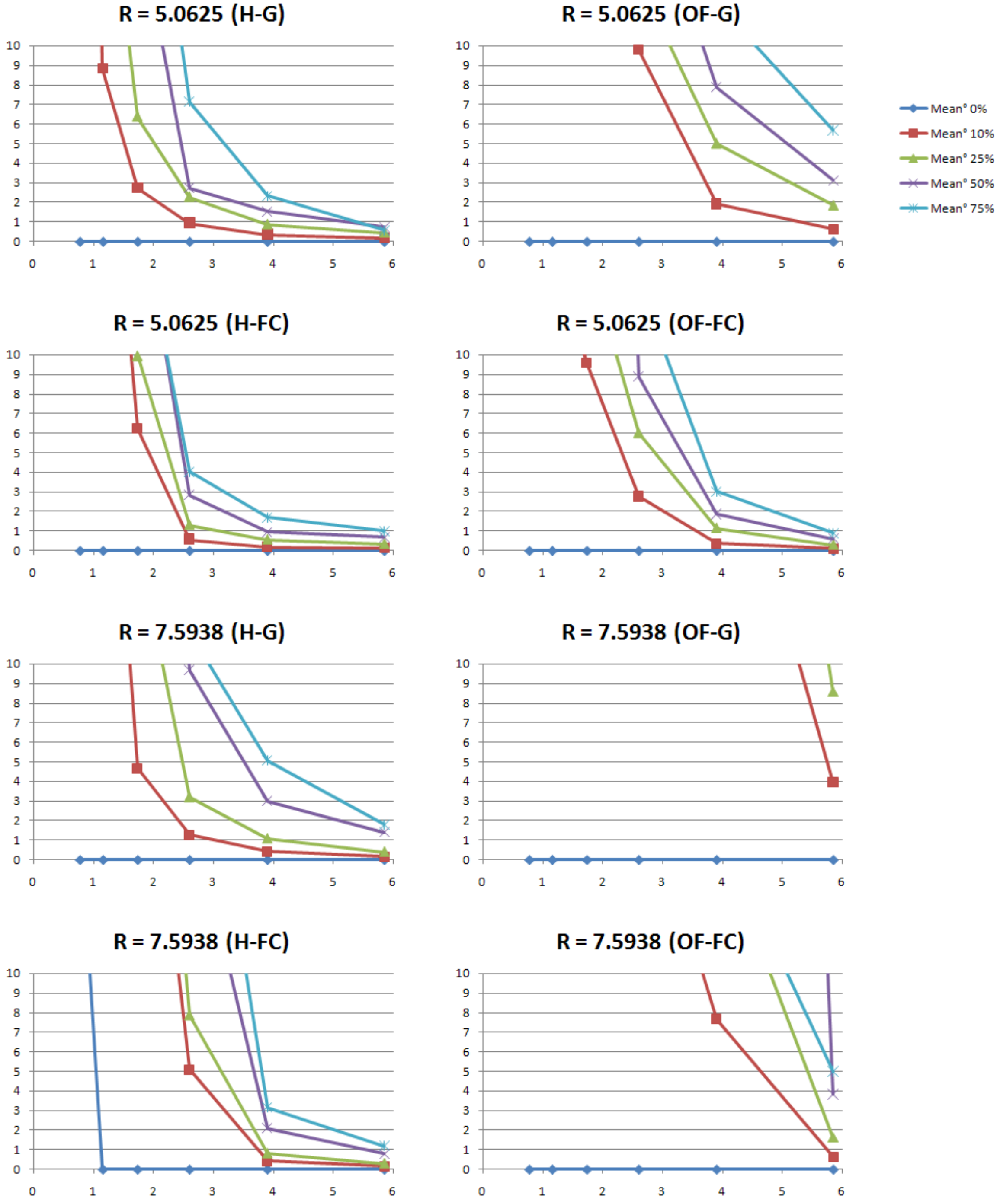

Figure 7.8: Same as Fig. 7.6 for $R = 5.0625$ and $R = 7.5938$

7.2.2 Multi-scale Extraction

7.2.3 Multi-scale Extraction with Correction

7.2.4 Dynamic Filtering and Heuristics (for Correction and Recovery)

7.3 Optimized Vessel Section Estimation

7.3.1 Introduction

In the previous section we have seen that the *Section Estimators* used in tracking procedures to estimate the local centerline position and orientation may fail due to the presence of noise, incorrect scaling or other undesired phenomena such as presence of adjacent spurious structures. This results in incorrect local sections that often lead to unrecoverable errors during the tracking procedure. On the other hand, improving the estimation of local section may be interesting in other procedures other than tracking, for example for quantification of the section geometry, local curvature, centerline length, etc.

Standard *Section Estimators* that provide a direct solution where demonstrated within the GVT Framework at fixed-scale 7.2.1, multiple scales 7.2.2, by incorporating a *Medialness Metric* for scale selection, and with a correction stage 7.2.3 that accounted for possible errors in the estimation.

In order to improve the accuracy and robustness of the section normal and radius estimation, we propose to combine the standard approach of obtaining a direct solution from the *Section Estimator* with a non-linear evolutionary optimization procedure. The current approach uses a 1+1 evolutionary strategy (ES) algorithm [159] for optimization and a cost function based on classical *Section Estimator* approaches such as the ones described before, in order to detect the local optimal orientation and size (radius) of the vascular structure. The optimization may also be useful to find the optimal parameters for the estimators.

7.3.2 Evolutionary Optimization Scheme for Section Estimation

The vascular feature detection with evolutionary optimization procedure consists of converting a vesselness measure into a cost function that is optimized with respect to a set of parameters. Currently, we use the optimization in order to obtain an optimal section estimator. For this purpose, the vesselness measure needs to be a medialness measure, with the largest values on the vessel axis. In our experiments, we have used the offset medialness measure of Krissian *et al.* [79] described in Chapter . The problem can be expressed mathematically as:

$$\arg\max_{u\in\Omega} R_\sigma(x_c,u), \quad \Omega=\left\{u=(n,r)\in\mathbb{R}^4\right\} \quad \text{s.t. } \|n\|=1 \tag{7.4}$$

The optimization procedure tries to find the optimal unit section normal n and radius r of the medialness at each section center point x_c(assuming that is the real vessel section center).

We could incorporate the unit normal constraint into the optimization by using Lagrange multipliers:

$$\arg \max_{u \in \Omega, \lambda \in \mathbb{R}} \Lambda(x_c u, \lambda) = R_\sigma(x_c, u) - \lambda \left(1 - \|n\|^2\right) \tag{7.5}$$

This would involve a 4D parameter space for optimization with a constraint. However, we can reduce the dimensionality of the parameter space and avoid the use of the Lagrange multipliers. For the first purpose, we observe that the components of the unit section normal, which are the director cosines, are related to each other by the expression:

$$\|n\| = \sqrt{n_x^2 + n_y^2 + n_z^2} = 1 \tag{7.6}$$

Then, the optimization procedure can be expressed as:

$$\arg\max_{u \in \Omega} R_\sigma(x_c, u), \quad \Omega = \left\{u = (n_x, n_y, r) \in \mathbb{R}^3\right\} \quad \text{s.t. } \left\{|n_x| < 1, \left|n_y\right| < 1\right\} \tag{7.7}$$

This means that we have a 3D search space with two unit normal coordinates and the radius of the detector since the last coordinate is calculated with the above formula[2].

On the other hand, the new constraints for the n_x and n_y coordinates can be implemented very easily by returning a zero value for the cost function when the constraints are not met. This is a fast and simple alternative to other more complex approaches such as using Lagrange multipliers.

Note that here the section center is not optimized and it is assumed to be previously calculated, but it could be incorporated into the procedure. The scale σ of the derivative calculations could also be included into the optimization. However, discrete Gaussian scale-space derivatives [92] are calculated locally using an implementation with discrete kernels [103] and this would require the calculation of a large kernel at each optimization step.

The procedure for obtaining the section normal then becomes a two stage method (see Figure 7.9), assuming that we are located on a vessel center point:

1. Estimate the local section using a standard non-optimized estimator. This gives a single solution for the section normal, given the scale, radius and center point. The initial parameters are chosen from the neighbor point if previously calculated. A multiscale approach tests a discrete range of scales and selects the scale that yields the maximum medialness value.

2. Compute the best parameters for the optimization problem in eq. 7.7 using a (1+1)-ES evolutionary optimizer. Take as starting point the parameters and value of the section normal and radius calculated on the first stage.

Next, we proceed to describe our experiments with real datasets that demonstrate the validity of the method.

---

[2] Note that this would not be true with standard variable-length vectors

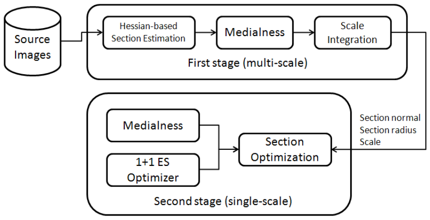

Figure 7.9: Two-stage vessel estimation scheme used in our experiments.

7.3.3 Incorporation into the GVT Framework

For the realization of the following experiments, we seamlessly incorporated the described scheme into our realization of the GVT Framework as a specific realization of the *Search Stage* (see 7.1.2.2) that uses an *Optimizer* component (see 7.1.2.1). In turn, the *Optimizer* uses a *Vesselness Metric* component adapted as a cost function. For the following experiments, we used a single algorithm both for the *Optimizer* and *Vesselness Metric*, but the software realization framework implemented in the IVAN library allows changing these individual components in order to test their influence individually. This demonstrates the validity and versatility of the framework for different experimental setups.

7.3.4 Experiments

We tested our optimization methods with real 3D datasets, one Contrast-enhanced Magnetic Resonance Image (MRI) of the liver, one Magnetic Resonance Angiography (MRA) of the abdomen and one Computerized Tomography Angiography (CTA) of the abdomen. The resolution of the data was variable, with the liver MRI 1.56x1.56x3.0 mm. spatial resolution, the CTA with 0.72x0.72x1.5 mm. and the MRA 1x1x1.5 mm.

For each dataset, we manually delineated the approximate centerline of one or two long vessels: one major liver vein in the MRI dataset, the aorta in the MRA dataset, and iliac arteries in the other two CTA datasets. The points were interpolated by a B-Spline curve which was then sampled in order to increase the number of centerline points.

First, we estimated the sections by the direct method of calculating the eigenvectors of the Hessian matrix. In order to select the scale, for each centerline point, we computed the offset medialness in the estimated section plane and chose the parameters for the best value (scale, section normal and radius). We used a discrete range of scales ranging from 1.0 to 7.0 using a step size of 1.0. The radius used was the scale times a factor of $\sqrt{3}$ which is a good radius estimate for Gaussian tubes [79]. For all our experiments we used $\xi = 0.5$ for the medialness asymmetry parameter.

Second, we computed the sections with our optimization scheme. In order to keep the two normal components in the range $[-1, 1]$, we simply returned zero as the medialness value outside this interval. The radius was also constrained in the range $[0, R_{max}]$ where R_{max} is chosen above the maximum expected radius value on the images. The scale was fixed in all our experiments to $\sigma = 1.0$, since we found out that the detection was more sensitive to the radius.

The optimization scheme used a non-linear optimization algorithm called (1+1)-Evolution Strategy (ES) [159] as implemented in [187], which belongs to the family of Evolutionary Algorithms [147]. As initial parameters, we chose the normal and the radius from the first step. The medialness was calculated each time on the estimated section. The stop condition was either 5000 iterations or a minimal search radius of 0.25 (Frobenius norm of the covariance matrix). Most of the times the procedure was finished after about 2000 iterations. Note, that our focus here was to test the validity of the approach and not the performance of the optimizer. The latter has quite a lot of margin for improvements, for example, by trying to reduce the search space or by tuning the parameters for optimal performance.

7.3.5 Results

Results of the described method for both stages are shown in Fig. 7.10. The 3D render shows the estimated sections and radius depicted as circles at each centerline point (actually we did not draw all the centerline points but only a subset). Note that the standard estimator works quite well at estimating the sections. This is normal since most of the vessels were clearly visible. However, there was a high variation in the scale and radius estimation along the vessels. The optimized procedure shows very precise results at estimating the section and radius, except maybe at bifurcations, where the first stage also fails. Note specially that the accuracy in the radius estimation is really high, which would be difficult to estimate by manually setting the parameter on the first stage.

It is important to note that our method can be applied to virtually any vesselness function. In this sense, the method can be thought of as both a shape and parameter estimator, thus decreasing the number of parameters of the original estimator. In our experiments, we have initialized the parameters for each section independently of the results of the previous optimization. However, the optimizer can be initialized with an initial position corresponding to the previously calculated point. In this way, the optimization procedure would be less time consuming.

The optimization stage is slower than the previous step (in the order of minutes, rather than in the order of seconds). In practice, it should only be used when we require accurate values of radius and section normal or when the value of the direct section estimator is likely to be incorrect. During a tracking procedure, this can be detected as an outlier, for example, when the normal exceeds an angle with respect the previous normal along the vessel path (assuming that the step size is small enough). It may also be used as a parameter estimator for the standard procedure obtaining parameter values to be used in a given application.

On the other hand, the scale for the medialness was fixed to a small value in the optimization stage. The reason is that the scale for this family of medialness function should be chosen according to the size of the vessel boundaries (the boundary is relatively thin) and not according to the diameter. Otherwise, precision would also be penalized, since we would have a poorer localization with higher scales. This is an important conclusion, since we see that, for these types of vesselness functions, we can operate at lower scales and with less variability. The reason is that the scale of the di-

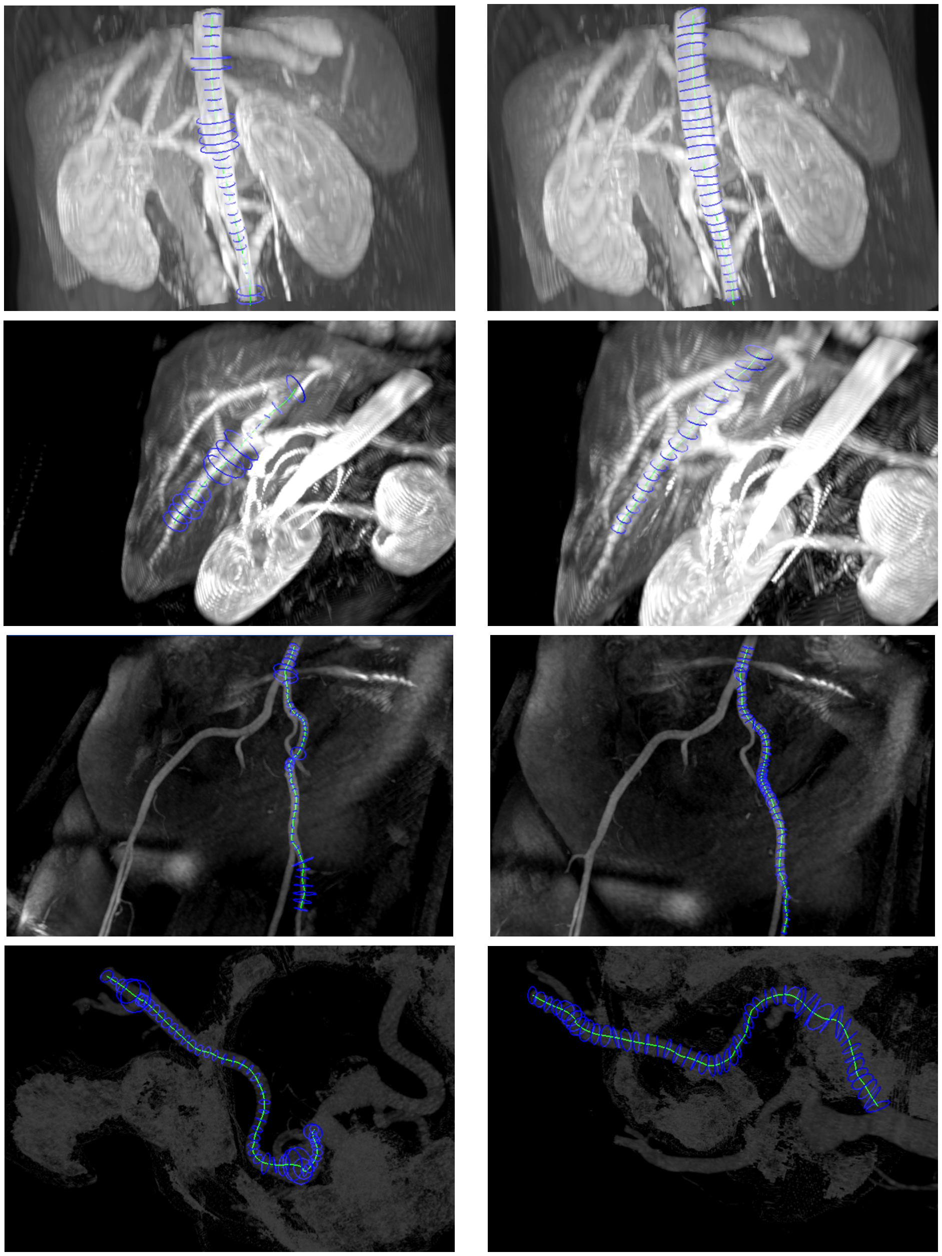

Figure 7.10: Volume rendering of real datasets with rendering of estimated vessel sections. Delineated centerlines are shown in green and estimated sections in blue. For each row, from top to bottom, results for an aorta in a MRI, one major liver vessel in the same MRI, and iliac arteries for a MRA (third row) and CTA (fourth row) study. Left column depicts the results of the first, direction estimation stage. Right column shows the results after the evolutionary optimization procedure.

ameters may vary considerably but the scale of the vessel boundaries not so much. For local calculations using discrete kernels, this supposes smaller kernels and less kernel recalculations, which is computationally faster. The procedure also does not require estimating the Hessian at each iteration, which makes it faster than expected.

Chapter 8

Analysis of Abdominal Aortic Aneurysms

Abdominal aortic aneurysms (AAAs) are one of the major complications in great blood vessels. Endovascular aneurysm repair (EVAR) is the preferred technique for its intervention and its success is measured on the basis of the bulge retraction in Computed Tomography Angiography (CTA) volumes. Thus, CTA image segmentation for AAA measurement is a relevant task for primary diagnosis and follow-up after intervention. This chapter describes and evaluates a refined version of a fast and accurate method for the segmentation of the thrombus of AAAs after EVAR based on a radial model approach. It uses a priori knowledge and spatial coherency for obtaining and initial thrombus contour which is then refined by removing spurious sectors. This approach provides a fast segmentation and easy parameter setup while maintaining a high degree of accuracy, which makes it suitable for clinical routine. We also consider the case where the thrombus is located in the bifurcation of the iliac arteries. Thrombus segmentation results are presented in real clinical CTA images used for EVAR follow-up which demonstrate the high speed and accuracy of the method.

The structure of the chapter is organized as follows. Section 8.1 gives an introduction to the medical problem and development of the chapter. Section 8.2 provides the state of the art in thrombus segmentation. Section 8.3 describes the initial approach to aortic lumen and AAA thrombus segmentation, reporting some experimental results. Section 8.4 discusses the issue of the iliac arteries. Section 8.5 presents the improved thrombus segmentation process with some experimental results. Section 8.6 gives conclusions on the AAA thrombus processes. Section 8.7 presents the endoleak detection process reporting experimental results. Finally, Section 8.8 gives our conclusions on the endoleak detection process.

8.1 Introduction

Abdominal Aortic Aneurysm (AAA) is a condition where the weakening of the aortic wall leads to its widening and the generation of a thrombus in the abdominal region of the aorta. AAAs are one of the most recurrent conditions in cardiovascular surgery, if untreated, AAA usually tends to wear and rupture with high risk of mortality [163]. To prevent a possible rupture of the aortic wall, AAA can be treated non-invasively by means of the Endovascular Aneurysm Repair technique (EVAR), consisting of placing a stent-graft inside the aorta by a cateter to exclude the aneurysm sac from the blood circulation. A cloth graft with a stent exoskeleton is placed within the lumen of the AAA, extending distally into the iliac arteries. This serves as a bypass and decreases the pressure exerted on the aortic wall, leading to a reduction in AAA size over time and a decrease in the risk of aortic rupture. An Intraluminal Thrombus (ILT) forms in the majority of abdominal aortic aneurysms. Correctly excluded aneurysms progressively shrink after EVAR surgery.

The pre-operative planning and prognosis are done on the basis of CTA imaging [12]. Close follow-up is required after endovascular repair, with CTA scans performed at one, six, and twelve months, and with a year periodicity after that. It has been suggested [170] that the aneurysm volume change is the best indicator to determine whether the surgery has been successful, which requires a segmentation of the thrombus. In a successful case it is expected to shrink completely until the aortic wall sticks to the stent graft.

A major complication is the presence of liquid blood turbulences, called *endoleaks*, in the thrombus formed in the space between the aortic wall and the stent-graft, due to incorrect positioning, displacement or torsion of the graft. Although endoleaks are more likely to occur soon after the intervention, lifelong surveillance is required [80]. Endoleaks can be classified in several types, depending on the cause [173, 174]. The most common are Type II endoleaks, which arise from persistent retrogade flow in collateral vessel branches. Some Type II endoleak thrombose spontaneously but some others don't, causing an increase in aneurysm size and risk of rupture. In these cases intervention is required, usually consisting in an embolization of collateral branches.

The characteristic CTA image feature of an endoleak is the presence of brighter material inside the excluded aneurysm sac [158, 161](see Figure 8.1 right). Type II endoleaks typically appear in the periphery of the aneurysm sac without touching the stent [158]. The actual image intensity value of the endoleak varies and depends on the size of the leak and the distribution of contrast material at the moment the image was acquired. They can be confused with with calcifications which appear in the outer aortic wall and are brighter, whereas Type II endoleaks appear typically close to the wall perfusing into the sac and showing an amorphous shape (see Figure 8.1). Since these endoleaks can be approximately characterized, we believe that an automatic detection and quantification system for Type II endoleaks, is possible and would be very helpful, specially in cases where endoleaks are not very clearly visible but may be made evident from the analysis of subtle changes in the image content.

8.1.1 Chapter contributions

This chapter addresses two related image analysis problems.

- First: the AAA thrombus segmentation. We propose a procedure working on a radial representation of the thrombus contours, enhanced with *a priori* knowledge and modeling of spatial coherence. As seen in the right hand of figure 8.1, thrombus may be touching with other structures of similar intensity, so their boundaries are quite difficult to find, even for a trained radiologist.

- Second: the semi-automatic detection of endoleaks in CTA images after the thrombus volume segmentation.
  - (a) Thrombus Connected Components (TCCs) obtained from segmentation of the thrombus image area using a Morphological Grayscale Watershed Transform [30]. Image content-based characteristics are obtained for each TCC.
  - (b) A Multilayer Perceptron (MLP) [56] classifier is built for the automatic detection of (Type II) endoleaks applied on the segmented lumen and thrombus of the AAA. Classification features are geometric and image content-based characteristics of the TCCs. Ground truth for training the MLP are provided by the human experts that classify a large sample of TCCs into two classes “endoleak” and “no-endoleak”.

Experimental results over a collection of AAA scans provided by the show good performance that the MLP is able to characterize and correctly classify image regions inside the aneurysm corresponding to endoleaks after training over the provided labeled sample. Endoleaks are not frequent, therefore imaging data featuring them is scarce. For this reason our system has to be validated at the level of 2D slices, however a 3D extension is easy and will be done when more data is available for training and validation.

The improved thrombus segmentation method, based on a radial model approach with appearance priors and spatial constraints is very fast and needs little human interaction for initialization or parameter tuning. Due to its nature, it can be easily incorporated into a user interface in order to provide visual feedback and easy correction to provide suitable results if, for any reason, the algorithm failed. It may also be easily adapted for the segmentation of AAAs in non-enhanced CT images. Our approach also considers the presence of the ramification of the iliac arteries in the thrombus region.

8.2 State of the art

The aorta lumen usually presents a high contrast in CTA, however, segmentation of the aneurysm thrombus is not a trivial task, due to low-contrast in the ILT region compared to adjacent structures (see Figure 8.1). Manual segmentation by trained radiologists is a time-consuming task, and suffers from intra- and inter-observer variability. With the advent of last generation CT scanners, the number of slices per examination has increased, and the manual delineation of tenths to hundreds of slices becomes impossible on a clinical routine . Hence, the development of automatic or semi-automatic methods for the segmentation of AAAs is required. Furthermore, quantitative assessment of evolution of aneurysms after EVAR is usually performed by taking the largest diameter or cross-sectional area on a single slice, but volume measurement has been demonstrated to show the smallest intra-observer variability [171]. Thus, a (semi)automatic

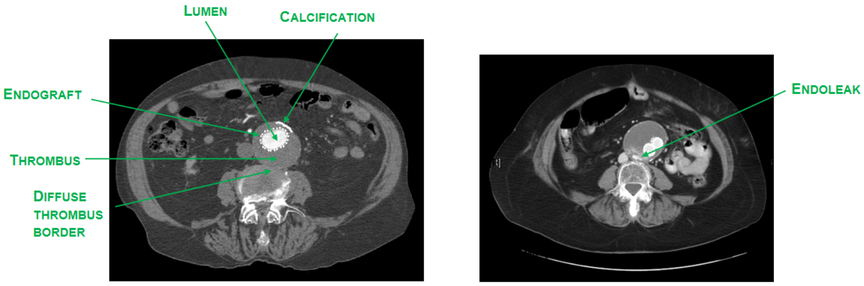

Figure 8.1: Slice showing Abdominal Aortic Aneurysm with different parts (left). A Type II endoleak appears as bright tissue in the thrombus area.

segmentation method would allow patient follow-up using volumetric measurements of aneurysm size.

Automatic or semi-automatic aneurysm segmentation in CTA images is hindered by noise and the similarity of Hounsfield Unit (HU) values for neighboring (touching) tissues. Thrombus segmentation strategies proposed in literature include active contours [191, 35, 123] which are time consuming and difficult to control, with complex stopping conditions. De Bruijne *et al.* used Active Shape Models (ASM) [36] which required a training set with prior segmentations. Dehmeshky *et al.* proposed a grayscale and geometric appearance model [36]. Similarly, we use prior knowledge on the appeareance of the aneurysm, but their method requires masking of several adjacent structures. Recently, 3D Active Object (3DAO) methods [151]have been proposed. Most of these approaches and are time consuming and require some degree of user interaction, sometimes difficult to implement in an interface for clinical routine.

The works presented in [160]and [**?**]need initial manual delineations to initialize their models; the method by de Bruijne *et al.* [**?**] needs posterior user intervention in case of thrombus boundary overflow. Olabarriaga *et al.* [123] employ a binary thresholding to obtain the lumen, which is used as an initialization for a deformable model to segment the thrombus. Simple thresholding takes into account other tissues not connected to the lumen, so further processing is usually needed to avoid those structures. Furthermore, the use of deformable models needs fine parameter tuning to obtain acceptable results. In this regard, [160] uses a level set approach, [**?**] applies an Active Shape Model (ASM). Zhuge *et al.* [191] also presents an algorithm based on a *level-set* approach whose main advantage is the automatization and parameter insensitivity. Nevertheless, the required computing time (in the order of several minutes) is a main drawback. The work by Borghi *et al.* [18] make use of region growing segmentation techniques in order to obtain the lumen boundary, but then use manual delineation of the aneurysm wall to obtain a 3D model of Thoracic Aortic Aneurysm (TAA). A computational study of the drag forces that can produce stent displacement is given in [50] for TAA. The work of Lee et al. [84] performs an initial estimation of the lumen region by region growing after anisotropic smoothing. Then both the lumen and the thrombotic surfaces are built up using a 3D graph search with cost functions specially designed for the lumen and the thrombus surfaces. Parameter values are empirically set, and the algorithm requires interactive guidance of the thrombus segmentation. Regarding endoleak detection, we have not found any work in the literature that adresses the problem of automatic detection and quantification of endoleaks in CTA images.

8.2.1 AAA Segmentation process

We briefly present the complete AAA segmentation process consisting of five stages:

1. *Lumen Segmentation*: an initial lumen segmentation is obtained using a region growing algorithm based on confidence measures from a pair or more seed points as implemented in [187]. A robust segmentation of the lumen and thrombus of the AAA is required as an input for the automatic endoleak detection system, in order to isolate the lumen and thrombus area.

2. *Lumen Centerline Extraction*: performed on a slice by slice basis using 2D image moments on the connected components (CCs). CCs not corresponding to the lumen are discarded by calculating distances of centroids to adjacent slices.

3. *Polar Reformatting*: a slice-based polar reformatting is generated, in order to obtain a linear representation of the radial model which is faster to process. For each slice, the reformatted is restricted to a certain distance a bit larger than the expected maximum thrombus diameter. Strictly, this does not constitute a reformatting on cylindrical coordinates but, rather, a generalized cylinder. This allows to adapt to the shape of the centerline, taking into account its curvature. The presence of a dominant vertical direction makes the method still valid.

4. *Initial Thrombus Segmentation*: based on the analysis of connected components (CCs) described both radially and at slice level. The result is a set of radial contours describing the thrombus outer boundary starting from the inner boundary. It requires a pre-processing step consisting on median filtering, in order to remove noise, and a raw thresholding which removes the hyperintense structure corresponding to the stent and other spurious structures. Note that, differently from other methods, we do not remove any structure outside the thrombus region. The results is a good approximation of the external thrombus contour, with the exception of some areas where the thrombus region invades adjacent structures.

5. *Thrombus Contour Correction*: based on the analysis of discontinuities in the initial contours and statistical information, outlier sectors in radial contours are identified and replaced by interpolation between valid contour segments.

We first describe the intial approach developed in , which is the basis for an improved correction algorithm developed later.

8.3 Lumen and Thrombus Segmentation

In this section, we describe the lumen segmentation, centerline extraction and thrombus segmentation. Our thrombus segmentation approach is based on a radial description of the thrombus contours.

Algorithm 8.1 Centerline extraction from 3D lumen region

```
Initialization of region: center line in first processed slice
for all slices in 3D image do
    Identify lumen connected components from the 3D lumen region
    for each lumen component in slice do
        Compute centroid
        Compute Euclidean distance to centerline point in previous slice
    end for
    Keep nearest centroid as the centerline point
end for
```

8.3.1 Region Growing-based Lumen Segmentation

Segmentation of the lumen is based on a 3D region growing algorithm [63] computed on the CTA volume. First, a Volume of Interest (VOI) is defined in order to reduce the extent of the data and then preprocessed to reduce noise. A manually given seed point on the lumen is at least required for the region growing algorithm. The algorithm includes voxels whose intensity values lie in a confidence interval defined over the current segmented region over an iterative process. At each iteration, all neighborhood voxels are visited and the confidence criterion is evaluated. Then, statistics are recomputed and the next iteration begins. The resulting identified region is smoothed by morphological closing, to fill possible small holes.

8.3.2 Centerline Extraction

The centerline computed as the approximate centroid of the lumen region at each slice is a good approximation of the morphological skeleton of the whole aorta. It serves as the starting point for the thrombus segmentation. A single point on the centerline is obtained for every slice using 2D image moments, since the aorta is almost normal to axial slices. Image moments provide information on the spatial distribution of a given image region corresponding to a structure. The moments of a 2D image are defined as

$$M_{p,q} = \sum_{y=0}^{Y-1} \sum_{x=0}^{X-1} x^p y^q I(x,y), \tag{8.1}$$

where $I(x,y)$ is a discrete image. The centroid is defined as the pair $\left[\frac{M_{10}}{M_{00}}, \frac{M_{01}}{M_{00}}\right]$.

At each slice, we select the 2D connected components obtained from the 3D lumen region corresponding. We compute the centroid of each such 2D lumen connected components. The centroid which is the nearest to the centerline point detected in the previous slice is kept as the next centerline point. The algorithm 8.1, yields a series of points that conform the centerline of the segmented lumen.

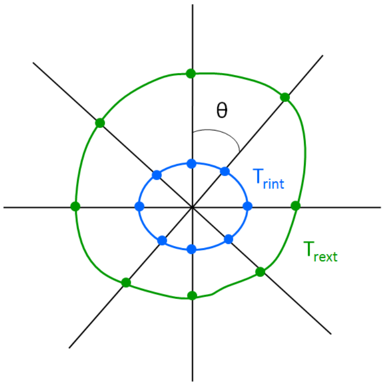

Figure 8.2: Radial model for the thrombus segmentation

8.3.3 Thrombus Segmentation

We model the internal and external radius of the thrombus of the aneurysm as radial distance functions in cylindrical coordinates. We can express the volume of interest around the lumen centerline as

$$\Psi = \Psi(r, \theta, z). \tag{8.2}$$

At every z value, corresponding to a slice of the CTA volume, we choose the origin of these functions to be the centerline point at the corresponding slice. The external and internal radii of the thrombus and the aneurysm can be defined as two contours given by functions of the angle in polar coordinates:

$$\begin{aligned} T_{rint} &= \Psi_{rint}(\theta, z), \\ T_{rext} &= \Psi_{rext}(\theta, z). \end{aligned} \tag{8.3}$$

This idea is depicted in Figure 8.2. The segmentation procedure consists of calculating the values of the internal and external radii T_{rint} and T_{rext} at every angle, which define the closed boundaries enclosing the region corresponding to the thrombus.

Conversion from Cartesian to polar coordinates requires resampling the input VOI. For every slice, a new image is obtained, where the X coordinate represents the radius, starting from the centerline point at the left, and the Y coordinate represents the angle θ, covering 360 degrees with the origin at the top. This polar representation is visualized as an image in Figure 8.3(b). The original CTA slice is shown in 8.3(a).

The polar representation presents several advantages. First, the VOI is converted to a quasi cylindrical VOI (it is not exactly cylindrical, because the centerline is not a vertical line), instead of the typical rectangular prism, but after that it is treated as a standard volume with a regular grid. Second, computation speed is increased, since resampling is only performed once and the polar slices are processed as conventional 2D images.

Next, polar slices are filtered using a median filter to remove speckle and additive noise coming both for the original image and the image resampling needed for the

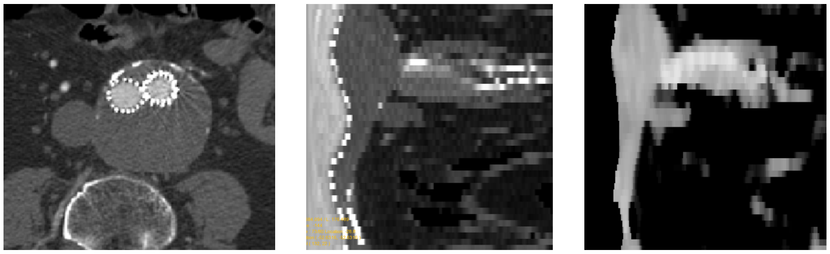
(a) (b) (c)

Figure 8.3: (a) AAA after EVAR viewed on axial slice, (b) polar representation, and (c) median filtered version with lumen and stent thresholded and removed. The origin for the polar coordinate representation of (b) is taken as the centerline in (a).

polar transformation visualization. In order to remove the lumen and the stent from the images without affecting the thrombus voxels, every slice is thresholded in such a way that those image values higher than a threshold Th_{lmn} are converted to a value I_{bgr}, which approximates the background value of the tissue around the thrombus. In our experiments we chose Th_{lmn}=150 HU[1] and I_{bgr}= -100 HU. The result of these operation is shown in 8.3(c). After noise filtering and lumen/stent thresholding, the thrombus appears as the brightest structure closest to the centerline and we can use this *a priori* information for the segmentation.

The internal thrombus radius T_{rint}, which corresponds to the lumen external contour when no endoprosthesis is present, can be found moving away from the centerline (which corresponds to moving along a row in the polar slice image), as the boundary where values different from I_{bgr} appear. The median filter removes the small regions with lower image values that may exist in between.

Localization of the external radius of the thrombus on each slice in polar coordinates is achieved by a local analysis based on two concepts: *radial connected components* (RCC) and *slice connected components* (SCC). We define an RCC as a connected segment over a row of a polar slice and a SCC as a 2D connected component on a polar slice. First, a row-by-row analysis is performed in all slices to create an image of RCCs of each slice. An RCC is created for consecutive pixels of a row that follow a given membership criterion. We use the absolute difference from the mean of the currently detected RCC with a threshold value Th_{RCC} (we use $Th_{RCC} = 20$HU in our experiments). Obtaining T_{rint} and RCC at each row can be done simultaneously. The algorithm 8.2 illustrates the process for creating the RCCs:

Next, we proceed to filter the RCCs. First, RCCs whose average values are not in the intensity range of $Th_{tlow} - Th_{thigh}$ are removed. In our experiments we used $Th_{tlow} = 0$ HU and $Th_{thigh} = 200$ HU which are conservative values to characterize the thrombus image intensity, that apply to most AAA CTA datasets. Second, RCCs that do not start from a distance d_{max} from the external lumen radius are removed too. This criterium is based on the fact that, if a thrombus exists, this must be almost close to the previously thresholded area for lumen and endoprosthesis. In our experiments

---

[1] HU = Hounsfield Units, a normalized CT image intensity value representing X-ray absorption.

Algorithm 8.2 Creating the Radial Connected Components (RCC)

```
Move to the origin of the first polar slice (upper left corner)
for all polar slices do
    for all rows in the current polar slice do
        create a new RCC and insert first pixel on the current row
        for all pixels in the current row do
            if ( intensity(pixel) $\in$ intensity confidence interval of the currentRCC) then
                insert pixel in the current RCC
            else
                calculate and store row internal thrombus radius
        end for
    end for
end for
```

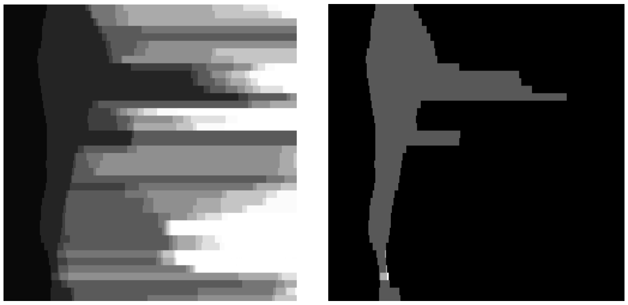

(a) (b)

Figure 8.4: (a) RCCs computed from figure 8.3(c). Different RCCs found along each row are represented in different color (from darker to brighter). (b) filtered RCCs

we also chose $d_{max} = 5$mm. also in a very conservative manner. Results of the RCC computation procedure are shown in Figure 8.4. It can be seen that the thrombus has been almost completely isolated, but some RCCs that are not part of the thrombus still remain (see Figure 8.4(b)).

SCCs are computed using 2D connectivity and the same intensity criteria used for the RCCs. Each SCC keeps a list of RCCs which are included in it. SCCs are used to filter RCCs by using spatial coherency information on each slice. First, SCCs (and corresponding RCCs) that contain less than N_{min} voxels (we use $N_{min} = 10$) are discarded since they are not significant at a slice level. Next, SCCs are filtered by the position of the centroid, having into account that most of the candidate RCCs at this moment are part of the thrombus. For each slice, the position of the centroid for all the RCCs and the corresponding centroid median value are calculated. The median value is a good indicator for the real position of the thrombus. Then we compute the distance from the centroid of every SCC on that slice to the median centroid value, and if the distance is greater than a threshold $d_{centroid} = 20$mm, the SCC is completely removed.

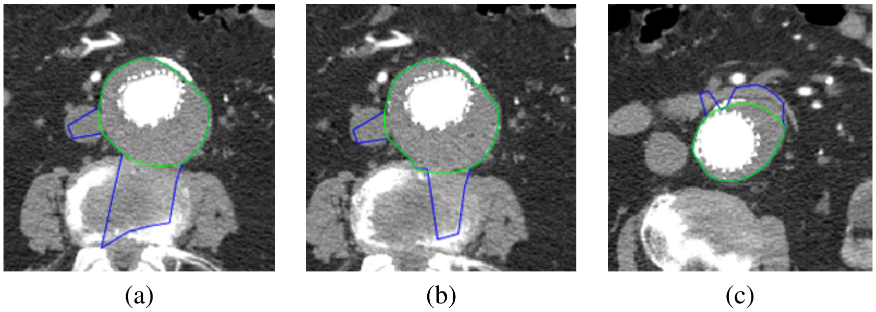

Figure 8.5: Thrombus segmentation results. Correction (green line) of the initial external thrombus radius (blue line). Examples of appropriate correction (a) and (b) and underestimation (c).

Initial values for the thrombus contours T_{rint} and T_{rext} are obtained by taking, for every row on all slices, the first index of the first RCC and the last index of the last RCC on that row (it is assumed that the RCCs remaining after filtering are part of the thrombus). This results in a good approximation to the real external thrombus contour, with the exception of some areas where the thrombus region invades adjacent structures and that represent a discontinuity in T_{rext} (see figure 8.5 blue contours). In order to solve this problem and regularize the contours, a continuity constraint is imposed over T_{rext} and the contour points whose radii are part of a discontinuity are interpolated. Discontinuities are identified as significant radius changes from line to line in the polar image. Then, the radii in these areas are linearly interpolated in order to obtain the final result (green contours in figure 8.5).

8.3.4 Experimental results thrombus detection

Our radial-based thrombus segmentation method has been tested on real human CTA datasets featuring endoleaks confirmed by radiologists, obtained from a LightSpeed16 CT scanner (GE Medical Systems, Fairfield, CT, USA) with 512x512x354 voxel resolution and 0.725x0.725x0.8 mm spatial resolution. Two points inside the lumen, defining the limits of the thrombus region in axial direction, were manually selected as seed points for the 3D region growing segmentation of the lumen. The lumen centerline is then extracted from it to be used as the origin for the polar representation in an area of radius 10 mm around the centerline at each slice. Finally, the described radial function-based model is used to segment the thrombus. Finally, the described radial function-based model is used to segment the thrombus. Some examples of results of the thrombus segmentation method have been shown in figure 8.5 where the initial estimation (blue) and the corrected external thrombus contours (green) are shown.

8.4 Iliac arteries bifurcation

One major problem on AAA thrombus segementation is the presence of double iliac arteries in the thrombus region as shown in Figures 8.6(a) and 8.6(c). Most of the methods assume that the thrombus is only present in the aortic area, where there is a single branch where the lumen may be found. However, this is not always the case, and the bulge may be present in the area where the iliac arteries start, even when the aneurysm itself was not present in this area before the intervention. In this case, the stent forces the two branches of the iliac arteries to be close to each other and we cannot talk any more about a single centerline.

One solution to this problem consists of first segmenting the lumens of both iliac arteries and then extend this segmentation in order to create a convex contour by filling the concave areas between both branches at each slice, as shown on Figure 8.7. This allows us to apply the rest of the segmentation algorithm for the thrombus without further modification.

The convex contour may be obtained easily using open and close morphological operations. The radius for the kernel used in such operations may be set manually or may be determined as the apparent radius obtained for each iliac artery, since this quantity is enough for ensuring complete convexity. In practice, one has two consider also the presence of the stent so the radius is usually a bit larger and complete convexity is not always needed for the algorithm to work (see Figure 8.6(c) where the mask is overlaid).

8.5 Improved Thrombus Contour Correction

The external thrombus contour correction is based on a continuity constraint imposed over the external contour T_{ext}.We assume that the thrombus is radially smooth, allowing for small discontinuities which are first identified as significant radial changes from point to point by using a discontinuity parameter δ.

In order to remove bias in the radius function, we first recompute the centroid and update the angles, which yields a new radial function T'_{rext} for the external contour in which discontinuities are easier to identify. This can be seen in Figure 8.8where the bias due to the offset of the centerline with respect to the thrombus contour was considerably removed. Note that the real center is still unknown and estimated centroid position can be influenced by the incorrect radial estimates.

After the identification of discontinuities, the contour is divided in radial sectors $S_i(\theta_i,\theta_{i+1})$ defined as

$$S_i(\theta_i,\theta_{i+1}) = \left\{T'_{rext}(\theta) : \theta \in [\theta_i,\theta_{i+1})\right\} : \left|T'_{rext}(\theta_i) - T'_{rext}(\theta_{i-1})\right| > \delta, \quad \left|T'_{rext}(\theta_i) - T'_{rext}(\theta_{i-1})\right| > \delta \tag{8.4}$$

Next we identify the spurious radial sectors. We calculate their average values comparing them with the standard deviation from the median of all radial values. That is, we mark a sector $S_i$as spurious if:

$$\mu(S_i) > \kappa\sigma_{median}(T'_{rext}) \tag{8.5}$$

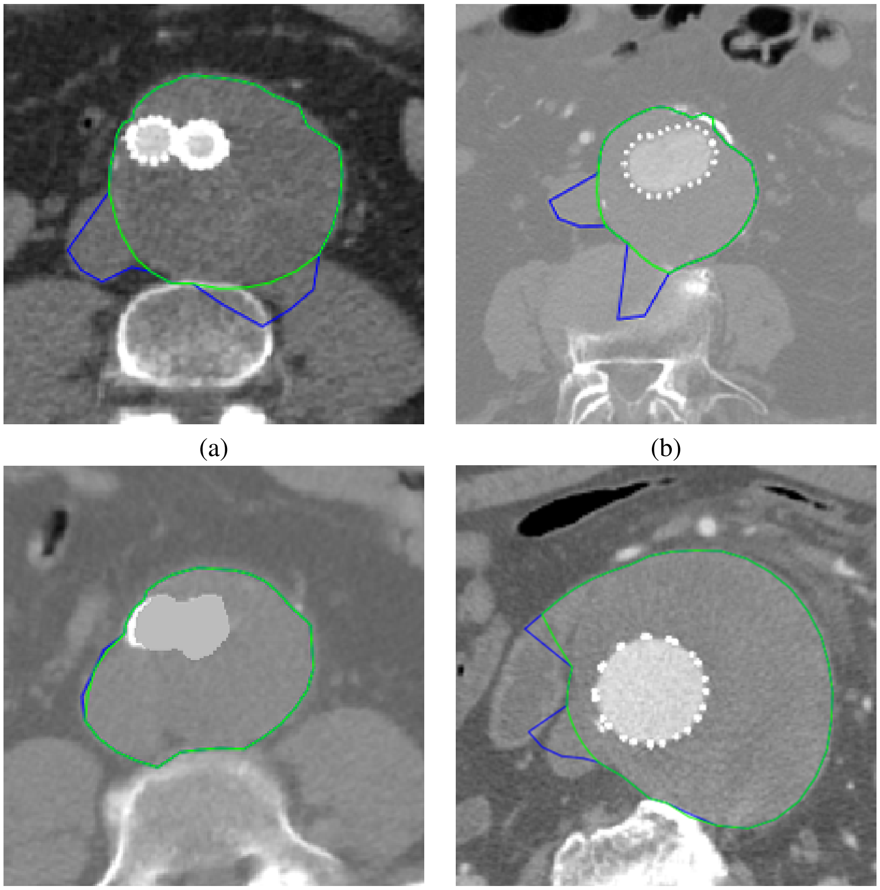

(a) (b)

(c) (d)

Figure 8.6: Segmented slices by our approach showing the initial (blue) and the corrected (green) contours. Note the accuracy in difficult areas. Figure (d) shows some problems found.

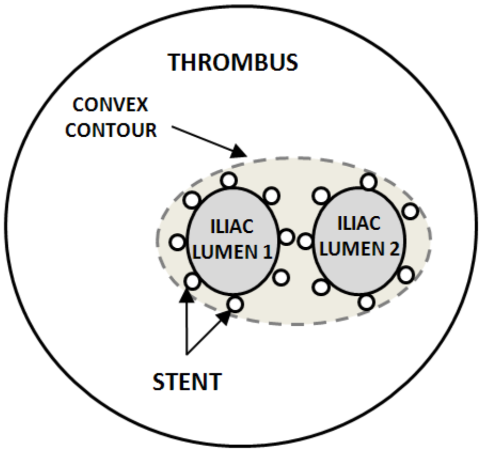

Figure 8.7: Proposed scheme for the lumen segmentation in presence of the iliac arteries in the thrombus region.

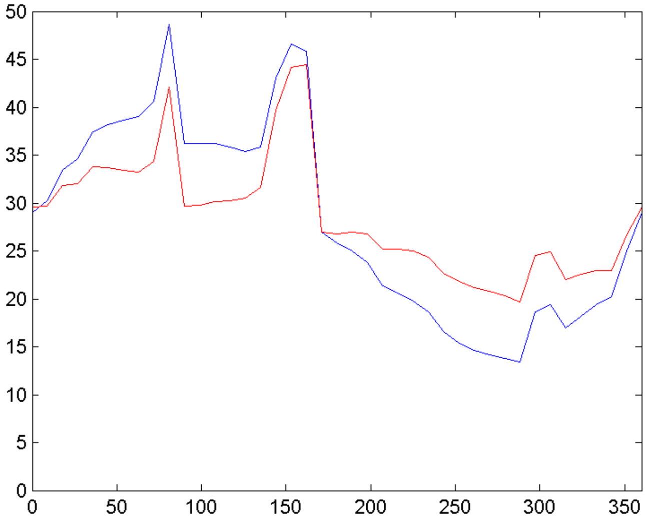

Figure 8.8: Partial removal of bias in radial function of external contour due to recentering. The initial contour is shown in blue and the recentered contour in red. The horizontal axis corresponds to the angle in degrees.

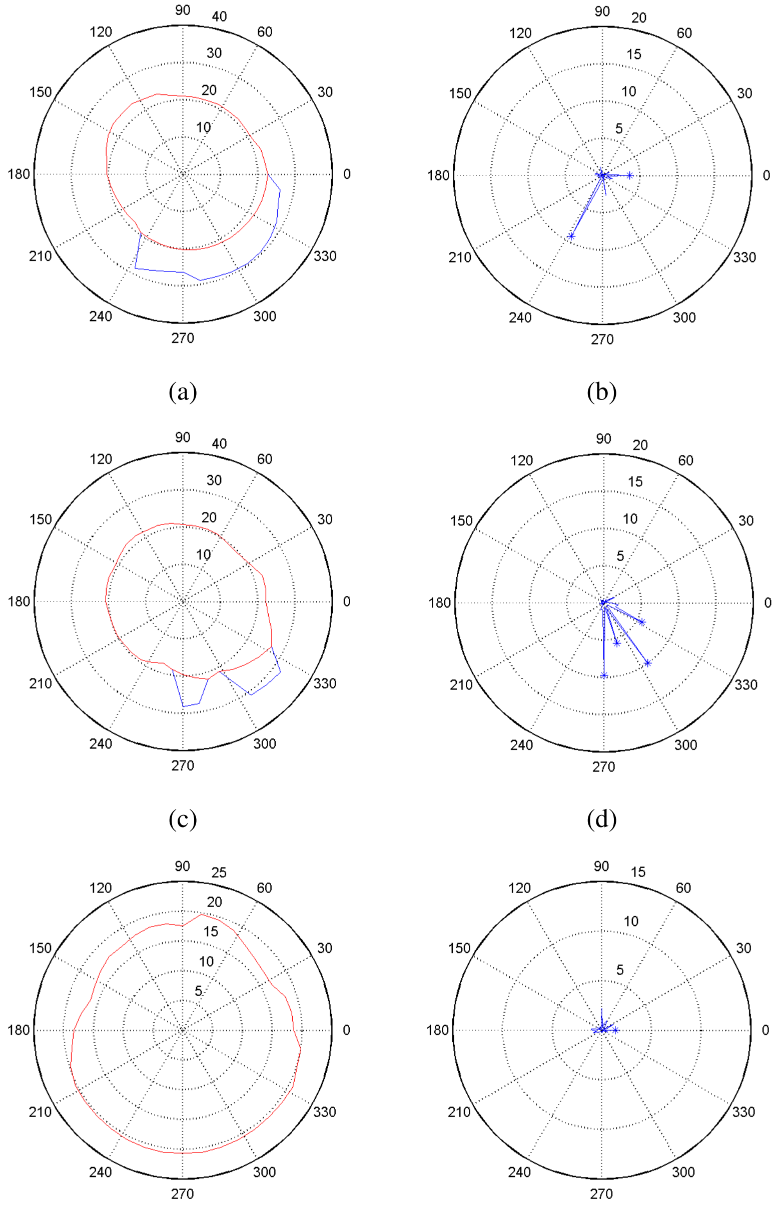

(a) (b)

(c) (d)

(e) (f)

Figure 8.9: Contour correction procedure. Each row corresponds to a diffent slice. Left column shows the initial contour (blue) and the corrected contour (red) in a polar plot. Right column shows derivative of initial contour and identified discontinuities.

where κ is a scaling factor and $\sigma_{median}(T'_{rext})$ is the standard deviation taking the median of radius values. The use of the median here, instead of the mean, avoids that spurious values influence the calculations by contributing with high radial values to the mean. Confirmed contiguous radial sectors are joined to obtain new sectors. Finally, discarded radial sector values are replaced by linearly interpolating between the boundary values of adjacent valid sectors. The procedure is depicted in Figure 8.9where several initial and corrected contours are depicted. Note how the correction removes the spurious sectors and how some small discontinuities are preserved, that appear naturally in the thrombus due to the presence of adjacent structures pushing it. If necessary, this can be adjusted with the discontinuity parameter δ.

8.5.1 Experimental Results of improved thrombus segmentation

Our method has been initially tested on 5 CTA datasets from real patients under follow-up after EVAR, obtained from a LightSpeed16 CT scanner (GE Medical Systems, Fairfield, CT, USA) with an average 0.725x0.725x0.8 mm. spatial resolution. For these datasets, manual segmentations were delineated by experts for comparison. A volume of interest was defined to reduce memory requirements and two seed points inside the lumen were selected for the segmentation of the lumen. From the lumen both the centerline and the polar representation of the image is obtained in an area of 10 mm around the centerline. The described radial approach is used to segment the thrombus contours and finally a mask is obtained by rasterization of the contour on the image grid. In all our experiments, we used 40 angular and 250 radial samples respectively (0.4 mm. radial resolution) for the polar reformatting. The parameters for the initial thrombus segmentation *were not changed* in our experiments. For the correction step we used values of δ in the range 1.5-3.5. The scaling factor κ was fixed to 1.5 except in one dataset which was 2.5. This allowed us to verify that the parameter sensitivity is low, which is good for routine applications. The results were accurate except in some slices with smooth spurious structures that showed no visible boundaries with respect to the thrombus. Furthermore, the processing time was extraordinarily fast and processing a single dataset of about 20 slices took less than 1 s. for the thrombus segmentation in all cases.

In order to assess the accuracy of the thrombus segmentation we performed an initial validation against manual segmentations carefully delineated by experimented raters. For this segmentation, the average overlapping ratio of the automated A and manual B segmentations was calculated as shown in Table 8.1. The first dataset is a typical case of a thrombus segmentation that our method solves with high accuracy (overlapping ratios of 93.52\% and 86.76\%). The four other datasets are from the follow-up of a single patient and can be considered a worst-case scenario. The thrombus has a region with double lumen in the iliac arteries and the lumen is very eccentrical. Yet good values are obtained. We also present some filtered values where we removed the slices were the contour was leaking in a few contour points in order to test the accuracy in the remaining slices. Note that these could be easily corrected changing the parameter values for those slices or by manual correction of the contour. Finally, we present a 3D reconstruction of the contours, depicted in Figure 8.10.

Dataset	(a)	(b)	(c)	(d)
1	93.52±2.51	86.76±5.17	-	-
2	89.86±7.28	83.55±7.07	95.43±2.67	89.79±3.35
3	93.95±8.86	83.88±10.47	96.07±2.32	89.07±3.54
4	89.91±9.28	81.85±10.33	94.98±2.38	88.73±3.04
5	92.10±6.69	79.65±9.63	93.95±5.72	86.72±4.27

Table 8.1: Overlapping areas in \% between proposed method segmentations and ground-truth manual segmentations. (a) = B/A$\bigcup$B, (b) = A$\bigcap$B/A$\bigcup$B. (c)=(a) and (d)=(b) both after removing incorrect contours. Table shows average values for all slices in each datasets.

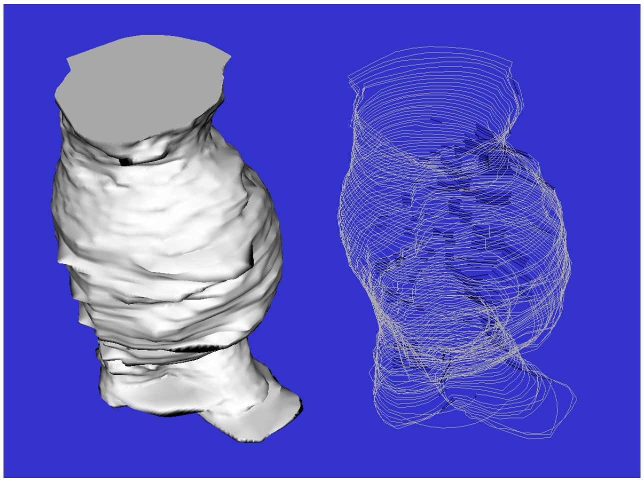

Figure 8.10: 3D polygonal reconstruction (left) and 3D contours (right) for dataset 1.

8.6 Conclusions on AAA thrombus segmentation

As can be seen in Figure 8.5, the method developed for thrombus segmentation shows good results in defining the external contour, where thrombus density is very similar to that of adjacent structures, and very prone to segmentation error in areas close to them. The obtained contour is very accurate due to the assumption of a radial model. The method needs the settings of several thresholds to work. However, our experience demonstrates that the sensibility of the method to these parameters is low as they were chosen very conservatively. One of the main advantages of the method is its computational speed. It took less than 20s to process 80 slices on a Pentium Core 2 Quad at 2.4 GHz. However, the method requires further improvements, since we have observed an underestimation of the radius in some places which were identified as leaks (see Figure 8.5 (c)). Results of this segmentation are comparable to the state of the art found in the literature [84] with less human intervention. Our algorithm does not depend on any user-defined contour or initial manual segmentation. User interaction is minimal: it only needs two seed points contained in the lumen and defining the range of slices of interest. Accurate segmentations are obtained in areas where it is difficult to distinguish the thrombus from adjacent structures. Moreover, the speed of the whole process makes it also suitable for routine clinical use.

One of the main advantages of the improved method is its efficiency, as it can process a large number of slices in a few seconds with high accuracy (Figure 8.6). The parameter setting is minimal and most of our experiments have used the same set of parameters. The value of δ could be changed in order to allow for some tolerance to discontinuities. Increasing the value of κ allows more deviation from the median radius value, in cases where the thrombus is very eccentrical with respect to the centerline. This makes the method suitable for clinical applications for follow-up after EVAR interventions, preoperative planning or for non-contrasted CT.

We emphasize that the improved method is well suited for the segmentation of AAAs by non image processing experts. The nature of the method, that makes use of a radial approach, makes it very easy to develop a user interface for fast segmentation of CTAs. The user simply would have to invalidate possible incorrect regions of the contour and mark only a few radial points at each erroneous section, either manually or by providing the radius value. This has been a major consideration in the design of the method, since we expect it to be part of a software for preoperative planning and follow-up of EVAR interventions. Most of the algorithms fail for one reason or other and we believe that it is important to provide alternatives to fix these errors easily, without fine tuning of complex parameters or complicated contour drawing.

The method provides really accurate results where other methods would fail due to absence of visible thrombus boundaries (Figure 8.6). We can see that the method also allows for some discontinuities that improve the accuracy with respect to some methods based on smooth curves or deformable models which involve complex calculations.

However, the segmentation still allows for some improvements. The method works on a slice-by-slice basis in order to take into account the symmetry with respect to the centerline and to reduce the influence of possible large leaks at volumetric level. However, some spatial coherence at volumetric level could be introduced, especially between adjacent or nearby slices. The polar representation is also advantageous, since

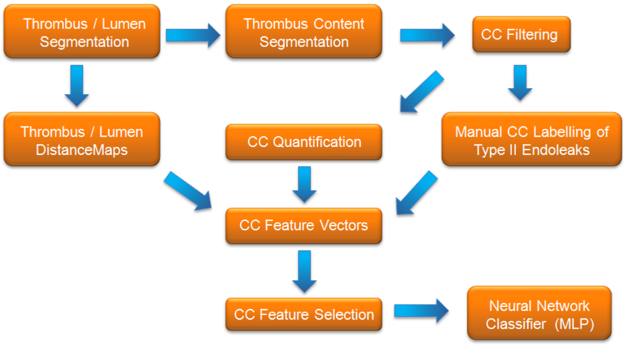

Figure 8.11: Processes of the Automatic Endoleak Classification System

it polar resampling is calculated only once, presents the data in the form of a generalized cylinder VOI around the centerline, which implicitly takes into account the radial symmetry, and allows fast calculations based on CCs and run-length encoding.

8.7 Endoleak detection

An overview of the processes involved in the automatic endoleak classification system can be seen in Figure 8.11. First the aneurysm lumen and thrombus are segmented using the proposed segmentation method described above. We start from a segmentation of the lumen, based on a 3D region growing algorithm, followed by the calculation of the aorta centerline. The thrombus contour is modeled as a function of the radial distance to the computed centerline. The volume of interest is resampled into polar coordinates centered in the aorta centerline.

The thrombus content is further segmented into Thrombus Connected Components (TCC) (section 8.7.1). Using this polar coordinate reference system, the watershed segmentation obtains the TCCs in the thrombus region at both radial and slice level using heuristics based on *a priori* knowledge and spatial coherence. The radial distance functions that describe the thrombus contour are obtained from the resulting connected components and define the target segmented region. The main advantages of this method are its robustness and speed, compared with the state of the art approaches described above. It does not employ sophisticated numerical methods nor needs fine parameter tuning. The TCC features are extracted to be used for classification (section 8.7.2). Once all the features for the TCCs are obtained, these are manually labelled by the experts as endoleaks or not endoleaks. A feature selection is performed (section 8.7.3) to remove redundant or confusing features. This data is used as input for the training and validation of the MLP neural network classifier. Our approach to endoleak detection is based on *a priori* knowledge of the possible location and appearance of endoleaks in CTA images according to what it is described in medical articles, the indications given by expert interventional radiologists, and their manual labelling of relevant TCCs corresponding to endoleaks.

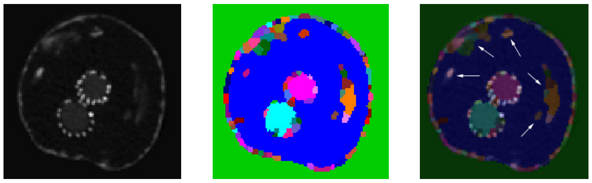
(a) (b) (c)

Figure 8.12: Extraction of Thrombus CCs. (a) Source slice with visible endoleaks, (b) result of Watersheds segmentation, and (c) blended result . Endoleaks are indicated by arrows in (c). Each endoleak corresponds to more than one coloured region (oversegmentation).

8.7.1 Thrombus Connected Component Extraction

After the initial thrombus and lumen segmentation, the thrombus is further segmented in Trombus Connected Components (TCCs) which will be later classified as being endoleaks or not. This segmentation is based on a Topological Grayscale Watershed Transform [30] applied on a slice by slice basis in the area of the segmented thrombus on each slice (see Figure 8.12). First, the image is smoothed using an edge-preserving smoothing filter based on a level-set modified curvature diffusion equation (MCDE) [172]. Two parameters are required for the filter: the conductance parameter, which controls the strength of the edges to preserve and the number of smoothing iterations, which controls the degree of smothing. After filtering, in order to define the watersheds basins, we then calculate the image gradient magnitude.

The Topological Grayscale Watershed Transform is an algorithm for calculating the well-known Watershed Transform [14] in which the image is segmented based on its topology. The gradient magnitude is interpreted as an elevation map and the image relief is flooded dividing it into catchment basins. The pixels of each basin share a local minima and the basin boundaries corresponds to the image edges. The Watershed transform calculation is controled by a single parameter, the Water Level, that controls the height of the flooding, merging adjacent regions as the 'water' ascends to reduce the effect of oversegmentation.

The parameters for all filters involved in this segmentation are chosen in order to distinguish the endoleaks from the background region corresponding to the thrombus, or other adjacent structures. Endoleaks can correspond to a single or several TCCs (oversegmentation) if the water level is low. If it is high, we would have TCC corresponding to both endoleak and other tissues (undersegmentation). Classifying oversegmented endoleaks is not a problem, but solving the undersegmentation problem is not easy, therefore the water level parameter is set to avoid undersegmentation.

8.7.2 Feature Extraction from TCC

We calculated the following geometric features for each labelled TCC that will be used by the MLP-based classification system to determine if the TCC is part of an endoleak region:

- *Area*: number of pixels of the TCC.
- *Area-region Ratio*: ratio of the TCC's bounding box and the area.
- *Binary Principal Moments*: TCC's principal moments of inertia (two features)
- *Equivalent Radius*: radius of a circle of the same area as the TCC and the following image content-based statistical features computed from the image intensity of the CTA image region corresponding to the TCC: *Mean*, *Sigma*, *Median*, *Kurtosis*, *Skewness* and *Elongation* (ratio of the largest to smallest principal image moments).

Besides these features, we need to incorporate another feature that describes the relative position of the TCC with respect to the lumen and thrombus boundaries. We can profit from the observation that Type II endoleaks typically appear close to the thrombus boundary and perfusing inwards. We need this feature to be normalized, since the radius and shape of the thrombus and lumen, and the eccentricity of the lumen with respect to the thrombus is not uniform. Moreover, the lumen can show two branches when the aorta splits in two forming the iliac arteries (see Figure 8.12(a)), so we cannot take the distance to the lumen centroid. Taking all this considerations into account, we propose a feature called Normalized Thrombus Distance (NTD). Two distance maps are first calculated from the thrombus boundary inwards (δ_{lm}) , and from the lumen thrombus boundary outwards (δ_{th}), using Danielsson's algorithm [33] (see distance visualization in figure 8.13). In the rest of image regions the NTD value is zero. Then, we calculate the NTD as:

$$NTD = \begin{cases} \frac{\delta_{lm}}{\delta_{th}} & \text{if} \quad \delta_{lm} \leq \delta_{th} \\ \frac{\delta_{th}}{\delta_{lm}} & \text{if} \quad \delta_{th} \leq \delta_{lm} \end{cases} \tag{8.6}$$

The NTD takes its maximum value of one at thrombus points that are equidistant to the lumen and thrombus boundaries. NTD minimum value is zero and it is taken at the thrombus boundary and outside the thrombus, and at the lumen boundary and inside the lumen. NTD takes values in $[0,1]$ inside the thrombus. For the thrombus and lumen boundaries used as input for the NTD, we can use the segmentation described in 8.3or a manual segmentation.

8.7.3 Reduced Feature Vector for MLP

Let us call the dependent indicative variable *IsLeak*. Its value is 0 for negative TCC and 1 for TCC inside endoleaks. In order to reduce the classifier system's complexity and increase the speed of the calculations, a subset of features is selected as input for the network based on the absolute value of the Pearson correlation coefficients between the dependent variable *IsLeak* and the rest of variables (features) defined as:

$$r = \frac{\sigma_{XY}}{\sigma_X \sigma_Y} \tag{8.7}$$

In figure 8.14we can see the results of calculating the absolute value of the Pearson Coefficients for the CCs of all the slices in the aneurysm region for a given dataset.

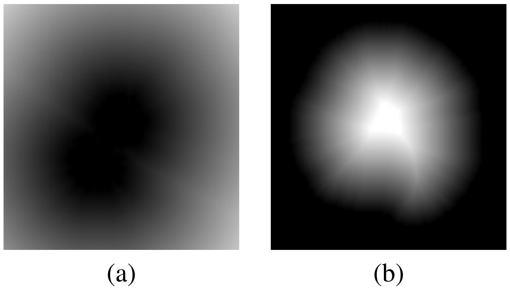

Figure 8.13: Visualization of the distance maps used to calculate the NTD feature. (a) distance to the lumen δ_{lm} and (b) distance to the thrombus δ_{th}.

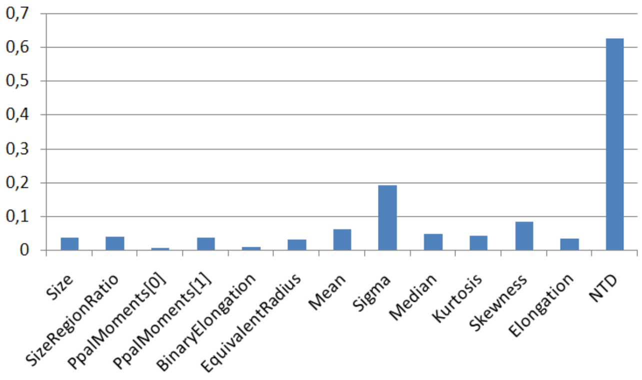

Figure 8.14: Absolute value of Pearson's Correlation Coefficients of each feature with the indicative variable *IsLeak*

As expected, we can see that the NTD feature is highly correlated with the dependent variable, since the feature was designed to incorporate the *a priori* knowledge of the spatial distribution of the endoleaks. We can see that the standard deviation value is also important, meaning that the image intensity value, also as expected, should play an importante role in the characterization of endoleaks. The experimental results show that the reduced feature vector obtain by this straighforward approach give comparable classification results.

8.7.4 Endoleak Detection Experimental Results

The classification scheme was tested independently on each single CTA volume from patients with Type II endoleak after EVAR treatment. The whole volumes consisted of 383 slices in a 512x512 matrix, with a in-plane spatial resolution of 0.703 mm. and a slice thickness of 0.8 mm. Due to the scarce availability of volumes from patients affected with endoleaks, we tested our approach independently on each volumen, working on a 2D slice-by-slice basis. In eachis case, we took as input for the MLP training

DataSet	Accuracy	Sensitiviy	Specificity
1	92.39	93.43	91.36
2	93.68	93.66	93.69
3	93.09	93.66	92.52
4	93.21	94.13	92.29
5	92.16	93.43	90.89
Av.	92.90	93.66	92.15

Table 8.2: Classification results for the training/test data build from full feature vectors, 10-fold crossvalidation. The table shows the total accuracy, sensitivity and specificity for each dataset. Last row shows the average across datasets. All calculations were performed with 3 hidden nodes, learning rate = 0.3 and training time = 550 epochs.

the results of a segmentation of the lumen and thrombus regions validated by expert radiologists. The Watershed-based segmentation was performed on the slices corresponding to the aneurysm region in each dataset using the implementation provided by the *Insight Toolkit* [63] for the Topological Grayscale Watershed Transform. We used the following parameters for the different filters involved in the watershed segmentation: smoothing conductance = 50.0, smoothing number of iterations = 10, Watersheds water level[2] = 9.0. The *NTD* distance-map feature was calculated from the input thrombus and lumen segmentations. The TCCs were manually labelled as being part of an endoleak. From the group of negative TCCs, we proceeded to select randomly an equal number of samples in order to obtain a balanced training/testing set.

Classification experiments were performed using the MLP implementation provided in [180]. The MLP neural network consisted feature described in section 8.7.2, a hidden layer with three neurons and two binary outputs, with sigmoid functions. Network training and validation was performed using 10-fold cross-validation in all computational experiments. Initially, we used the full training/test set consisting of the full feature vectors described in section 8.7.2. The results are shown in table 8.2. Results are above 90% accuracy, with a high sensitivity which is very interesting because the cost of false negatives is much higher than that of false positives.

Next, we test the improvement in the classification results by testing reduced sets of features selected according to the correlation results found in section 8.7.3 (Figure8.14). The best results were obtained by selecting the following features: *Area*, *Mean*, *Sigma* and *NTD*, . We can see in Table 8.3 that the classification rate improves, reaching 93.65% accuracy with a sensitivity of 94.37% and a specificity of 92.94%. The best results give a success rate of 94.73% with a sensitivity of 94.37% and a specificity of 95.09% for the second dataset.

Figure 8.15 shows the influence of several parameters of the MLP in the classification performance measures. We can see that the best results are obtained for a training

---

[2] as a percentage of current image dynamic intensity range

DataSet	Accuracy	Sensitivity	Specificity
1	93.79	94.84	92.76
2	94.73	94.37	95.09
3	93.68	94.60	92.76
4	93.33	94.13	92.52
5	92.74	93.90	91.59
Av.	93.65	94.37	92.94

Table 8.3: Classification results for the training/test data build from reduced feature vector, 10-fold crossvalidation. The table shows the total accuracy, sensitivity and specificity for each dataset. Last row shows the average across datasets. All calculations were performed with 3 hidden nodes, learning rate = 0.3 and training time = 550 epochs.

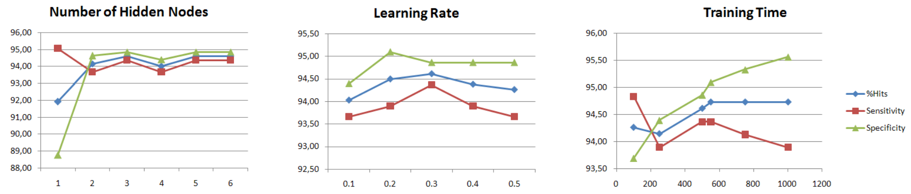

(a) (b) (c)

Figure 8.15: Influence of Neural Network Parameters. Accuracy, sensitivity and specificity are calculated. Parameters tested are number of hidden nodes (a), learning rate (b) and training time measured in number of epochs (c).

time of 550 epochs, a learning rate = 0.3 and 3 hidden nodes. These sensitivity experiments, were performed on the training/test dataset that gives best results on the reduced feature vector (dataset 2).

8.8 Conclusions on endoleak detection

We have demonstrated an automatic system for the detection of (Type II) endoleaks in CTA images of Abdominal Aortic Aneurysms. The classification results show that the system is able to detect endoleaks with high accuracy based on the analysis of extracted TCCs. The use of neural networks is specially adequate for this case, since we do not need to explicitly incorporate the clinical *a priori* knowledge in terms of precise parameters and thresholds for image intensities, distances, etc. This is a common characteristic in many classification problems in medical imaging, in which the specialist is able to discriminate at first sight the object of interest, but is not able to explicitly indicate the rules that guide their mental discourse while diagnosing, which is usually the product of accumulated experiencie and observations.

Classification results over several real datasets shwon in Tables 8.2 and 8.3 show that the system obtains accuracy results above 90% with high sensitivity, which is specially important given the high cost of not recognizing endoleaks present in the image. We have also demonstrated that a careful selection of features, decreases the complexity of the problem and improves the results. There is no similar work in the literature, therefore the results can be assumed as a initial reference for future works.

Regarding the parameters used for the MLP model, in the case of using five features, we have seen that results are very similar when the number of hidden unist is two or more. Using five, six or more nodes does not improve the results and so the best balance is found with three nodes. It can be seen that the influence of the learning rate is limited when the number of epochs is high enough (around 500). With respect to the training time, best results are obtained with 550 epochs and global classification results do not improve by increasing this number. However, the plots show that the sensitivity decreases as the specificity increases, keeping a constant rate of total hits. This is undesiderable since we want the sensitivity to be high, and thus the optimum is found at 550 epochs.

In the near future, we expect to extend the system to 3D analysis of TCCs, and to the detection of endoleaks obtained from several datasets. Since the diagnosis of endoleaks is not totally certain, we also expect to incorporate a fuzzy or probabilistic description in order to determine which TCCs are endoleaks. Another possible improvement to the system, is the classification of other types of endoleaks (I, III, IV and V), since currently the system was trained only to identify Type II endoleaks. This would probably need the incorporation of other types of features for the analysis. Finally, the system would need deeper clinical validation in order to integrate it in clinical environments for diagnosis support of the evolution of AAAs treated with EVAR.

Bibliography

[1] M. Abramowitz and I.A. Stegun, editors. *Handbook of Mathematical Functions with Formulas, Graphs, and Mathematical Tables*. 1972.

[2] D. Adalsteinsson and J. A. Sethian. A fast level set method for propagating interfaces. *J. Comput. Phys.*, 118(2):269–277, 1995.

[3] G. Agam, S. G. Armato III, and C. Wu. Vessel tree reconstruction in thoracic ct scans with application to nodule detection. *IEEE Trans. Med. Imaging*, 24:486–499, 2005.

[4] G. J. Agin and T. O. Binford. Computer description of curved objects. *IEEE Trans. on Computers*, 25(4):439–449, Apr 1976.

[5] S. Aharinejad, W. Schreiner, and F. Neumann. Morphometry of human coronary arterial trees. *The Anatomical Record*, 251:50–59, 1998.

[6] K. Akitaa and H. Kugaa. A computer method of understanding ocular fundus images. *Pattern Recognition*, 15(6):431–443, 1982.

[7] G. E. Andrews, R. Askey, and R. Roy. *Encyclopedia of Mathematics and its Applications. Vol. 71. Special Functions*. Cambridge University Press, 1999.

[8] L. Antiga, B. Ene-Iordache, and A. Remuzzi. Computational geometry for patient-specific reconstruction and meshing of blood vessels from mr and ct angiography. *Medical Imaging, IEEE Transactions on*, 22(5):674 –684, May 2003.

[9] L. Antiga and D. A. Steinman. Robust and objective decomposition and mapping of bifurcating vessels. *Medical Imaging, IEEE Transactions on*, 23(6):704 –713, june 2004.

[10] S. R. Aylward and E. Bullitt. Initialization, noise, singularities, and scale in height ridge traversal for tubular object centerline extraction. *IEEE Trans. Med. Imaging*, 21(2):61–75, February 2002.

[11] J. Babaud, A. P. Witkin, M. Baudin, and R. O. Duda. Uniqueness of the gaussian kernel for scale-space filtering. *IEEE Trans. Pattern Anal. Machine Intell.*, 8:26–33, 1 1986.

[12] R. Balm, R. Kaatee, J. Blankensteijn, W. Mali, and B. Eikelboom. Ct-angiography of abdominal aortic aneurysms after transfemoral endovascular aneurysm management. *European Journal of Vascular and Endovascular Surgery*, 2:182–188, 1996.

[13] M. Basu. Gaussian-based edge-detection methods - a survey. *IEEE Trans. Systems, Man and Cybernetics*, 32:252–260, 3 2002.

[14] S. Beucher and Ch. Lantuejoul. Use of watersheds in contour detection. In *Int. Workshop on Image Processing, Real-Time Edge and Motion Detection/Estimation*, 1979.

[15] L. Bezold. Coronary artery anomalies, Jan 2010.

[16] K. Bühler, P. Felkel, and A. La Cruz. Geometric methods for vessel visualization and quantification - a survey. In *Geometric Modelling for Scientific Visualization*, pages 399–420. Springer-Verlag, 2002.

[17] H. Blum. A transformation for extracting new descriptors of shape. In Weiant Wathen-Dunn, editor, *Models for the Perception of Speech and Visual Form*, pages 362–380. MIT Press, 1967.

[18] A. Borghi, N.B. Wood, R. H. Mohiaddin, and X.Y. Xu. 3D geometric reconstruction of thoracic aortic aneurysms. *BioMedical Engineering OnLine*, 5(59), 2006.

[19] T. Boskamp, D. Rinck, F. Link, B. Knmmerlen, G. Stamm, and P. Mildenberger. New vessel analysis tool for morphometric quantification and visualization of vessels in ct and mr imaging datasets. *Radiographics*, 24:287–297, 2004.

[20] S. Bouix, K. Siddiqi, and A. Tannenbaum. Flux driven automatic centerline extraction. *Medical Image Analysis*, 9(3):209–221, June 2005.

[21] R.N. Bracewell. *The Fourier Transform and its Applications, 3rd Ed.* McGraw-Hill, 2000.

[22] U. Brandes, M. Eiglsperger, I. Herman, M. Himsolt, and M. S. Marshall. Graphml progress report: Structural layer proposal. In *Graph drawing. International symposium No9, Vienna, LNCS*, volume 2265, pages 501–512, 2002.

[23] E. Bullitt, S. Aylward, K. Smith, S. Mukherji, M. Jiroutek, and K. Muller. Symbolic description of intracerebral vessels segmented from magnetic resonance angiograms and evaluation by comparison with x-ray angiograms. *Medical Image Analysis*, 5:157–169, 2001.

[24] E. Bullitt, G. Gerig, S. Aylward, S. Joshi, K. Smith, M. Ewend, and W. Lin. Vascular attributes and malignant brain tumors. In *Medical Image Computing and Computer-Assisted Intervention (MICCAI 2003), LNCS*, volume 2878, pages 671–9. Springer, 2003.

[25] E. Bullitt, I. Jung, K. Muller, G. Gerig, S. Aylward, S. Joshi, K. Smith, W. Lin, and M. Ewend. Determining malignancy of brain tumors by analysis of vessel shape. In *Medical Image Computing and Computer-Assisted Intervention (MICCAI 2004), LNCS*, volume 3217, pages 645–653, 2004.

[26] E. Bullitt, K.E. Muller, I. Jung, W. Lin, and S. Aylward. Analyzing attributes of vessel populations. *Medical Image Analysis*, 9:39–49, 2005.

[27] Ali Can, Hong Shen, James N. Turner, Howard L. Tanenbaum, and Badrinath Roysam. Rapid automated tracing and feature extraction from retinal fundus images using direct exploratory algorithms. *IEEE Trans. Inform. Technol. Biomed*, 3:125–138, 1999.

[28] J. Canny. A computational approach to edge detection. *IEEE Trans. Pattern Analysis and Machine Intelligence,*, 8(6):679–698, 1986.

[29] J.F. Carrillo, M. Hernández-Hoyos, E.E. Dávila-Serrano, and M. Orkisz. Recursive tracking of vascular tree axes in 3d medical images. *Int. J. of Computer Assisted Radiology and Surgery*, 1(6):331–9, 2007.

[30] M. Couprie and G. Bertrand. Topological grayscale watershed transform. In *SPIE Vision Geometry VI*, volume 3168, pages 136–146, 1997.

[31] M. A. Creager, T. F. Lüscher, F. Cosentino, and J. A. Beckman. Diabetes and vascular disease: Pathophysiology, clinical consequences, and medical therapy: Part i. *Circulation*, 108:1527–32, 2003.

[32] G. Cumming, L. K. Harding, K. Horsfield, K. Prowse, S. S. Singhal, and M. J. Woldenberg. Morphological aspects of the pulmonary circulation and of the airway. *Fluid Dynamics of Blood Circulation and Respiratory Flow*, 65:230–6, 1970.

[33] P.E. Danielsson. Euclidean distance mapping. *Computer Graphics and Image Processing*, 14:227–248, 1980.

[34] Per-Erik Danielsson and Qingfen Lin. Efficient detection of second-degree variations in 2D and 3D images. *Journal of Visual Communication and Image Representation*, 12:255–305, 2001.

[35] B. Das, Y. Mallya, S. Srikanth, and R. Malladi. Aortic thrombus segmentation using narrow band active contour model. In *In Proc. IEEE Eng. Med. Biol. Soc.*, volume 1, pages 408–11, 2006.

[36] M. de Bruijne, B. van Ginneken, M.A. Viergever, and W.J. Niessen. Interactive segmentation of abdominal aortic aneurysms in cta images. *Medical Image Analysis*, 8:127–138, 2004.

[37] T. Deschamps and L. Cohen. Deschamps, t., cohen, l., 2001. fast extraction of minimal paths in 3d images and applications to virtual endoscopy. med. image anal. 5 (4), 281-299. *Medical Image Analysis*, 5(4):281–299, 2001.

[38] E. W. Dijkstra. A note on two problems in connection with graphs. *Numerische Mathematik*, pages 269–271.

[39] G. Dos-Reis and J. Järvi. What is generic programming? In *Proc. of the First International Workshop of Library-Centric Software Design (LCSD'05)*, Oct 2005.

[40] David Eberly. *Ridges in Image and Data Analysis*. Kluwer Academic Publishers, 1996.

[41] M. Erdt, M. Raspe, and M. Suehling. Automatic hepatic vessel segmentation using graphics hardware. In *Proc. 4th Int. Workshop on Medical Imaging and Augmented Reality*, MIAR'08, pages 403–412, Berlin, Heidelberg, 2008. Springer-Verlag.

[42] P. Felkel, A. Kanitsar, A. L. Fuhrmann, and R. Wegenkittl. Surface models of tube trees. In *In Computer Graphics International*, pages 70–77, 2002.

[43] L.M.J. Florack, B. M. Haar Romeny, J.J. Koenderink, and M.A. Viergever. Scale and the differential structure of images. *Image and Vision Computing*, 10(6):376–388, 1992.

[44] J. Folkman. Incipient angiogenesis. *J. Natl. Cancer Inst.*, 92:94–5, 2000.

[45] A. Frangi, W. Niessen, R. Hoogeveen, T. van Walsum, and M. Viergever. Model-based quantitation of 3-d magnetic resonance angiographic images. *IEEE Trans. Medical Imaging*, 18(10):946–956, 1999.

[46] A. Frangi, W. J. Niessen, P. J. Nederkoorn, O. van Elgersma, and M. A. Viergever. Three-dimensional model-based stenosis quantification of the carotid arteries from contrast-enhanced mr angiography. In *IEEE Workshop on Mathematical Methods in Biomedical Image Analysis*, 2000.

[47] A.F. Frangi, W.J. Niessen, K.L. Vincken, and M.A. Viergever. Multiscale vessel enhancement filtering. In *Medical Image Computing and Computer-Assisted Interventation (MICCAI)*, pages 130–137. Springer-Verlag, 1998.

[48] W.T. Freeman and E.H. Adelson. The design and use of steerable filters. *IEEE Trans. Pattern Anal. Machine Intell.*, 13:891–906, 9 1991.

[49] I. Fridolin and L. G. Lindberg. Optical non-invasive technique for vessel imaging: I. experimental results. *Phys. Med. Biol.*, 45(12):3765–78, 2000.

[50] G.S.K. Fung, S.K. Lam, SW.K. Cheng, and K.W. Chow. On stent-graft models in thoracic aortic endovascular repair: A computational investigation of the hemodynamic factors. *Computers in Biology and Medicine*, 38(4):484 – 489, 2008.

[51] E. Gamma, R. Helm, R. Johnson, and J. Vlissides. *Design Patterns: Elements of Reusable Object-Oriented Software*. Addison-Wesley, 2000.

[52] G. Gerig, T. Koller, G. Székely, C. Brechbuhler, and O. Kubler. Symbolic description of 3d structures applied to cerebral vessel tree obtained from mr angiography volume data. In *Information Processing in Medical Imaging '93, LNCS 687*, pages 94–111, 1993.

[53] R.C. González and R.E. Woods. *Digital Image Processing, 2nd Ed.* Prentice Hall, 2002.

[54] M. Hernández-Hoyos, P. Orlowski, E. Piatkowska-Janko, P. Bogorodzki, and M. Orkisz. Vascular centerline extraction in 3d mr angiograms for phase contrast mri blood flow measurement. *Int. J. Computer Assisted Radiology and Surgery*, 1(1):51–61, March 2006.

[55] M. Heron, D. L. Hoyert, S. L. Murphy, J. Xu, K. D. Kochanek, and B. Tejada-Vera. Deaths: Final data for 2006. Report, Division of Vital Statistics, U.S. Dep. of Health and Human Services, 2009.

[56] J.A. Hertz, A.S. Krogh, and R.G. Palmer. *Introduction To The Theory Of Neural Computation, Volume I (Santa Fe Institute Studies in the Sciences of Complexity).* Westview Press, 1991.

[57] J. Holash, P. C. Maisonpierre, D. Compton, P. Boland, C. R. Alexander, D. Zagzag, G. D. Yancopoulos, and S. J. Wiegand. Vessel cooption, regression and growth in tumors mediated by angiopoietins and vegf. *Science*, 284(5422):1994–8, 1999.

[58] R.M. Hoogeveen, C.J. Bakker, and M.A. Viergever. Limits to the accuracy of vessel diameter measurement in mr angiography. *J. Magnetic Resonance Imaging*, 8:1228–35, 6 1998.

[59] K. Horsfield. Morphometry of the small pulmonary arteries in man. *Circulation Research*, 42:593–7, 1978.

[60] K. Horsfield. Diameters, generations, and orders of branches in the bronchial tree. *Journal of Applied Physiology*, 68:457–461, 1990.

[61] K. Horsfield and I. Gorden. Morphometry of pulmonary veins in man. *Lung*, 159:211–8, 1981.

[62] W. Huang, R. T. Yen, M. McLaurine, and G. Bledsoe. Morphometry of the human pulmonary vasculature. *Journal of Applied Physiology*, 81:2123–33, 1996.

[63] Ng L. Cates J. Ibanez L., Schroeder W. *The ITK Software Guide*. Kitware Inc., 2003.

[64] S. Izumiya and N. Takeuchi. Generic properties of helices and bertrand curves. *Journal of Geometry*, 74:97–109, 2002.

[65] M. Jacob and M. Unser. Design of steerable filters for feature detection using canny-like criteria. *IEEE Trans. Pattern Analysis and Machine Intelligence*, 26:1007–19, 8 2004.

[66] R. K. Jain. Normalizing tumor vasculature with anti-angiogenic therapy: a new paradigm for combination therapy. *Nature Med.*, 7:987–998, 2001.

[67] D. G. Kang, D. C. Suh, and J. B. Ra. Three-dimensional blood vessel quantification via centerline deformation. *IEEE Trans. Medical Imaging*, 28(3):405–414, March 2009.

[68] K. L. Karau, G. S. Krenz, and C. A. Dawson. Branching exponent heterogeneity and wall shear stress distribution in vascular trees. *AJP Heart and Circulatory Physiology*, 280:1256–63, 2001.

[69] G. S. Kassab. Scaling laws of vascular trees: of form and function. *AJP Heart and Circulatory Physiology*, 290:894–903, 2006.

[70] G. S. Kassab, C. A. Rider, N. J. Tang, and Y. C. Fung. Morphometry of pig coronary arterial trees. *Am. J. Physiol.*, 265:350–365, 1993.

[71] C. Kirbas and F. Quek. A review of vessel extraction techniques and algorithms. *ACM Computing Surveys*, 36(2):81–121, June 2004.

[72] A. Klein, W. K. J. Renema, L. J. Oostveen, L. J. Schultze Kool, and C. H. Slump. A segmentation method for stentgrafts in the abdominal aorta from ecg-gated cta data. In X. P. Hu; A. V. Clough, editor, *Proc. SPIE Medical Imaging 2008: Physiology, Function, and Structure from Medical Images*, volume 6916, 2008.

[73] R. Klein, A. Schilling, and W. Strasser. Reconstruction and simplification of surfaces from contours. In *Proc. 7th Pacific Conf. on Comp. Graphics and App.*, 1999.

[74] J.J. Koenderink. The structure of images. *Biological Cybernetics*, 50:363–370, 1984.

[75] A. J. F. Kok and R. van Liere. A multimodal virtual reality interface for 3d interaction with vtk. *Knowledge and Information Systems*, 13(2):197–219, Oct 2007.

[76] T. Koller, G. Gerig, and G. Székely. Object-centered description for analysis and display of the cerebral vascularity. In H.U. Lemke et al., editor, *Computer Assisted Radiology CAR'95*, pages 183–188. Springer-Verlag, 1995.

[77] T. M. Koller, G. Gerig, G. Székely, and D. Dettwiler. Multiscale detection of curvilinear structures in 2-d and 3-d image data. In *In Proc. Fifth International Conference on Computer Vision (ICCV'95)*, pages 864–9. IEEE Computer Society Press, 1995.

[78] K. Krissian, G. Malandain, N. Ayache, R. Vaillant, and Y. Trousset. Model based detection of tubular structures in 3d images. *Computer Vision and Image Understanding*, 80(2):130–171, 2000.

[79] K. Krissian, G. Malandain, N. Ayache, R. Vaillant, and Y. Trousset. Model based detection of tubular structures in 3d images. *Computer Vision and Image Understanding*, 80(2):130–171, 2000.

[80] R.J.F. Laheij, J. Buth, P.L. Harris, F.L. Moll, W.J. Stelter, and E.L.G. Verhoeven. Need for secondary interventions after endovascular repair of abdominal aortic aneurysm. intermediate-term follow-up results of a european collaborative registry. *British Journal of Surgery*, 87(12):1666–73, 2002.

[81] T. Lange, S. Eulenstein, M. Huumlnerbein, and P. M. Schlag. Vessel-based non-rigid registration of mr/ct and 3d ultrasound for navigation in liver surgery. *Computer Assisted Surgery*, 8(5):228–240, 2003.

[82] M.W.K. Law and A.C.S. Chung. Three dimensional curvilinear structure detection using optimally oriented flux. In P. Torr D. Forsyth and A. Zisserman, editors, *In Proc. European Conference of Computer Vision (ECCV'08)*, volume LNCS 5305, pages 368–82, 2008.

[83] J. Lee, P. Beighley, E. Ritman, and N. Smith. Automatic segmentation of 3d micro-ct coronary vascular images. *Medical Image Analysis*, 11(6):630–647, 2007.

[84] K. Lee, R.K. Johnson, Y. Yin, A. Wahle, M.E. Olszewski, T.D. Scholz, and M. Sonka. Three-dimensional thrombus segmentation in abdominal aortic aneurysms using graph search based on a triangular mesh. *Computers in Biology and Medicine*, 40(3):271 – 278, 2010.

[85] J. H. Legarreta, F. Boto, I. Macía, J. Maiora, G. García, C. Paloc, M. Graña, and M. de Blas. Hybrid decision support system for endovascular aortic aneurism repair follow-up. In *Proc. of 5th Int. Conf. on Hybrid Artificial Intelligent Systems (HAIS'10)*, page Submitted, 2010.

[86] D. Lesage, E. Angelini, I. Bloch, and G. Funka-Lea. Medial-based bayesian tracking for vascular segmentation: Application to coronary arteries in 3d ct angiography. In *IEEE Int. Symp. Biomed. Imaging (ISBI'08)*, pages 268–271, 2008.

[87] D. Lesage, E.D. Angelini, I. Bloch, and G. Funka-Lea. A review of 3d vessel lumen segmentation techniques: Models, features and extraction schemes. *Medical Image Analysis*, 13(6):819–845, December 2009.

[88] D. Lesage, E.D. Angelini, I. Bloch, and G. Funka-Lea. A review of 3d vessel lumen segmentation techniques: Models, features and extraction schemes. *Medical Image Analysis*, 13(6):819–845, December 2009.

[89] Q. Lin. *Enhancement, Extraction and Visualization of 3D Volume Data*. PhD thesis, Institute of Technology, Linköpings Universitet, 2003.

[90] T. Lindeberg. Scale-space for discrete signals. *IEEE Trans. Pattern Analysis and Machine Intelligence*, 12:234–254, 3 1990.

[91] T. Lindeberg. Discrete derivative approximations with scale-space properties: A basis for low-level feature extraction. *J. Math. Imaging Vision*, 3:349–376, 4 1993.

[92] T. Lindeberg. Discrete derivative approximations with scale-space properties: A basis for low-level feature extraction. *J. Math. Imaging Vision*, 3:349–376, 1993.

[93] T. Lindeberg. *Scale-space Theory in Computer Vision*. Kluwer Academic Publishers, 1994.

[94] T. Lindeberg. Edge detection and ridge detection with automatic scale selection. *Int. J. of Computer Vision*, 30:465–470, 1996.

[95] T. Lindeberg. Edge detection and ridge detection with automatic scale selection. *Int. J. Comput. Vision*, 30:117–156, 1998.

[96] Tony Lindeberg. Feature detection with automatic scale selection. *International Journal of Computer Vision*, 30:79–116, 1998.

[97] S. Liu, A. H. B. Duffy, R. I. Whitfield, and I. M. Boyle. Integration of decision support systems to improve decision support performance. *Knowledge and Information Systems*, 22(3):261–286, Feb 2009.

[98] W. E. Lorensen and H. E. Cline. Marching cubes: A high resolution 3d surface construction algorithm. *Computer Graphics, Vol. 21, Nr. 4, July 1987*, 21(4):163–9, 1987.

[99] L.M. Lorigo, O. Faugeras, W.E.L. Grimson, R. Keriven, R. Kikinis, and C.F. Westin. Co-dimension 2 geodesic active contours for mra segmentation. In *IPMI*, pages 126–139, 1999.

[100] D. Lowe. Object recognition from local scale-invariant features. In *In Proc. Int. Conf. on Computer Vision (ICCV'99)*, 1999.

[101] M M. de Bruijne, B. van Ginneken, W. J. Niessen, M. Loog, and M. Viergever. Model-based segmentation of abdominal aortic aneurysms in cta images. In *Proc. SPIE Med. Imaging*, volume 5032, pages 1560–71, 2003.

[102] I. Macía. Generalized computation of gaussian derivatives using itk. *Insight Journal*, 8, Jul-Dec 2007.

[103] I. Macía. Generalized computation of gaussian derivatives using itk. *The Insight Journal*, Dec. 2007.

[104] I. Macía, M. Graña, C. Paloc, and F. Boto. Neural network-based detection of type ii endoleaks in cta images after endovascular repair. *Computers in Biology and Medecine*, page Submitted, 2010.

[105] I. Macía, J. H. Legarreta, C. Paloc, M. Graña, J. Maiora, G. García, and M. de Blas. Segmentation of abdominal aortic aneurysms in ct images using a radial model approach. In E. Corchado; H. Yin, editor, *Proc. Intelligent Data Engineering and Automated Learning, 10th Int. Conference (IDEAL'09)*, volume 5788 of *Lecture Notes in Computer Science (LNCS)*, pages 664–671, Burgos, Spain, Sep 2009. Springer.

[106] I. Macía, D. Wald, and C. Paloc. Extraction and analysis of patient-specific hepatic anatomy from mr images. In *Int. J. of Computer Assisted Radiology and Surgery. Proc. of the 22st Int. Congress and Exhibition (CARS'08)*, volume Suppl. 1, pages 399–401, Barcelona, Spain, Jun 2008.

[107] J. Maiora, G. García, I. Macía, J. H. Legarreta, F. Boto, C. Paloc, M. Graña, and J. Sánchez. Thrombus volume change visualization after endovascular abdominal aortic aneurysm repair. In *Proc. of 5th Int. Conf. on Hybrid Artificial Intelligent Systems (HAIS'10)*, page Submitted, 2010.

[108] J. Maiora, G. García, I. Macía, J. H. Legarreta, C. Paloc, M de Blas, and M. Graña. Thrombus change detection after endovascular abdominal aortic aneurysm repair. In *Proc. of Computer Assisted Radiology and Surgery (CARS'10)*, page In press, 2010.

[109] J. Maiora, G. García, A. Tapia, I. Macía, J. H. Legarreta, C. Paloc, M. Graña, and M. de Blas. Stent graft change detection after endovascular abdominal aortic aneurysm repair. In E. Corchado; H. Yin, editor, *Intelligent Data Engineering and Automated Learning - IDEAL 2009 10th Internationa Conference, Proceedings*, volume 5788 of *Lecture Notes in Computer Science (LNCS)*, page 826, Universidad de Burgos, Burgos, Spain, Sep 2009. Springer.

[110] D. Marr and E. Hildreth. Theory of edge detection. *Proc. of the Royal Society of London. Series B, Biological Sciences.*, 207(1167):187–217, 1980.

[111] K. Martin and B. Hoffman. *Mastering CMake 4th Edition*. Kitware, Inc., USA, 2008.

[112] J. H. Metzena, T. Krögerb, A. Schenk, S. Zidowitz, H. O. Peitgen, and X. Jiang. Matching of anatomical tree structures for registration of medical images. *Image and Vision Computing*, 27(7):923–933, Jun 2009.

[113] J. Mille and L. D. Cohen. Deformable tree models for 2d and 3d branching structures extraction. In *IEEE Conf. on Computer Vision and Pattern Recognition Workshops*, 2009.

[114] R. D. Millán, L. Dempere-Marco, J. M. Pozo, J. R. Cebral, and A. F. Frangi. Morphological characterization of intracranial aneurysms using 3-d moment invariants. *IEEE Trans Med Imaging*, 26(9):1270–82, 2007.

[115] M. Miyazaki, N. Ichinose, S. Sugiura, H. Kanazawa, Y. Machida, and Y. Kassai. A novel mr angiography technique: Speed acquisition using half-fourier rare. *Journal of Magnetic Resonance Imaging*, 8(2):505–7, 2005.

[116] C. Murray. The physiological principle of minimum work, i: the vascular system and the cost of blood volume. *Proc. Natl. Acad. Sci. USA*, 12(3):207–214, 1926.

[117] M. Näf. *3D Voronoi Skeletons: a Semicontinuous Implementation of the 'Symmetric Axis Transform' in 3D Space*. PhD thesis, ETH Zürich, 1996.

[118] O. Nilsson, D. Breen, and K. Museth. Surface reconstruction via contour metamorphosis: An eulerian approach with lagrangian particle tracking. In *In Proc. 16th IEEE Visualization (VIS'05)*, 2005.

[119] D. A. Nordsletten, S. Blackett, M. D. Bentley, E. L. Ritman, and N. P. Smith. Structural morphology of renal vasculature. *AJP Heart and Circulatory Physiology*, 291:296–309, 2006.

[120] T. O'Donnell, T. Boult, X. Fang, and A. Gupta. The extruded generalized cylinder: A deformable model for object recovery. In *Proc. of Computer Vision and Pattern Recognition (CVPR'94)*, pages 174–181, 1994.

[121] S. Oka and M. Nakai. Optimality principle in vascular bifurcation. *Biorheology*, 24(6):737–751, 1987.

[122] S. Olabarriaga, M. Breeuwer, and W. J. Niessen. Minimum cost path algorithm for coronary artery central axis tracking in ct images. In *Med. Image Computing and Computer Assisted Intervention (MICCAI'03)*, 2003.

[123] S.D. Olabarriaga, J.M. Rouet, M. Fradkin, M. Breeuwer, and W.J. Niessen. Segmentation of thrombus in abdominal aortic aneurysms from cta with nonparametric statistical grey level appearance modelling. *IEEE Trans. Med. Imag.*, 24:477– 485, 4 2005.

[124] M. Orkisz, L. Flórez-Valencia, and M. Hernández-Hoyos. Models, algorithms and applications in vascular image segmentation. *Machine Graphics and Vision*, 17(1/2):5–33, 2008.

[125] S. Osher and J. A. Sethian. Fronts propagating with curvature-dependent speed: Algorithms based on hamilton-jacobi formulations. *J. Comput. Phys.*, 79:12–49, 1988.

[126] M.A. Oskoei and H. Hu. A survey on edge detection methods, technical report ces-506. Technical report, University of Essex, 2010.

[127] K. Palágyi, E. Sorantin, E. Balogh, A. Kuba, C. Halmai, B. Erdohelyi, and K. Hausegger. A sequential 3d thinning algorithm and its medical applications. In *Proc. of the 17th Int. Conf. on Information Processing in Medical Imaging (IPMI'01), LNCS*, volume 2082, pages 409–415. Springer Verlag, 2001.

[128] M. Paradowski, H. Kwasnicka, and K. Borysewicz. Capillary blood vessel tortuosity measurement using graph analysis. In *Knowledge-Based and Intelligent Information and Engineering Systems, 13th Int. Conf. (KES 2009)*, 2009.

[129] J. Park and S. Lee. Keyword search in relational databases. *Knowledge and Information Systems*, In print, 2010.

[130] M. Piccinelli, A. Veneziani, D. A. Steinman, A. Remuzzi, and L. Antiga. A framework for geometric analysis of vascular structures: Application to cerebral aneurysms. *Transactions on Medical Imaging*, 28(8):1141 –55, Aug 2009.

[131] S. M. Pizer, D. Eberly, B. S. Morse, and D. S. Fritsch. Zoom-invariant figural shape: The mathematics of cores. *Computer Vision and Image Understanding*, 69:55–71, 1998.

[132] S. M. Pizer, K. Siddiqi, G. Székely, J. N. Damon, and S. W. Zucker. Multi-scale medial loci and their properties. *International Journal of Computer Vision*, 55(2-3):155–179, 2003.

[133] T. Pock, C. Janko, R. Beichel, and H. Bischof. Multiscale medialness for robust segmentation of 3d tubular structures. In *10th Computer Vision Winter Workshop*, 2005.

[134] A. Puig, D. Tost, and I. Navazo. Hybrid model for vascular tree structures. In Liere R. van Leeuw, W. de, editor, *Data Visualization 2000 : Joint Eurographics and IEEE TCVG Symposium on Visualization, Amsterdam, The Netherlands*, pages 125–135. Springer-Verlag, 2000.

[135] F.K.H. Quek and C. Kirbas. Vessel extraction in medical images by wave-propagation and traceback. *IEEE Trans. Med. Imaging*, 20(2):117–131, February 2001.

[136] J. R. Reichenbach, R. Venkatesan, D. J. Schillinger, D. K. Kido, and E. M. Haacke. Small vessels in the human brain: Mr venography with deoxyhemoglobin as an intrinsic contrast agent. *Radiology*, 204:272–7, 1997.

[137] E. L. Ritman. Micro-computed tomography of the lungs and pulmonary-vascular system. *Proc. of the Am. Thoracic Society*, 2:477–480, 2005.

[138] L. M. Sangalli and S. Vantini. Registration of functional data: Aligning inner carotid artery centerlines. In *Proceedings of the XLIV Riunione Scientifica Società Italiana di Statistica*, 2008.

[139] W. P. Santamore and A. A. Bove. Why arteries are the size they are. *Journal of Applied Physiology*, 104:1259, 2008.

[140] Y. Sato, S. Nakajima, N. Shiraga, H. Atsumi, S. Yoshida, T. Koller, G. Gerig, and R. Kikinis. 3d multi-scale line filter for segmentation and visualization of curvilinear structures in medical images. *Medical Image Analysis*, 2(2):143–168, June 1998.

[141] Y. Sato, S. Nakajima, N. Shiraga, H. Atsumi, S. Yoshida, T. Koller, G. Gerig, and R. Kikinis. 3d multi-scale line filter for segmentation and visualization of curvilinear structures in medical images. *Medical Image Analysis*, 2(2):143–168, June 1998.

[142] M. Schaap, C.T. Metz, T. van Walsum, A.G. van der Giessen, A.C. Weustink, N.R. Mollet, C. Bauer, H. Bogunovic, C. Castro, X. Deng, E. Dikici, T. O'Donnell, M. Frenay, O. Friman, M. Hernández Hoyos, P.H. Kitslaar, K. Krissian, C. Kühnel, M.A. Luengo-Oroz, M. Orkisz, Ö. Smedby, M. Styner, A. Szymczak, H. Tek, C. Wang, S.K. Warfield, Y. Zhang, S. Zambal, G.P. Krestin, and W.J. Niessen. Standardized evaluation methodology and reference database for evaluating coronary artery centerline extraction algorithms. *Medical Image Analysis*, 13(5):701–714, 2009.

[143] C. Scharlach. Ridges and the description of image structure. In *In Proc. V Conf. on Diff. Geom. and Vision*, 1992.

[144] W. Schroeder, K. Martin, and B. Lorensen. *The Visualization Toolkit: An Object-Oriented Approach to 3D Graphics*. Kitware, 4th edition edition, 2006.

[145] B. G. Schunck. Edge detection with gaussian filters at multiple scales. *In Proc. IEEE Comp. Soc. Work. Comp. Vis.*, pages 208–210, 1987.

[146] M. Schwarz, M. P. Nguyen, U. Kiencke, C. Heilmann, R. Klemm, C. Benk, F. Beyersdorf, and H. J. Busch. Integration of the circle of willis into avolio's model of the arterial hemodynamics. In *6th IASTED Int. Conf. on Biomedical Engineering*, 2008.

[147] H. P. Schwefel. *Evolution and Optimum Seeking*. Wiley, 1995.

[148] D. Selle, B. Preim, A. Schenk, and H. O. Peitgen. Analysis of vasculature for liver surgical planning. *IEEE Trans. Med. Imaging*, 21:1344–57, 2002.

[149] M. Shah, A. Sood, and R. Jain. Pulse and stair case edge models. *Comput. Vis. Graph. Image Process.*, 34:321–343, 1986.

[150] T. F. Sherman. On connecting large vessels to small: the meaning of murray's law. *Journal of General Physiology*, 78:431–453, 1981.

[151] J. Shum, E.S. DiMartino annd A. Goldhamme, D.H. Goldman, L.C. Acker, G. Patel, J.H. Ng, G. Martufi, and E.A. Finol. Semiautomatic vessel wall detection and quantification of wall thickness in computed tomography images of human abdominal aortic aneurysms. *Med. Phys.*, 37:638–48, 2010.

[152] K. Siddiqi and B. B. Kimia. A shock grammar for recognition. cvpr'96:507-513, san francisco, ca, ieee. In *IEEE Computer Vision and Pattern Recognition (CVPR'96)*, pages 507–13, 1996.

[153] K. Siddiqi and S. Pizer. *Medial Representations: Mathematics, Algorithms and Applications*. Springer, 2008. ISBN 978-1402086571.

[154] S. Singhal, R. Henderson, K. Horsfield, K. Harding, and G. Cumming. Morphometry of the human pulmonary arterial tree. *Circulation Research*, 33:190–7, 1973.

[155] F. M. Sones and E. K. Shirey. Cine coronary arteriography. *Modern Concepts of Cardiovascular Disease*, 31:735–8, 1962.

[156] C. Steger. Extracting curvilinear structures: A differential geometric approach. In *Proc. 4th European Conference on Computer Vision*, pages 630–641. Springer-Verlag, 1996.

[157] A. N. Strahler. Hypsometric (area-altitude) analysis of erosional topology. *Geological Society of America Bulletin*, 63(11):1117–42, 1952.

[158] S.W. Stravopoulos and S.R. Charagundla. Imaging techniques for detection and management of endoleaks after endovascular aortic aneurysm repair. *Radiology*, 243(3):641–55, 2007.

[159] M. Styner, C. Brechbuhler, G. Székely, and G. Gerig. Parametric estimate of intensity inhomogeneities applied to mri. *Trans. Med. Imag*, 19(3):153–165, 2000.

[160] M. Subasic, S. Loncaric, and E. Sorantin. 3d image analysis of abdominal aortic aneurysm. In *In Proc. SPIE Med. Imag. Proc.*, volume 4684, pages 1681–9, 2002.

[161] A.J. Tolia, R. Landis, P. Lamparello, R. Rosen, and M. Macari. Type II endoleaks after endovascular repair of abdominal aortic aneurysms: Natural history. *Radiology*, 235:683–6, May 2005.

[162] R. Torii, M. Oshima, T. Kobayashi, K. Takagi, and T. E. Tezduyar. Influence of wall elasticity in patient-specific hemodynamic simulations. *Computers & Fluids*, 36(1):160–8, 2007.

[163] G.R. Upchurch and T.A Schaub. Abdominal aortic aneurysm. *Am. Fam. Physician*, 73(7):1198–204, April 2006.

[164] C. van Bemmel, O. Wink, B. Verdonck, M. Viergever, and W. Niessen. Blood pool contrast-enhanced mra: Improved arterial visualization in the steady state. *IEEE Trans. Medical Imaging*, 22(5):645–652, 2003.

[165] I. van Herzeele, R. Aggarwal, and I. Malik. Use of simulators in vascular training. *Heart*, 95:613–4, 2009.

[166] P. M. A. van Ooijen, G. de Jonge, and M. Oudkerk. Coronary fly-through or virtual angioscopy using dual-source mdct data. *Eur Radiol.*, 17(11):2852–59, Nov 2007.

[167] D. Vukadinovic, T. van Walsum, R. Manniesing, S. Rozie, R. Hameeteman, T. T. de Weert, A. van der Lugt, and W. J. Niessen. Segmentation of the outer vessel wall of the common carotid artery in cta. *IEEE Transactions on*, 29(1):65–76, Jan. 2010.

[168] S. Wang, J. Chen, X. Yang, and X. Zhang. Patient-specific hemodynamic analysis for cerebral aneurysm. In *Proc. Bioinformatics and Biomedical Engineering (ICBBE'08), 2nd Int. Conf. on*, 2008.

[169] Z. Weiping and S. Huazhong. Detection of cerebral vessels in mra using 3d steerable filters. In *In Proc. IEEE Engineering in Medicine and Biology, 27th Annual Conference*, pages 3249–52, 2005.

[170] J. Wever, J. Blankensteijn, W. Mali, and B. Eikelboom. Maximal aneurysm diameter follow-up is inadequate after endovascular abdominal aortic aneurysm repair. *European J. of Vasc. and Endovasc. Surg.*, 20:177–182, 2 2000.

[171] J.J. Wever, J.D. Blankensteijn, J.C. Van Rijn, I.A. Broeders, B.C. Eikelboom, and Mali WP. Inter- and intraobserver variability of ct measurements obtained after endovascular repair. *American Journal of Roentgenology*, 175:1279–82, 2000.

[172] R.T. Whitaker and X. Xue. Variable-conductance, level-set curvature for image denoising. In *International Conference on Image Processing (ICIP'01)*, volume 3, pages 142–145, 2001.

[173] G.H. White, J. May, and R.C. Waugh. Type i and type ii endoleak: A more useful classification for reporting results of endoluminal aaa repair. *Journal of Endovascular Surgery*, 5(4):378–80, 1998.

[174] G.H. White, J. May, R.C. Waugh, X. Chaufour, and W. Yu. Type iii and type iv endoleak: Toward a complete definition of blood flow in the sac after endoluminal aaa repair. *Journal of Endovascular Surgery*, 5(4):305–9, 1998.

[175] C. M. Wilson, K. D. Cocker, M. J. Moseley, C. Paterson, S. T. Clay, W. E. Schulenburg, M. D. Mills, A. L. Ells, K. H. Parker, G. E. Quinn, A. R. Fielder, and J. Ng. Computerized analysis of retinal vessel width and tortuosity in premature infants. *Investigative Ophthalmology and Visual Science*, 49(8):3577–3585, 2008.

[176] O. Wink, W.J. Niessen, and M.A. Viergever. Multiscale vessel tracking. *IEEE Trans. Med. Imaging*, 23(1):130–133, 2004.

[177] T. Wischgoll, S. Choy J, and G. S. Kassab. Extraction of morphometry and branching angles of porcine coronary arterial tree from ct images. *AJP Heart and Circulatory Physiology*, 297:1949–55, 2009.

[178] A.P. Witkin. Scale-space filtering. *Proc. 8th Int. Joint Conf. Art. Intell.*, pages 1019–22, 1983.

[179] N. Witt, T. Y. Wong, A. D. Hughes, N. Chaturvedi, B. E. Klein, R. Evans, M. McNamara, S. A. M. Thom, and R. Klein. Abnormalities of retinal microvascular structure and risk of mortality from ischemic heart disease and stroke. *Hypertension*, 47:975–981, 2006.

[180] I.H. Witten, E. Frank, L. Trigg, M. Hall, G. Holmes, and S.J. Cunningham. Weka: Practical machine learning tools and techniques with java implementations. In Ko K. Kasabov N., editor, *ICONIP/ANZIIS/ANNES'99 Workshop on Emerging Knowledge Engineering and Connectionist-Based Information Systems*, pages 192–196, Dunedin, New Zealand, 1999.

[181] D. A. Woodrum, A. J. Romano, A. Lerman, U. H. Pandya, D. Brash, P. J. Rossman, L. O. Lerman, and R. L. Ehman. Vascular wall elasticity measurement by magnetic resonance imaging. *Magnetic Resonance in Medicine*, 56:593–600, 2006.

[182] S. Worz and K. Rohr. Segmentation and quantification of human vessels using a 3-d cylindrical intensity model. *IEEE Trans. on Image Processing*, 16(8):1994–2004, 2007.

[183] S. Wörz and K. Rohr. Segmentation and quantification of human vessels using a 3-d cylindrical intensity model. *IEEE Trans. Image Processing*, 16(8):1994–2004, 2007.

[184] X. Wu, V. Kumar, J. R. Quinlan, J Ghosh, Q. Yang, H. Motoda, G. J. McLachlan, A. Ng, B. Liu, P. S. Yu, Z. H. Zhou, M. Steinbach, D. J. Hand, and D. Steinberg. Top 10 algorithms in data mining. *Knowledge and Information Systems*, 14(1):1–37, 2008.

[185] J. Yang, L. X. Yu, M. Y. Rennie, J. G. Sled, and R. M. Henkelman. Comparative structural and hemodynamic analysis of vascular trees. *AJP Heart and Circulatory Physiology*, 298:1249–59, 2010.

[186] Q. Yang, J. Liu, S. R. S. Barnes, Z. Wu, K. Li, J. Neelavalli, J. Hu, and E. M. Haacke. Imaging the vessel wall in major peripheral arteries using susceptibility-weighted imaging. *Journal of Magnetic Resonance Imaging*, 30(2):357–365, 2009.

[187] T. S. Yoo, M. J. Ackerman, W. E. Lorensen, W. Schroeder, V. Chalana, S. Aylward, D. Metaxas, and R. Whitaker. Engineering and algorithm design for an image processing api: a technical report on itk - the insight toolkit. *Stud. Health. Technol. Inform.*, 85:586–592, 2002.

[188] A. L. Yuille and T. A. Poggio. Scaling theorems for zero-crossings. *IEEE Trans. Pattern Analysis and Machine Intelligence*, 8:15–25, 1986.

[189] L. Zhou, M. S. Rzeszotarski, L. J. Singerman, and J. M. Chokreff. The detection and quantification of retinopathy using digital angiogram. *IEEE Trans. Med. Imaging*, 13:619–626, 1994.

[190] Y. Zhou, G. S. Kassab, and S. Molloi. On the design of the coronary arterial tree: a generalization of murray's law. *Phys. Med. Biol.*, 44:2929–45, 1999.

[191] F. Zhuge, G.D. Rubin, S. Sun, and S. Napel. An abdominal aortic aneurysm segmentation method: level set with region and statistical information. *Med. Phys.*, 33:1440–53, 5 2006.